Multimodal *in vivo* evaluation of experimental therapies for myocardial infarction

Thesis submitted for the degree of Doctor of Philosophy

University College London

Zhiping Feng

Declaration

‘I, Zhiping Feng confirm that the work presented in this thesis has been composed solely by myself. Except where states otherwise by reference or acknowledgment, I confirm that this has been indicated in the thesis.’

Signature:……. ……. Date:

Acknowledgement

I would like to convey my most profound appreciation to my primary supervisor, Professor Daniel Stuckey, for his immeasurable guidance, unwavering support, and limitless patience throughout my entire PhD journey. His professional expertise, insightful feedback, and constant encouragement have always been indispensable for my advancement. Likewise, I am also sincerely grateful to my secondary supervisor Professor Tammy Kalber for continuously supporting, advising and encouraging me. Her mentorship has been invaluable throughout this journey. Thank you both for believing in me and inspiring me.

I am also thankful to my colleagues at CABI and the technical assistance I received from Imperial College London I particularly wish to acknowledge Dr Mohamed Bellahcene, who instructed and trained me in the surgical skills for developing myocardial infarction animal models. His invaluable guidance and counsel facilitated my rapid growth as an independent researcher. I am deeply grateful to the leader of CABI, Professor Mark Lythgoe, for his expert advice, incisive insights, and encouragement. Special thanks are extended to Dr Stephen Patrick for his expertise in biomaterial labelling and tracking, as well as guidance on data presentation; Dr Annalisa Bettini for her suggestions on thesis writing and data analysis; Adama Saccoh, Dr Emily Lupton, Shahrani Janudin, and everyone at CABI for providing a supportive and inspiring environment that has been critical for my progression.

A heartfelt thank you to Funds for Women Graduates, Henry Lester Trust, and Great Britain-China Educational Trust for offering me financial support.

Lastly, I express my profound gratitude to my family. Every member of my family has provided limitless patience, support, encouragement, and faith in me. Their support has been a source of strength and motivation during the challenging time.

Abstract

Myocardial infarction (MI) remains a leading cause of mortality worldwide. Current clinical therapies alleviate symptoms and slow progression but cannot regenerate damage. Consequently, various regenerative therapies, including stem cell-based, biomaterial-based, and gene transfer—have been developed to promote cardiac regeneration.

Here I established a mouse model of myocardial infarction and used advanced four-dimensional ultrasound and speckle tracking echocardiography to quantify dysfunction. The model was then used to evaluate cells, biomaterial and gene therapies for MI.

To improve stem cell delivery, an alginate patch was developed which could be injected under ultrasound-guidance. Patches were radiolabeled with ^{111}Indium allowing their location to be monitored using single-photon emission computed tomography (SPECT). Patches injected under ultrasound guidance did not remain on the epicardium, so iterative modifications to the patch formulation and delivery method were tested with SPECT used to determine delivery success. An adhesive chitosan-coated patch was developed which could be surgically attached to the epicardium and remained in location for over 7 days. Luciferase expressing epicardial cells were loaded onto ^{111}Indium labeled patches and attached to the epicardium. SPECT and bioluminescence imaging demonstrated that the patch remained on-target and cells remained viable over 7 days, highlighting how multimodal imaging can be useful in optimizing delivery of therapeutic cells.

To investigate the activation of cardiomyocyte cycling via adeno-associated virus (AAV)-gene therapy, I injected AAVs encoding an activator, and a luciferase reported of the YAP pathway. Bioluminescence imaging identified *in vivo* activation of the YAP pathway, whilst ultrasound and MRI identified focal hyperplasia and deterioration of cardiac function after YAP activation. This multimodal *in vivo* system can monitor gene expression and resultant changes in cardiac function, allowing optimization of gene therapies.

This thesis shows how multimodal imaging can be used for minimally invasive

delivery and direct monitoring of therapeutics in combination with accurate functional measurements, making an ideal platform for developing therapies.

Impact Statement

Cardiomyocyte regeneration, the process of replacing damaged heart muscle cells, continues to present a significant challenge in the treatment of MI. To address this, this thesis explored experimental therapies, including stem cell-based, biomaterial-based, and gene transfer approaches. This research aimed to enhance therapeutic delivery efficiency via ultrasound guidance injection and validate these strategies using multimodal imaging techniques.

In this thesis, a consistent and robust MI animal model was first established with optimized surgical procedures. This surgical methodology ensures the reproducibility and reliability of subsequent experiments aimed at validating advanced ultrasound techniques and evaluating potential therapeutic interventions. Then advanced ultrasound techniques such as 4D ultrasound and STE have been validated as reliable tools for evaluating experimental therapies with detailed assessments of structural abnormalities in the heart and regional cardiac function, contributing to enhanced research outcomes. The surgical model has also been used in a range of collaborative projects which will result in high impact publications across different fields of heart disease and regenerative medicine.

In the third part of this project, a shape-memory patch has been developed and optimized with chitosan coating to serve as a promising stem-cell carrier, advancing regenerative therapies of MI by targeted and controlled delivery of therapeutic stem cells. Meanwhile, minimally invasive ultrasound-guided delivery was performed and tested for precise SMP placement. This technique overcomes the limitations associated with traditional invasive delivery methods. Under the guidance of real-time imaging, it enables accurate delivery of the biomaterial within the target tissue, thereby enhancing treatment efficacy while minimizing patient discomfort and recovery time. Furthermore, a multimodal imaging system was established with SPECT-CT and BLI to track and localize the implants and monitor luciferase-expressing stem cells *in vivo*, respectively. This integrated imaging approach addresses a critical need in current research by enabling comprehensive visualization of both the implanted biomaterials and the behaviours of labelled stem cells over time within living organisms. This rapid and translational imaging platform has a broad-reaching impact across diverse

applications utilizing alginate-based biomaterials for therapeutic purposes.

In the last part of my thesis, AAV-mediated gene transfer was delivered via ultrasound-guided injection and the biodistribution of AAV was tracked serially using BLI. Meanwhile, MRI and ultrasound were performed to assess the structural and functional alterations within the heart following gene therapy. Despite the absence of promising results in terms of the improvement of cardiac function and regenerative effect, the multimodal imaging system established here allows for the first time serial, *in vivo* monitoring of pathway activation by a gene therapy and could have wide-ranging applications for enhancing therapies whose goal is to modulate expression of therapeutics or disease pathways.

In summary, this work addresses the key challenges confronted by current studies, namely the invasive or non-targeted delivery of biomaterials and the lack of *in vivo* serial tracking and monitoring of implants/stem cells. The approach presented in this work involves minimally invasive delivery via ultrasound-guided injection and serial tracking and monitoring of delivered biomaterials and cellular therapies *in vivo* through multimodal biomedical imaging. The integration of multimodal imaging techniques not only enables comprehensive visualization but also facilitates quantitative analysis, allowing for a more thorough understanding of therapeutic outcomes. To develop innovative therapeutic approaches, the multimodal imaging system established here provides a powerful framework for evaluating and optimizing experimental therapies based on a robust MI animal model.

Publications and Presentations

Publications:

X-Ray Visible Protein Scaffolds by Bulk Iodination

Carlos Flechas Becerra, Lady V Barrios Silva, Ebtehal Ahmed, Joseph C Bear, Zhiping Feng, David YS Chau, Samuel G Parker, Steve Halligan, Mark F Lythgoe, Daniel J Stuckey, P Stephen Patrick. 2024. Advanced Science, 11, 2306246

Manuscripts in preparation:

Image guided optimization of regenerative graft attachment to the heart

Zhiping Feng, Emily Lupton, Chris Pope, Adama Saccoh, Annalisa Bettini, Ioanna Mylonaki, Daniel Hachim Diaz, Maria Colzani, Sanjay Sinha, Molly M Stevens, Sian E Harding, Mark F Lythgoe, Tammy Kalber, P. Stephen Patrick, Daniel J Stuckey.

***In vivo* monitoring of activators of cardiomyocyte proliferation**

Zhiping Feng, Chiara Collesi, Rebecca Artioli, Daniel Stuckey, Mauro Giacca *et al*.

Four-dimensional ultrasound and speckle tracking imaging provide novel insights into disease progression in mouse models of heart disease

Zhiping Feng, Adama Saccoh, Mark F Lythgoe, Tammy Kalber, Daniel J Stuckey.

Manganese enhanced MRI can delineate area at risk of infarction in a mouse ischemia-reperfused model of myocardial infarction

Zhiping Feng, Daniel J Stuckey.

Contrast enhanced micro-CT for evaluating diffuse fibrosis in mice

Emily Lupton, Zhiping Feng, Annalisa Bettini, Tammy Kalber, P Stephen Patrick, Mark F Lythgoe, Daniel J Stuckey.

Self-doped and biodegradable glycosaminoglycan-PEDOT conductive hydrogels facilitate electrical pacing of iPSC-derived cardiomyocytes

Daniel Hachim, Olivia Hernández-Cruz, James E.J. Foote, Richard Wang, Matthew W. Delahaye, Daniel J. Stuckey, Zhiping Feng, Jonathan P. Wojciechowski, Luke C. B. Salter, Junliang Lin, Sian E. Harding, Molly M. Stevens.

Multimodal assessment of infarct size in a mouse model of myocardial infarction

Emily Lupton, Zhiping Feng, Tammy Kalber, Mark F Lythgoe, Daniel J Stuckey.

Presentations:

Division of Medicine Research Retreat (11th May 2023):

Optimization of injectable biomaterial patches for minimal invasive delivery of therapeutic grafts

FujiFilm Visual Sonics Cardio UK User Meeting (24th Nov 2022)

Evaluation of regenerative therapies using advanced ultrasound in a mouse model of myocardial infarction

The British Society for Cardiovascular Research (7th June 2022)

Echocardiographic evaluation of left ventricular function and myocardial deformation in a reperfused mouse model of myocardial infarction

Table of Content

List of Figures

List of Tables

Abbreviations List

A

AAR – area at risk

AAVs – adeno-associated virus

ACEI – angiotensin-converting enzyme inhibitors

AHA – American Heart Association

AL – light chain

AMI – acute myocardial infarction

Ant. Free – anterior free wall

AO – ascending aorta

ApoE KO – apolipoprotein E knockout

ARB – angiotensin II receptor blocker

αSMA – α-smooth muscle actin

ATP – adenosine triphosphate

ATTR – transthyretin amyloid

ATTR-CM – transthyretin amyloid cardiomyopathy

B

BLI – bioluminescent imaging

B-mode – brightness mode

C

Ca^{2+} – calcium ions

CABG – coronary artery bypass graft

CAD – coronary artery disease

CHD – coronary heart disease

circRNAs – circular RNAs

CM – cardiomyocyte

CO – cardiac output

CSC – cardiac stem cells

CT – computed tomography

CVDs – cardiovascular diseases

D

DPD – ^{99m}Tc-3,3-diphosphono-1,2-propanodicarboxylic acid

E

ECG – electrocardiogram

ECM – extracellular matrix

ESCs – embryonic stem cells

ECM-CMs – embryonic stem cells-derived cardiomyocytes

EF – ejection fraction

Epi-hESCs – epicardial cells derived from human embryonic stem cells

F

^{18}F-FDG – ^{18}F-Fluorodeoxyglucose

H

HF – heart failure

HFpEF – heart failure with preserved ejection fraction

HFrEF – heart failure with reduced ejection fraction

HSCs – hematopoietic stem cells

HSV1-tk – herpes simplex virus type 1 thymidine kinase

G

GCS – global circumferential strain

Gd – gadolinium

GelMA – gelatin methacrylate

GLS – global longitudinal strain

GPCRs – G-protein-coupled receptors

GRS – global radial strain

I

IC – intracoronary infusion

IGF – insulin-like growth factor

^{111}In – ^{111}Indium

Inf. Free – inferior free wall

IM – intramyocardial

iPSC – induced pluripotent stem cell

iPSC-CM – induced pluripotent stem cells-derived cardiomyocyte

IR – ischemia reperfusion

ISO – isoproterenol

ITRs – Inverted Terminal Repeats

IV – intravenous injection

K

K^+ – potassium ions

L

LA – left atrium

LAD – left anterior descending

LCX – left circumflex

LDL – low-density lipoprotein

LDL-R KO – low-density lipoprotein receptor knockout

LGE – late gadolinium enhancement

LncRNAs – long non-coding RNAs

LOA – level of agreement

LUC – luciferase

LV – left ventricle/ left ventricular

LVEDV – left-ventricular end diastolic volume

LVESV – left-ventricular end systolic volume

LVEF – left-ventricular ejection fraction

LVAWd – left ventricular anterior wall thickness in end-diastole

LVAWs – left ventricular anterior wall thickness in end-systole

LVEDA – left ventricular end-diastolic area

LVESA – left ventricular end-systolic area

LVEDL– left ventricular end-diastolic length

LVESL – left ventricular end-systolic length

LVIDd – left ventricular internal diameter in end-diastole

LVIDs – left ventricular internal diameter in end-systole

LVPWd – left ventricular posterior wall thickness in end-diastole

LVAWs – left ventricular posterior wall thickness in end-systole

M

MCF – myocardial contraction fraction

MI – myocardial infarction

MiRNAs – microRNAs

M-mode – motion mode

MMPs – matrix metalloproteinases

mMSCs – mouse mesenchymal stem cells

MRI – magnetic resonance imaging

MST – mammalian sterile 20-like protein kinases

N

Na^+ – sodium ions

O

ORF – open reading frame

P

PAm – polyacrylamide

PCL – polycaprolactone

PET – positron emission tomography

PEG – polyethylene glycol

PSAX – parasternal short-axis

PL – permanent ligation

PLA – polylactic acid

PLSAX – parasternal long-axis

PPCI – primary percutaneous coronary intervention

PVA – polyvinyl alcohol

Q

qPCR – quantitative PCR

R

RCA – right coronary artery

RCS – regional circumferential strain

RELAPS – relative apical sparing

RF – radio frequency

RLS – region longitudinal strain

ROI – region of interest

ROS – reactive oxygen species

RRS – regional radial strain

RV – right ventricle

S

SAB – septal apical to basal longitudinal strain

STE – speckle tracking echocardiography

SMP – shape memory patch

SPECT – single photon emission computed tomography

SV – stroke volume

T

TE – transendocardial

TEAD – transcriptional enhance associate domain

TEF-1 – transcriptional enhancer factor-1

TTC – triphenyl tetrazolium chloride

V

VEGF – vascular endothelial growth factor

W

WHO – World Health Organization

Y

YAP – Yes-associated protein

Chapter 1 Introduction

1.1 Acute myocardial infarction

Acute myocardial infarction (AMI) remains the leading cause of death globally [1]. AMIs primarily occur when a major coronary artery becomes suddenly blocked due to the rupture of an atherosclerotic plaque. This leads to irreversible damage to a portion of the myocardium as a result of inadequate blood flow (Figure 1-1) [2]. Data from the 2023 update of the National Health Service (NHS) across the United Kingdom (UK) indicated that the total annual direct cost of AMI to the health and care system is approximately £9 billion, with an overall economic impact of £19 billion on the UK economy as a whole [3].

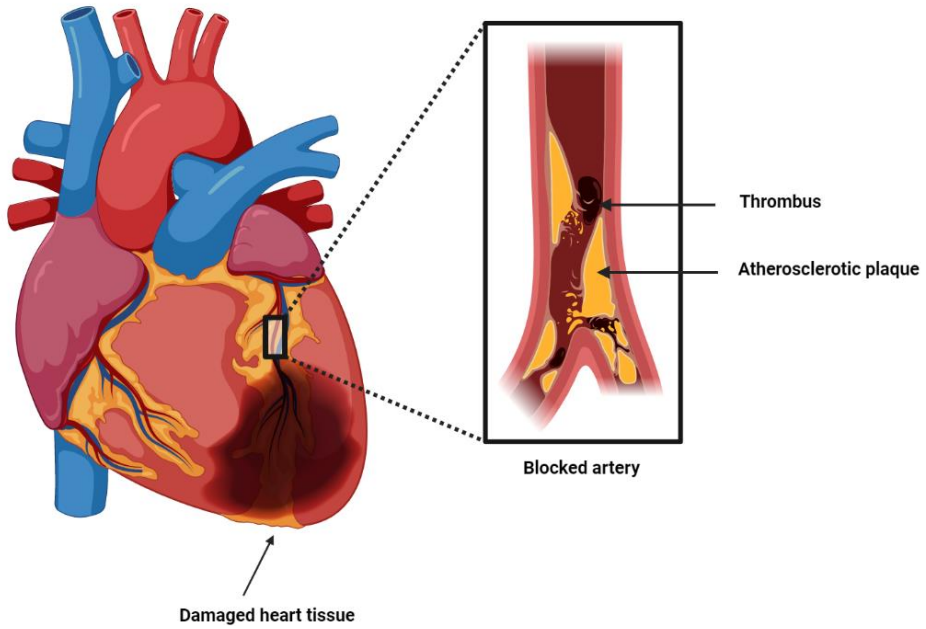

Figure 1-1. Illustrations of MI. MI is induced by a sudden blockage of the coronary artery due to thrombosis or a prolonged narrowing of the artery caused by atherosclerotic plaque. MI, myocardial infarction. Created with Biorender.

1.1.1 Pathophysiology of myocardial infarction

During MI, the occlusion of coronary arteries results in decreased oxygen concentration and initiates a decline in tissue partial pressure of oxygen (hypoxia), subsequently leading to a reduction in intracellular adenosine triphosphate (ATP) levels [4]. This depletion of energy disrupts the ionic balance and contributes to the death of cardiac cells. The loss of cardiomyocytes (CMs), particularly across extensive regions of the myocardium, results in a diminished contractile force of the heart. This subsequently leads to a reduction in ejection fraction (EF) and impaired left ventricular

(LV) function.

The pathogenesis of MI consists of three stages: inflammation stage, tissue repair, and structural and functional remodeling. Acute post-infarction inflammation occurs through various processes, including complement cascade activation, production of reactive oxygen species (ROS), and release of injury-related molecules, leading to the secretion of cytokines and chemokines that trigger immune responses involving neutrophils, leukocytes, lymphocytes, and macrophages in order to eliminate necrotic cell debris [5, 6]. The released proteinases, such as matrix metalloproteinases (MMPs) from local neutrophil populations, lead to intracellular collagen degradation between CMs, resulting in infarct expansion characterized by disproportionate thinning and early ventricular dilation and increased diastolic and contractile wall stress [7]. During the tissue repair phase, fibroblasts undergo proliferation and deposit extracellular matrix (ECM) to form scar tissue. This collagenous scar tissue loses its contractile functionality and leads to an increase in tissue rigidity, resulting in a reduced EF and impaired cardiac pumping capacity. Consequently, this hampers the delivery of oxygen and blood supply to peripheral organs and tissues [8].

Hence, there is a need for an increase in blood output per cardiac cycle to compensate for the lack of nourishment in the myocardium [9]. Structural and functional remodeling takes place. The remaining CMs undergo hypertrophy as they attempt to offset the decrease in EF by augmenting the volume of blood entering the ventricles during each cycle [19]. Additionally, heart rate increases to facilitate more blood within the same timeframe, while vasoconstriction occurs to elevate blood pressure through activation of the renin-angiotensin system [5]. The progression of chronic MI results in the development of hypertrophy in the non-infarcted segment, expansion and thinning of the infarcted wall, dilation of the LV, and formation of scar tissue. These changes ultimately lead to diminished contractility, cardiac dysfunction, and eventual onset of heart failure (HF) and mortality (Figure 1-2) [11]. Therefore, there is an urgent need for the development of innovative treatments and approaches in the early stage to mitigate remodeling processes, reverse myocardial thinning, and reduce the risk of irreversible HF, particularly within the field of regenerative medicine.

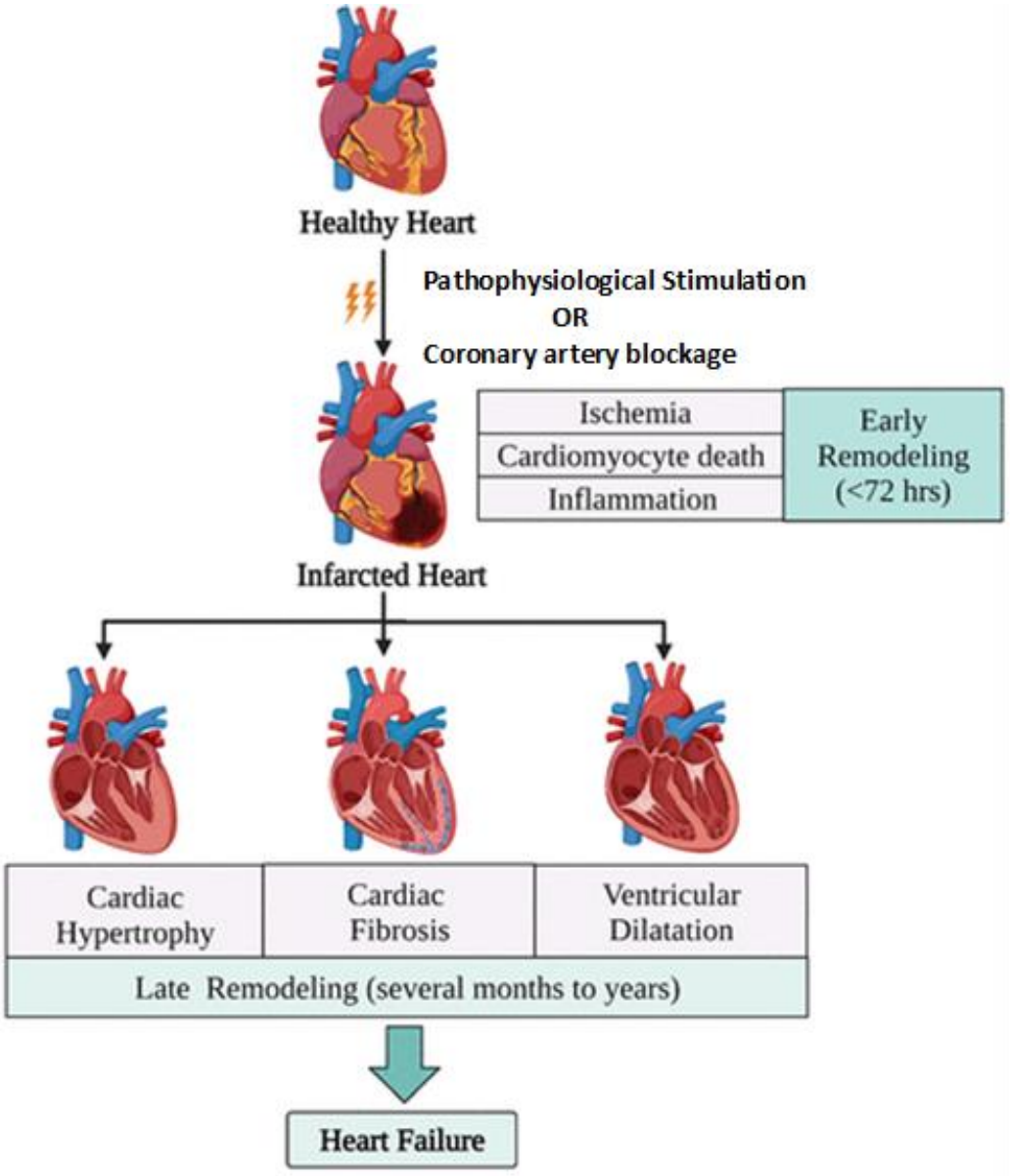

Figure 1-2. Diagram of cardiac remodeling post-MI. MI triggers ischemia, CM death and inflammation in the early remodeling stage and eventually leads to ventricular dysfunctions, thinning and dilation of the LV wall, and ultimately progress to heart failure. MI, myocardial infarction; CM, cardiomyocyte; LV, left ventricular. Reproduced from Tariq *et al.,* 2022 [7].

1.1.2 Reperfusion injury

Timely and complete restoration of blood flow to the ischemic region is the most effective therapeutic intervention to salvage the ischemic myocardium [12]. Early reperfusion of the ischemic region provides a time frame for preserving the viability of CMs and reducing adverse heart remodeling [13]. In clinics, reperfusion can be conducted via thrombolytic medicines, coronary angioplasty, or primary percutaneous coronary intervention (PPCI) (ibid). Research has shown that within 20-30 minutes of

blockage of the LAD, the ischemic CMs were still viable. Beyond 30 minutes of blockage, more ischemic CMs were irreversibly damaged (CM necrosis). By 40 minutes post-MI, most of the ischemic CMs in the subendocardial zone were irreversibly injured, while most of the ischemic CMs in the mid- and subepicardial regions were still viable. After more than 60–90 minutes of ischemia, irreversibly damaged CMs extended to subepicardial layers [14, 15]. Reperfusion of ischemic myocardium prior to necrosis is, therefore, imperative for enhancing myocardial function and minimizing infarct size. Scholz *et al.* demonstrated that in the clinical setting, timely reperfusion within 90 minutes of initial medical contact is most effective in patients who developed symptoms less than 1 hour between the onset of symptoms and initial medical contact [16].

Reperfusion of viable myocardium seems beneficial for substantial improvements in HF rates and in-hospital mortality. However, it triggers the secondary onset of ischemic cellular damage and death, termed 'reperfusion injury' [17]. This process is attributed to the complex interaction between a burst of oxygen free radicals and intracellular calcium, leading to accelerated cellular dysfunction, myocardial stunning, reversible microvascular injury, fatal arrhythmias, apoptosis, and CM death [18, 19]. Therefore, after myocardial reperfusion, the percentage of infarct size was larger than expected due to myocardial reperfusion injury (Figure 1-3) [20]. This has crucial clinical implications, as any additional injury during reperfusion presents an opportunity for intervention with cardiac protectants [11]. Despite a better understanding of the precise pathophysiology underlying reperfusion injury following MI, there are currently no specific treatments available to mitigate such injury post-MI, as shown in many failed clinical trials [21, 22]. Hence, new therapeutic interventions aimed at protecting the heart from reperfusion injury are under development. If successful, this will significantly reduce mortality from AMI and ultimately improve clinical outcomes [23, 24].

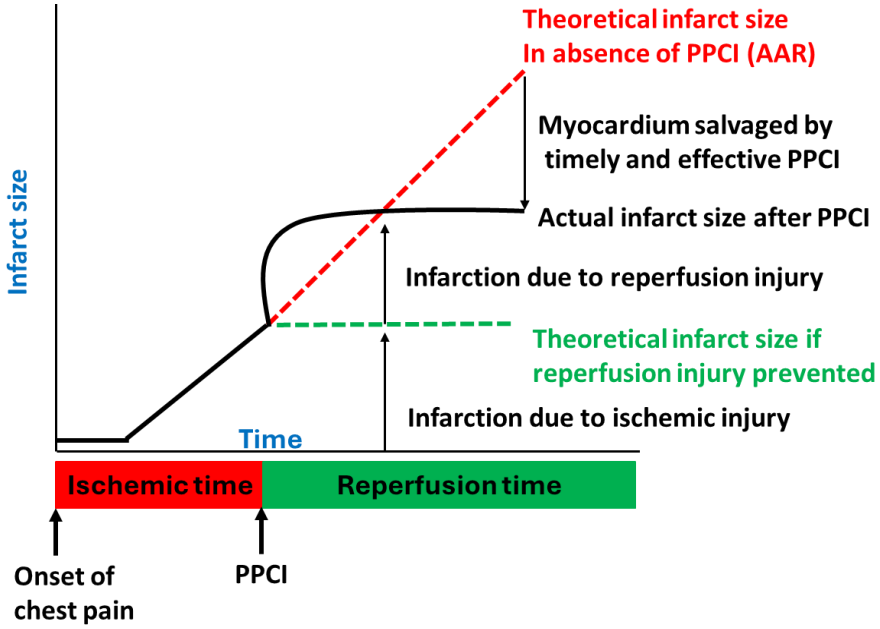

Figure 1-3. The hypothetical scheme of the effect of reperfusion injury on final infarct size in MI patients. The black curve depicts the final infarct size of a theoretical patient presenting with an AMI medically reperfused by PPCI or thrombolysis. The red dashed line displays the theoretical infarct size after acute occlusion of the LAD without PPCI. The green dashed line shows the theoretical infarct size after PPCI in the absence of reperfusion injury. As a result, following reperfusion, the infarct size is smaller than expected due to the medical reperfusion therapy. However, the reperfusion process attenuates the benefit of PPCI, in which the infarct size is larger than expected. AMI, acute myocardial infarction; PPCI, primary percutaneous coronary intervention. Reproduced from Hausenloy and Yellon, 2013 [25].

1.2. *In vivo* animal models of myocardial infarction

Experimental animal models have emerged as an indispensable tool in the study of MI [26]. A desirable MI model should exhibit physiological similarities to humans and manifest the cardinal pathology that can be clinically translated [27]. Various species are employed as animal models for MI studies, each differing in size, anatomical structure, genetic and phenotypic expression, and possessing unique advantages and disadvantages, so an appropriate model should be selected based on the research purpose (Table 1-1) [28, 29].

Animal models of cardiac injury, regeneration, repair and remodelling					
	Zebrafish	**Neonates**	**Mouse/rat**	**rabbit**	**Large animals (dog, sheep, pig)**
Rapid breeding	✓✓✓	✓✓	✓✓	✓✓	✓
Genetic modification	✓	✓	✓	Possible, not common	Possible, not common
Anatomical similarities to human	✗	✓✓	✓✓	✓✓	✓✓✓
Physiological similarities to human	✓✓	✓	✓✓	✓✓✓	✓✓✓
Injury response					
Regeneration	✓	✓	✗	✗	✗
Scarring	✗	✗	✓	✓	✓
Inflammation	✓	✓	✓	✓	✓
Tissue volume for analysis	Very limited	Very limited	Very limited	✓✓	✓✓
Cost	✓✓✓	✓✓	✓✓	✓	✗

Table 1-1. Comparison of small and large animals utilized in cardiovascular research. Reproduced from Macdonald *et al.,* 2021 [5].

Animals such as rats and mice offer the benefits of being small mammalian models, easy to handle and feed, having short breeding cycles, and providing a large number of subjects to enhance the statistical power of experiments. The high genetic similarity of mice to humans allows for the creation of related transgenic and knockout strains with relevant phenotypes [30]. Their small physical size reduces the cost of novel therapeutic drugs and molecules, which are often dosed based on body weight [31]. The small size of rodents also allows for research aimed at developing new imaging modalities and tracers for noninvasive evaluation of myocardial viability and cardiac function, thereby enabling the testing of innovative treatments [32].

As the work presented within my thesis was focused on developing and testing new cardiac regenerative approaches using advanced *in vivo* imaging methods, I chose to perform studies in mice. The small body mass of mice makes them more suitable than rats for some imaging methods, including *in vivo* bioluminescence/fluorescence

imaging and ultrasound. Additionally, the ready availability of genetically modified and immunocompromised mice, along with mouse cell lines made them a suitable choice for this research.

1.2.1. Mouse model of heart disease

Various methods can be employed to generate mouse models of heart disease, with one common approach being to induce microembolization by promoting atherosclerosis in the coronary arteries [33]. This can be accomplished with genetically modified mouse strains such as the low-density lipoprotein receptor knockout (LDL-R KO) mice and the apolipoprotein E knockout (ApoE KO) mice, which are widely utilized due to their high susceptibility to atherosclerosis [34]. When subjected to a high-fat diet, LDL-R KO mice and ApoE KO mice can develop obvious atherosclerosis within more than six weeks [35]. However, the resulting plaques are typically confined to the aorta and its outflow tract, as well as the proximal great vessels, but rarely in the coronary artery. Hence, this method is not commonly employed due to its potential time-intensive nature and limited ability to accurately mimic the progression of MI in humans, as well as the challenges associated with controlling the degree of ischemia [2, 36].

The second way to establish a rodent model is based on drug-induced cardiotoxicity, which initially causes cardiac muscle dysfunction that progressively leads to cardiac damage and HF. In the animal model of isoproterenol (ISO)-induced cardiotoxicity, this synthetic catecholamine acts as a β-adrenergic receptor agonist. When administered to animals, it triggers the generation of free ROS and oxidative stress, resulting in progressive mitochondrial damage and alterations in cardiac biochemical parameters, resembling the cardiac impairment that occurs in humans [37, 38]. Researchers have consistently manifested that acute exposure to a single high dosage of ISO caused reversible myocardial injury characterized by CM ablation and temporary alterations in cardiac function in mice [39]. This activates the endogenous cardiac stem cells (CSCs), leading to a sudden burst of new CM formation that substitutes for those lost due to ISO and restores normal cardiac contractility. This model offers substantial superiority concerning the regenerative potential of endogenous CSCs that might be impaired in a surgically induced infarct animal model [40].

Doxorubicin (DOX), a widely utilized antitumor agent with a broad spectrum of antineoplastic activities, is another type of drug to induce heart disease via cardiotoxicity to the heart [41]. Numerous mechanisms have been proposed to explain the cardiotoxic effects of doxorubicin, including the generation of ROS, mitochondrial impairment, iron-dependent oxidative damage to macromolecules, release of vasoactive amines, lipid peroxidation, intracellular calcium overload-induced CM injury, inhibition of cardiac tissue energy metabolism via fatty acid oxidation disruption, alterations in molecular signaling/regulation pathways, suppression of CM-specific gene expression and cytotoxicity [41-43]. However, doxorubicin-induced cardiotoxicity models exhibit poor survival rates. In Kelishomi *et al.*'s study, 50% of the animals died before completion of the experiment and displayed significantly lower body weight compared to the control group throughout most stages of observation [44]. Elshaer *et al.,* on their part, demonstrated that doxorubicin-based models exhibited both low survival rates and limited reliability [45].

The third approach to induce the MI model involves a surgical intervention to partially constrict or completely occlude the coronary artery originally described by H. Selye and colleagues [46, 47]. In brief, after anesthesia, endotracheal intubation and left thoracotomy, the coronary artery is carefully dissected and ligated in the proximal segment using a fine suture thread. The infarction can be identified by blanching of the distal tissue at the ligation site [46]. The advantage of this type of MI animal models over others lies in their ability to precisely determine the timing, location, and extent of coronary events, resulting in more reproducible outcomes. Additionally, these surgical-induced MI models can effectively recapitulate the patient's response to acute MI and disease progression towards HF [48]. However, the surgical procedure produces a high mortality rate and variable infarct sizes ranging from 4% to 59%, which is significantly affected by various factors, such as the duration of ischemia, the degree of collateral blood flow, and the extent of microvascular dysfunction in the coronary arteries [2].

1.2.2. Animal models of ischemia reperfusion

Ischemia reperfusion (IR) model determines by temporary ligation of the LAD for a defined period to induce an ischemic event, followed by removal of the ligature to allow reperfusion and generation of IR injury. Reperfusion can be confirmed by hyperemia in previously pale areas (Figure 1-4) [49]. Area at risk (AAR) refers to the area of the heart muscle supplied by the infarct-related artery. If timely reperfusion does not occur, there is a high risk of tissue death in this area. With reperfusion treatment, the proportion of the AAR that ultimately survives is the salvaged myocardium. This salvaged region can be calculated as AAR-infarct size [50].

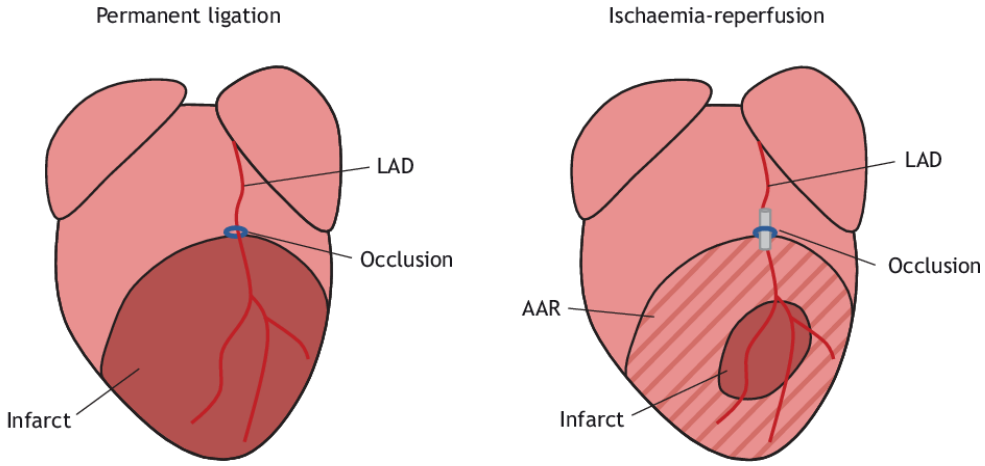

Figure 1-4. Surgery induced myocardial infarction models: permanent ligation and ischemia-reperfusion. Adapted from Villiers and Riley, 2020 [50].

The permanent ligation (PL) model differs fundamentally from the IR model in terms of objectives and pathophysiological relevance. As both MI animal models are clinically relevant, the selection of the optimum model is an important factor to consider when addressing different research questions. The PL model mimics the clinical situation of MI without timely reperfusion [51]. IR model represents the clinical scenario of a patient who has been optimally treated [52]. The PL model is suitable for studying ventricular remodeling, post-MI cardiac dysfunction, and HF progression [52]. The IR model enables the study of cardioprotection, reperfusion injury, and new catheter-based techniques during PPCI [49].

There has been limited research conducted to identify the most effective MI mouse model for evaluating the effectiveness of novel regenerative interventions, such as gene transfer and stem cell-based therapies. In Chapter 2, refined and improved

conventional surgical procedures were applied to achieve an MI mouse model featuring a decreased mortality rate and more consistent cardiac functional impairment. Meanwhile, a comparative cardiac functional analysis was carried out on PL and IR mouse models of MI to determine the differences between these two models and their suitability for studies of cardiac experimental therapies.

1.3. Current treatment for myocardial infarction

1.3.1. Current management principles in myocardial infarction

Standard pharmacological therapies for MI are well-established and significantly improve outcomes for patients. It is generally advisable to administer drugs targeting the renin-angiotensin-aldosterone system, such as angiotensin-converting enzyme inhibitors (ACEIs) and angiotensin receptor blockers (ARBs) [53]. Current guidelines recommend both ACEI/ARB and β-blockers for AMI patients with LVEF below 40% [54].

Timely coronary reperfusion therapies play an important role in mitigating adverse cardiac events, with pharmacological reperfusion therapy, PPCI and coronary artery bypass grafting (CABG) all falling under this category [55]. Pharmacological reperfusion involves three fundamental components: core fibrinolytic agent, concomitant antithrombotic therapy, and antiplatelet combination therapy [56]. Despite being highly effective in clot dissolution, thrombolytic medications can also give rise to complications such as spontaneous bleeding (e.g., subcutaneous hemorrhage, mucosal bleeding), as well as life-threatening intracranial hemorrhage [57].

PPCI is now recognized as the preferred and effective strategy for timely reperfusion [58]. Following identification of the site of the most recent thrombus occlusion during coronary angiography, a wire is inserted through the thrombus, and a balloon catheter (with or without a stent) is placed over it and inflated to mechanically restore anterior flow [59]. PPCI successfully restores normal blood flow in more than 90% of patients, as evidenced by angiographic images, whereas fibrinolysis achieves this in only 50% to 60% of such patients [60]. PPCI may occasionally induce complications, such as hematoma, hemorrhage, pseudoaneurysm, and arteriovenous fistula at the access site. About 4.3% of patients who undergo the PPCI will develop ventricular arrhythmia or

atrial fibrillation [60].

CABG is a surgical procedure that employs an autologous artery or vein as a conduit to circumvent a partially or completely obstructed coronary artery caused by atherosclerotic plaque deposition. CABG demonstrates superior efficacy in alleviating angina and reducing the requirement for repeated revascularization, and it is widely performed in cases of complex multivessel coronary artery disease or left main disease; however, it does carry an increased risk of procedural stroke [61].

The field of cardiac surgery has made significant progress over the past decade on improving outcomes for patients undergoing PPCI or CABG surgery. However, current treatment approaches for MI solely focus on reestablishing blood supply to the occluded coronary artery region, lacking effective regulation of abnormal remodeling changes and exhibiting limited efficacy in promoting myocardial tissue regeneration following ischemic injury. The renewal of CMs occurs. However, the rate at which the heart regenerates remain below 1% per year at age 25 and 0.45% at age 75 in humans [62]. This emphasizes that endogenous cardiac regeneration inadequately repairs the millions of lost CMs in infarcted tissue. Consequently, there is a shift in the research focus on the regeneration of myocardial tissue.

1.3.2. Regenerative approaches

1.3.2.1 Stem cell therapy

For decades, stem cell therapy has been proposed as a novel and encouraging approach to repair damaged or regenerate lost myocardium in heart disease [63]. These clonogenic cells have two distinctive characteristics: multipotency and self-renewal. Multipotency is the ability to differentiate into multiple mature cell types, and self-renewal is the ability to simultaneously replenish the stem cell pool [64, 65]. The first cell source extensively investigated in both animal models and human subjects was autologous skeletal myoblasts. Although these myoblasts established stable grafts within the heart, they did not differentiate into CMs and were unable to enhance myocardial function [66]. Autologous bone marrow mononuclear cells, which exhibit a broader differentiation potential compared to myoblasts, have also been evaluated in various animal models and clinical studies. In clinic trial, Autologous Stem-Cell

Transplantation in Acute Myocardial Infarction (ASTAMI) study included 47 patients who received an intracoronary stem cell injection a median of 6 days post-MI. The mean change in LVEF was 7.6±10.4% from baseline to the six-month follow-up among all participants [67]. In preclinical studies, numerous rodent studies conducted post-MI have provided compelling evidence supporting the functional benefits of this cell type; however, the underlying mechanisms responsible for these benefits remain a topic of considerable debate.

The underlying mechanisms of stem cell-based treatment of MI are not fully understood. Based on experimental models and humans, stem cells can regenerate damaged heart tissue through three main mechanisms: secreting diverse paracrine/autocrine factors into the damaged microenvironment, inducing endogenous proliferation and differentiation of cardiac stem/progenitor cells, as well as generating and migrating new CMs and vascular ECs towards the lesion site and establish electromechanical coupling with the host myocardium [68-70]. Stem cells serve as abundant sources of soluble factors and extracellular vesicles that modulate endogenous repair processes by promoting angiogenesis, attenuating fibrosis, enhancing CM survival, and regulating immune response [71] (Figure 1-5).

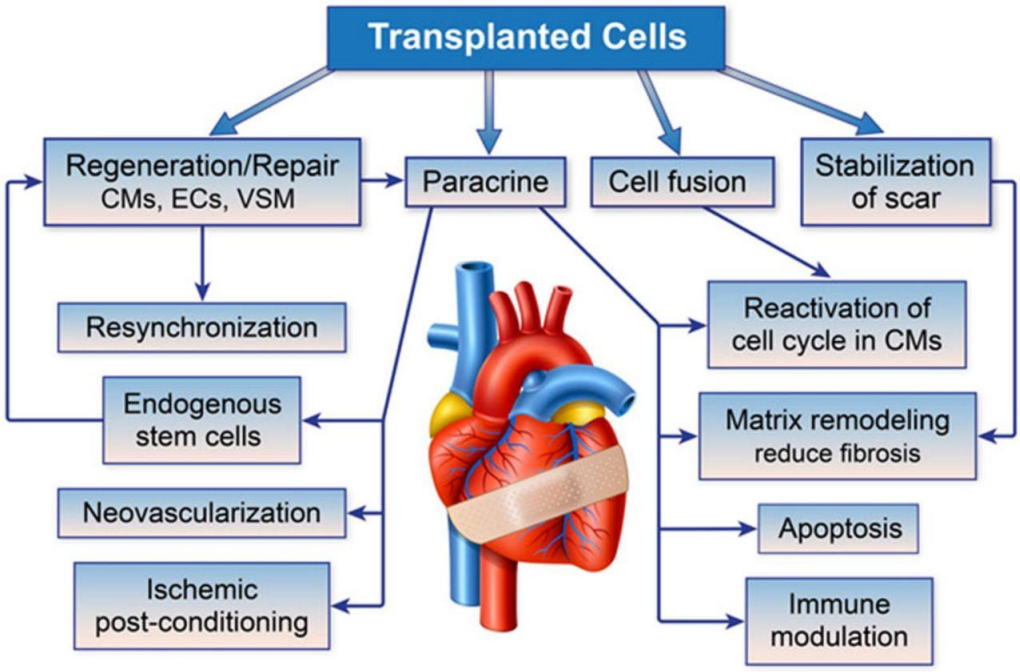

Figure 1-5. Potential mechanisms of stem cell therapy post-myocardial infarction. CM, cardiomyocyte; EC, endothelial cell; VSM, vascular smooth muscle. Adapted from Pratik *et al.,*2014 [71].

Currently, two primary categories of stem cells are being utilized in the field of cardiac regenerative medicine: (1) multipotent adult stem cells and (2) pluripotent embryonic stem cells (ESCs) and iPSCs [72]. The category of adult stem cells can be further classified into various groups, including mesenchymal stem cells (MSCs), skeletal muscle cells (SMs), CSCs, endothelial progenitor cells; human umbilical cord-derived stem cells, adipose tissue-derived stem cells, and hematopoietic stem cells (HSCs) [73]. MSCs, for example, are a type of adherent pluripotent cells capable of expressing a variety of cytokines, including stem cell factor (SCF), interleukin-6 (IL-6) and interleukin-1 (IL-1). MSCs have been mainly used in clinical trials so far because they are easily accessible and have high transfection efficiency [74]. These cells can be derived from fibroblast-like cells located in the bone marrow, adipose tissues, and other sources. They have the potential to differentiate into specific cell types such as adipocytes, osteoblasts, and chondrocytes. While MSCs rarely differentiate into functional CMs under normal physiological conditions, they primarily facilitate cardiac injury repair through paracrine mechanisms rather than direct differentiation into myocardial tissue [75].

Overall, the multipotent adult stem cells can be harvested and isolated from patients for autologous transplantation without the risk of immune rejection, rendering them more feasible and convenient for use in clinical trials. However, clinical studies have indicated that, particularly in patients with more severe LV dysfunction following MI or chronic HF, the clinical efficacy of these cells seems to be less remarkable or negative, possibly due to their limited direct cardiogenic potential for achieving true myocardial regeneration. At the same time, indirect effects such as paracrine signaling may represent the primary mechanism underlying improved cardiac function post-transplantation [74, 76].

The second-generation stem cell types include CSCs/progenitor cells (CPCs), hESCs and hiPSCs [64, 77, 78]. CSCs and CPCs are present and dispersed in the interstitial tissue of the hearts of embryos, newborns and adult mammals. They are characterized by pluripotency and clonogenicity and the existence of common stem cell markers like c-kit and Sca-1, as well as cardiac markers such as isl1, Nkx2.5, and GATA4 [79]. hESCs and hiPSCs represent crucial pluripotent cell types with the capacity to differentiate into various specific cell lineages, including CMs [80]. hESCs are derived

from the inner cell mass of preimplantation-stage blastocysts and possess unlimited self-renewal potential [81]. A preclinical study conducted in macaque monkeys demonstrated the potential of transplantation of hESC-CMs in promoting cardiac regeneration by reducing scar tissue and restoring cardiac function through tissue grafts and electromechanical junctions with the host myocardium. However, a subset of animals exhibited ventricular arrhythmias associated with the graft [82]. Nevertheless, hESCs face ethical issues in that obtaining hESCs requires the destruction of embryos, which restricts their availability [83]. The clinical application of this cell type has encountered setbacks due to concerns regarding immune rejection and the production of teratomas [84].

In 2006, Takahashi and Yamanaka successfully reprogrammed mouse fibroblasts to hiPSCs, exhibiting similar morphology and developmental potential as ESCs by ectopically expressing four crucial pluripotent factors Oct-3/4, Sox2, c-Myc, and Klf4 [85]. Patient-specific iPSCs have distinct characteristics compared to hESCs that can overcome ethical concerns and significantly reduce the risk of immune rejection during transplantation [86]. Graft-associated arrhythmia is a prevalent adverse reaction following stem cell transplantation, even in hiPSCs-induced regenerative therapy [82]. Moreover, maturity remains a significant concern regarding iPSC-derived CMs. These cells typically display spontaneous beating patterns that are more akin to fetal-like CMs with mixed atrial and ventricular phenotypes, rather than mature ventricular CMs. Consequently, when these immature CMs are transplanted into the myocardium without forming appropriate cell–cell connections necessary for synchronization with host heartbeats, there is an elevated risk of arrhythmia in the heart. In addition, the risk of developing teratoma due to the pluripotency of these cells after transplantation continues to raise potential safety concerns [87].

Clinical trials have demonstrated the safety and potential benefits of stem cell transplantation therapy, as summarized in Table 1-2. However, challenges remain in their clinical application due to limited cell survival rates, low retention and delivery efficiency post-transplantation, as well as inadequate engraftment of the transplanted cells [88]. It has been estimated that obtaining enough CMs for transplantation at the infarct site requires 5×10^9 undifferentiated hESCs. However, hESC exhibits long population doubling cycles lasting 36-48 hours, and previous reports demonstrated cell

retention rates falling below 5-10% within minutes to hours after being delivered to the infarct region, thereby compromising the regenerative potential of these cells [72, 89]. To optimize the therapeutic efficacy of stem cell transplantation, the additional utilization of biomaterials holds great potential in enhancing targeted delivery and retention of cells within infarcted cardiac tissue [72].

Table 1-2. Current clinical stem cell trials in myocardial infarction. Reproduced from Kim e***t al.,*** 2012 [90].

Study	**Cell Type and Delivery**	**Time of Delivery (Days after MI)**	**Results**	**End points (month)**	**Patient (Age)**
van Ramshorst et al.	Autologous BM-MNC, 1×10^8 cells, intramyocardial injection	Chronic myocardial ischemia	Modest improvement of summed stress score, LVEF at 3 months; quality of life ↑ at 6 months	3, 6	Placebo: 25 (62), Cell: 25 (64)
Meyer et al., BOOST trial	Autologous BMC, 24.6×10^8, IC	5 days	EF: Control (-3.3±9.5%), BMC (-2.5±11.9%); no sustained EF improvement	61	Control: 30 (59.2), BMC: 30 (53.4)
Tendera et al., REGENT trial	BM-MNC (1.78×10^8), CD34+ (1.9×10^6), IC	PCI after 12-hour MI onset	EF: Control (39 to 39), MNC (37 to 40), CD34+ (35 to 38)	6	Control: 40 (59), MNC: 80 (55), CD34+: 80 (58)
Beitnes et al., ASTAMI trial	BMC, 7×10^7, IC	4-7 days	Safe long-term; small ↑ in exercise time; minimal EF change	36	Control: 50 (56.7), BMC: 50 (58.1)
Hare et al., Prochymal	Allogeneic BM-MSC, 0.5, 1.6, 5×10^6 cells/kg, IV	1-10 days	EF ↑	12	Placebo: 21 (55.1), hMSC: 39 (59.0)
Assmus et al., REPAIR-AMI	Auto BMC, $236\pm174\times10^6$, IC	3-7 days after reperfusion	Safe	24	Placebo: 103 (57), BMC: 101 (55)
Grajek et al.	BMC, $2.34\pm1.2\times10^9$, IC	4-6 days after PCI	No difference in EF, LVEDV, LVESV, or stress test results	6, 12	Control: 14 (50.9), BMC: 31 (49.9)
Arnold et al., TECAM study	BM-MNC, $97.6\pm61.4\times10^6$, IC	STEMI, <9±3 days after reperfusion	No differences in lumen diameter, stenosis, artery changes, or plaque volume	9	Control: 37 (59.8), TECAM: 37 (58.6)
Strauer et al., STAR-heart study	BMC, $6.6\pm3.3\times10^7$, IC	Chronic HF, EF <35%	Haemodynamics, exercise capacity, oxygen uptake, LV contractility enhanced, reduced long-term mortality	3, 12, 60	Control: 200 (60), Stem Cell: 191 (59)

Seth et al., ABCD trial	BM-MNC, IC (with coronary sinus blockage)	Dilated cardiomyopathy, EF <35%	EF ↑ (6 mo: 5.4%, 36 mo: 22.5±8.3 to 28.4±11.8); ESV ↓; no change in EDV	36	Control: 20 (45), Stem Cell: 24 (49)
Traverse et al.	Auto BMC 1×10^8, IC	STEMI	EF: Placebo (48.6±8.5 to 57±13.4), BMC (49±9.5 to 55.2±9.8); LVEDP ↓	6	Placebo: 10 (57.5), BMC: 30 (52.5)
Williams et al.	Transendocardial, intramyocardial injection of auto BM-MNC or MSC (1 or 2×10^8)	Ischemic cardiomyopathy	EDV ↓ (208.7±20.4 to 167.4±7.32 mL); infarct size ↓; regional function ↑ (3 months); no chamber dimension changes (6 months)	12	Stem Cell: 8 (57.2)
Santoso et al.	G-CSF (10 mg/kg/day) for 5 days, PBSC harvested, recombinant erythropoietin + PBSC ($15\text{-}25\times10^6$, IC)	15 days after PCI with DES	No LVEDV/LVESV changes (3 months); ↑ (1 year)	12-30	18 (55.4)
Mansour et al., COMPARE-AMI	CD133+ HSC, 1×10^7, IC	3-7 days post-PCI	Safe; EF ↑ from 41.2±1 to 52.3±2 over 12 months	12	Placebo: 20, Cell: 20 (52.2)
Hirsch et al., HEBE trial	BM 296±164×10^6 or PB MNC 287±137×10^6, IC	4-7 days	No differences in EF between control, BM, or PB groups	4	Control: 65 (55), BMC: 69 (56), PBMC: 66 (57)
Penn et al.	Allo MultiStem (adventitia of infarct vessel), 2×10^7, 6×10^7, 1×10^8	2-5 days	EF ↑: 20 M (4.1%), 50 M (8.7%), 100 M (none); LV stroke volume: ↑ at 50 and 100 M	4	Control: 6 (53), MultiStem: 20 M: 6 (64), 50 M: 7 (54)
Bolli et al., SCIPIO	CSCs, IC (1M or 0.5M)	EF <40%, CABG, ischemic cardiomyopathy	EF ↑: 35.9% to 42.5% (12 months); infarct size ↓ (32.6 to 22.8)	12	Control: 7 (57.3), Treatment: 16 (56.0)
Moreira et al.	BM-MNC, 1×10^8, IAC or IVC	<24 hours	Cell retention comparison: IAC > IVC at 4 hours and 24 hours	24 hours	Control: 6 (57.2), IAC: 14 (59.7), IVC: 10 (53.6)
Solheim et al.	BM-MNC, 68×10^8, IC	6 days	No prothrombotic marker changes	3	Control: 50, Cell: 50 (57.4)
Roncalli et al., BONAMI trial	Auto BMC, IC	9.3 days after STEMI	↑ myocardial viability: Control (16%), BMC (34%); smoking had a significant adverse effect	3	Control: 49 (55), BMC: 52 (56)

Ahmadi et al.	BM-CD133+BMC, $1.77\times10^{6}\pm1.14\times10^{6}$ cells, intramyocardial	CABG candidate	Safe, no benefit	60	Control: 5, BMC: 13

BM: bone marrow, EDV: end-diastolic volume, EF: ejection fraction, IC: intracoronary infusion, MNC: mononuclear cells, MSC: mesenchymal stem cells, BMC: bone marrow cell, MI: myocardial infarction, PCI: percutaneous coronary intervention, STEMI: ST segment elevation myocardial infarction, HF: heart failure, DES: drug-eluting stent, LVEF: left ventricular ejection fraction, LVEDV: left ventricular end diastolic volume, LVESV: left ventricular end systolic volume, ESV: end-systolic volume, AMI: acute myocardial infarction, CABG: coronary artery bypass graft, PB: peripheral blood, LV: left ventricle, G-CSF: granulocyte colony stimulating factor, PBSC: peripheral blood stem cell, LVEDP: left ventricular end diastolic pressure, CSC: cardiac stem cell.

1.3.2.2 Biomaterial strategies

Over the past decade, biomaterials such as injectable hydrogels and cardiac patches represent distinct strategies to provide an optimal microenvironment for cellular functionality and viability [91, 92]. The ideal implantable biomaterial must satisfy a range of strict criteria [93]. First, the biomaterial should exhibit excellent biocompatibility, ensuring no immune response within the human body [94]. Second, it should possess low reactivity towards non-foreign bodies, thereby avoiding inflammation or other adverse reactions [95]. Third, the material should demonstrate robust stress and strain resistance to withstand physiological loads and cardiac movement effectively [96]. Fourth, implantable biomaterial should also show proficient degradation and reabsorption capabilities [97]. This implies that implants should degrade gradually and be absorbed by the body to prevent long-term retention and complications while generating non-toxic by-products that can be easily eliminated from the body [94]. Last, an optimal implantable biomaterial would possess time-dependent release mechanisms for growth factors, gene signals, and other proteins, which aid in promoting cell proliferation, differentiation as well as tissue regeneration processes, thereby promoting tissue healing [93, 98].

1.3.2.2.1 Injectable hydrogels

A hydrogel is a three-dimensional (3D) polymer network capable of absorbing substantial quantities of water or biological fluids while preserving their underlying molecular architecture, enabling them to mimic the microenvironment of human tissue [99]. Hydrogel-forming polymers possess hydrophilic functional groups, such as amine (NH_2), hydroxyl (-OH), amide (-CONH-, -$CONH_2$), and sulfate (-SO_3H), within their polymeric structure [100]. The injectable hydrogel can rapidly undergo a phase

transition from solution to gel state, enabling the minimal invasive injection for delivery compared to other biomaterials [101]. Hydrogels possess a distinctive porous structure, and their cross-linking density can be readily adjusted, which is an advantageous physical characteristic for carrying and delivering small molecule proteins, growth factors, drugs, and other components essential for cell growth and differentiation [101, 102].

Hydrogels can be derived from both natural and synthetic polymers. Commonly used natural polymers for preparing hydrogels include proteins, polysaccharides, and decellularized tissues such as chitosan, collagen, gelatin, alginate, agarose, cellulose, *etc* [103]. The hydrogels based on synthetic polymers primarily consist of polyethylene glycol (PEG), polyacrylamide (PAm), polyvinyl alcohol (PVA), polylactic acid (PLA), polycaprolactone (PCL) and other materials, exhibiting a diverse range of physical, chemical, and mechanical properties [104] (Table 1-4). Additionally, hybrid hydrogels/scaffolds are other important types of injectable hydrogels in myocardial repair [103, 105].

Table 1-3. Natural and synthetic injectable hydrogels for the treatment of myocardial infarction. Adapted from Liao *et al.,* 2020 [106].

Biomaterial	**Animal Model**	**MI Model / Processing Time Point after Successful MI Model**	**End-Point after Treatment**	**Injection Site**	**Results Compared to Control**	**References**
Gelatinized Alginate Hydrogel	Rats	Acute Myocardial Infarction Model / 48h	48h / after 4 weeks	Myocardium	Associated with improved left ventricular function after MI in rats, and may provide a long-term supply of Angiotensin-(1-7)	Rocca et al., 2016
pcECM	Rats	Chronic Myocardial Infarction / 12 weeks	4 weeks or 8 weeks	Myocardium	Preserved heart functions and alleviated MI damage	Efraim et al., 2017
Sericin	Mice	Acute Myocardial Infarction Model / Immediate	6 weeks	Myocardium	Reduces scar formation and infarct size, increases wall thickness and neovascularization, and inhibits MI-induced inflammatory responses and apoptosis	Song et al., 2016
hpECM	Rats	Acute Myocardial Infarction Model / 30 min	1h	Myocardium	A significant reduction in scar volume along with normal electrical activity of the surviving tissue, as determined by optical mapping	Francis et al., 2017
Chitosan CSCl-RoY Hydrogel	Mice	Acute Myocardial Infarction Model	4 weeks	Myocardium	Remarkably decreased the infarction size and improved heart function	Von et al., 2018
Type I Collagen Hydrogel	Rats	Acute Myocardial Infarction Model / 10 min	2h, 1 and 28 days	Myocardium	Enhances the grafted cell survival in the myocardium, contributing to increased neovascularization and decreased interstitial fibrosis	Xia et al., 2015
TEMPOGel	Rats	Acute Myocardial Infarction Model / 30	24h	Myocardium	Reduced infarction/reperfusion injury and preserved	Zhu et al.,

		min			left ventricle geometry	2018
HA	Ovine	Acute Myocardial Infarction Model / 30 min	8 weeks	Myocardium	Contractility in BZ was significantly higher, and ES fiber stress was also greatly reduced	Wang H. et al., 2018

MI, myocardial infarction; pcECM, porcine cardiac extracellular matrix cells; hpECM, human placenta-derived hydrogel; CSCL-Ro, chloride-Ro hydrogel; TEMPOGel, 2,2,6,6-tetramethylpiperidine-1-oxylhydrogel; HA,hyaluronicacid; BZ,extensionof the border zone; ES, end-systolic

Hydrogels exhibit diverse properties depending on the source, composition, or structure of the polymer, enabling researchers to select the most appropriate hydrogel for their specific research objectives [107]. Natural biomaterial-based gels pose challenges due to their limited mechanical strength, which hinders their ability to provide sustained support for cardiac contraction and relaxation. Additionally, the potential for a host immune response presents another limitation [108]. The application of synthetic hydrogels as biomaterials is limited due to the lack of biological activity [109]. Hybrid hydrogels are showing a new trend in biomedical applications, offering biological properties as well as precisely controlled mechanical strength and degradation profiles by combining the superior properties of natural and synthetic polymers [110]. Kong *et al.* developed an injectable hybrid hydrogel by coordinating a decellularized ECM-based hydrogel derived from the porcine heart with synthesized glycopeptide, aiming to restore the native structure similar to autogenous heart tissue and provide binding ligands for host cell homing, adhesion, and infiltration. The results demonstrated reduced inflammation, increased angiogenesis and improved CM survival, ultimately leading to alleviation of infarct size and improvement in cardiac contractility [111]. An electrically conductive scaffold has been developed to facilitate the propagation of electrical impulses between CMs and enhance their synchronized contractions. For instance, a newly formulated *in situ* double-network hydrogel derived from oxidized alginate and ECM with 3-(2-aminoethyl amino) propyltrimethoxysilane (APTMS) was utilized to improve the electrical conductivity of the synthesized hydrogels [112].

The feasibility of injectable hydrogels has been validated in stem cell-based cardiac regenerative studies, highlighting their potential for cardiac tissue regeneration by enhancing cell adhesion and proliferation [113]. However, injectable hydrogels still exhibit several limitations, such as inadequate mechanical properties, potential immunogenicity, susceptibility to cardiac washout, and limited cell or drug retention, thereby compromising therapeutic effectiveness [114]. To address these challenges, the development of cardiac patches has gained great attention.

1.3.2.2.2 Cardiac patches

Cardiac patches can serve as a vehicle for delivering cells or bioactive factors that

adhere to the host myocardium, offering temporary support to the infarct region while concurrently restoring the impaired myocardium [115]. Table 1-4 demonstrates the recent studies on cardiac patches for repairing and regenerating the heart after MI. Mostly, cardiac patches are fabricated from synthetic polymers, natural biomaterials, decellularized ECM or hybrid materials similar to injectable hydrogel as previously described [116]. Similar to injectable hydrogel, cardiac patches should possess the following properties: (1) Biocompatibility: The materials should be highly biocompatible to avoid harmful reactions when implanted onto the heart surface. (2) Mechanical properties: The biomaterials need to be compliant and have certain mechanical properties to withstand the demands of the ventricle, with stiffness ranging from 10–20 kPa at systole to 200–500 kPa at diastole [117]. (3) Porosity: The biomaterial scaffolds should be porous to preserve and release cells or bioactive factors onto damaged areas for improved therapeutic efficacy (the porosity of a cell-loaded patch is generally more than 90% with pore sizes between 100 to 150μm) [118]. (4) Biodegradability: The biomaterials are biodegradable and degrade at a rate consistent with new tissue formation to avoid long-term side effects in the body, with degradation products also being biocompatible [119].

Table 1-4. Recent studies on cardiac patches for repairing and regenerating the heart after MI. Adapted from Gil-Cabrerizo *et al.,* 2023 [200].

Biomaterial/ Therapeutic Agent	**MI Animal Model**	**Type of MI Model / Processing Time Point after MI**	**End-Point after Treatment**	**Therapeutic Effect**	**References**
Neonatal rat CMs	Rats	Acute Myocardial Infarction Model / Immediate	4-6 weeks	Increased vascularization and maintained electrical function	(Jackman et al., 2018)
Fibrin, Thrombin, and hiPSC-CM/EC/MSCs	Swine	Acute MI Model / Immediate	4 weeks	Reduced infarct size and improved cardiac function	(Gao et al., 2020)
CDCs	Rats	Acute MI Model / Immediate	4 weeks	Reduced CM apoptosis, restored myocardium volumes, and reduced fibrosis, EF % ↑ : 10.0 ± 14.9	(Yeung et al., 2019)
Fibrin and hiPSC-CMs	Rabbit	Acute MI Model / Immediate	4 weeks	Improved function and reduced scar size (35%)	(Jabbour et al., 2021)
PECUUS and porcine dECM + hADSCs	Rats	Acute MI Model	8 weeks	Enhanced cardiac function and neovascularization in the peri-infarct zone	(Kashiyama et al., 2022)
Polyaniline, Gelatin, and PVA + hADSCs	Rats	Acute MI Model / Immediate	4 weeks	Prevented ventricular fibrosis and remodeling	(Yu et al., 2022)
Porcine dECM + hiPSCs-ECs and MSC (SDF-1α)	Rats	1-day post-MI	8 weeks	Induced neovascularization	(Kim et al., 2022)
Chitosan and Fibroin + hADSCs	Rats	Acute MI Model / Immediate	4 weeks	Increase in microvascular density and alleviated cardiac fibrosis	(Chen et al., 2018)
Fibrin and Engineered Microvessels + CDCs	Rats and Swine	Acute MI Model / Immediate	4 weeks	Promoted cardiac function, EF% ↑ : 28.3 ±5.67, reduced scar size, promoted neovascularization, suppressed inflammation	(Su et al., 2020)

GelMa and PGDA + hiPSC-CMs, hECs, and hMSCs	Mice	Acute MI Model	4 months	Increased cell engraftment and vasculogenesis, infarct size: ~4.6 ± 0.8% decreased, EF% ↑ 8.2±2.5	(Cui et al., 2020)
Ionically crosslinked starch	Rats	Acute MI Model	4 weeks	Reduced pathological cardiac remodeling	(Lin et al., 2019)
Porcine dECM	Rats	Acute MI Model	4 weeks	Improved cardiac function, EF% ↑ : 20.3±4.5	(Shah et al., 2019)
GO and Silk Fibroin	Rats	Acute MI Model	4 weeks	Improved cardiac function, EF% ↑ : 22-36%	(Zhao et al., 2022)

ADSCs: adipocyte tissue-derived stem cells; CDCs: cardiosphere-derived cells; CM: cardiomyocytes; dECM: decellularized extracellular cardiac matrix; ECs: endothelial cells. GelMA: gelatin methacryloyl; GO: graphene oxide; PEGDA: Polyethylene glycol diacrylate

Successful engraftment of cardiac patches with the host myocardium is imperative for optimizing therapeutic efficacy, particularly in augmenting cardiomyogenesis and angiogenesis within the injured heart. Unlike injectable hydrogels that can be easily administered via syringe injection in most *in vivo* studies, conventional epicardial patches require time-consuming fixation by suturing onto the heart tissue [121, 122]. However, while suturing allows for firm adherence to the desired site, it also poses risks such as disrupting the blood supply to the patch, bleeding, damage to healthy tissue, and infection. Such trauma may even worsen LV function and expand the extent of damage [123].

To address the limitations of current epicardial patches, some research teams have recently been exploring alternatives such as fibrin glue. Melhen *et al.* utilized a biocompatible external fibrin glue directly applied onto the patch, allowing it to dry and adhere to both the patch and heart surface, presenting a novel method for attaching delicate cell-encapsulating therapeutic patches [124]. While fibrin glue is more convenient and less invasive, it may not possess sufficient adhesive strength to secure a large heart patch under dynamic conditions. Additionally, the use of glue may result in an undesired gap between the cardiac patch and the epicardium, thereby impeding the infiltration of cell secretions into the myocardium [123]. Therefore, the development of modified patches without suturing or glue has been pursued.

Therapeutic integration of cardiac patches greatly benefits from the enhanced delivery efficiency; however, most current cardiac patch implantations require open-chest surgery that patients with MI may not be strong enough to recover from the surgical damage and inflammation [121, 125]. Therefore, minimally invasive delivery of cardiac patches is highly necessary. In Chapter 4, an ultrasound-guided minimally invasive delivery system was utilized for the implantation of an alginate-derived cardiac patch. One primary purpose of this study is to validate the delivery approach and various methods to enhance the attachment of the cardiac patch onto the heart, therefore providing a promising and innovative strategy for regenerative therapy of MI.

1.3.2.2.3 Other biomaterials

Apart from injectable hydrogels and cardiac patches, biomaterials such as microsphere-based technologies and self-assembled peptide nanofibers are considered

innovative in the field of cardiac tissue engineering and regeneration [126]. Microspheres, also known as microcarriers, are injectable scaffolds used in tissue engineering, ranging from 20 to 200μm [127]. Microspheres exhibit outstanding biocompatibility, customizable structures (such as stiffness, porosity, and composition), and high efficiency in encapsulating therapeutic agents (such as drugs and cells) [128]. Prior to injection into a damaged area, microspheres allow for cell adhesion and growth on their surfaces. The gaps between the microspheres facilitate cell migration and proliferation, thereby promoting the accelerated formation of new tissue [126].

Microspheres, either alone or in conjunction with multifunctional composites, have been formulated and subjected to *in vivo* testing for regenerative therapy targeting heart diseases. Li *et al.* demonstrated that the combination of microspheres and ECM-derived hydrogel can effectively regulate the behavior of macrophages and myogenic cells. The positive effects on tissue regeneration were observed through enhanced vascularization, neomuscle formation, and neuralization at 2 months after implantation in a rat model of heart injury [129].

Self-assembled peptide nanofibers are another type of biomaterial that consists of natural amino acids and other macromolecules that undergo self-assembly to form molecular structures under physiological conditions [130]. The versatility of peptides as building blocks lies in their ability to achieve the design of self-assembled biomaterials with intricate 3D structures, nanoscale characteristics, and adjustable physical properties through secondary structures dictated by primary amino acid sequences [131]. They exhibit inherent biocompatibility, biodegradability, and the ability to mimic natural structures and materials, making them highly promising for various biomedical applications, including drug delivery systems, enhancing cell viability, and facilitating improved cell adhesion [109].

Recently, a class of modified and functionalized self-assembling peptides have been engineered for the delivery of protein/therapeutic agents or the promotion of stem cell survival, proliferation, and differentiation, as well as the improvement of cardiac function in an MI model. For example, Guo and coworkers applied a self-assembled peptide to provide the sustained delivery of vascular endothelial growth factor (VEGF) for at least 1 month and subsequently observed decreased scar size and significantly

reduced collagen deposition [132]. In a separate study, the researchers successfully synthesized a novel self-assembling peptide nanofiber by incorporating the RGDSP cell adhesion motif into the RADA16 self-assembling peptide. BMSCs were introduced into this composite biomaterial. The results of *in vitro* experiments demonstrated that these self-assembled peptide nanofibers promoted the pluripotent BMSCs growth and effectively protected them from hypoxia-induced apoptosis and necrosis. Improved cardiac function and significantly reduced collagen deposition were observed in an experimental rat MI model [133].

The development of biomaterials plays a crucial role in the field of regenerative medicine, with the ultimate aim being to effectively load stem cells and enhance their viability and retention within the body. In Table 1-5, various biomaterials are compared based on their ability to support stem cell viability, on-target cell retention, proliferation, cell-to-cell connections, integration with host, mechanical support, paracrine effect, and electrical connection, providing valuable insights into their potential applications in regenerative medicine.

Table 1-5. Comparison of virous biomaterials for enhancing stem cell-based therapy.

	Cell suspension	**Hydrogel**	**Patch**	**Microsphere**
Cell viability	✓	✓✓	✓✓	✓✓
On-target cell retention	×	✓	✓✓	✓✓
Cell-cell connections	×	×	✓✓	✓✓
Integration with host tissue	✓✓	✓	×	✓
Mechanical support	×	✓	✓✓	×
Paracrine effect	✓	✓✓	✓✓	✓✓
Electrical connection	×	×	✓	✓✓

1.3.2.3. Gene therapy

After Nabel *et al.* launched a study in 1989 that focused on a technique of transferring ECs and *in vivo* expression of recombinant genes to explore potential therapeutics for cardiovascular disease in mini pigs, the realm of gene therapy research has seen significant growth [134]. In recent years, gene transfer has been extensively investigated in the field of cardiovascular gene therapy, with several completed clinical trials focusing on therapeutic blood vessel growth, improvement of calcium handling, reprogramming resident FBs, *etc.* [135] (Table 1-7).

Therapeutic angiogenesis is a promising strategy for sustaining the efficacy of angiogenic growth factors in amplifying collateral artery development, enhancing ischemic tissue function through stimulation of vasculogenesis, augmenting tissue perfusion, and facilitating tissue regeneration and repair [136, 137]. This is particularly crucial due to the limited half-life of growth factors, as evidenced by randomized placebo-controlled double-blind clinical trials involving recombinant VEGF and fibroblast growth factor-2 (FGF-2) in coronary artery disease (CAD) and peripheral arterial disease, which yielded disappointing results [138]. In a phase 1 clinical trial involving patients with severe CAD and intractable angina pectoris, the replication-deficient adenoviral vector AdVEGF121, encoding the human VEGF 121 cDNA to induce therapeutic angiogenesis, was administered via intramyocardial injection. The results demonstrated that this therapeutic intervention was well tolerated and provided early indications of its potential to mitigate myocardial ischemia [139]. Another phase I, a two-year follow-up trial, was undertaken to evaluate the safety and efficacy of high-dose plasmid-VEGF 165 (pVEGF165) gene transfer in CAD patients. The treatment demonstrated a favorable safety profile, with no adverse effects related to either the injection procedure or the plasmid observed during the 24-month follow-up period [140].

As HF is a progressive disease characterized by the heart's inadequate ability to contract, gene therapy offers promise for reversing HF by enhancing the capacity of CMs to store calcium through increased expression of sarcoplasmic reticulum calcium ATPase (SERCA2a), thereby improving CM contractility [141, 142]. A phase 2 trial was conducted on intracoronary gene therapy targeting sarcoplasmic reticulum Ca2+-

ATPase in 39 patients with advanced HF (CUPID). This research demonstrated the impact of AAV1/SERCA2a on preventive clinical outcomes, including no pro-arrhythmic effect and reduced cardiovascular hospitalization [143]. AAV1/SERCA2a was well tolerated and showed clinical indications of enhanced SERCA2a biological activity, such as improvements in HF symptoms, functional status, natriuretic peptide levels, and beneficial reverse LV remodeling. Similar findings have been demonstrated in several preclinical models of HF [144, 145].

Directly reprogramming FBs into CMs is an innovative approach to cardiac regeneration [146]. Following cardiac injury, the regenerative capacity of adult CMs is limited. Damaged CMs are then replaced by activated cardiac FBs, which transform into myofibroblasts to maintain structural integrity. Unfortunately, this process often results in fibrosis and decreased myocardial contractility, leading to impaired heart function [147]. Recently, research demonstrated that the overexpression of cardiac transcription factors Gata4, Mef2c, and Tbx5 (GMT) can effectively convert murine cardiac FBs into CMs *in vitro* [148]. Qian and the group reprogrammed murine cardiac non-myocytes into CM-like cells *in vivo* by delivering GMT retrovirally following MI. The induced CMs exhibited binucleation, sarcomere assembly, and CM-like gene expression. *In vivo,* GMT delivery reduced infarct size and moderately improved cardiac function for up to 3 months after MI [149]. However, the reprogramming efficiency of infected FBs to induced CMs with GMT was found to be low, at 10–15% in Qian's study and only 3% in Inagawa's research, and these cells exhibited significant variability [150]. Cardiac FBs are heterogeneous, and a subpopulation of FBs to direct reprogramming of the heart needs to be identified [151]. For example, Hirai and colleagues found that embryonic FBs produce induced CMs more, suggesting that embryonic tissue maintains greater epigenetic plasticity, which diminishes over developmental time [152]. In recent studies, various module combinations have been investigated to enhance reprogramming efficiency. Christoforou *et al.* utilized multiple transcription factors, including MYOCD, SRF, Mesp1, and SMARCD3, to enhance the cardio-inducing effect of GTM during direct cellular reprogramming [153]. Nam *et al.* demonstrated that the addition of MYOCD to GHM reprogramming of FBs significantly increased the conversion of CMs from ~1.5% to ~17% [154].

Table 1-6. Clinical trials of gene therapy for the treatment of cardiovascular disease. Reproduced from Wang et al., 2021 [155].

NCT Number	Gene Target	Disease	Administration Route	Delivery Method	Clinical Phase	Current Status	Results	References
NCT01643330	SERCA2a	Advanced heart failure	Percutaneous/ intracoronary administration	AAV1 vector	Terminated in phase 2b	Terminated	Safe but no improvement in outcomes in phase 2b	[9–13]
NCT00787059	Adenylyl cyclase type 6 (AC6)	Congestive heart failure	Intracoronary administration	Adenovirus-5 (Ad5)	Phase 2 and FDA approved phase 3	Completed	Improvement in LV function	[14]
NCT02694575	SDF-1	Chronic heart failure	Endocardial injection	Plasmid DNA	Phase 2	Completed	Increased EV and SV at 12 months	[15]
NCT03039751	VEGF-D	Severe coronary heart disease	Endocardial injection	Adenovirus	Phase 2	Recruiting	\	[16,17]
NCT00936819	Endothelial nitric oxide synthase (eNOS)	Acute myocardial infarction (AMI)	Intracoronary injection	Endothelial progenitor cells transfected with linear polyethyleneimine (jetPEI)	Phase 2b	Recruiting	\	[18,19]
NCT00135850	VEGF 165	Ischemic cardiopathy	Intramyocardial injection	Plasmid	Phase 2	Completed	Safe but transient improvement in myocardial perfusion	[20,21]
NCT02928094	FGF-4	Myocardial infarction	Intracoronary administration	Adenovirus-5 (Ad5)	Phase 3	Not yet recruiting	Terminated for ASPIRE; not yet recruiting for AFFIRM	[22–25]
NCT04125732	VEGF	Refractory angina coronary	Transthoracic epicardial procedure	XC001 (AdVEGFXC1)	Phase 2	Recruiting	\	[26]
NCT04179643	I-1 transgene (AA 1-65 with T35D)	Heart failure	Intracoronary infusion	BNP116 AAV	Phase 1	Recruiting	\	[27]

Given the limited regenerative capacity of CMs themselves following injury, stem cell transplantation has presented the most promising outcomes; nevertheless, ethical and practical issues may emerge during the isolation of stem cells for therapeutic purposes [156]. To avoid these concerns, researchers now have focused on strategies aimed at enhancing the reentry and division of healthy CMs located in the peri-infarct area to treat MI, with gene transfer being involved in reintroducing the signaling pathways activated during the fetal stage to promote CM proliferation [157, 158]. The summary of *in vivo* studies conducted on transgenic mouse models manipulating the CM cell cycle is presented in Table 1-7 [156].

Table 1-7. *In vivo* studies of manipulating the cardiomyocyte cell cycle in transgenic mouse model. Reproduced from Bicknell *et al.,* 2006 [156].

Gene	Modification	Effect	References
Cyclin D1	Cardiac-specific over-expression	Developmental hyperplasia; increased heart size; increased nuclear content and multinucleation; sustained DNA synthesis	[60, 61]
Cyclin D2	Cardiac-specific over-expression	Developmental hyperplasia; increased heart size	[61]
Cyclin D3	Cardiac-specific over-expression	Developmental hyperplasia; increased heart size	[61]
Cyclin D1+D2+D3	Germ-line knockouts	Embryonic lethal between E15.5–16.5; thinned ventricular walls and ventricular septal defect; severe cardiac output failure	[125]
Cyclin E	Germ-line knockout	Viable; no cardiac phenotype	[126]
Cyclin A2	Cardiac-specific over-expression	Age-dependent increased heart size; smaller mononuclear cardiomyocytes; increased DNA synthesis; prolonged post-natal hyperplasia	[69]
Cyclin B1	Germ-line knockout	Embryonic lethal (<E10)	[127]
Cyclin B2	Germ-line knockout	No cardiac phenotype reported	[127]
CDK2	Cardiac-specific over-expression	Developmental hyperplasia; sustained DNA synthesis; exaggerated hypertrophic response to pressure overload	[66]
p130	Germ-line knockout	Strain-dependent embryonic lethality; thinned ventricular walls in Balc/cJ mice	[86, 87]

pRB+p130	Germ-line knockouts	Increased heart size; increased DNA synthesis and histone H3 phosphorylation	[82]
p27	Germ-line knockout	Developmental hyperplasia; increased heart size; smaller cardiomyocytes	[65]
Jumonji	Germ-line knockout	Strain-dependent embryonic lethality; developmental hyperplasia	[93–96]
c-Myc	Cardiac-specific over-expression	Developmental hyperplasia; increased number of smaller cardiomyocytes; accelerated switch to hypertrophic growth in neonate heart	[101–103]
p38α	Cardiac-specific knockout	Increased DNA synthesis and histone H3 phosphorylation in neonatal cardiomyocytes	[112]

1.3.2.3.1 Overview of the Hippo signaling pathway

In recent years, numerous studies have focused on promoting CM proliferation by inducing re-entry into the cell cycle for cardiac repair following MI. CM proliferation involves a variety of signaling pathways, with the Hippo signaling pathway being the most widely studied one [159]. The Hippo signaling pathway, originally discovered in the Drosophila genus, is an evolutionarily conserved mechanism that restrains cell proliferation [160]. This pathway plays crucial roles in a range of biological functions in both Drosophila and mammals, such as organ size regulation, cell fate determination, stem cell biology, tumor suppression, and tissue homeostasis [161]. The core of the Hippo pathway is a kinase cascade that negatively regulates the activities of two key proteins: the transcriptional co-regulator Yes-associated protein 1 (YAP) and its homologue transcriptional coactivator with a PDZ-binding motif (TAZ) [162]. The YAP and TAZ proteins are important transcriptional coactivators, yet they cannot bind DNA directly. Thus, after activated YAP/TAZ translocates to the nucleus, they bind to transcription factors, notably transcriptional enhance associate domain (TEAD). In mammals, the TEAD transcription factor was first recognized as a nuclear protein and considered a vital component of the Hippo signaling pathway, which is widely believed to be modulated by the presence or the absence of nuclear YAP and TAZ [163]. The TEAD family contains four homologous members: TEAD1-4. Almost all tissues express at least one TEAD gene [164]. TEAD1, also referred to as transcriptional enhancer factor 1 [TEF-1], is predominantly found in the heart. A null mutation in

TEAD1 results in embryonic lethality, with affected mice exhibiting pronounced heart defects. Given that TEAD1 enhances the expression of genes specific to cardiac tissue, it is posited to play an important role in CM differentiation [165].

In mammals, the Hippo pathway primarily comprises core components such as mammalian sterile 20-like protein kinases 1 (MST1) and MST2, large tumor suppressor kinases 1 (LATS1) and LATS2, Salvador homolog 1 (SAV1), Mps one binder kinase activator-like 1A/1B (MOB1A), and co-activators YAP1/TAZ, among others [159]. The pathway is influenced by upstream signals and stressors, including cell polarity, energy stress, G-protein-coupled receptors (GPCRs), and ECM stiffness [166]. Upon stimulation, MST1/2 and SAV1 undergo phosphorylation, activating and leading to the phosphorylation of the LATS1/2–MOB1 complex. LATS1/2 then directly phosphorylates YAP1 and TAZ. Post-phosphorylation, the YAP1/TAZ complex either binds to the 14-3-3 protein, resulting in either their cytoplasmic retention or ubiquitin-mediated degradation. In the absence of LATS1/LATS2 kinase activity, unphosphorylated YAP/TAZ translocate to the nucleus. Although YAP and TAZ lack a DNA-binding domain, they interact with the TEAD to regulate target gene expression. Consequently, in an inactive Hippo pathway, YAP and TAZ accumulate in the nucleus, and YAP/TAZ-TEAD complex orchestrates the transcription of target gene expression, which can promote cell growth, proliferation, migration, and survival after injury (Figure 1-6) [160, 166-307].

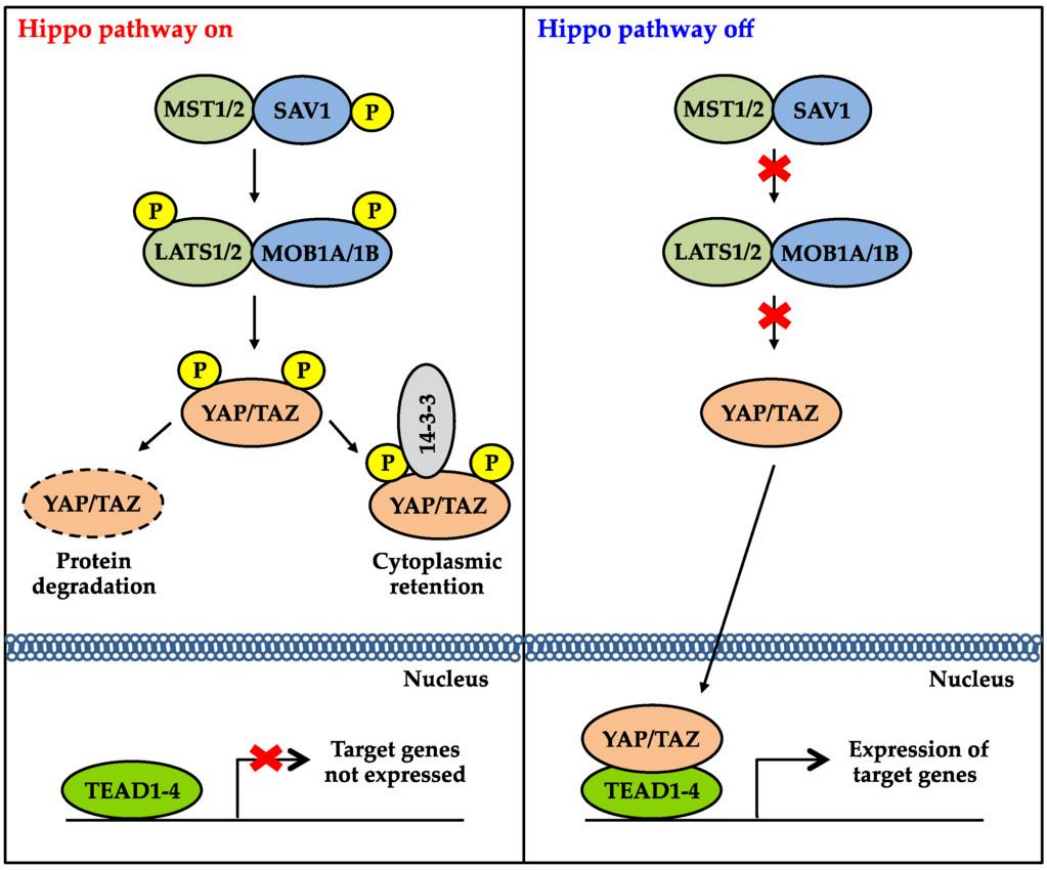

Figure 1-6. Overview of the regulation of the Hippo–YAP1/TAZ pathway mammals. Hippo Pathway "On": MST1/2 and SAV1 activation: The proteins MST1/2 and SAV1 are shown as being phosphorylated (indicated by the "P"), suggesting they are activated. LATS1/2 and MOB1A/1B activation: MST1/2, once activated, leads to the phosphorylation and activation of LATS1/2 and MOB1A/1B. YAP/TAZ phosphorylation and degradation: The phosphorylation cascade continues with LATS1/2 phosphorylating YAP/TAZ. Once phosphorylated, YAP/TAZ can be directed for protein degradation or can be retained in the cytoplasm by binding to the 14-3-3 protein. Target genes not expressed: Due to YAP/TAZ degradation or cytoplasmic retention, YAP/TAZ cannot translocate to the nucleus and bind to the TEAD1-4 transcription factors. As a result, target genes are not expressed. Hippo Pathway "Off": Inactive LATS1/2 and MOB1A/1B: The proteins LATS1/2 and MOB1A/1B are shown with red "X" marks, indicating they are not phosphorylated or activated. YAP/TAZ nuclear translocation: Since LATS1/2 is not active, YAP/TAZ remains unphosphorylated and is free to translocate to the nucleus. Expression of target genes: In the nucleus, YAP/TAZ binds to the TEAD1-4 transcription factors, leading to the expression of target genes. Adapted from Juan & Hong 2016 [168].

The Hippo signaling pathway comprises a serine/threonine kinase cascade that phosphorylates the YAP protein at serine sites, normally serine 127. This phosphorylation results in the retention of YAP within the cytoplasm, which in turn restricts its ability to activate transcription [169]. Although serine 127 is considered the classic phosphorylation site within the Hippo signaling pathway, further research has discovered a constitutively active mutant of YAP that all five serine residues changed to alanine (named YAP5SA), showing stronger capacity to promote cell

growth and oncogenic transformation compared to the wild-type YAP. YAP5SA regulates YAP activity by exhibiting resistance to inhibition by the Hippo signaling pathway and is broadly used as a mimic of Hippo signaling pathway inactivation [170, 171]. When the Hippo signaling pathway is inactivated by YAP5SA, YAP and TAZ complex translocate into the nucleus and cooperate with TEAD family transcription factors to induce target gene expression [172].

Several studies have defined the essential roles of the Hippo-YAP signaling pathway in organ size control, tissue regeneration, and self-renewal [167] (Table 1-8). In two separate studies, researchers investigated the role of Hippo signaling in regulating liver size in mammals via a YAP overexpression approach to simulate pathway inactivation. These investigations demonstrated that induction of YAP expression in adult mouse livers led to a substantial three- to fourfold increase in liver mass attributed to enhanced cell proliferation. Notably, cessation of YAP overexpression resulted in rapid restoration of liver size, indicating activation of an intrinsic size control mechanism, potentially involving reduction of cell numbers through apoptosis [173, 174]. In recent years, numerous studies have greatly expanded our understanding of the Hippo signaling pathway network in angiogenesis. In this process, tip cells are identified by their numerous filopodia that guide the leading front of angiogenic vessels. Deletion of YAP/TAZ in mice resulted in significant reductions in tip cells, sprouts, and branching. Conversely, overactivation of YAP/TAZ led to excessive filopodia and branches, as well as hyperplastic vascular growth [175].

Table 1-8. Studies of Hippo-YAP pathway in myocardial infarction. Adapted from Zheng *et al.,* 2022 [176].

Model	Species	Methods	Outcomes	Ref.
Myocardial infarction	Mouse	Cardiomyocyte-specific overexpression of dominant negative Mst1	Improve heart function, decrease infarct size and fibrosis; Decrease CM apoptosis	(79-81)
Myocardial infarction	Mouse	Cardiomyocyte-specific deletion of Sav	Improve heart function, decrease infarct size and fibrosis; Increase vascularization	(6)
Ischemia reperfusion	Pig	Knockdown Sav via sub-endocardial injection of AAV9-shRNA	Improve heart function, decrease infarct size and fibrosis; Increase capillary density	(86)
Myocardial infarction	Mouse	Cardiomyocyte-specific overexpression of human Yap using Cre-flox and AAV9 respectively	Both improve heart function, reduce infarct size; Both increase CM proliferation	(83)
Myocardial infarction	Mouse	Cardiomyocyte-specific homozygous inactivation of Yap	Impair heart function, increase infarct size and fibrosis; Increase CM apoptosis	(84)
Myocardial infarction	Neonatal mouse	Cardiomyocyte-specific overexpression of YAPS112A	Improve heart function, decrease infarct size and fibrosis; Increase CM proliferation	(85)
Myocardial infarction	Neonatal mouse	Cardiomyocyte-specific deletion of Yap	Impair heart function, increase infarct size and fibrosis	(85)
Myocardial infarction	Mouse	Cardiomyocyte-specific heterozygous deletion of Yap	Impair heart function, increase infarct size; Increase CM apoptosis, decrease CM proliferation	(84)
Ischemia reperfusion	Mouse	Transient activation of human Yap via modified mRNA	Improve heart function, reduce scar size; Reduce CM necrosis	(87)
Myocardial infarction	Mouse	Epicardial-specific deletion of Yap and Taz	Impair heart function, increase infarct size and fibrosis, increase mortality	(89)

Ischemia reperfusion	Mouse	Myeloid cell-specific deletion of Rassf1A	Impair heart function, increase in infarct size and fibrosis	(90)
Myocardial infarction	Mouse	Myeloid cell-specific deletion of Yap/Taz	Improve heart function, reduce infarct size and fibrosis; Increase vascularization	(91)
Myocardial infarction	Mouse	Myeloid cell-specific overexpression of Yap	Impair heart function, increase in infarct size and fibrosis	(91)
Myocardial infarction	Mouse	Myeloid cell-specific deletion of Mst1/2	Improve heart function, decrease infarct size and fibrosis	(92)
Myocardial infarction	Mouse	Fibroblast-specific deletion of Yap	Improve heart function, decrease infarct size and fibrosis; Decrease CM apoptosis; Decrease fibroblast activation and proliferation	(93)
Baseline	Mouse	Fibroblast-specific deletion of Lats1/2	Impair heart function, spontaneous fibrosis	(94)
Myocardial infarction	Mouse	Fibroblast-specific deletion of Lats1/2	Impair heart function, increase fibrosis and mortality	(94)
Myocardial infarction	Mouse	Fibroblast-specific deletion of Yap and Taz	Improve heart function, decrease infarct size and fibrosis; Decrease fibroblast activation and proliferation	(96)
Myocardial infarction	Mouse	Fibroblast-specific overexpression of Yap	Impair heart function, increase fibrosis; Increase fibroblast activation	(96)
Baseline	Mouse	Fibroblast-specific overexpression of Yap via AAV	Impair heart function, increase fibrosis; Increase fibroblast activation	(97)

1.3.2.3.2 Gene delivery vehicles: nonviral versus viral vectors

Gene delivery vehicles are categorized into two types: nonviral and viral vectors. Fundamental differences exist between these vectors in terms of gene transfer mechanisms at the cellular level [177]. The primary non-viral gene transfer method is through plasmid DNA, which is a small, circular piece of DNA. Plasmid DNA offers several advantages in gene therapy, including its ability to carry large genetic payloads, remarkable organ specificity and its non-immunogenic nature [178]. Plasmid DNA

typically does not integrate into the host genome, thus avoiding the potential risk of insertional mutagenesis. However, plasmid DNA may just induce transient transfection, as the DNA may be rapidly degraded by DNAse and removed by the mononuclear phagocyte system [179]. Also, only a small fraction of genes reach the nucleus where the desired gene can be transcribed and subsequently translated into protein, as most plasmid DNA remains in the cytoplasm, causing low transfection efficiency (transduction rate in CMs: ~0.1% at the injection site) [180].

Given the limitations of nonviral delivery mechanisms, substantial research over recent years has focused on exploiting the intrinsic ability of viruses to transport genes to cells. Currently, the viral systems derived from retrovirus, lentivirus, adenovirus and adeno-associated virus (AAVs) are the predominant vehicles utilized in cardiovascular gene therapy studies and clinical trials [181]. The primary benefit of viral vectors lies in their superior transduction efficiency [182]. Compared to plasmid methods, virus-mediated gene delivery using AAVs, or adenoviral vectors achieved a 30- to 360-fold increase in cardiac transduction levels following direct intramyocardial injections in rabbits [183].

Among the viral vectors, AAVs are regarded as a favorable option for gene therapy as they have displayed a specific affinity for particular organs and tissues in the body. For example, AAV1, AAV4 and AAV6-10 exhibited high affinity for heart tissue (Figure 1-7) [184]. Currently, 13 AAV serotypes and over 100 AAV variants have been identified, among which AAV 1-9 are the most studied serotypes [185, 186]. AAV2 was the first serotype to be studied for retinopathy gene therapy and is regarded as the most used serotype in all AAVs' studies [185, 186]. The main strengths of AAVs in cardiovascular gene therapy include high, robust, and long-term cardiac gene expression, lack of pathogenicity, and moderate immunogenicity. More importantly, their ability to transduce nondividing cells such as CMs enables the regenerative potential of heart tissue [187, 188].

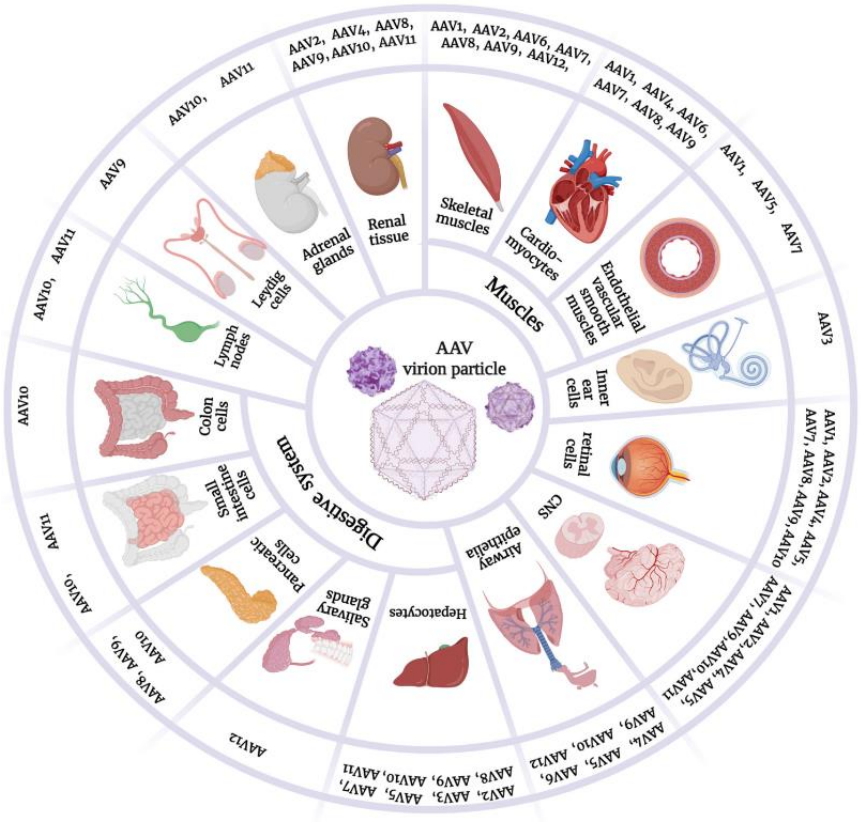

Figure 1-7. Tropism of AAV serotypes to human organs and tissues. Reproduced from Issa *et al.,* 2023 [184].

Researchers have revealed that serotypes naturally derived from primate heart tissues (AAV7, 8, 10, and AAVrh.10) and human isolate (AAV9) induced effective cardiac transduction in rodents following systemic administration [189]. Zincarelli *et al.* studied the distribution of serotypes AAV1-9 after systemic administration in a rodent model. The results showed that AAV9 had a rapid onset, superior genome distribution, and the highest protein levels compared to all other AAVs [190]. However, these AAV variants exhibited proficiency not just in the heart but also in transducing other organs, such as the liver and skeletal muscles [189, 191]. The inadvertent targeting and transduction of non-target organs by viral vectors, along with the unspecific expression of transgenes in these organs, may present significant safety hazards [192]. As indicated in the study by Prasad *et al.,* AAV9 demonstrated extremely high efficiency in cardiac gene delivery, showing an efficacy 232 times higher than AAV2. The study also observed a low level of expression in the livers of mice injected with AAV9, indicating the potency of AAV9 and its constrained capacity to enter the bloodstream after intramyocardial injection [193]. Therefore, AAV9-based vectors currently

represent the most effective approach for gene delivery to cardiac tissue in mice [142]. In Chapter 5, AAV9-mediated gene transfer was performed and tested as a novel treatment for MI. By utilizing AAV9 as a carrier, this study aims to transfer therapeutic genes directly into the heart muscle, potentially reversing cardiac damage caused by MI and improving cardiac function.

1.3.2.4 Delivery route of regenerative therapeutics

The field of cardiac regenerative medicine integrates stem cell therapy, biomaterial-based engineering, and gene transfer to enhance cardiac function and repair heart tissue. They can be utilized either singly or in combination. A range of techniques for delivering/implanting these therapeutics to the heart have been developed and employed in both preclinical and clinical investigations (Figure 1-8) [194].

Intramyocardial injection (IM) delivers therapeutics such as stem cells directly to the targeted area of the heart, usually the border zone of the infarct, which has a better blood supply and is crucial for post-MI remodeling [195]. This technique ensures high cell retention and engraftment and no risk of coronary embolism, making it suitable for administering larger cells like skeletal myoblasts and MSCs. However, this method has minimal paracrine effects [196]. Intracoronary infusion (IC) of stem cells is the preferred and safe delivery method, as it allows for more even distribution of cells in the damaged area and promotes higher cell survival rates due to the rich oxygen and nutrient content in the coronary circulation [197]. Additionally, IC causes less damage to the heart muscle and is associated with minimal inflammation post-transplantation. However, it has limitations such as minimal cell retention and the inability to deliver larger cells or doses due to the risking obstruction of coronary arteries, ischemia, and myocardial cell death [196, 198].

The intravenous (IV) approach is a simple and minimally invasive procedure that has been found to attract cells to the site of injury by relying on physiological homing signals to the injured myocardium. It also offers the option of multiple intermittent infusion treatments [199]. However, this technique is less effective than the IM and IC routes due to concerns about poor cell retention and engraftment. Most of the cells are either retained in the lung or cleared by phagocytic cells within the reticuloendothelial system [196, 200]. The transendocardial pathway (TE) is another minimally invasive

approach and offers greater cell retention. However, it requires specialized catheters and imaging modalities to deliver the cells to the target area. The stem cells are injected directly into the ischemic myocardium using a retrograde catheter with a needle, which is inserted through the aortic valve into the LV guided by electrical potential from a myocardial electromechanical mapping device [201]. While efficient and effective, stem cell injections are challenging to apply multiple times and a long-term use. Each surgical puncture of the femoral artery also carries the risk of major bleeding [202].

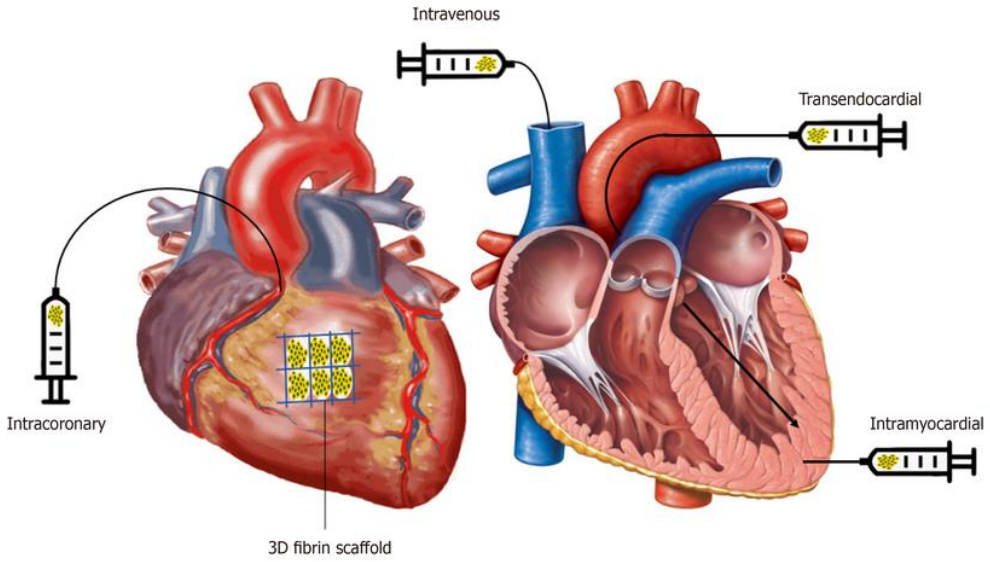

Figure 1-8. Delivery route of stem cells to the heart. Reproduced from Rheault-Henry, 2021 [196].

An alternative approach for delivering stem cells is by integrating them into multifunctional biomaterials (3D scaffold) to shield them from hypoxia and immune attacks [203]. Hydrogel serves as an optimal carrier for delivering regenerative therapeutics and can be applied through minimally invasive approaches to avoid the need for open surgery [204]. Currently, various strategies are employed for hydrogel administration, with the most common ones including IM and IC injections to achieve localized release of therapeutic agents at the site of injury [205]. These methods have strict requirements for the hydrogel properties due to their potential to cause re-embolization of coronary arteries, making it challenging to apply in the clinics [206]. The cardiac patch is engineered to enhance stem cell activity and promote the restoration of cardiac function without the risk of re-embolization of coronary arteries. It can be positioned over the injury site on the myocardial surface and within the tissue.

However, a limitation in its clinical application lies in the requirement for an open-chest procedure. To address this, a minimally invasive delivery method, such as an endoscope or catheter-based system, could be utilized to access the pericardial sac through the abdomen and diaphragm [207].

In the field of gene therapy, the efficiency of nucleic acid delivery is primarily determined by two key parameters: the gene vector and the administration route [208]. Viral vectors possess the intrinsic capability to enter cells and effectively deliver their DNA or RNA cargo into the nucleus with superior efficiency compared to non-viral vectors. AAVs emerge as an alternative to adenovirus due to their low immunogenicity, prolonged and elevated levels of transgene expression, and cardiotropism exhibited by certain serotypes [194]. Similar to other regenerative agents, the most common route of administration for gene delivery is direct IM injection, which can be achieved through either thoracotomy followed by transepicardial delivery or transendocardial delivery; however, they also present similar limitations: open-chest surgery, significant trauma, and bleeding [208].

Minimally invasive delivery techniques for regenerative therapeutics have become increasingly important in the medical field. The combination of minimally invasive procedures and regenerative therapeutics has proven to be particularly effective in treating MI. In Chapters 4 and 5, ultrasound-guided injections were applied and tested as a minimally invasive approach to administer the cardiac patch and target gene. It allows for the precise delivery of therapeutic agents to the target site, ensuring maximum efficacy and minimizing the risk of adverse reactions.

1.4. Evaluation of cardiac function with biomedical imaging techniques

The assessment of cardiac function offers invaluable diagnostic and prognostic insights following MI [209]. In patients with sustained MI and chronic LV dysfunction, parameters such as LV volumes and LVEF are important in predicting clinical outcomes [210]. The stroke volume (SV) refers to the amount of blood ejected from the LV during each cardiac cycle. However, not all the blood that fills the heart at end-diastole (end-diastolic volume, EDV) can be expelled during the systole, resulting in a residual volume known as end-systolic volume (ESV). SV is calculated by

subtracting ESV from EDV, thus yielding SV = EDV – ESV [211]. LVEF has long been regarded as the primary parameter for diagnosing and management of patients with HF. LVEF is calculated by dividing SV by EDV. It serves as a valuable tool in distinguishing between two types of HF: diastolic HF or HF with preserved EF (HFpEF) characterized by an EF ≥50% and systolic HF or HF with reduced EF (HFrEF) defined by an EF <40% [212].

Currently, non-invasive *in vivo* imaging plays an important role in cardiovascular research utilizing murine models. However, the small size and rapid motion of mouse hearts pose significant challenges for cardiac imaging, which requires costly equipment and advanced expertise. Given that the LV wall thickness is less than 1 mm, a high spatial resolution of the imaging technique is required. Simultaneously, the fast heart movement (400 to 600 beats per minute) demands high temporal resolution [213]. Table 1-10 displays several imaging techniques currently employed to evaluate the morphological and functional changes of the cardiovascular system in mice, such as high-resolution ultrasound (2D and 3D), X-ray computed tomography (CT), magnetic resonance imaging (MRI), and nuclear medicine imaging techniques. These imaging modalities have yielded significant and advantageous outcomes and contributed to the principles of reduction, refinement, and replacement in preclinical studies [214].

Biomedical imaging modalities, such as MRI, ultrasound and SPECT-CT, have been extensively utilized in both preclinical and clinical settings to evaluate cardiac function. Among these modalities, ultrasound distinguishes itself as a fast, widely accessible, and user-friendly technique, making it a preferred choice for routine cardiac assessments. However, with the growing advancements in regenerative therapies—such as stem cell delivery, biomaterial engineering, and gene therapy—there is an increasing need for more precise and localized evaluation of regional functional and morphological changes. These evaluations are vital for accurately reflecting the therapeutic effects and guiding treatment strategies. Consequently, the development and application of advanced biomedical imaging technologies have become indispensable. In Chapter 3, advanced ultrasound techniques, including 4D ultrasound and speckle-tracking echocardiograph (STE), are validated as powerful tools for assessing cardiac function with improved precision and detail using a MI model. Furthermore, the applicability of STE is extended to a clinically relevant mouse model

of cardiac amyloidosis, demonstrating their versatility and potential for broader applications in studying various cardiac conditions.

Table 1-9. Comparison of different imaging techniques for cardiac functional and left ventricular remodeling assessment. Reproduced from Frantz, 2022 [215].

Imaging modality	Benefits	Limitations	Development implications
Echocardiography			
2D	• Widely available • Low cost • Fast acquisition • Well tolerated by patients • Bedside studies possible	• Significant inter-individual and inter-operator variability • Challenges in patients with comorbidities (e.g. obesity)	• Guides medical/device therapy • Method of choice for clinical routine
3D	• Increased accuracy • Representative even in altered ventricular geometry	• High level of operator experience required • Additional post-processing necessary • Not widely available	• Guides special interventions for acquired (ischemic) valve disease
Contrast echo	• Improved accuracy and reproducibility	• Likely limited to experienced centers • Time consuming	• May improve earlier detection of LV remodeling
CMR			
Imaging	• Gold standard for assessment of cardiac volumes and function • High reproducibility, low variability • Multi-organ imaging • Possibly reduction in sample size for clinical trials • RV and valve assessment independent of anatomy	• Resource and cost intense • Limited availability • Longer acquisition • Reduced patient compliance • Prone to artefacts due to implants (devices, valves, etc.)	• Provides excellent assessment quality for challenging cases • May identify reversible causes of remodeling
LGE	• Non-invasive assessment	• Prone to breathing artefacts	• Territory guided revascularization

Imaging modality	Benefits	Limitations	Development implications
	validated histologically • Assessment of viability/MVO, ischemia, blood flow and fibrosis • Equally potent for clinical and research applications	• Limited suitability for patients with severe renal disease • Possible long-term deposition of gadolinium in cerebral tissue	• Anti-fibrotic therapies
Parametric mapping	• Native T1-mapping can determine the etiology of cardiac injury • Contrast-enhanced T1-mapping enables the calculation of ECV for diffuse fibrosis • T2*-mapping can detect IMH/MVO	• Parametric mapping sequences are largely research techniques without clinical validation • Prone to artefacts by breathing or arrhythmia • Sequences and values not universally agreed across different vendors/systems	• May allow identification and phonetization of subgroups benefiting from intensive and early treatment • Assessment of area at risk and scar size post-infarction may improve risk stratification
MR spectroscopy	• Investigation of high-energy phosphate metabolism and mitochondrial function (^{31}P-MRS) • *In vivo* assessment of metabolic pathways (hyperpolarized MR)	• Only applied in the research setting • Requires center-experience and specialist input and equipment	• Early identification of treatment response • Possibly reducing cost for drug development by providing early *in vivo* readouts with limited patient numbers
Nuclear imaging			
SPECT/PET	• Plethora of molecular radiolabeled molecules allows *in vivo* assessment of perfusion, metabolic substrate usage and inflammation	• Currently research use mostly • Costly and resource intense • Limited availability of tracers	• Image-guided molecular therapy • Identification of novel targets and biomolecules

Imaging modality	Benefits	Limitations	Development implications
	• Multi-organ assessment • Improved assessment of treatment response		

2D, two dimensional; 3D, three dimensional; ^{31}P-MR, ^{31}phosphorus magnetic resonance; CMR, cardiac magnetic resonance; Echo, echocardiography; ECV, extracellular volume, IMH, intramyocardial hemorrhage; LGE, late gadolinium enhancement; MRS, magnetic resonance spectroscopy; MR, magnetic resonance; MVO, microvascular obstruction; PET, positron emission tomography; RV, right ventricle; SPECT, single photon emission computed tomography.

1.5. *In vivo* biomedical imaging techniques for monitoring and tracking regenerative therapeutics

Molecular imaging techniques are generally divided into two main categories: direct imaging, which involves the use of contrast agents such as radioactive tracers or magnetic particles, and reporter gene-based techniques, which depend on the expression of receptors, proteins, or enzymes in cells that can specifically bind with molecular probes containing imaging biomarkers [216, 217] (Figure 1-9).

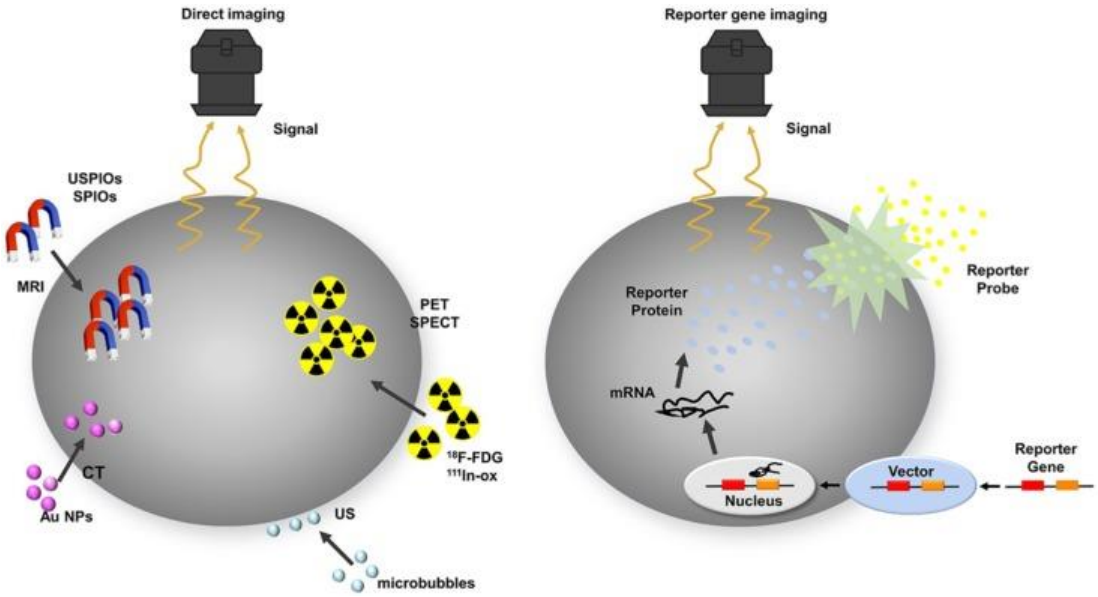

Figure 1-9. Illustration of commonly used *in vivo* molecular imaging approaches. Adapted from Li *et al.,* 2018 [216].

Direct labeling is particularly advantageous for visualizing the delivery process and short-term homing of stem cells in various organs. Among imaging modalities, MRI stands out for its exceptional spatial resolution and near-real-time image guidance during cell delivery. However, MRI has lower molecular sensitivity compared to radionuclide-based techniques such as PET, SPECT, or optical imaging (OI) such as fluorescence imaging (FLI), bioluminescence imaging (BLI). PET and SPECT, known for their high sensitivity, are widely used for cell tracking, although their spatial resolution may be insufficient for certain applications.

For long-term monitoring of stem cell viability and function, indirect labeling through reporter gene imaging is a more suitable approach. This method can be achieved using optical imaging techniques, including bioluminescence or fluorescence, as well as radionuclide imaging with PET or SPECT. Optical imaging offers exceptional

molecular sensitivity but is limited by poor anatomical localization and its applicability primarily to small animal models. In contrast, PET and SPECT provide a balance of good sensitivity and precise anatomical localization, making them ideal for translational research and long-term studies in both preclinical and clinical settings [218]. Monitoring of gene expression is essential for investigating the responses of gene therapy and elucidating gene function in diverse environments. Currently, a variety of sensitive imaging modalities, including MRI, optical imaging techniques PET and SPECT hold the greatest clinical potential for reporter gene/gene therapy imaging [216, 219] (Figure 1-10).

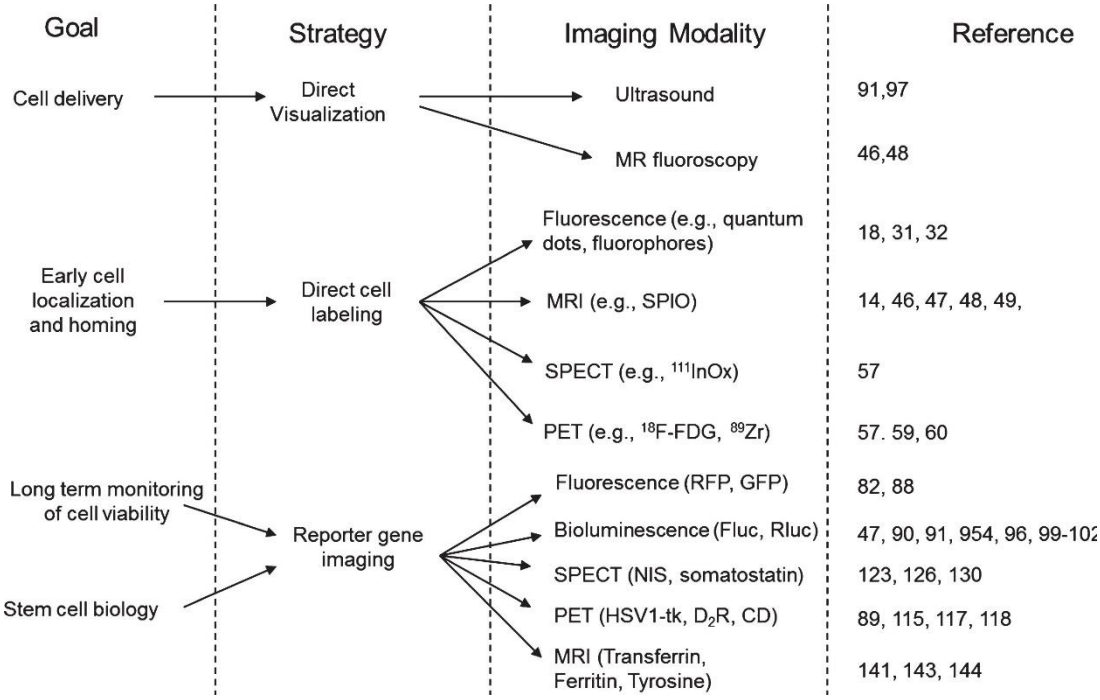

Figure 1-10. Imaging strategies applied to assess the delivery, short- and long-term monitoring of stem cell viability and biology. MRI: magnetic resonance imaging, SPECT: single photon emission computed tomography, PET: positron emission tomography, RFP: red fluorescent protein, GFP: green fluorescence protein, Fluc: firefly luciferase, Rluc: renilla luciferase, NIS: sodium iodine symporter, HSV1-tk: herpes simplex virus type 1 thymidine kinase, D_2R: dopamine receptor type 2, CD: cytosine deaminase. Adapted from Fakhar *et al.,* 2019 [220].

1.5.1. MRI

MRI is a molecular imaging technique that exhibits exceptional spatial resolution (10–100 μm [small animal MRI]; 500–1500 μm [clinical]), high temporal resolution, and sensitivity without radiation [221, 222]. Two types of contrast agent that generates sufficiently detectable positive or negative signals from the background have been used for stem cell tracking [223].

The first group comprises gadolinium (Gd)-based contrast agents, primarily offering positive T1 contrast effects. The other type of contrast is achieved by utilizing superparamagnetic iron oxide particles (SPIONs) to induce robust negative T2/T2* contrast effects [222, 223]. Guenoun *et al.* demonstrated the application of water-soluble Gd chelating agents (Gd-DTPA) in tracking stem cells through MRI both *in vitro* and *in vivo*. Prolonged in vivo imaging of 500,000 Gd-labeled cells was successfully achieved for at least 2 weeks without any adverse effects on cell viability, proliferation, and differentiation [224]. Compared to SPIONs contrast agents, the Gd chelate exhibits a lower molecular weight, enabling it to evade macrophage reuptake following cellular release, such as in cases of cell death. This advantageous characteristic is particularly crucial in an *in vivo* setting as it enhances the specificity of the MRI signal, facilitating a comprehensive assessment of overall cell viability subsequent to cell transplantation [224].

In addition, the clinical translation of Gd-based contrast agents for cell labeling and tracking has been impeded by concerns regarding their inherent toxicity and safety, as Gd^{3+} ions are highly toxic when administered in low doses as free ions. This toxicity can affect both the labeled cells themselves and the surrounding host tissues [225]. Gd^{3+} contrast agents have also been reported to induce nephrogenic systemic fibrosis in patients with impaired kidney function or renal failure [226]. Therefore, to improve biocompatibility for clinical applications of Gd^{3+} ions, they must be complexed with chelating ligands that exhibit high stability. For instance, the complexation of Gd^{3+} ions with chelating ligands such as diethylenetriaminepentaacetic acid (DPTA) forms stable complexes that were designed and approved for clinical usage in 1988 [227].

The T_2 agents based on SPIONs are considered the preferred MRI contrast agents for stem cell monitoring, exhibiting high sensitivity and excellent biocompatibility compared to Gd-based contrast agents [228]. The sensitivity of SPIONs is attributed to the substantial dipolar magnetic field gradient experienced by protons in close proximity to the particles, resulting in prominent "blooming" hypointensities in images. This effect is further enhanced through cellular internalization and particle clustering [229]. Therefore, the dual capability of SPIONs, enabling their cellular internalization and responsiveness to external magnetic fields, has rendered them invaluable tools for stem cell labeling and tracking by MRI [230]. Also, the biodegradability of SPIONs

within the human body through the endogenous iron metabolic pathway, as well as their utilization in hemoglobin formation, confers distinct advantages over other metal contrast agents [231]. Vandergriff *et al.* demonstrated that intracoronary infusion of SPIONs-labeled human cardio-sphere-derived stem cells in a rat MI model resulted in increased acute cell retention, leading to reduced LV remodeling and improved therapeutic efficacy at 3 weeks post-treatment [232]. However, the contrast specificity to the presence of cells poses a significant concern. It should be noted that even after cell death, the hypointense signal persists. Therefore, it is important to acknowledge that the MRI signal from iron oxide nanoparticles does not represent exogenously labeled stem cells only but also includes extracellular SPIONs complexes or SPIONs engulfed by macrophages [221, 229].

For biomaterial tracking, distinguishing biomaterials in tissue regeneration, MRI contrast agents/nanoparticles are utilized and incorporated into the implant [233]. Hill *et al.* successfully developed an engineered protein-iron oxide hybrid material by templating high-density ultra-small SPIONs onto a mesofibrous scaffold. The resulting hybrid material exhibited excellent and sensitive T_2^*-weighted MRI darkening, providing powerful material-tracking imaging capabilities [234]. Moreover, the SPIONs are functionalized for the purpose of monitoring material degradation. A study conducted on a 22-day time course confirmed that on days 8, 15, and 22 post-implantation the consistently stable MRI signal indicated no degradation of the scaffold material. This finding was further supported by size measurements and histological analysis [235]. However, T_2 contrast agents-based MRI techniques are associated with certain limitations, such as interference with nearby tissue signals and the inability to differentiate from various inherently negative contrast sources like air/tissue interfaces, blood clots, or iron deposits [233]. To enhance the specificity of detection, T_1 contrast agents are preferable alternatives since very few endogenous species exhibit naturally high signals on T_1-weighted imaging [236].

1.5.2. Radionuclide labeling imaging techniques

Radionuclide molecular imaging is a readily available technology for the early tracking of stem cells in relation to their homing and quantification within diseased tissues, such as PET and SPECT modalities. Several radionuclides have the potential

for stem cell labeling, with the most commonly utilized ones being ^{18}F-fluorodeoxyglucose (^{18}F-FDG) (T½ = 110 min) for PET imaging and ^{111}Indium (^{111}In) oxyquinoline (T½ = 2.8 days) and ^{99}mTc-hexamethylpropylenamineoxime (^{99}mTc-HMPAO) (T½ = 6 hours) for SPECT imaging [223, 237-239]. Due to their exceptional sensitivity in the picomolar range (<10−9 M), PET and SPECT imaging modalities enable the detection of biological processes at extremely low concentrations [240]. These modalities enable cell tracking over a sufficient duration (hours) to evaluate acute cell retention and facilitate image quantification for obtaining an estimation of cell numbers in a specific organ [241]. For instance, the well-established method of labeling embryonic cardiomyoblasts with ^{111}In enables detection of the associated ^{111}In signal using SPECT imaging of the heart for up to 96 hours following engraftment [242]. The study conducted by Tran *et al.* demonstrated that approximately 60% of injected ^{111}In-oxine labeled MSCs were estimated to be retained within the hearts for a duration of 7 days [243].

PET and SPECT imaging have also been employed for *in vivo* monitoring of engineered tissues. For instance, Wolf *et al.* utilized PET-CT with ^{18}F-FDG as a metabolic tracer, combined with MRI, to non-invasively monitor the complete life cycle of tissue-engineered vascular grafts in an ovine model [244]. Patrick *et al.* developed a technique for incorporating the nuclear imaging radio-metal ^{111}In into alginate hydrogel structures, enabling non-invasive *in vivo* nuclear imaging to detect the delivery and retention of hydrogels throughout the entire body over time [245].

The major advantages of utilizing radionuclide probes for tracking stem cells and biomaterials include their inherently high signal-to-noise ratio and the ability to quantify levels of radionuclide probes. However, due to their short half-lives, these tracers only allow for nuclear imaging during short examination periods. Subsequently, zirconium-89 oxinate [^{89}Zr] Zr-oxine emerged as a potential radiometal for labeling stem cells, offering a longer half-life (T½ = 78.4 h) that enables monitoring of cell migration over several days with high sensitivity, resolution, and specificity [246]. A similar outcome was observed in a study by Sato, Wu *et al.* where the use of ^{89}Zr-oxine complex allowed for extended cell tracking up to 7 days [247]. Additionally, the efficiency may also be limited by the efflux of the radiotracer/radionuclide from the radiolabeled cells *in vivo*, and information on *in vivo* cell proliferation cannot be

obtained due to label dilution caused by redistribution of the radionuclide probe during cell division [248].

1.5.3. X-Ray imaging and micro-CT

Computed tomography (CT) mode imaging generates a 3D reconstruction of the targeted sample by capturing transmitted X-rays from different angles by a multi-array detector [249, 250]. The CT contrast is highly sensitive to materials that attenuate X-ray transmission. The current development of more sensitive techniques, such as micro-CT and nano-CT, has significantly improved resolution and enabled the study of morphology and 3D structure of various scaffold geometries at sub-micron scale [250, 251].

Micro-CT offers the advantages of MRI while significantly reducing scan time and achieving even better spatial resolution (<1 μm) [252]. Additionally, micro-CT provides non-destructive and direct 3D models and non-invasive qualitative analysis. In particular, micro-CT allows for 3D analysis, including density estimation, porosity assessment, structural thickness measurement and morphometric analysis [253, 254]. However, the low X-ray absorption in soft tissues presents a limitation for micro-CT scanners due to the resulting low contrast, which can be addressed with contrast [255]. Iodine is currently the most used element for intravascular CT contrast in clinical practice [256, 257]. The use of iodine solution presents a straightforward, cost-efficient, and non-toxic option for enhancing the contrast of soft tissues, as well as aiding implant positioning [258]. Becerra *et al.* have developed an X-ray visible scaffold through selective iodination of tyrosine residues. After implanting into a mouse model, the implants maintained significant X-ray contrast for up to 3 months while retaining an unchanged degradation rate and inflammatory response [259].

Micro-CT is considered a rapid technique due to its scan times ranging from a few minutes to several hours, depending on scan parameters. However, higher magnification and resolution will result in longer scanning times, leading to increased radiation doses that must be considered in longitudinal studies using in vivo micro-CT scanners. The size of the structure is another important factor to consider, as structures smaller than a certain size may not be detectable by micro-CT [260].

1.5.4. Non-invasive reporter gene imaging

MRI reporter genes can be classified into three categories based on the types of encoded genes: (1) encode enzymes (e.g., tyrosinase and β-galactosidase); (2) cell surface receptors (e.g., transferrin receptor (TfR)); and (3) endogenous reporter genes (e.g., ferritin reporter gene) [218, 261]. Liu *et al.* investigated the potential of non-invasive monitoring of BMSCs transduced with the tyrosinase reporter gene for acute MI rat model using *in vivo* MRI, revealing prominent signals in the injected area of the infarcted myocardium on PAI/MRI/PET images [262]. The researchers developed an MRI probe that was activated in the presence of therapeutic protein expression and utilized this technology to track β-galactosidase enzyme expression following AAV gene therapy in a mouse model. This innovative approach provides a non-invasive means to monitor gene expression over time in patients [263]. In another study, ferritin-tagged cells were transplanted into infarcted rodent hearts and demonstrated that ferritin overexpression did not adversely impact cell viability, proliferation, or differentiation. It allowed for accurate quantification of graft size within the heart through MRI detection both *in vitro* and *in vivo* after transplantation [264]. The utilization of reporter genes for MRI-based cell tracking presents two significant advantages over particle-based techniques: (1) gene expression is closely associated with cell viability, in contrast to particle retention, and (2) when integrated into the genome, transgene-based reporters are less susceptible to signal loss through cell division, making them uniquely suitable for longitudinal monitoring of cell transplants [264].

Radionuclide-based reporter gene imaging techniques, such as SPECT and PET, are highly sensitive methods for detecting low-level reporter gene expression at picomolar tracer levels. Cells stably transfected with reporter genes expressing proteins that facilitate radiotracer binding or accumulation in the cell of interest can be visualized using radioactive PET or SPECT probes, enabling repeated imaging to track cell migration and function [265]. Three types of radionuclide imaging reporter genes have been created based on receptors, transporters, or enzymes: intracellular entrapment by encoded kinases that phosphorylate specific PET probes (e.g., HSV-tk1 for FHBG), binding of specific PET probes to cell surface protein receptors (e.g., D2R for FESP), or facilitating specific PET probes into the cell through cell membrane transporters

(e.g., NIS for I-124) [261, 266].

A prominent finding is that receptor-based reporter genes promote the generation of cell receptors, which can then be specifically targeted by imaging tracers [248]. Studies have examined the sodium iodine symporter protein, which is not naturally present in the heart but facilitates cellular uptake of ^{99}mTc or ^{124}I, allowing for cell tracking through SPECT or PET imaging, respectively. NIS expression enables non-invasive *in vivo* stem cell tracking in the myocardium using both SPECT and PET [267]. Additionally, enzyme-based reporter genes enable cell tracking through enzymatic trapping of radiotracers within genetically modified cells. For instance, genetic modification of cells to express herpes simplex virus type 1 thymidine kinase (HSV1-tk) and cardiac SPECT reporter gene imaging based on HSV1-tk as a reporter gene and 131I-FIAU as a reporter probe has been utilized for noninvasive SPECT imaging of gene therapy in cardiac diseases [268]. In a similar study, imaging of cardiac HSV1-sr39tk expression was effectively conducted in live rats using PET [269]. Ultimately, these techniques related to reporter gene imaging by SPECT/PET hold promise for potential application to human gene therapy studies.

1.5.5. Bioluminescent imaging

BLI has been a widely utilized tool in the past decade for noninvasive monitoring of cell location and proliferation [270]. BLI relies on a reporter gene, such as firefly luciferase (Fluc), which is genetically modified to express a luciferase enzyme in cells. In the presence of cofactors (ATP, Mg^{2+}, and oxygen), the luciferase enzyme catalyzes the oxidation of its substrate, D-luciferin, to produce visible light [271, 272]. This method is used for *in vivo* monitoring of cell viability in small animal models due to its ability to detect photon signals produced only by metabolically active cells dependent on ATP acquisition [240, 273].

Recent studies have demonstrated the effective use of BLI for monitoring and quantifying the proliferation status of luciferase-expressing stem cells seeded in hydrogel scaffolds over extended periods (90 days) [274]. Although BLI does not directly visualize the biomaterial, it can indirectly reflect the function of scaffolds in maintaining cells with higher cell viability and proliferation. In the study, BLI demonstrated a higher level of cell viability in the patch adhered to the epicardium of

the infarcted region in rat hearts compared to the group receiving intra-myocardial injections [275]. Additionally, BLI can be used as a preferred noninvasive technique to track delivered cells and evaluate new delivery platforms designed to increase cell homing, retention, and engraftment. For example, studies applied BLI as a sensitive and specific imaging approach for monitoring both the distribution and number of injected cells over time [276].

Compared to other imaging modalities such as MRI and nuclear imaging, BLI offers a straightforward, rapid, cost-effective, easily implementable, and highly sensitive alternative (10^{-15}–10^{-17} mol/L) without background [271]. However, the clinical applicability of traditional bioluminescence is constrained by limited tissue penetration, rendering them impractical for use in patient trials. In Chapter 4 and Chapter 5, BLI was validated as a reliable imaging technique to monitor the viability of the seeded stem cells on a cardiac patch and track the distribution of gene *in vivo* serially.

1.5.6. Multi-modality imaging

There has been notable progress in the development of advanced molecular imaging techniques to assess stem cells, scaffold, and gene-based regenerative therapies. Nevertheless, each imaging modality possesses its strengths and limitations. Radionuclide imaging is recognized for its high sensitivity but limited spatial resolution, as well as short-term tracking due to the short half-life of tracers. MRI demonstrates superior soft tissue contrast but is constrained by low sensitivity. BLI offers relatively high sensitivity and spatial resolution but lacks the ability to image deep tissues. Multimodality imaging has been actively developed in recent years to overcome these limitations by integrating different modalities to achieve enhanced spatial resolution and provide functional and molecular insights in regenerative therapies [277, 278].

Studies have explored the integration of multimodality imaging and indicated that multimodality imaging provides advantages over single-modality imaging. One study demonstrated that BLI combined with multimodality MRI could be utilized for visual and dynamic monitoring of the biological behavior of BMSCs transplanted into a mouse model. In this study, double-labeled mouse BMSCs with firefly luciferase and ultrasmall superparamagnetic iron oxide (USPIO) were implanted in a mouse model.

The results demonstrated that the BLI trace signal persisted for 7 days *in vivo*, while the MRI signal lasted up to 3 days. However, MRI offered more detailed pathophysiological information than BLI, such as signs of inflammation and fibrosis [279]. In a separate study utilizing multimodal imaging techniques to monitor the behavior of stem cells, transduced adipose-derived stem cells were observed in the heart using both BLI and PET/CT imaging. This observation contributed to the regeneration of CMs and angiogenesis in the implanted areas. In comparison with BLI monitoring, PET/CT data provided accurate localization for cell retention [280]. Another paper highlighted the complementary analysis of cell localization and viability using reporter gene imaging with 124I-PET and MRI labeling with iron oxides. While iron labeling quickly lost specificity for cell viability due to the phagocytosis of iron particles released from dead cells, reporter gene expression provided specific information on the number of surviving cells [281].

Above all, multimodal imaging plays a crucial role in advancing regenerative medicine. This allows researchers to gain comprehensive insights into the behavior of stem cells, the distribution of biomaterials, and the expression of therapeutic genes. These imaging modalities enable real-time monitoring, precise localization, and assessment of treatment efficacy. As regenerative therapies continue to evolve, multimodal imaging remains an indispensable tool for optimizing patient outcomes and accelerating the translation of innovative treatments from the lab to clinical practice.

In Chapter 5, diverse imaging techniques were utilized to assess the AAV9-mediated gene therapy. Ultrasound served as a non-invasive delivery method and functioned as a modality for cardiac functional assessment. MRI was employed to monitor changes in heart morphology and provide comprehensive information on infarct size, heart mass, *etc*. Importantly, BLI was utilized for visualizing the location of the injected gene and quantifying gene expression through signal intensity over time. The combination of these imaging modalities provided a detailed understanding of how gene therapy affected not only structural changes in the heart but also its functional aspects over time. These imaging techniques established a platform that enables researchers to gain valuable insights into the efficacy and long-term effects of AAV9-mediated gene therapy in preclinical models.

1.6. Hypothesis and aims

The hypothesis of this thesis is as follows: the integration of diverse imaging modalities provides a reliable platform for assessing various experimental therapies in a murine model of myocardial infarction.

To test this hypothesis, the aims of the project were:

1. Establish a reliable and robust mouse model of MI for testing experimental therapies and validating biomedical imaging techniques.
2. Compare two types of clinically relevant MI mouse models—PL and IR—to determine an optimal ischemia duration and examine the potential effects of reperfusion on cardiac function.
3. Assess the reliability and accuracy of 4D-US by comparing conventional ultrasound modes with MRI as a reference.
4. Validate STE-derived strain analysis for both global and regional evaluation of cardiac function in a mouse model of MI, providing additional and comprehensive information on regenerative therapeutics in a mouse MI model.
5. Optimize biomaterials to enhance their attachment to the heart and improve the survival and retention of stem cells.
6. Validate SPECT-CT imaging to achieve a long-term visualization and localization of the implants.
7. Test ultrasound-guided injection of stem cell-loaded biomaterials and target genes into the heart to achieve minimally invasive delivery therapeutics.
8. Demonstrate a reliable imaging platform for AAV9-mediated gene therapy, including ultrasound guidance for delivery, BLI for localization and monitoring gene expression, as well as ultrasound and MRI for evaluating potential therapeutic effects in treating MI.

Aim-specific objectives are detailed in the relevant chapters.

Chapter 2 Establishing a mouse model of myocardial infarction: comparison of permanent ligation and ischemia-reperfusion

Graphic abstract

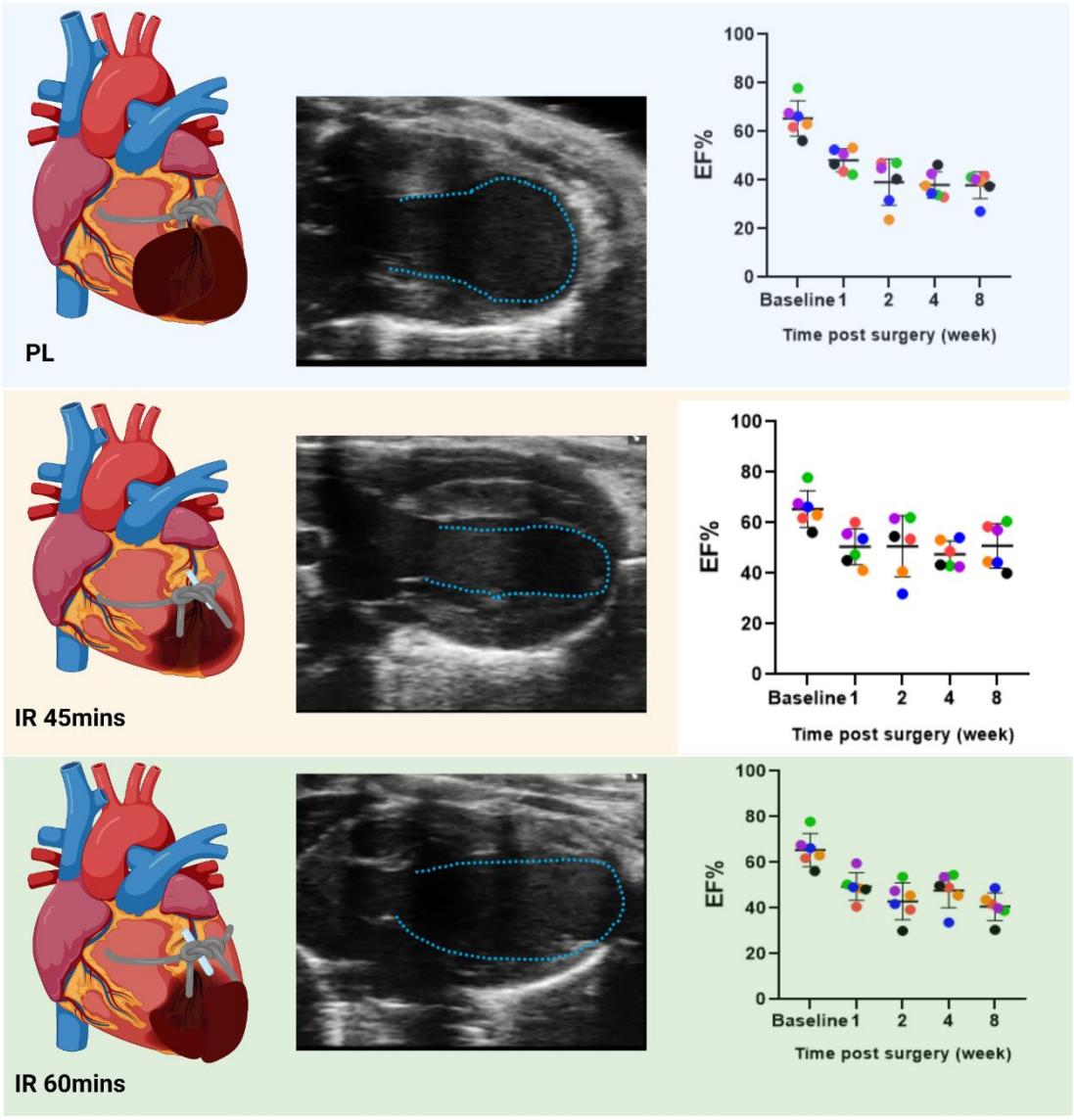

Abstract

Animal models for myocardial infarction have been crucial for studying its underlying mechanisms and developing new treatments, in which surgical-induced permanent ligation (PL model) of left anterior descending coronary artery (LAD) and temporary LAD occlusion with reperfusion (IR model) being widely used in preclinical research. However, the challenging nature of the conventional surgical procedure is renowned for generating considerable variability in infarct size. Additionally, the long-term impact of initial infarct size or reperfusion injury on resultant cardiac function has not been comprehensively investigated.

This study aims to refine conventional MI surgery to establish a robust and reliable MI model and assess cardiac function via ultrasound as a means of comparing two types of MI models from the early to late phases of MI.

Eighteen Balb/C mice underwent open-chest surgery to induce PL and IR 45mins and IR 60mins models (n=6 each group) by ligating the LAD at 1-2mm below the tip of the left auricle. Ultrasound was performed at baseline, weeks 1, 2, 4 and 8. PL had significantly lower EF than IR 45mins in weeks 2 and 8. However, no significant differences in EF were found between the IR groups over 8 weeks, as well as between the PL group and IR 60 mins group. A higher variability in EF within the IR models with a larger standard deviation (IR 45mins: 35.51 ± 15.05%; IR 60 mins: 44.24 ± 13.88%) compared to the PL group (57.29 ± 9.12%).

This study established a reliable and reproducible PL model. IR 45mins experienced sufficient cardiac functional impairment with an EF of less than 55%, to be a reliable IR model, while IR 60mins had less cardiac functional impairment than those in the PL group, indicating that there was still salvageable myocardium. This study provides robust MI models for future research aimed at testing experimental treatment (PL model) and studying the underlying mechanism of myocardial ischemia-reperfusion injury (IR model).

2.1 Introduction

Cardiac ischemia and reperfusion injury stand as the primary causes of HF and mortality worldwide [282]. Early reperfusion therapy is correlated with enhanced myocardial salvage aligns conceptually with the findings of large-scale clinical trials investigating reperfusion strategies in acute MI [17]. However, the reperfusion process triggers harmful effects that cause the immediate death of previously viable cardiac myocytes, worsen acute and long-term ischemic damage, and increase the infarct size [11]. It is hypothesized that this may account for the fact that, despite optimal myocardial reperfusion, the mortality rate following an AMI remains at nearly 10%, and the incidence of HF post-acute MI approaches 25% [283, 284]. Therefore, novel cardioprotective interventions are needed to promote more effective tissue repair and minimize reperfusion injury and its associated adverse outcomes.

Over the past decades, MI animal models have proven to be invaluable tools in developing diagnosis methods, as well as investigating the underlying mechanisms of MI pathogenesis. Moreover, they significantly contribute to the development of novel treatment strategies [285]. There are several ways to induce MI mouse models, with the most commonly employed *in vivo* approaches being permanent left anterior descending coronary artery (LAD) occlusion (PL model) and temporary LAD occlusion for inducing ischemia-reperfusion injury model (IR model) [48]. The main differences between PL and RI models are summarized in Table 2-1 [286].

	Permanent ligation model	Ischemia-reperfusion injury model
Injury Assessment	Infarct size 	Area at risk 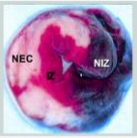
Infarct Size	Large infarct; 40-60% of LV infarcted	Small infarct; area at risk <30% of infarct region
Study Goal	•Prevention of heart failure •Assessment of inflammation and scar formation, cardiac repair •Evaluation of cell-cell crosstalk	•Refinement of current optimal therapy •Assessment of cardioprotection •Evaluation of cell-cell crosstalk
Survival	Mortality due to LV rupture, arrhythmias, or heart failure	Mortality due to early arrhythmias
LV Structure & Physiology	•Significant infarct wall thinning due to myocyte loss •LV becomes dilated •Limited LV functional recovery	•Little to no infarct wall-thinning •LV shape maintained •Limited loss of LV function
Cellular/ Molecular Physiology	•Excessive myocyte injury & cell death •Can generate multi-organ dysfunction •Intense inflammation •Leukocyte kinetics & signaling •Angiogenesis	•Partial myocyte injury & cell death •Generates focal injury limited to heart •Brief inflammatory response •Leukocyte kinetics & signaling •Angiogenesis

Table 2-1. Major differences between the permanent ligation MI model and ischemia-reperfusion injury MI model. In the permanent ligation MI model, the ventricles are cut from base to apex and stained with 1% triphenyl tetrazolium chloride to distinguish viable myocardium (red) from infarcted tissue (white). In contrast, for the ischemia-reperfusion injury heart, the mid-myocardial sections are stained with Evans blue and 1% triphenyl tetrazolium chloride to illustrate necrotic zone (white), nonischemic zone (blue), and ischemic zone (red and white). MI, myocardial infarction. Adapted from Lindsey *et al.,* 2021 [52].

In general, PL typically results in a relatively large infarct, with the average size ranging between 30% and 60% of the myocardium area. However, there is considerable variation observed, ranging from as low as 4% to as high as 65% [287]. The severity of MI and infarct size can be influenced by various factors, including operator experience, mouse strain, and most importantly, the location of LAD and the site of ligation [288, 289]. The majority of the literature offers only a broad overview of the approximate location of LAD within the anterior wall of the heart; nevertheless, its precise position is not consistently fixed due to interindividual variations in branching patterns and orientations (Figure 2-1). This variability contributes to heightened surgical complexity and potential complications [290]. In addition to variations in the distribution patterns of LAD, the location of LAD ligation also plays a crucial role in the determination of the infarct size. Proximal ligation sites are associated with larger infarct sizes, which significantly impact LV remodeling and mortality [291]. Villiers and Riley have reported that larger infarcts can lead to acute HF or ventricular rupture, resulting in an increased mortality rate of approximately 27% [292]. However, distal ligation sites may not effectively occlude the LAD due to

anatomic variations such as 'dual LAD,' which consists of two branches supplying the typical distribution of the LAD, and the prevalence of dual LAD ranges from 0.68% to 6% in various case series [293, 294]. Hence, it is important to establish a consistent and reproducible PL model through the precise determination of the LAD ligation position to ensure reliable data generation, as wide variability in results has compromised their statistical significance and limited their values.

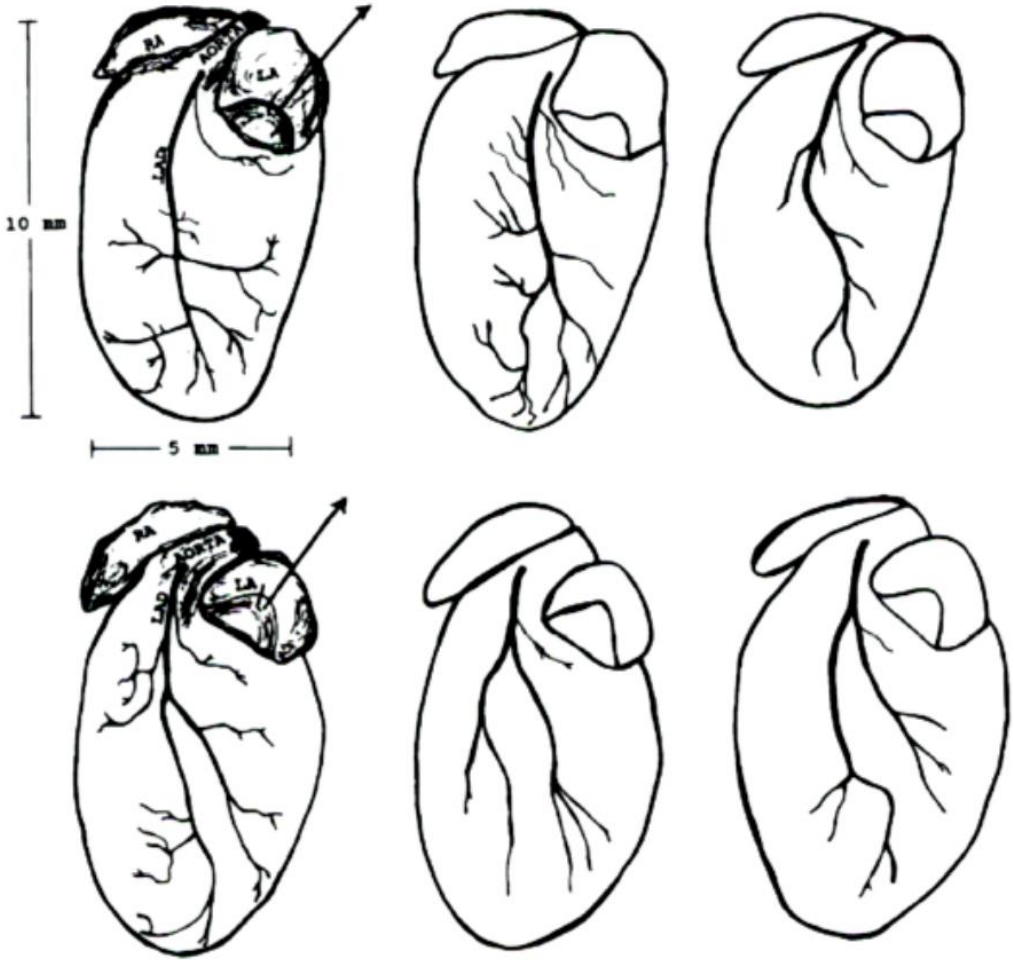

Figure 2-1. Coronary arterial anatomy in six mouse hearts. Top Row: a common pattern characterized by a prominent singular LAD. Bottom Row: another pattern featuring a significant bifurcation of the LAD. Reproduced from Michael *et al.,* 1995 [295].

Considerable variability in infarct size also has been observed after ischemia-reperfusion [296]. Accurately predicting the extent of myocardial ischemia saved by reperfusion is essential. In addition to factors such as differences in LAD distribution or ligation points, collateral blood flow, animal strain, and surgeon expertise contributing to this variability, the duration of reperfusion introduces another significant level of unpredictability to the final infarct size, which can be challenging

to assess in individual patients [297]. A shorter reperfusion time is associated with reduced infarct size, as well as indications of improved myocardial salvage and decreased 6-month mortality rates [298]. According to the literature describing the IR mouse model, the duration of ischemic occlusion prior to reperfusion ranged from 15 minutes to 2 hours, with 30 minutes being commonly cited as the most adopted duration. However, there is insufficient data provided to justify 30 minutes as the optimal duration of ischemia for a reliable and consistent IR model [49]. The researchers demonstrated that following 30 minutes of ischemia, mice may exhibit infarct sizes ranging from as low as 4%, indicative of mild injury with no impact on cardiac function or further pathology, to as high as 30%, which is considered the minimum infarct size to elicit a detrimental effect [49, 299, 300]. As mice exhibit greater tolerance to myocardial injury than humans, it may be more clinically relevant to extend the ischemia duration in a mouse model to achieve a moderate infarction size and LV dysfunction [49].

Studies have compared PL and IR models by assessing infarct size, which can be quantified through TTC staining in the PL model and Evans-TTC staining in the IR model. However, Evans-TTC staining is routinely performed within a time window ranging from 4 hours to 7 days after ischemia, with the most prevalent timeframe being 24-48 hours post-reperfusion [301]. Thus, it is of limited accuracy to compare the initial infarct resulting from reperfusion with the PL model at extended time points, such as weeks or months. Nevertheless, the long-term impact of initial infarction or reperfusion injury on cardiac function based on these models has not been comprehensively investigated. Specifically, the duration of ischemia is considered an essential factor in interpreting changes in cardiac function, providing valuable insights into investigating the contribution of reperfusion injury to cardiac dysfunction and determining optimal intervention timing. Hence, in this study, rather than quantifying infarct size or viable myocardium, cardiac function was assessed as a means of comparing two types of MI models from the early to late phases of MI. Cardiac function assessment by imaging techniques is a critical approach for evaluating the establishment of animal models, with Simpson’s multiplane ultrasound playing a significant role in both preclinical and clinical settings.

2.2. Aims

- Achieve a reliable and reproducible PL model that yields a larger and more consistent infarct size/cardiac function impairment associated with lower morbidity and mortality by improving the surgical technique of ligation of nonvisible coronary artery branches in mice.
- Achieve temporary LAD ligation (IR) model that induced moderate infarction size and LV dysfunction as the foundation of developing novel therapies.
- Explore the impact of different durations of ischemia on cardiac function following PL and IR mouse models while also examining the potential effects of reperfusion on ventricular remodeling and cardiac function.
- Identify an optimal ischemia duration in the IR model by comparing different LAD occlusion times and evaluating their impact on the model's performance and accuracy. This will involve conducting a comprehensive analysis of different occlusion times (45- and 60 minutes), assessing their cardiac functional changes, and determining the ideal occlusion time in the IR model that achieves the balance between model efficiency and accuracy.

2.3. Materials & Methods

The section below details the materials and methods needed to generate mouse models of MI. I initially learned the protocol from a colleague at Imperial College London, then adapted the methods as required. It is hoped that the detailed protocol below will be of use to future researchers learning the technique.

2.3.1. Surgical ligation LAD: A mouse model of myocardial infarction

2.3.1.1. Materials

Surgical instruments:

- Y connector to tracheal tube
- Spring scissors
- Strabismus scissors
- Castroviejo micro needle holder
- Micro locking forceps

- Chest retractor
- 3-0 silk suture, taper needle
- 6-0 silk suture, taper needle
- Fine bore polythene tubing
- Anesthesia and Analgesia
- Isoflurane
- Buprenorphine
- 1 % Lidocaine HCl

Others

- Hair removal gel
- MiniVent Type 845 mouse ventilator
- 1 mL Syringe w/blunted 23G needle
- Rectal temperature probe and heating pad
- 70 % (v/v) EtOH in H_2O
- Surgical gauze
- Endotracheal intubation stand
- Fiber optic light source
- Eye gel
- Surgical tape

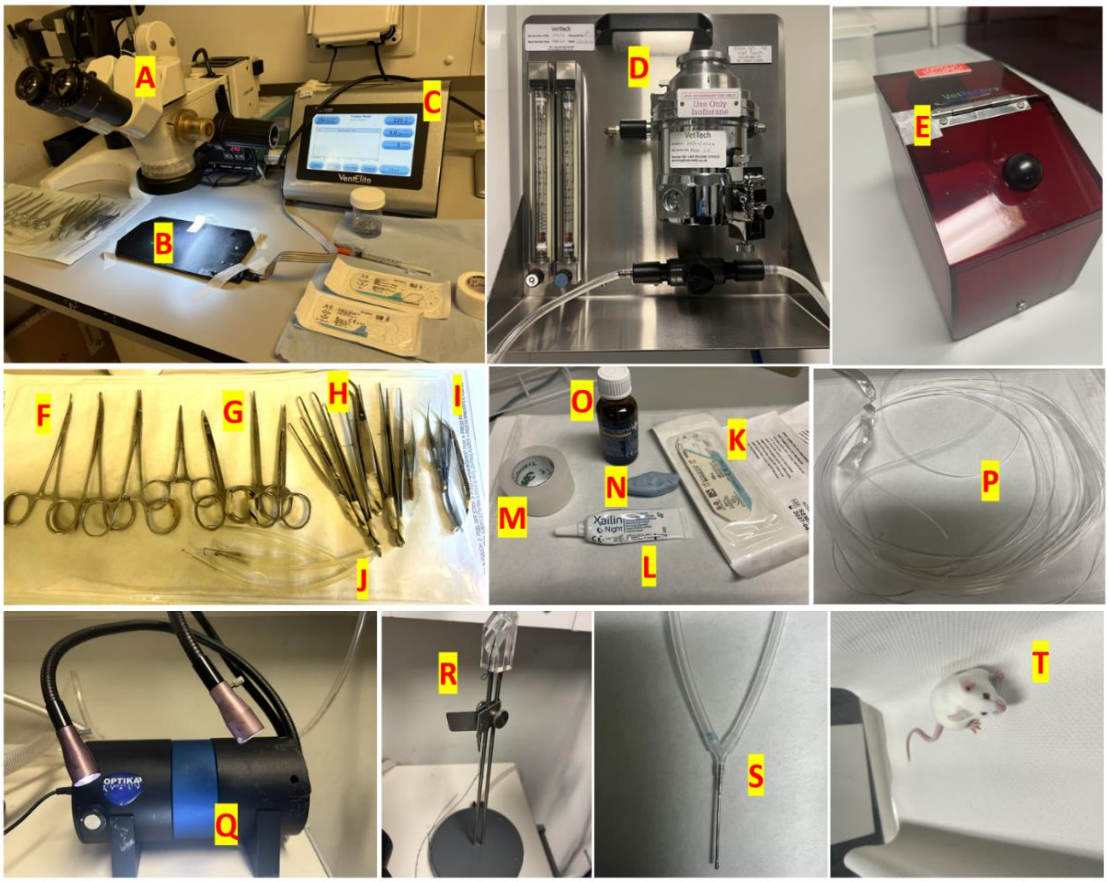

Figure 2-2. Surgical equipment for establishment of PL and IR models. A: Microscope; B: Heating pad; C: Ventilator; D: Isoflurane equipment; E: Induction box; F: Needle holders; G: Surgical scissors; H: Tweezers; I: Micro locking forceps; J: Chest retractors; K: Silk suture, taper needle; L: Eye gel; M: Surgical tape; N: Blue tack; O: 1% Lidocaine HCl; P: Fine bore polythene tubing; Q: Fiber optic light source; R: Endotracheal intubation stand; S: Tracheal tube; T: Balb/C mouse.

2.3.1.2. Protocol

2.3.1.2.1. Animal husbandry

All procedures were performed in accordance with the Home Office Animals (Scientific Procedures) Act and local ethical rules under PPL PP1692884. Eighteen female Balb/C mice weighing 20-26 g at an age of 8 to 12 weeks were housed under conventional conditions with free access to food and water and a 12-hour light/dark cycle. During the procedure, lubricant was used for the eyes and the body temperature was maintained at 37 °C via a heating pad. Analgesia was administered before surgery and for the following two days. Local analgesia was placed on the muscle and skin after closing the incision. Mice were kept in the heating chamber maintained at 36 °C after surgery for at least 1 hour, then re-housed with the mice that had the surgery on

the same day. Animal body weight and distress scoring were recorded before surgery and each day after surgery.

2.3.1.2.2. Non-invasive tracheal intubation

- The mouse was anesthetized in an induction box with 4% isoflurane and then maintained with 2.0% during the whole procedure. The mouse was ready for operation after the loss of a toe-pinch reflex. A sufficient depth of anesthesia before intubation of the trachea minimizes the risk of hyperreactive airway reflexes leading to bronchospasm.
- Mouse hair was trimmed at the area of the neck and the left side of the ribcage. Any remaining loose hair was removed by wet cotton wiping.
- An endotracheal intubation stand was used to suspend the mouse by fixing the top incisor teeth.
- A fiber-optic light source was placed 1 to 2 cm from the surface of the skin to illuminate the area of the thyroid and sternum for transillumination of the upper trachea.
- Blunt-end forceps were used to locate the tongue and draw it out of the oral cavity gently, and then a wooden depressor was used to maintain the tongue aside.
- The light was orientated so that the trachea was visible, and by observing periodic dilation of the tracheal opening, the metal cannula was inserted.
- The mouse was then quickly transferred to the heat pad, and the cannula was connected to a ventilator.
- To confirm that the cannula is properly inserted into the trachea and proper ventilation is achieved, it is necessary to observe the rhythm of breathing that matches the ventilator. Uniform bilateral chest expansion was observed as an indicator of proper cannula insertion.
- Lower abdominal movement or overpressure warning of ventilator indicated wrong access to the esophagus. In this case, the cannula was removed, and the animal could re-intubate up to two more times. More than three attempts at intubation are not feasible due to the high risk of trauma on the trachea.
- Once the intubation was successfully performed, the mouse was placed in a supine position on the heating pad and the rectal temperature probe was applied

to monitor the body temperature.

- The tracheal intubation tube was fixed in position using surgical tape to prevent the air tube from moving and falling off. If the endotracheal tube was accidentally displaced or detached during surgery, the first and most critical step was to close the skin and cover the chest to prevent the lung from collapsing. After that, the mouse should be reintubated.
- The lubricant was placed on the eyes, and analgesia was administered. The mouse was positioned for the thoracic incision and the limbs, and tail were taped to the surgical surface. The mouse was then ready for the surgery.

2.3.1.2.3. Thoracotomy

- The surgical incision site around the sternum was prepared by 70% alcohol cleaning with three scrub cycles.
- Thoracotomy was performed by making a 1 cm longitudinal incision approximately 2 mm away from the left midclavicular line using surgical scissors.
- The subcutaneous tissue was dissected bluntly toward the axilla.
- After the margin of the major pectoralis muscle was confirmed, blunt dissection was performed from the minor pectoralis muscle and the rib cage was fully exposed by pulling the minor pectoralis muscle to the right.
- After exposure of the rib cage, the left lung was typically visible under the chest cavity, covering most of the heart. The animal was gently adjusted its position posteriorly by a piece of blue tack adhesive to the heating pad by the right of the mouse to guide the left lung out of the operation area.
- After identifying the fourth and fifth intercostal space, a small incision was made at approximately 2–3 mm away from the left sternal border. The ribs were gently lifted using a tweezer and the tip of the forceps was used to penetrate bluntly and expanse the intercostal space to a 6-8 mm incision into the thorax cavity.
- Four metal chest retractors were inserted to spread and maintain the operating window to approximately 8–10 mm in width, and a clear view of the heart, including of the left auricle, should be achieved.
- Once the heart was visible, the pericardium was then gently lifted and separated

with a pair of curved forceps to reveal the coronary vessels.

2.3.1.2.4. Permanent LAD Ligation

- LAD is not easily visible to the naked eye because it is embedded within the myocardium. The left auricle and some superficial coronary veins are regarded as anatomical landmarks for identifying the LAD.
- By picking up the left auricle with curved forceps, the origin of the LAD artery from the aorta was located. Under the microscope, the LAD was visualized as a pulsating bright red pipe with a blurred border within the myocardial wall extending vertically from the left atrium to the apex of the heart.
- Once the ligation point was identified, the LAD was reconfirmed by gently pressing the subsequent artery below the ligation point with curved forceps to enhance arterial filling and pulsation. The location of the ligation depends on the desired infarct size. According to the literature to establish an MI model with consistent infarction size, in this study, the ligation position of the LAD was 1-2mm below the tip of the left auricle.
- Under the dissecting microscope, a 6-0 non-adsorbable suture with a needle was passed through the myocardial wall (~ 1mm thick) underneath the LAD, ensuring that the LAD was surrounded. When placing the ligation under the LAD, it is important not to pass the needle too deep through the ventricular cavity. It is also not so superficial that the ligation will cut through the ventricular wall.
- The 6-0 non-adsorbable suture ligature was then tied with three knots in the PL model. A successful LAD ligation was confirmed by the color of the anterior wall turning pale. If the sign was not clearly visible, a second attempt could be made slightly superior to the first.
- After confirmation of the ligation, the retractors were removed from the incision. The mouse was kept on the ventilator before the closure of the chest.
- The upper and lower ribs were then secured together using Prolene 6/0 suture to ensure there were no gaps or dislocations. At the same time, pressure was applied to the chest wall to reduce the free air in the thoracic cavity.
- The layers of muscles would automatically return to their original positions upon release of the retractor, or they can be closed using Prolene 6/0 suture if

necessary. The blue tack was then removed, and the lungs were restored to their initial positions.

- The skin was sutured using Prolene 3/0, as previously described.
- A few drops of lidocaine were applied to the incisions.
- The administration of isoflurane was discontinued, and oxygen was maintained until the mouse regained consciousness. Following the observation of a normal respiratory pattern, the endotracheal tube was slowly removed to prevent lung aspiration.

2.3.1.2.5. Ischemia-reperfusion surgery

- To establish the IR model, following the identification of the ligation point, the ligation was performed with a loose double knot with a 2–3 mm diameter loop. A 2 mm long PE-10 tubing was inserted into the loop parallel to the LAD.
- The loop of the ligation was gently tightened around the artery and tubing, and then a slipknot was made to secure the ligature. Excessive pull of the suture when tightening the ligature can damage the myocardial wall.
- The incision was temporarily closed with a suture on the skin and covered with wet gauze during the ischemic period. The duration of ischemia time is determined by the specific experimental design, which in this study was set at 45 and 60 minutes. After the ischemic time had passed, the suture on the skin was removed, and the retractors were inserted to open the incision and expose the thoracic cavity.
- The PE-10 tubing was removed by untying the slipknot. After that, the blood flow was restored, and the heart tissue was reperfused, as evidenced by the left ventricle returning to a normal red color within 20 seconds.
- If TTC and/or Evans blue staining is to be performed on the IR models to identify the area at risk zone, the ligature should be left in place after removing the PE-10 tubing as an indicator for the reocclusion of LAD.

2.3.1.2.6. Postoperative care

- Pre-warmed sterile saline was administered i.p. in the abdominal region.
- The mouse was monitored by observing the signs of recovery from anesthesia,

including the tail or whisker movement. After recovering from anesthesia, the mouse was transferred to a 36 °C recovery chamber.

- Buprenorphine (0.05 mg/kg) was administered i.p. after surgery when the first dose had been given over 4 hours on the same day.
- Buprenorphine was then given twice daily for the following 2 days. Accessible water and soft food were provided after surgery.
- Ibuprofen (0.2 mg/mL) was added to the drinking water for additional pain relief for up to a maximum of 7 days after surgery.

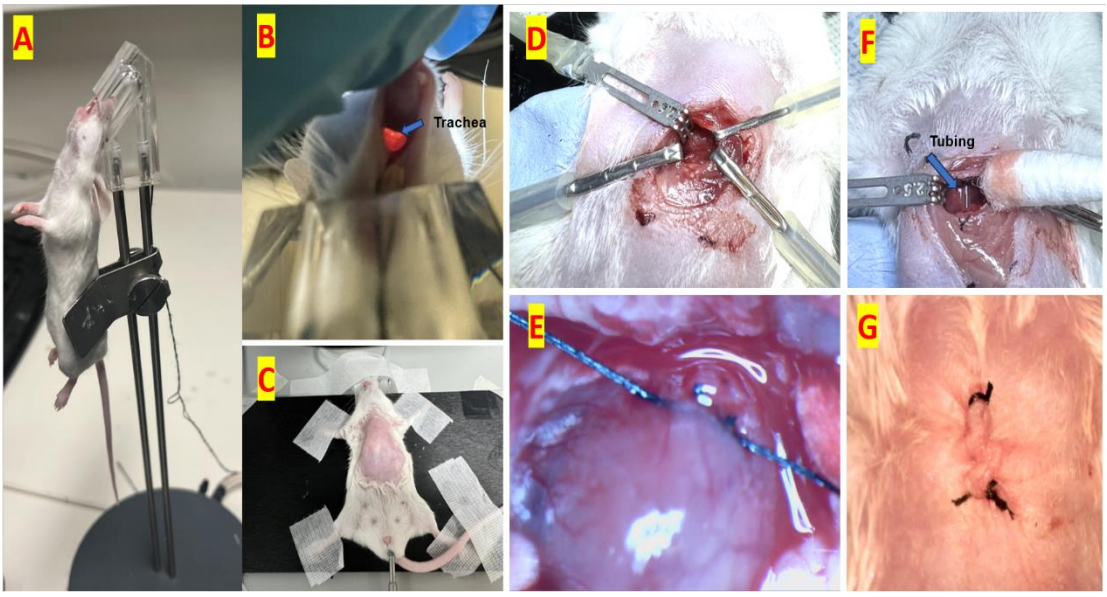

Figure 2-3. Procedures of surgical-induced PL and IR MI models. A: The mouse was suspended on an endotracheal intubation stand. B: The upper trachea was transilluminated and exposed by a fiber-optic light source, then the cannula was inserted for intubation. C: The mouse was positioned for the thoracic incision on a heating pad. D: Thoracotomy to expose the heart. E: Successful LAD ligation was confirmed by the color of the anterior wall turning pale. F: A piece of PE-10 tubing was placed parallel to the LAD to induce the IR model. G: The skin was sutured to close the chest. PL: permanent ligation; IR: ischemia–reperfusion.

2.3.2. Echocardiography

The ultrasound imaging system and image acquisition will be described in detail in Chapter 3. In this study, ultrasound scans were performed at the following time points: baseline, 1-, 2-, 4-, and 8 weeks post-surgery. In this study, the baseline ultrasound scan, performed prior to MI surgery, as the control for cardiac function assessment. It serves as a reference point for evaluating changes in cardiac function over time, eliminating inter-animal variability. Mice were anesthetized using 2.0% isoflurane mixed with oxygen administered via a nose cone. The hair on the chest was removed.

The mice were positioned in a supine position on the operating pad and kept at a temperature of 37 °C using a heating pad. Surface ECG limb electrodes were used to monitor the ECG and heart rate. The heart rate was maintained between 400 and 500 bpm during imaging by adjusting the concentration of isoflurane. The Vevo 3100 ultrasound imaging system (FUJIFILM VisualSonics, Toronto, Canada) with VisualSonic MX550S linear array transducer was utilized for all image acquisitions. In the long-axis view, structures such as the aortic valve, proximal course of the aortic root and ascending aorta, and LV apex are visible indicators. The base-to-apex axis is parallel to the transducer's orientation. Simpson's multi-plane mode was employed to quantify LV volumes (EDV & ESV) at three levels: basal level, level of papillary muscles, and apical level by tracing endocardial boundaries during both diastole and systole in each plane. EF was calculated by (EDV-ESV)/EDV * 100%.

2.3.3. Statistical analysis

Data is presented as mean and standard deviation (±SD). For all statistical tests, $p \leq 0.05$ was considered significant. Analysis of statistical significance for two or more groups was performed using a one-way ANOVA followed by Tukey's post-hoc test with Geisser-Greenhouse correction applied.

2.4. Results

2.4.1. Comparison of left ventricular function in permanent ligation and reperfusion injury mouse models of myocardial infarction

Eighteen mice underwent baseline ultrasound imaging using Simpson's multi-slice technique prior to surgery and were subsequently randomly assigned to one of three groups: (i) permanent LAD ligation (PL, n=6); (ii) 45-minute occlusion followed by reperfusion (IR 45mins, n=6); and (iii) 60-minute occlusion followed by reperfusion (IR 60mins, n=6). After surgical intervention, ultrasound examinations were performed at 1-, 2-, 4-, and 8-weeks following MI. Short-axis ultrasound images of the left ventricles from different MI groups exhibited distinct geometric variations among the surgical cohorts at various time points (Figure 2-4). At baseline, the LV displayed a symmetrical elliptical shape; however, MI was evident as akinetic on the anterior and lateral walls, with varying sizes observed in the PL and IR groups from week 1 onwards. The regions marked by blue dashed lines indicated that mice in the PL group

displayed the largest noncontractile region, followed by those in the IR 60mins and IR 45mins groups.

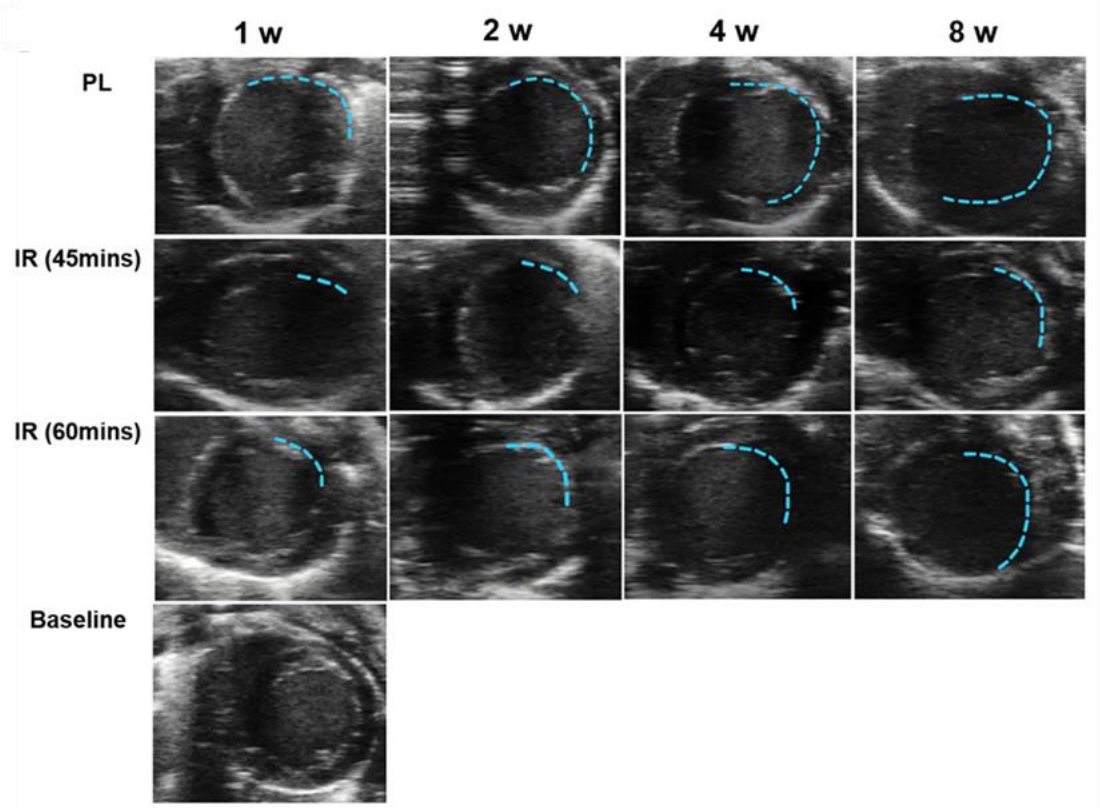

Figure 2-4. Representative ultrasound images in a short-axis view of the infarcted LV obtained at different time points post-LAD ligation in baseline, PL or IR models (n = 6 per group). The regions outlined in dashed blue lines are indicative of ischemic damage. PL, permanent ligation; IR, ischemia–reperfusion.

The assessment of EDV, ESV, and EF for individual animals in different MI groups was displayed at baseline, 1-, 2-, 4-, and 8 weeks post-MI. Gradual increases in EDV and ESV were observed in the majority of animals within each group over eight weeks. In week 8, EDV in the PL group reached 111.36 ± 22.96µl, 81.86 ± 12.01µl in the IR 45mins group and 90.23 ± 19.59µl in the IR 60mins group (Figure 2-5a, b, c). Similarly, ESV in the PL group increased to 81.22 ± 12.65 µl, 49.38 ± 8.12 µl in the IR 45mins group and 62.71 ± 9.55 µl in the IR 60mins group (Figure 2-5d, e, f). EF gradually decreased by 57.29 ± 9.12% in the PL group from week 1 to week 8, by 35.51 ± 15.05% in the IR 45mins group, and by 44.24 ± 13.88% in the IR 60mins group (Figure 2-5g, h, i).

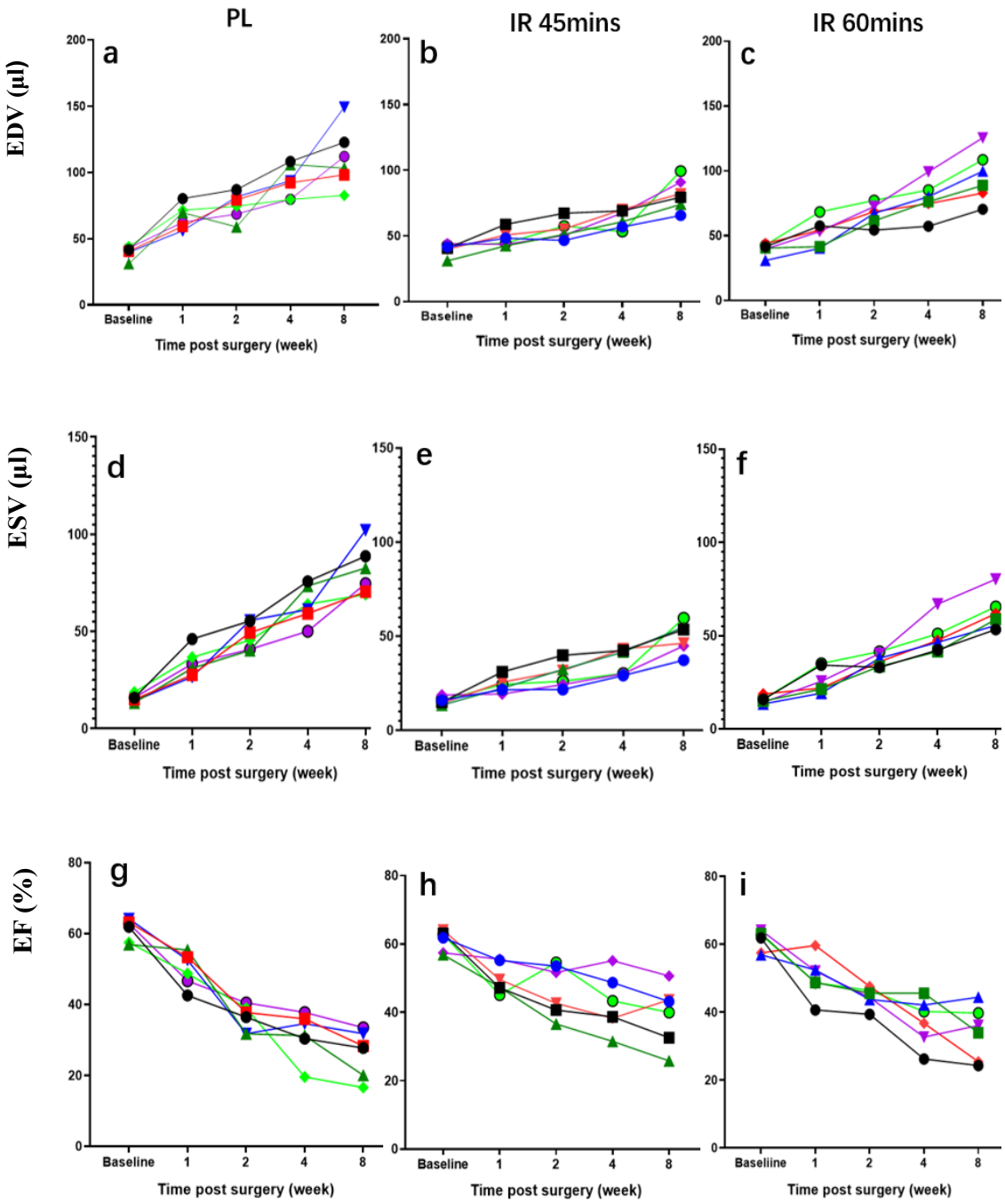

Figure2-5. Comparisons of EDV, ESV, and EF in individual MI groups at different time points. Data are presented as mean ± SD, n = 6 per group. PL, permanent ligation; IR, ischemia–reperfusion; EDV, end-diastolic volume; ESV, end-systolic volume; EF, ejection fraction.

A comparative analysis of EDV, ESV and EF between baseline and different MI groups revealed increased EDV and ESV in the PL group as early as 1-week post-MI (p<0.05). By 2 weeks post-MI, both EDV and ESV were elevated in the IR 60 mins group (p<0.05). However, no significant increases in EDV were observed in the IR 45 mins group until week 4, and there were no significant increases in ESV even in 8 weeks.

EF was significantly reduced in all MI groups from week 1 compared with baseline (p<0.01).

Similar changes were revealed in EDV, ESV, and EF between the PL and IR 60 mins groups over time, with the only distinction being a significantly smaller increase in EDV in the IR 60 mins group at 8 weeks (p<0.01). The IR 45 mins group exhibited significantly higher EF than the PL group at 2 and 8 weeks (p<0.05), as well as lower ESV than both the PL (p<0.001) and IR 60-minute groups at 8 weeks (p<0.05). EF in the PL and IR 60 mins groups consistently showed a decline over the 8 weeks (p<0.01), while mice in the IR 45mins group maintained consistent EF values from 1 to 8 weeks, although these values were still below 55% (Figure 2-6). A clinical trial revealed that the presence of ischemic etiology and LVEF ≤55% were identified as robust predictors for the development of HF [302].

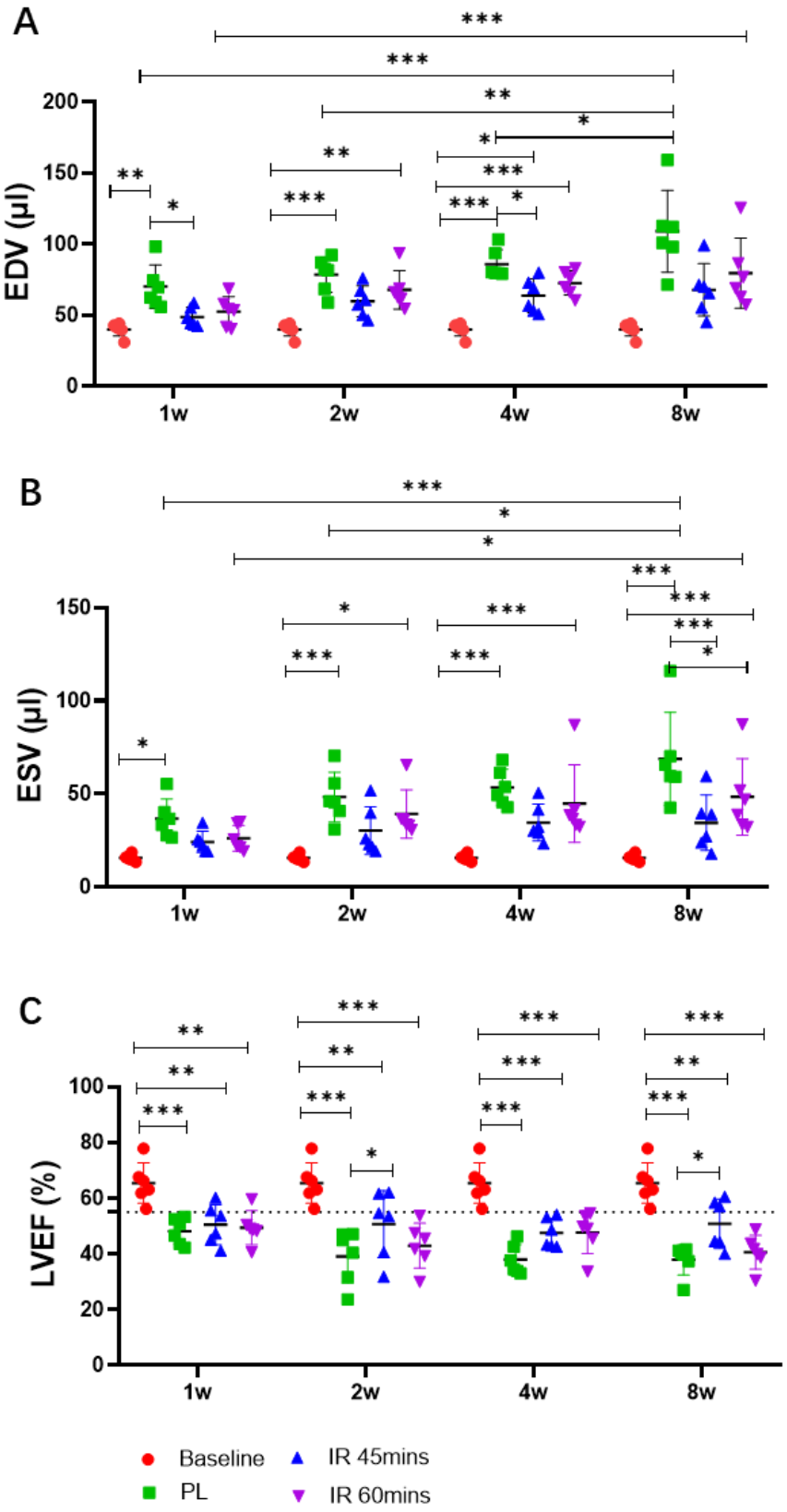

Figure 2-6. Comparisons of EDV, ESV and EF in different MI groups and baseline at different time points. Data were shown as mean ± SD. Statistical analysis was performed using one-way ANOVA followed by Tukey's post hoc test. The red dashed line indicates the EF = 55%.

N = 6 per group. PL, permanent ligation; IR, ischemia–reperfusion; EDV, end diastolic volume; ESV, end systolic volume; EF, ejection fraction.

2.5. Discussion

For effective clinical translation, representative animal models of MI are essential tools to mimic the clinical situation to assess the efficacy and safety of the treatments. Most preclinical studies were conducted to investigate the effect of reperfusion post MI on infarct size within a short observation period [303]. However, limited research focuses on the alterations of cardiac function by comparing different ischemia times over the long term. Therefore, this study aimed to establish a consistent MI model with optimized surgical procedures and compare cardiac function among groups with different ischemia times (permanent ligation, 45 minutes and 60 minutes of reperfusion), and offer insights for selecting the optimal MI model for evaluating experimental therapies.

2.5.1. Relevance of modified surgical technique optimizing MI mouse model

Modified surgical-induced MI model was performed in this study. The conventional surgical procedure involves a thoracotomy to expose the heart, followed by the ligation of the LAD. Currently, the "popped out" model represents an innovative surgical technique for inducing MI developed by researchers based on traditional surgical methods. The popped-out model is performed without a large incision but rather by popping out the heart through a small chest incision. This approach offers several advantages: it eliminates the need for intubation and ventilation during surgery, allows for rapid completion of the procedure, and utilizes the heart itself to seal off the mini thoracotomy during ligation, thereby preserving lung function [304]. The popped-out method can be completed in 5.52 ± 0.28 minutes compared to traditional ligation, which requires 25 ± 5 minutes; additionally, it results in reduced tissue damage, faster post-surgery recovery, and lower incidence of cardiac arrhythmias [305]. However, despite its high efficiency and minimal tissue damage, this method requires extensive training and experience. In Gao's group, over 20,000 cases were performed to achieve rapid surgeries in under 2 minutes [306]. In my study, fewer than 60 cases were operated on to acquire the technique to establish a stable MI model within a time frame of 25 ± 5 minutes. Furthermore, the popped-out model does not allow for reperfusion or intramyocardial delivery of biomaterial and stem cell treatments as these would

prolong the surgery, and the intubation and proper exposure of the heart are needed.

Pneumothorax, bleeding, and ventricular rupture are the most common causes of post-MI mortality. In my study, pneumothorax accounted for 5.0% (3/60) of deaths, while bleeding, ventricular rupture and unknown reasons were responsible for 6.7% (4/60), 15.0% (9/60), and 5.0% (3/60) of deaths, respectively. The overall survival rate at 28 days post-MI was determined to be 68.3% (41/60) in my study compared to Gao's research, which reported a survival rate of 68% (29/43). Additionally, Gao noted that there were no significant differences in infarct size or post-MI cardiac function between the conventional surgery and the popped-out method used in their study. Overall, when comparing the surgical method employed in my study to the popped-out model approach, no specific evidence suggests that the latter method holds an advantage over the former, except for reduced surgery time. However, it is important to note that the lack of ventilation and the requirement to temporarily externalize the heart for less than 30 seconds during ligation pose technical challenges. Extensive practice is necessary to achieve optimal prognostic outcomes, which limits the applicability of the popped-out model in research studies.

Compared to conventional MI-induced surgery, which entails the dissection of pectoral muscles and ribs for heart visualization, I have adapted the procedures to minimize damage to muscles and ribs. This was achieved by separating the major and minor pectoralis muscles through blunt dissection without incising into the muscle. Then, a small incision was made with fine scissors while retractors were applied to enlarge and maintain the window for heart visualization. These procedures avoided massive damage to muscle and ribs. To avoid the injury to the lungs during surgery, Yue *et al.* used forceps to lift the fourth rib in order to keep it away from internal organs when operating thoracotomy [307]. However, based on my experience, this procedure may cause intubation failure due to chest movement. Hence, in my surgical procedures, I utilized blue tack adhesive on the right side of the mouse's chest to displace the internal organs, especially the lungs. Additionally, the blue tack could also keep the left lungs out of the surgical field until the surgery was completed.

As a result, compared to conventional surgical methods, my approach minimized tissue damage and hemorrhaging while avoiding the necessity for muscle suturing

post-surgery. Ultrasound was utilized as a valuable tool in this study to monitor the morphology changes and cardiac function, where the imaging quality might be influenced by the suturing or damaged tissue. Therefore, the refined surgical techniques (reduced bleeding, smaller incision, and less suturing) in my study enable rapid acquisition of reliable and comparable ultrasound data. Possible causes and solutions for complications in the surgically induced MI model are summarized in Table 2-2.

2.5.2. Establishment of reproduceable MI model with consistent infarct size

Animal models with high reproducibility are essential for subsequent comparative and quantitative studies evaluating the therapeutic effects of drugs or biomaterials. However, surgical-induced MI models have inherent variability that depends on both the experimenter's skills and biological differences between animals. Adequate and rigorous training is necessary to achieve model reproducibility. The anatomical diversity of coronary arteries in mice presents challenges to achieving consistent surgical ligation, leading to variability in the size after ligation. Infarct size depends on individual variations in main coronary artery length, level of bifurcation, number of branches, presence of collaterals, and area supplied by these branches - all unique to each animal [308]. Kainuma group evaluated the distribution of coronary arteries in the C57BL6/J mice. The left coronary artery, starting from its proximal end, is typically embedded by the myocardium and poses challenges in identification even when observed under a microscope [287]. Salto-Tellez *et al.* evaluated the distribution of coronary arteries in C57BL6/J mice and found that ligating at a specific point, 1-2 mm distal to left atrial appendage immediately after major left coronary artery bifurcation, resulted in uniform infarct size (26.9±1.5%) [309].

In a separate study conducted by Kainuma *et al.,* infarct size in a rodent model (n=50) varied depending on the site of ligation and the branching pattern of the LCX. Among these models, 66% exhibited LCX branches originating from the relatively long left main coronary artery distally. In comparison, 34% had LCX branches originating from either the proximal septal artery or the short left main coronary artery. When ligation was performed at a distance of 2 mm from the left atrial appendage, MI occurred in the anterior myocardium regardless of the LCX branch. However, when ligation was

performed just below the left atrial appendage, extensive MI involving both anterolateral and local anterior regions occurred in 64% and 36% of cases, respectively [287]. In other words, by ligating directly below the left atrial appendage in a similar way employed by well-trained researchers, there was an approximately one-third risk that MI models would develop relatively small-sized infarct located in the anterior wall, which was smaller than expected. Therefore, to achieve consistent infarct sizes, ligation at a distal point 2 mm away from the left atrial appendage would be optimal.

Based on these findings, in my study, to achieve a reproducible and rigorous experimental model of MI, I performed LAD ligation at approximately 2 mm below the level of the left atrium, ensuring consistent affected region across all subjects. Histology is an end-point operation that cannot be applied to assess the same animal during different time points, especially when evaluating the therapeutic effects of the regenerative therapies, or more animals are required for such results. In contrast, imaging techniques such as MRI and ultrasound offer the advantage of monitoring changes in cardiac structure and quantifying cardiac function after MI, providing reliable and reproducible information on cardiac architecture and function. Previous studies have shown a close correlation between the extent of LV dysfunction post-MI and the size of the infarcted area [310]. Miranda *et al.* demonstrated that ultrasound-based assessment of cardiac function can accurately predict the size of infarcts in rat models [311]. Thus, ultrasound was employed in my study as a straightforward monitoring imaging system. This modality adds minimal procedural complexity but facilitates precise evaluation of MI severity by evaluating the extent of LV dysfunction through precise measurement of EDV, ESV, and EF serially.

2.5.3. Impact of ischemia time on cardiac functional changes in MI mouse models

PL and IR are the two predominant approaches for developing MI models. The comparison between these two models continues to be ongoing due to two primary reasons: firstly, it is exceedingly challenging to accurately assess the individual effects of reperfusion. Secondly, there remains a lack of effective strategies for preventing ischemic reperfusion injury [18]. Extensive research has been conducted to investigate the variances in cardiac morphology and infarct size between these two models

subjected to varying durations of ischemia. The pivotal role of cardiac function in determining optimal IR models yet remains relatively underexplored. In this study, I performed IR models with different durations of ischemia, 45 minutes and 60 minutes, and compared them to the PL model in terms of cardiac function using standard non-invasive ultrasound. Ultrasound revealed a more severe impairment in cardiac function following permanent ligation of LAD compared to IR 45mins and IR 60 mins groups. Prolonging the duration of ischemia from 45 minutes to 60 minutes resulted in significant differences in EDV between PL and IR 60 mins groups at week 8.

There were significant differences observed in the EF between baseline and MI groups from week 1 onwards, and PL had significantly lower EF than IR 45mins at weeks 2 and 8. However, no significant differences in EF were found between the IR 45mins and IR 60mins groups over 8 weeks, as well as between the PL group and IR 60 mins group over 8 weeks. These findings suggest that mice subjected to reperfusion for only 45 minutes of ischemia experienced sufficient cardiac functional impairment (EF <55%) to serve as a reliable IR model, while mice with an ischemic period of 60 minutes had less cardiac functional impairment than those in the PL group, indicating that there was still salvageable myocardium presented after infarction even at this time point.

Kjoller *et al.* demonstrated that surgical ligation of a coronary artery can lead to extensive local wall motion dyskinesia, which may be compensated by regional hyperkinesia in the unaffected remote myocardium at early stage of MI, resulting in no significant changes in EF [312]. This could explain why EF levels were similar between the PL and IR groups in week 1. Then the loss of myocardial tissue triggers a hypertrophic growth response in the border zone of the LV to maintain cardiac output. Nonetheless, this hypertrophic remodeling may only provide temporary compensation for cardiac function and ultimately leads to maladaptation, arrhythmias, sudden death, and HF [313]. During the 2-week post-MI period up to week 8, there was no significant difference in EF values between the IR 45 mins and IR 60 mins groups. However, a notable difference was observed between PL and IR at 45 mins in weeks 2 and 8. This indicates that the heart, when exposed to 45 minutes of ischemia, may only suffer a small amount of tissue damage. As a result, the heart was able to compensate for any impairment in cardiac function over 8 weeks without experiencing significant

reductions in EF, as illustrated in Figure 2-6c. This observation was supported by the finding of a small area of necrosis upon reperfusion initiation 45 minutes after occlusion in a porcine model established in Garcia-Dorado's laboratory [303]. According to the findings of my study, the EF in the 60 mins IR group exhibited a deteriorated cardiac function compared to the 45 mins IR group yet demonstrated less cardiac impairment than the PL model. This suggests that prolonged ischemic durations result in more severe myocardial injury, while delayed reperfusion at 60 minutes still confers a protective effect on the cardiac tissue. Collateral blood flow may significantly contribute to this phenomenon, as evidenced in clinical studies indicating that the extent of residual blood flow to the infarct zone is the primary determinant of salvage when late reperfusion therapy is administered [314, 315].

It would have been interesting to undertake additional experiments that could define the AAR, and the area of myocardium salvaged through reperfusion at 45 and 60 minutes after infarction. This could have been performed by excising the heart, reoccluding the LAD and infusing Evans blue dye to stain the unoccluded tissue, then staining viable tissue with TTC. However, this work aimed to follow cardiac function serially *in vivo* rather than sacrifice animals to evaluate infarct size. Histological staining could have been performed at the end of the study. However, the feasibility of being able to reocclude the LAD and the extensive cardiac remodeling that occurred over 8 weeks was likely to make these measurements inaccurate.

2.5.4. The selection of MI animal models for evaluating the efficacy of experimental therapies

Both PL and RI MI models are clinically relevant. The choice of the most appropriate model depends on the specific experimental question being addressed. To determine the most suitable MI models for my research projects, it is crucial to thoroughly consider several critical factors. The results of this study indicate a higher variability in EF within the IR models, as evidenced by a larger standard deviation in the IR groups (IR 45mins: 35.51 ± 15.05%; IR 60 mins: 44.24 ± 13.88%) compared to the PL group (57.29 ± 9.12%). The data can be used in power calculations to determine the sample size needed for future studies. To perform a statistically valid comparison between a treated and a control group with a therapeutic effect size of 15% change in

EF, 17 mice would be required if the IR 45min MI model was used, 14 mice for the IR 60 min MI model, and only 7 mice if the PL model was used. This highlights the importance of generating and utilizing reproducible animal models in preclinical trials of therapies and suggests that many studies are underpowered, leading to both type 1 and type 2 errors.

Christian *et al.* have demonstrated that EF may offer limited insights into the initial myocardium at risk and be less accurate in certain patients following reperfusion due to myocardial stunning [316]. Additionally, the biological variability in the distribution of coronary vascular beds (coronary collateral circulation) and certain disparities in the selection of the LAD ligation site may contribute to variations in the AAR, thereby influencing the final infarct size in the IR model [303]. Considering my PhD work primarily focuses on experimental therapies for MI where consistent and robust cardiac dysfunction is crucial for evaluation purposes. Despite the IR model holding greater clinical relevance overall, the PL model would be optimal for further studies presented within this thesis.

2.6. Limitations

This study has certain limitations, including the absence of histological analysis following heart collection, which would have enabled the determination of infarct size using TTC-Evans blue staining. However, the chronic progression of myocardial infarction poses challenges for re-ligating the LAD in the IR model, limiting the applicability of this staining technique. Furthermore, TTC-Evans blue staining only provides infarct size at the terminal stage and does not support longitudinal assessment at multiple time points. To address these limitations in future research, non-invasive imaging modalities such as MRI and PET/SPECT-CT should be explored. These advanced techniques offer the potential for detailed, repeated evaluations of infarct size over time, providing a more comprehensive understanding of the progression and impact of MI. Besides, several issues or limitations that affect the translatability of MI animal models to patients need to be considered when applying them to further studies. Animal models lack comorbidities commonly observed in MI patients, such as diabetes, hypertension, and hyperlipidemia [317].

In this study, we employ a homogeneous population of healthy and young animals for

conducting MI surgery, and they are occasionally criticized for their lack of individual heterogeneity. However, the capacity to manipulate a specific aspect of human heterogeneity in mice is actually a strength of these models, rendering them well-suited for reverse translation [313, 317]. The large differences in animal species and anatomical structure from the human body, the small size of mouse heart, and the difficulty in applying these findings to clinical practice are the main bottlenecks that hinder the introduction of novel therapies into clinics [313, 318]. However, data derived from MI models involving small rodents provides a valuable resource for further research when applied to larger animals or even humans, facilitating early critical assessment of the safety and potential effectiveness of innovative therapeutics for MI and other diseases. Although these models may not perfectly represent the complexities observed in larger species, they offer a cost-effective and logistically manageable alternative for initial explorations [317].

2.7. Conclusion

This study established a reliable and reproducible PL model that induces a more pronounced and consistent cardiac functional impairment by refining the surgical technique for ligation of nonvisible coronary artery branches in mice. Additionally, an IR model with varying ischemic durations confirmed 45 minutes as the optimal duration for inducing ischemic reperfusion injury with moderate cardiac functional impairment. Extending the ischemic duration to 60 minutes still demonstrated a protective effect on cardiac tissue. Both MI models are clinically relevant; however, the PL model is selected for further studies within this thesis due to its consistent and robust induction of cardiac dysfunction.

Table 2-2. Possible causes and solutions of surgical complications.

Complications	**Possible causes**	**Solutions**
1. Induction of anesthesia and intubation		
Irregular respiratory movement	Ventilation cannula in esophagus	Reintubation: attempts should be less than three times
	Anesthesia: too light or too deep	Toe-pinch reflex check: ♦ Reduce isoflurane when deep gasps occur. ♦ Increase isoflurane when frequent shallow gasps occur.
	Blockage of ventilation cannula: confirmed by submerging the tubing in water and no bubbles come from ventilator exhaust.	♦ Before intubation: replacement of cannula ♦ During surgery: (i) Before the thoracotomy: remove the intubation cannula and clean to unblock, then reintubate. (ii) After thoracotomy: terminate experiment
2. Thoracotomy		
Difficulty identifying 4th intercostal space	Due to individual differences in mice, lungs and its margins cannot be used as a reference.	To rotate the heart and lungs via a blue sticker and count ribs to identify 4th intercostal space.
Bleeding when dissecting pectoralis muscle and intercostal space	Bleeding from pectoralis muscle and intercostal vessels.	♦ Avoid damaging the axillary vein. ♦ Avoid contact with the intercostal vessels located above the cranial margin of the rib. ♦ Cotton applicator / cautery is used to stop the bleeding.

Damage of the underlying lung	The inflated lung covers over the heart.	♦ Push the lung to the left side via a blue sticker. ♦ The intercostal space should be bluntly dissected with curved forceps and relatively superficial.
Left atrium and left ventricle are not visible after thoracotomy	Incorrect intercostal space. i) Only left atrium: incision at third intercostal space. ii) Only apex of left ventricle: incision at fifth intercostal space.	Incision at the right intercostal space and then suture three ribs to close the chest wall after surgery.
3. Ischemia-reperfusion		
Difficulty identifying LAD	LAD – vessel runs deeper into the myocardium.	♦ Identify LAD by finding small vein originating at the caudal margin of the right atrium's auricle, in which the LAD most often runs parallel and laterally to this vein. ♦ Using cotton swab to press the possible area of LAD gently, inducing paleness of the myocardium and the LAD turns to bright red.
	Variants of coronary arteries.	Familiar with anatomy of the coronary artery and summary different patterns of LAD during experiment.
Bleeding after placing suture	The needle penetrated the myocardium.	♦ The left ventricular wall thickness in mice is 1.5-1.8mm, so make sure the needle does not go too deep to penetrate the myocardium. ♦ If the bleeding is severe, terminate experiment.
	The needle passed through the coronary artery.	
	Ligature caused by excessive force or pulling in different directions, inducing heart rapture.	Sacrifice the mouse if the myocardium ruptures or the bleeding is severe.
No visible myocardial color	Suture too shallow	♦ The diameter of LAD in mice is 0.4 mm—make sure the suture not too shallow.

change or ST-segment elevation on ECG after ligature	Ligature was not tight enough to fully block the LAD.	♦ Another attempt to ligate the LAD.
	Incorrect identify of the LAD.	Identify the LAD before placing the suture since it was not visible mostly.
Myocardial color changed from pale back to red or ST-segment resolution on ECG during ischemic period	The suture to fix the tubing loosened during ischemic period so that the tubing dropped off.	Terminate experiment.
No visible myocardial color changed or ST-segment resolution on ECG after reperfusion	Surgical damage to LAD or surrounding myocardium.	Terminate experiment.
	Due to long time of occlusion, the blood flow of LAD restoration may slightly delay.	Keep observing for one minute to determine whether LAD has been fully reperfused. If not, terminate the experiment.
4. Chest closure		
Pneumothorax	The intercostal space was not fully closed.	Terminate experiment.

After chest closure, gasping immediately occurs.	Unsuccessful re-inflation of the lungs may induce gasping.	Further compress the ribs on both sides while gasping to remove residual air in the chest.
5. Recovery		
Independent breathing failed to recover within 10 minutes.	The anesthesia was too deep during the procedure. Surgery time was longer than 45mins in permanent ligation models or 1.5hs in 45mins reperfusion injury models.	Keep waiting 5-10 mins more. If the independent breathing failed to resume following 20mins, stop the ventilation to observe the chest movement. If there was no sign of breathing moving, terminate experiment.
	A lung injury occurred during the operation.	Bubbles under skin may indicate lungs injury. Terminate experiment.

Chapter 3. Advanced ultrasound evaluation of cardiac function after myocardial infarction

Graphic abstract

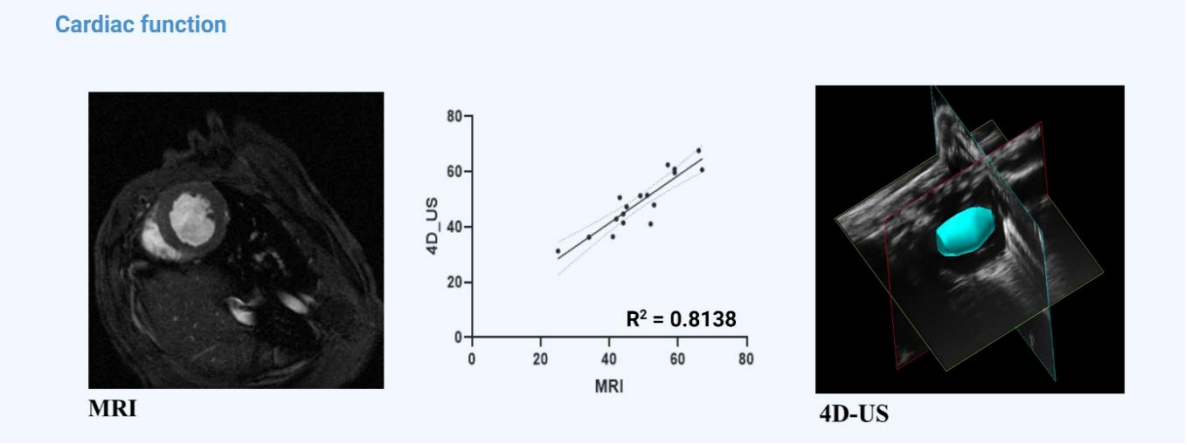

Abstract

Echocardiography has long been an invaluable imaging modality for assessing cardiac function. This study aimed to assess the feasibility and reproducibility of advanced echocardiographic techniques: 4D-ultrasound and speckle tracking imaging-derived strain analysis.

This study initially compared LV volumes and EF determined by conventional echocardiography (Simpson's multiplane, SAX M-mode, PSLAX B-mode, and PSLAX M-mode) with 4D ultrasound in an MI model using MRI as a standard reference on 17 mice 2 weeks or 4 week post-MI. I then assessed the capability of global and regional strain analysis for evaluation of cardiac function on 6 mice 2 weeks post-MI across longitudinal, circumferential, and radial planes. Finally, I applied strain analysis to a mouse model of cardiac amyloidosis to identify and track the development of cardiac dysfunction.

All conventional ultrasound methods measured LV volumes strongly correlated with MRI findings (EDV: $R^2 > 0.60$, ESV: $R^2 > 0.60$); whereas in EF assessment, 4D-US demonstrated the highest correlation with MRI (R^2=0.82), followed closely by Simpson's method (R^2=0.79), outperforming other conventional ultrasound techniques. The global strain values were significantly lower in the MI group (n=17) compared to the control group (n=6) across all three planes. RLS analysis revealed a significant decrease in all anterior segments as well as posterior apical regions of the MI hearts, while RCS and RRS showed decreased strain values primarily within Anterior Free wall & Lateral regions alongside decreased RRS values within Posterior & Inferior segments, respectively. In the amyloidosis model, RLS-derived clinical parameters: relative apical sparing (RELAPS) and septal apical to basal longitudinal strain (SAB), revealed that 36% and 30% of mice in the amyloidosis group exhibited cardiac functional impairment at 9 and 12 months, respectively.

This study concluded that advanced 4D-US and Simpson's multiplane can be used as reliable techniques for assessing cardiac function post-MI, with advanced 4D-US approach offering additional advantages. Strain analysis could effectively differentiate between infarcted and non-infarcted myocardium in an MI mouse model and can be used as a reliable approach to quantify dysfunction in cardiac amyloidosis.

3.1. Introduction

Mouse models of MI are indispensable for investigating the pathophysiological mechanisms underlying ischemic injury and reperfusion, as well as for developing and refining new therapeutic strategies [319]. In Chapter 2, a murine MI model was successfully established and refined through surgical ligation of the LAD, enabling its application in evaluating novel experimental therapies.

To confirm the successful establishment of the MI model, researchers employed ECG to verify effective LAD ligation. However, a subset of ligated mice may not manifest a typical infarction pattern on ECG during the acute phase [320]. Measurable and quantifiable biomarkers, such as cardiac troponin I, have been identified to accurately diagnose and predict outcomes in patients with acute MI [321]. However, the collection of blood samples in mice poses challenges due to their small blood volume, and the actual troponin level may be misleading as a result of the washout phenomenon following reperfusion therapy [321]. Histological analysis is commonly utilized for evaluating infarct size in preclinical studies, which is closely correlated with the degree of cardiac dysfunction following MI. However, it is a terminal procedure and does not allow for longitudinal evaluation [322]. As a result, the growing interest in utilizing imaging techniques as research tools due to their unique ability to provide longitudinal data from individual animals. Also, these imaging techniques enable non-invasive observation of internal cardiac structures and functions, reducing the need for invasive procedures and minimizing potential distress to the animals involved in scientific studies.

In clinical practice, there is a broad range of imaging methods available and as discussed in Chapter one, each has distinct advantages and disadvantages depending on their application. Many of these imaging methods have been adapted to permit small animal imaging, which offers a new set of challenges. Cardiac MRI is to date recognized as the preferred technique and the gold standard for assessing cardiac function and cardiac morphology due to its exceptional spatial resolution and high-contrast anatomical visualization capacity [323]. However, MRI scanners are associated with high costs (5 to 10 times higher than an ultrasound), the need for dedicated physics support, relatively slow data acquisition rates, limited availability in laboratories, and limitations in animals with implanted devices such as mini pumps

[324]. Similarly, radionuclide techniques such as SPECT/PET-CT imaging have emerged as non-invasive tools for highly sensitive evaluation of cardiac function. However, they have limitations such as being expensive, taking longer to gather data, requiring the use of intravenous contrast agents, low resolution and exposing animals to ionizing radiation [325].

The conventional echocardiographic techniques, such as M-mode and B-mode, are well accepted as cheap, safe and non-invasive diagnostic tools for the assessment of cardiac function by evaluating parameters such as EDV, ESV, and EF [326]. Despite continuous development in hardware and post-processing software leading to improved image quality, these echocardiographic techniques still possess inherent limitations. A well-recognized challenge in conventional echocardiography is its reliance on geometric assumptions that consider the heart as a symmetric shape rather than an asymmetric shape, thereby limiting measurement accuracy and sufficient information in cases of heart diseases, particularly those involving abnormally shaped ventricles [327].

The recent development in 4D ultrasound has attracted attention due to its capability to evaluate LV function and provide additional insights into the post-MI cardiac geometry, irrespective of irregularities [328]. The application of 4D ultrasound offers potential advantages over traditional ultrasound, as it enables visualization of the 3D representation of the LV while accounting for the dynamic movement of the heart during the cardiac cycle. Therefore, the need for geometric assumptions is eliminated [329, 330]. Prior to the effective application of 4D ultrasound in evaluating therapeutic effects, it is necessary to validate the reliability of this technique for the assessment of cardiac function in the animal model.

In the field of preclinical study and clinical practice, numerous echocardiographic parameters have been developed to assess cardiac function. Among these, LVEF, the percentage of blood ejected from the LV during systole, is identified as the most reliable parameter and is well-measured by M-mode and B-mode echocardiography [331]. Nevertheless, despite its extensive clinical utility, LVEF also has certain limitations. First, it provides solely an indirect estimation of myocardial contractile function as it is calculated as (EDV-ESV)/EDV * 100% [332]. Second, EF is a

relatively insensitive indicator of regional pathological myocardial deformation and cardiac regional function, rendering it inadequate for identifying subclinical myocardial injury, which is important in studies evaluating changes in cardiac functional dynamics induced by cardiac regeneration therapy [333]. Collectively, it is essential to explore alternative methods for a more comprehensive assessment of LV function, capable of detecting early LV dysfunction prior to changes in EF and capturing regional changes.

In recent years, the development of speckle-tracking echocardiography (STE) has significantly changed the prospect of echocardiography being applied in preclinical and clinical studies. STE is an emerging ultrasound technique which enables the measurement of myocardial contractility and quantification of regional myocardial deformation. Myocardial strain is an important parameter to characterize the regional movement of the myocardium, quantify intraventricular desynchrony and evaluate myocardial lengthening and shortening, which are not totally reflected in EF measurements [334, 335]. Strain refers to the fractional, or the percent change in the length, of the myocardial segments [336]. STE analyzes the motion of speckles, which are the natural acoustic markers in the B-mode ultrasound. These tracking speckles are statistically equally distributed throughout LV endocardial and epicardial borders at the papillary muscle levels in both long- and short-axis views to semi-automatically trace the region of interest from frame to frame [337].

Strain can be used to assess both global and regional myocardial function in three perpendicular axes (Figure 3-1). The radial axis is perpendicular to the epicardium and points out of the cavity. The longitudinal axis is perpendicular to the radial axis, tangential to the epicardium, pointing towards the bottom of the ventricle and away from the apex. The circumferential axis is perpendicular to both the radial and longitudinal axis [334]. Longitudinal strain reflects the percent change in LV length (from the apex to the base). Radial strain detects the percent change in myocardial wall thickness along the long- and short-axis. Circumferential strain analysis is performed along the short axis to assess the percent change in myocardial circumference [335, 336]. In strain analysis, negative strain reflects the wall shortening, whereas positive values display the thickening of the myocardial segment. During systole, the LV wall shortens and thickens, so the values of longitudinal strain

and circumferential strain (wall shortening) are negative, whereas the radial strain value (wall thickening) is positive [333, 336]. Strain is calculated as the change in length (L_1) of the object along a specific direction relative to its original or baseline length (L_0): Strain = $(L_1-L_0)/L_0$ (%) [360]. A total of 303 healthy subjects were encompassed in a clinical study to illustrate normal global strain values as -15.9 ± 2.4% in longitudinal, -30.6 ± 2.6% in circumferential, and 35.6 ± 10.3% in radial [337].

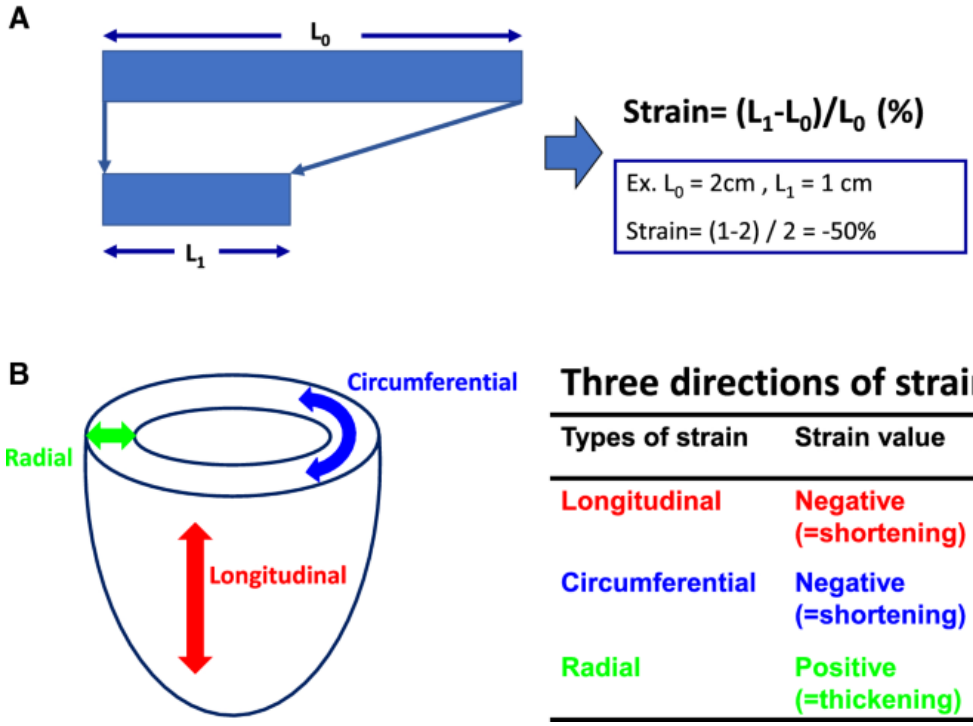

Figure 3-1. Speckle-tracking strain echocardiography. A. Calculation of strain values. B. Three types of strain in longitudinal, circumferential and radial. Adapted from Negishi & Negishi, 2022 [338].

It can be used as a quantitative ultrasound technique for accurately assessing both global and regional myocardial function, where strain represents an essential parameter reflecting the deformation of the myocardium. Strain can be rapidly measured offline after adequate image acquisition by tracking the displacement of the speckles identified on the conventional 2D echo greyscale in the longitudinal, circumferential, and radial planes during the cardiac cycle [339, 340]. In regional strain analysis, the LV myocardium is divided into six segments in both the long and short axes. In the long axis, it is segmented into anterior basal, anterior mid, anterior apex, posterior basal, posterior mid and posterior apex segments; in the short axis, it is divided into Anterior, Lateral, Posterior, Inferior, Septal, and Anterior Septum

segments (Figure 3-2) [341]. In a healthy heart, all segments should move at similar velocities, peaking at similar times. Under pathological conditions, certain segments may move at different rates and thus peak at different times, leading to dyssynchronization. Regional differences in specific LV segments can be reported as peak regional strain values [335].

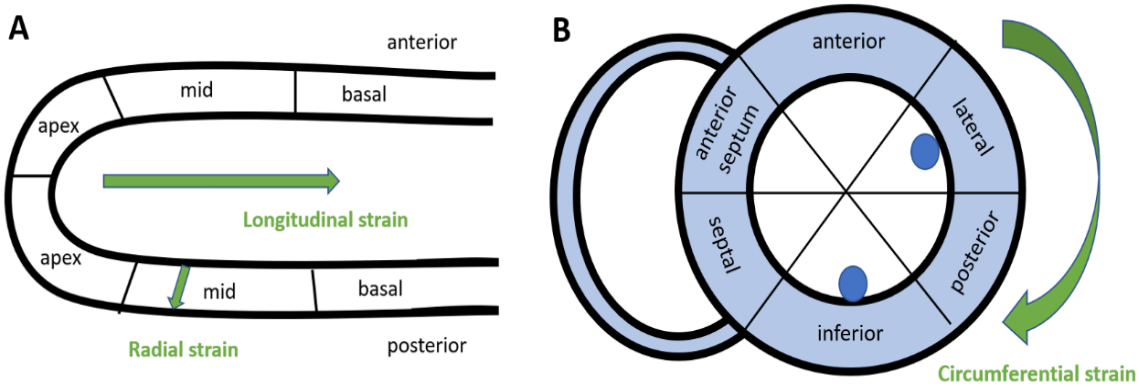

Figure 3-2. Regional strain in three perpendicular axes. A. Segmentation of the myocardium in long-axis view. B. Segmentation of the myocardium in short-axis view.

In clinical settings, global longitudinal strain (GLS) has demonstrated strong correlations with LVEF and the extent of MI and scarring in patients [342, 343]. Additionally, regional longitudinal strain (RLS) provides clinicians with detailed insights into myocardial deformation at the level of individual LV segments, enabling early detection of systolic dysfunction in patients with preserved LVEF [344]. In preclinical studies, strain analysis has emerged as a promising tool for evaluating the effectiveness of regenerative treatments for MI, providing valuable insights into the therapeutic impact on local myocardial structure and function. Also, the application of strain analysis extends beyond assessing treatment efficacy to offering supplementary diagnostic capabilities for conditions that currently lack validated clinical methods. For instance, it presents an opportunity to enhance our understanding and diagnosis of diseases such as HF with preserved EF and cardiac amyloidosis, where traditional diagnostic approaches may fall short.

Cardiac amyloidosis is defined as a form of restrictive cardiomyopathy (CM) characterized by the extracellular accumulation of misfolded protein fragments within the atria, ventricles, and perivascular space (predominantly in small vessels) as well as within the valves and conduction system in some cases [345]. In such

conditions, it often triggers a highly aggressive form of cardiac disease, including atrial fibrillation, aortic stenosis, ventricular arrhythmias, thromboembolic complications, conduction disorders, and HF [346]. Cardiac amyloidosis is primarily classified as either light chain (AL) or transthyretin amyloidosis (ATTR). AL is caused by the misfolding of monoclonal immunoglobulin light chains due to clonal plasma cell dyscrasia. ATTR involves a protein synthesized by the liver, formerly known as prealbumin, that typically transports hormones such as thyroxine and retinol-binding proteins [347, 348]. Transthyretin amyloid CM (ATTR-CM) is categorized into non-hereditary wild type, characterized by the accumulation of wild-type transthyretin as the aging progresses without mutations or hereditary, associated with genetic variants of TTR [349]. In ATTR-CM, the process of fibrillogenesis necessitates the dissociation of the TTR homotetrameric structure into misfolded monomers, which subsequently self-assemble into soluble oligomeric species that further undergo misassembly to form amyloid fibrils and deposit within the myocardium [350].

Wild-type ATTR-CM is an under-recognized cause of HF in older populations. In the clinic, the diagnosis of this type of ATTR-CM poses a challenge primarily due to the clinical phenotype characterized by myocardial wall thickening [351]. In addition, HF may be accompanied by other common diseases, such as hypertrophic cardiomyopathy or aortic stenosis. The heart is frequently involved in systemic amyloidosis. When other organs have already been diagnosed with amyloidosis, symptoms arising from the heart can be readily attributed to its involvement in the disease [352]. Unfortunately, in cases where cardiac amyloidosis is an isolated disorder or when undiagnosed multi-organ amyloidosis primarily manifests as cardiac symptoms, the diagnosis is often overlooked and significantly delayed [353]. In particular, the lack of optimal diagnostic modalities results in patients with ATTR-CM often progressing to advanced stages with few clinical signs and symptoms. It is therefore associated with poor prognosis [349].

Dr Paul Simons and Prof. Marianna Fontana's group from the National Amyloidosis Centre, UCL, have recently developed a humanized ATTR-CM mouse model of cardiac ATTR by deleting the mouse TTR gene, overexpressing a mutant form of human TTR gene and then seeding mice with mutant TTR [354]. Our research group

has successfully confirmed the presence of amyloid deposition within the cardiac tissue of mice with ^{99}mTc-3,3-diphosphono-1,2-propanodicarboxylic acid (DPD) scans using SPECT-CT imaging. This finding was consistent with a recent clinical study demonstrating improved diagnostic accuracy and non-invasive quantification of amyloid burden with 3D visualization in patients using SPECT/CT for bone scintigraphy [355]. However, MRI and Simpson's ultrasound failed to identify systolic dysfunction in the ATTR-CM model as evidenced by no significant differences observed in EF, EDV, and ESV values between the control group and ATTR-CM group at two time points (9- and 12-months post-seeding). This preserved systolic function is often present in patients and can lead to misdiagnosis. Hence, more advanced strain imaging has been used to identify patients suffering from cardiac ATTR-CM.

In clinics, strain analysis using STE has been recognized as a quantitative technique for evaluating LV deformation in patients with ATTR-CM. This method demonstrates a distinctive pattern of 'apical sparing,' wherein the strain values are reduced at the basal and midwall regions while being preserved at the apical region [356]. Therefore, reduced GLS and increased relative apical sparing (RELAPS) have been frequently used as cardiac deformation indicators associated with a diagnosis of ATTR-CM [357]. Currently, there is no validated modality to accurately assess the progression of cardiac dysfunction in preclinical studies of ATTR-CM animal models, including MRI. Here, I applied STE as a novel imaging modality for detecting cardiac functional impairment and following disease progression noninvasively in the ATTR-CM model.

Aims

This project consists of three studies:

1. The first study aimed to assess the reliability and accuracy of 4D ultrasound for the assessment of cardiac function. This study conducted a comparison of LV volumes and EF determined by conventional echocardiography with 4D ultrasound in an MI model, with cardiac MRI assessment serving as the reference standard.

2. The second study aimed to assess the potential of strain analysis in experimental MI therapies by evaluating STE's ability for global and regional cardiac function assessment in an MI mouse model.
3. The third study aimed to assess the reliability of STE as a robust modality in validating the ATTR-CM model and offering valuable tools for evaluating novel therapies targeting ATTR-CM. This study employed LS analysis on an ATTR-CM mouse model to identify and track the development of cardiac dysfunction at two specific time points (9 and 12 months). Additionally, CS and RS were utilized to explore their potential for enhancing the diagnosis of ATTR-CM.

3.2. Materials and methodology

3.2.1. Myocardial infarction mouse model

All procedures were conducted in compliance with the Home Office Animals (Scientific Procedures) Act and local ethical regulations under PPL PP1692884. The surgical induction of the MI model was thoroughly described in Chapter 2. In this study, 17 female Balb/C mice weighing 20-26 g at the age of 8 to 12 weeks underwent MI-induced surgery. 6 mice had open-chest surgery without LAD ligation, which were used in control group. Cine-MRI and ultrasound examinations were carried out at either 2- or 4 weeks post-MI. At each point, ultrasound was performed first, typically on the initial day, and Cine-MRI was then conducted the following day. This schedule helped ensure accurate results and reduced the effects of anesthesia on the imaging outcomes.

3.2.2. Magnetic resonance imaging

Cine-MRI was performed in the short-axis view to acquire nine slices from the apex to the base of the LV to assess cardiac function. A cardiac- and respiratory-gated gradient echo sequence was used to acquire cine images. Imaging parameters were as follows: TE = 1.18 ms, TR = 5 ms, flip angle = 15°, slice thickness = 1 mm, FOV = 25.6 × 25.6 mm, matrix size = 128 × 128, number of signal averages = 3. The freely available software Image J was used to analyze the cardiac function from cine images. EDV was obtained by segmentation of the LV endocardium in all end-diastole slices. Similarly, ESV was obtained from endocardial segmentation in all end-systole slices. EF = (EDV-ESV)/EDV*100.

3.2.3. Echocardiography

3.2.3.1. Ultrasound imaging system and animal preparation

Ultrasound imaging in this study was conducted on a VisualSonics Vevo 3100 system (FUJIFILM VisualSonics, Toronto, Canada) using a VisualSonic MX550S linear array transducer (Figure 3-3). Mice were anesthetized using 2.0% isoflurane in 2 L/min O_2 delivered by nose cone. The hair was removed with hair removal cream (Veet, UK) to reduce the attenuation of the ultrasound signal. Animals were positioned on the operation platform in a supine position. The body temperature was monitored via a rectal probe and maintained at 37 °C. The ECG and heart rate were monitored via surface ECG limb electrodes that were placed on the platform with paws taped with a small amount of coupling gel. The heart rate was maintained between 400 and 500 bpm during imaging by adjusting isoflurane concentration (Figure 3-4).

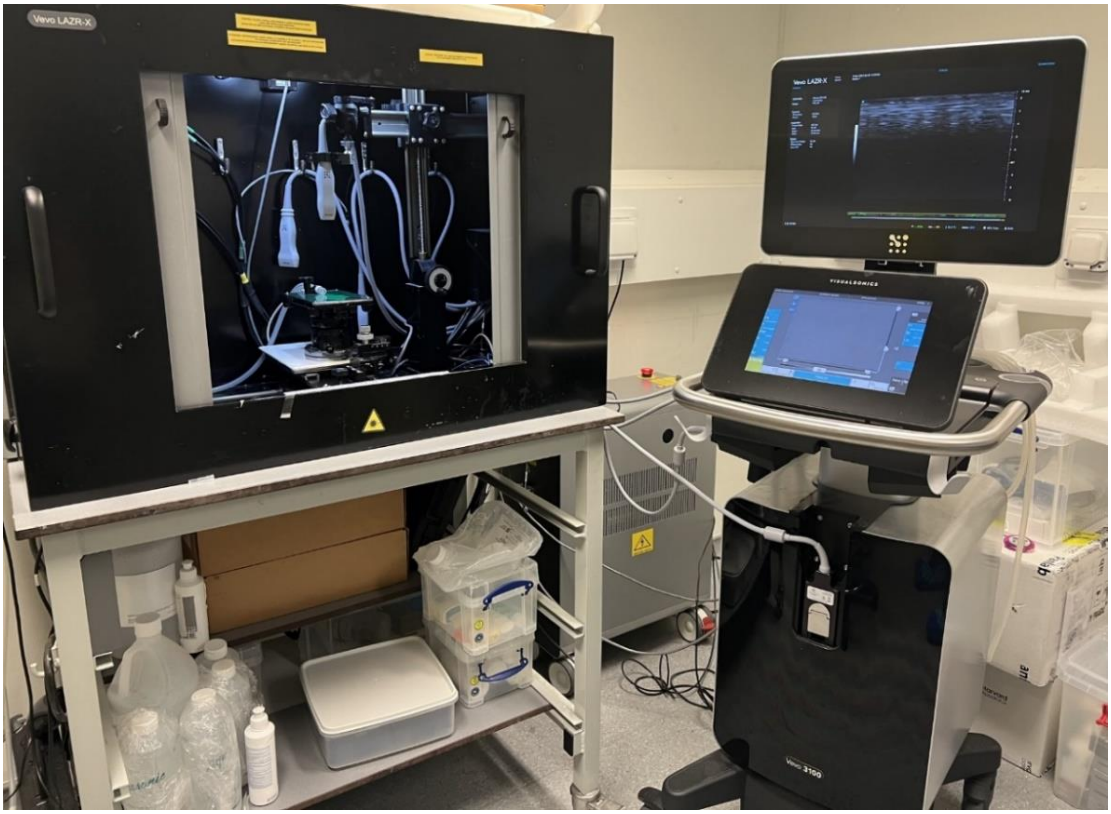

Figure 3-3. Ultrasound imaging system. VisualSonics Vevo 3100 system with a VisualSonic MX550S linear array transducer and hardware to control the system.

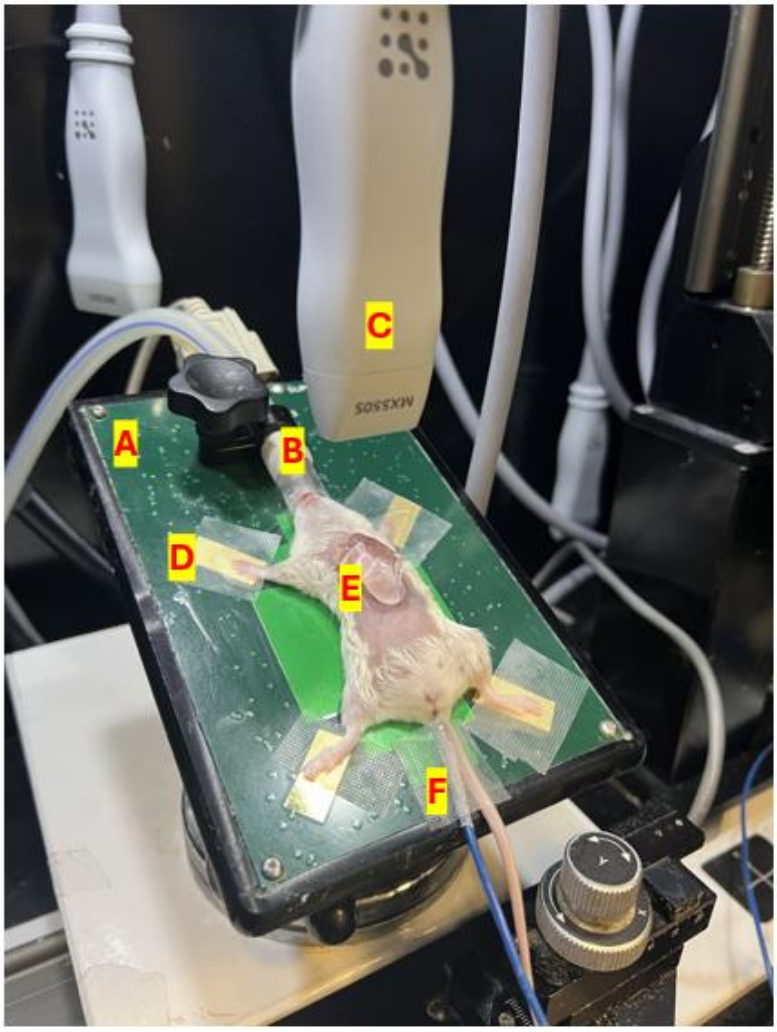

Figure 3-4. Animal preparation for ultrasound acquisition. A: Ultrasound platform; B: Nose cone; C: Probe; D: ECG pad; E: Coupling gel; F: Temperature probe.

3.2.3.2. Ultrasound imaging acquisition

The heart is imaged in parasternal long- and short-axis views. The parasternal long axis view (PSLAX) is typically the initial view captured during 2-D mode echocardiography, taken from the left parasternal region with the ultrasound beam parallel to the base-apex (long-axis) of the heart. The parasternal short-axis view (PSAX) is then obtained by rotating the probe 90 º clockwise from the PSLAX view (Figure 3-5).

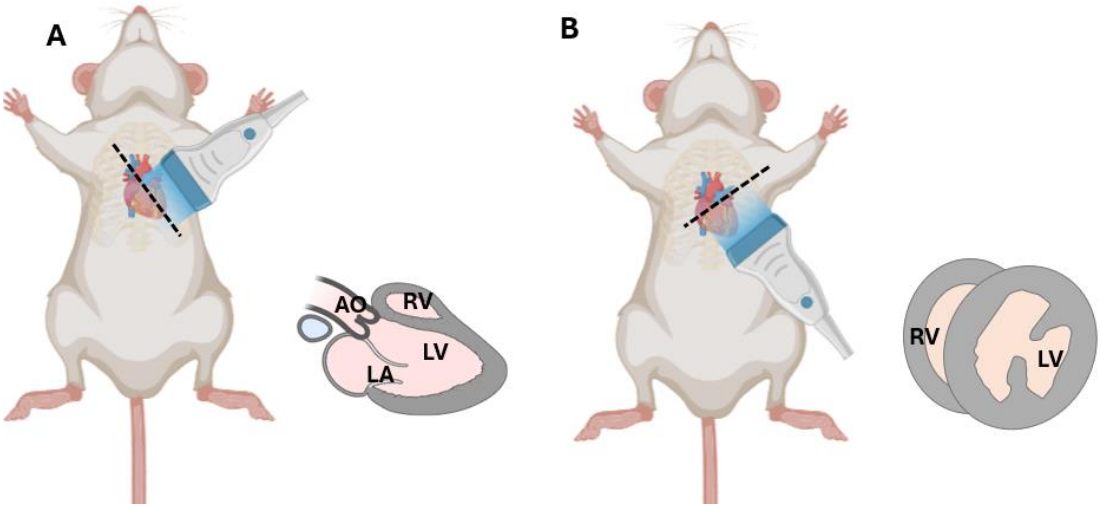

Figure 3-5. Ultrasound image acquisition of the heart in two planes. A: The parasternal long-axis view; B: The parasternal short-axis view. Left atrium (LA), left ventricle (LV), right ventricle (RV), ascending aorta (AO) can be seen in the parasternal long-axis view. RV and LV are identifiable in the parasternal short-axis view. Created with Biorender.

3.2.3.2.1. M-mode

In the assessment of cardiac function, M-mode ultrasound provides a comprehensive 1D temporal profile depicting the alterations in LV diameter and wall thickness during both systole and diastole [576]. The evaluation of LV systolic function in M-mode ultrasound can be achieved by quantifying measurements obtained from PSLAX M-mode and PSAX M-mode in both end-diastolic and end-systolic stages: anterior wall thickness (LVAWs and LVAWd), posterior wall thickness (LVPWs and LVPWd), as well as internal diameters (LVIDs and LVIDd). Based on these measurements, EDV, ESV, and LVEF can be calculated using the Teichholz method (Table 3-1) [576].

M-mode ultrasound

Ultrasound images:

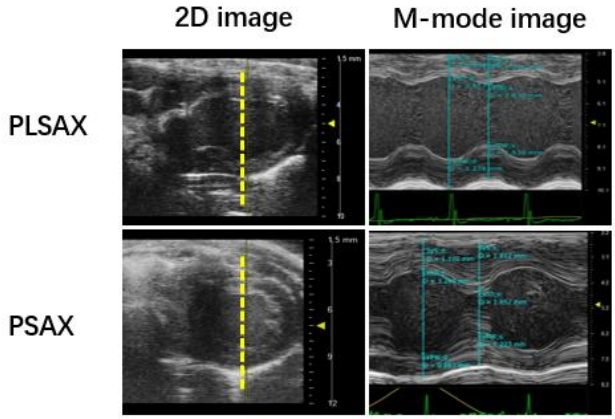

Schemic diagram:

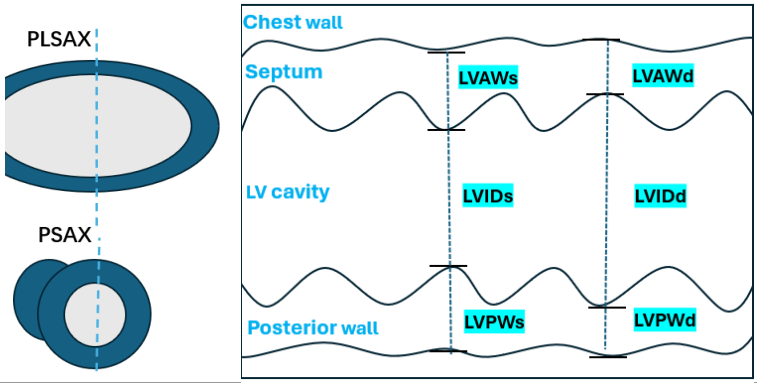

Equation

$$\mathbf{LVESV} = \left(\frac{\mathbf{7}}{\mathbf{2.4 + LVIDs}}\right)\mathbf{x\ LVIDs^3}$$

$$\mathbf{LVEDV} = \left(\frac{\mathbf{7}}{\mathbf{2.4 + LVIDd}}\right)\mathbf{x\ LVIDd^3}$$

$$\mathbf{EF}(\%) = \frac{\mathbf{LVEDV - LVESV}}{\mathbf{LVEDV \times 100}}$$

Table 3-1. Acquisition of the M-mode ultrasound in parasternal long- and short-axis views. LVAWs and LVAWd: anterior wall thickness in end-systole and end-diastole; LVPWs and LVPWd: posterior wall thickness in end-systole and end-diastole; LVIDs and LVIDd: internal diameters in end-systole and end-diastole.

3.2.3.2.2. B-mode

3.2.3.2.2.1. Single-plane B-mode:

B-mode ultrasound, as a fundamental imaging technique, allows for 2D visualization of the heart, providing more comprehensive information compared to M-mode. The utilization of the single-plane B-mode in PSLAX (PSLAX B-mode) enables the

acquisition of a significant number of systolic indexes and volumes. This is achieved by accurately tracing the endocardial border around the LV cavity at both systole and diastole to generate the LV end-diastolic area and LV end-systolic area (LVEDA and LVESA) and the length of the LV at end-diastole and end-systole to provide LV end-diastolic length (LVEDL) and LV end-systolic length (LVESL) values. EDV and ESV can then be calculated using the following formulas (Table 3-2).

Single-plane B-mode
Ultrasound images: 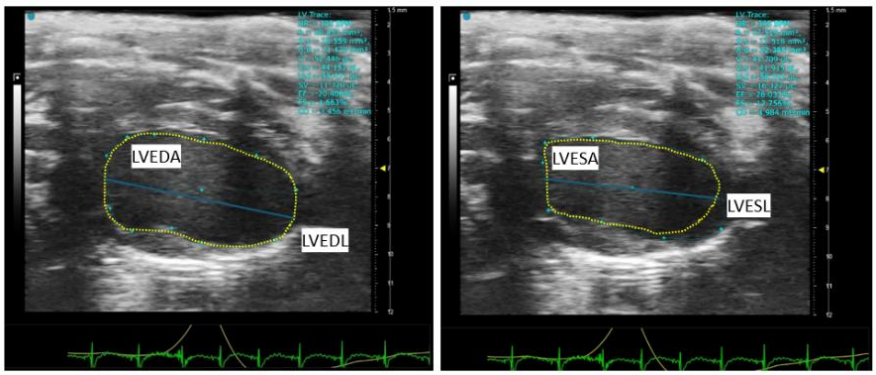
Equation: $$\mathbf{LVEDV} = \frac{\mathbf{8} \times \mathbf{LVEDA^2}}{\mathbf{3}\boldsymbol{\pi}\mathbf{LVEDL}}$$ $$\mathbf{LVESV} = \frac{\mathbf{8} \times \mathbf{LVESA^2}}{\mathbf{3}\boldsymbol{\pi}\mathbf{LVESL}}$$ $$\mathbf{EF}(\%) = (\mathbf{LVEDV} - \mathbf{LVESV})/\mathbf{LVEDV} \times \mathbf{100}$$

Table 3-2. Acquisition of the single-plane B-mode in parasternal long-axis view. LVEDA and LVESA: left ventricular end-diastolic area and end-systolic area; LVEDL and LVESL: left ventricular end-diastolic length and end-systolic length.

3.2.3.2.2.2. Multi-plane B-mode:

The multi-plane B-mode in the PSAX view, commonly known as the 'Simpson's method,' is the preferred approach for detecting echocardiographic evidence of cardiac disease in the clinics [576]. In this mode, the LV endocardium can be delineated during both diastole and systole to calculate total LV volume by summing

a stack of elliptical disks. Subsequently, images of the LV are analyzed at three parallel slices: (i) at the base level, (ii) at papillary muscle levels, and (iii) at the apex level. Measurements of LVEDL and LVESL are then performed from the PSLAX view. EDV and ESV were then calculated through a modified Simpson's rule, wherein A1, A2, and A3 represent LV areas at the basal level, papillary muscles level, and apex level during diastole and systole, respectively (Table 3-3).

Multi-plane B-mode (Simpson's multiplane)

Ultrasound images:

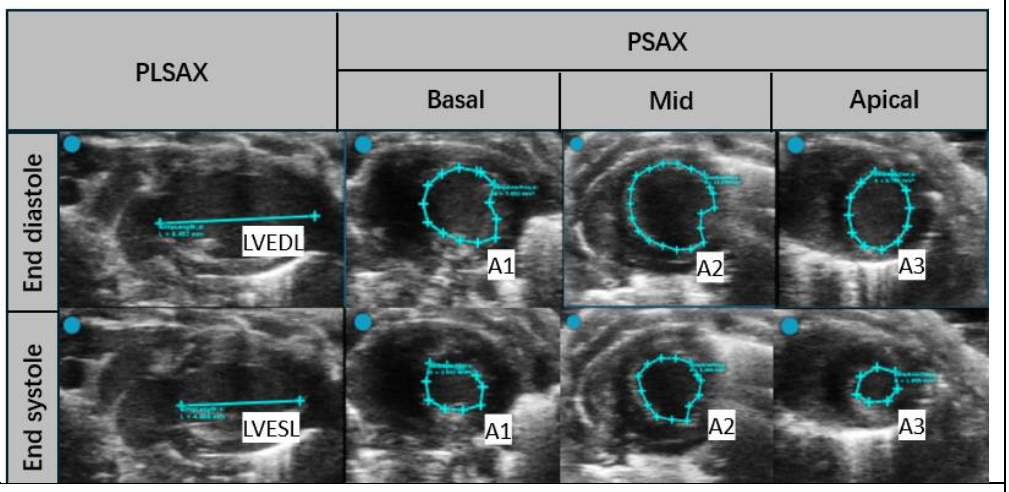

Schemic diagram:

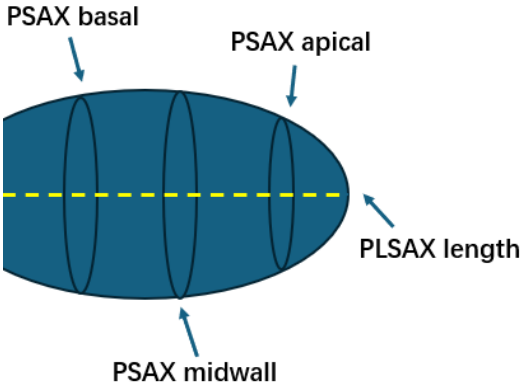

Equation:

$$\mathbf{LVEDV} = (\mathbf{A1} + \mathbf{A2}) \times (\mathbf{LVEDL}/\mathbf{3}) + (\mathbf{A3}/\mathbf{2}) \times (\mathbf{LVEDL}/\mathbf{3}) + (\boldsymbol{\pi}/\mathbf{6}) \times (\mathbf{LVEDL}/\mathbf{3})^{\mathbf{3}}$$

$$\mathbf{LVESV} = (\mathbf{A1} + \mathbf{A2}) \times (\mathbf{LVESL}/\mathbf{3}) + (\mathbf{A3}/\mathbf{2}) \times (\mathbf{LVESL}/\mathbf{3}) + (\boldsymbol{\pi}/\mathbf{6}) \times (\mathbf{LVESL}/\mathbf{3})^{\mathbf{3}}$$

$$\mathbf{EF}(\%) = (\mathbf{LVEDV} - \mathbf{LVESV})/\mathbf{LVEDV} \times \mathbf{100}$$

Table 3-3. Acquisition of the B-mode multi-plane in parasternal short-axis view. A1, A2, and A3: left ventricular areas at the basal level, papillary muscles level, and apex level during diastole and systole. LVEDL and LVESL: left ventricular end-diastolic length and end-systolic length.

3.2.3.2.3. 4D ultrasound

4D-US works by stacking 2D cross-sectional images of full-volume visualization of the heart to form a 3D representation during cardiac cycles [410]. 4D ultrasound

captures these volumes in real-time, enabling the visualization of cardiac kinetics over time. ECG- and respiratory gating are performed to synchronize periodic events and minimize motion artifacts, which place a foundation to spatiotemporally combine data from multiple acquisitions. A transducer is displaced along the PSAX to collect successive ECG- and respiratory-gated 3D-US images (step size: 80–130 μm, frame rate: 300–400 Hz). The acquired 3D volumes are reconstituted into a dynamic 4D dataset. The 4D-US images are then analyzed to directly obtain EDV, ESV, and EF through volumetric analysis after delineating the endocardial boundaries (Table 3-4).

4D ultrasound

Image acquisition:

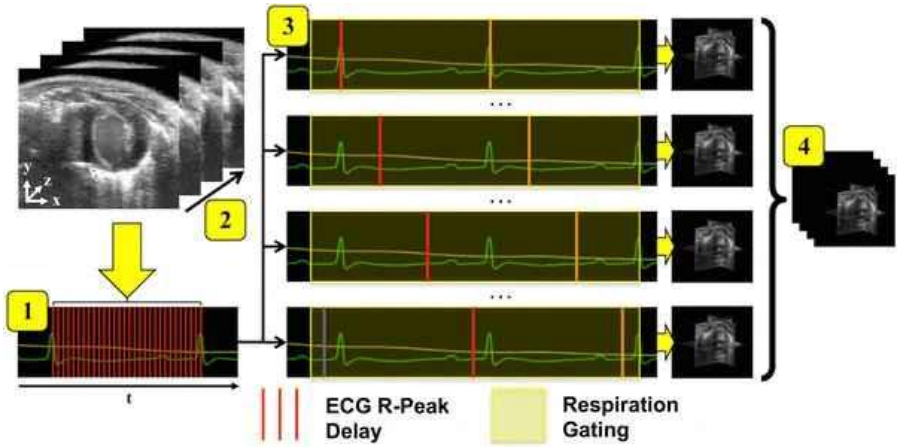

4D-US images:

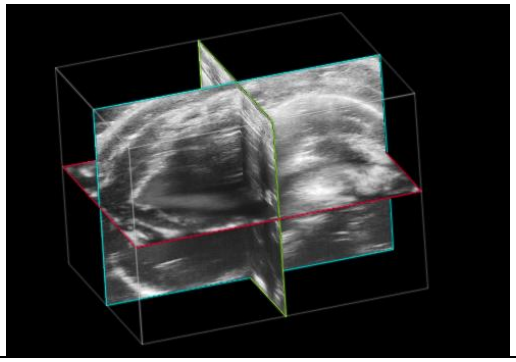

Analysis:

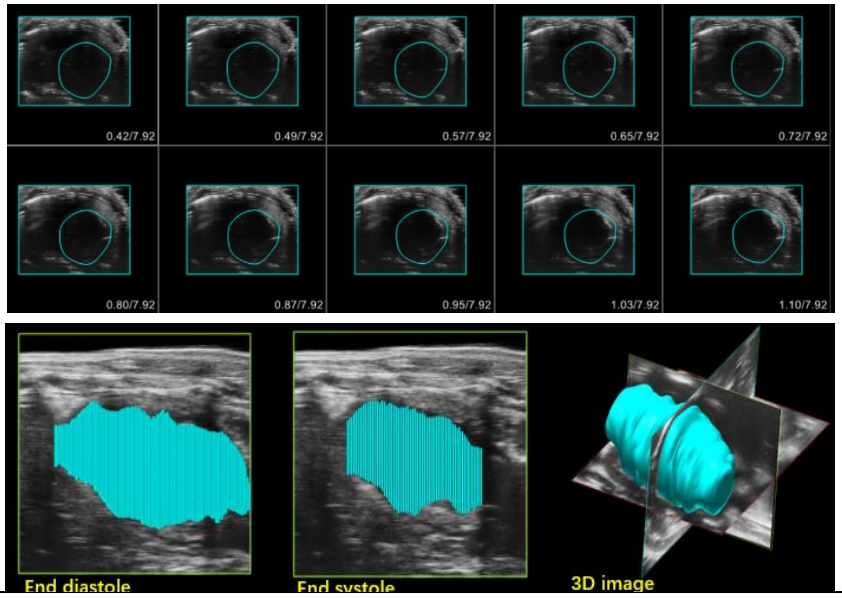

Table 3-4. 4D ultrasound. Acquisition of 4D ultrasound imaging: (1) respiratory- and ECG-gated 2D cine loops are acquired at a 350 frame rate from a specific anatomical location, (2) transducing the probe via the motor and repeating step one at each anatomical location, (3) integrating the extracted frames from each cine loop, based on their temporal alignment within the cardiac cycles, to generate 3D volumes at each corresponding time-point, and (4) temporally concatenating these volumes to produce 4D datasets. LV volumes and EF are

measured directly after delineating the endocardial boundaries. Reproduced from Soepriatna *et al.,* 2017 [410].

3.2.3.2.4. Strain analysis

Strain analysis is performed via the Vevo Strain software in longitudinal, circumferential, and radial planes in long- and short-axis images. After obtaining high-quality echocardiographic images with consistent ECG, the identification of the end-diastolic and end-systolic frames provides crucial reference points for subsequent strain analysis. Manual or semi-automatic drawing of endocardial and epicardial contours in both long- and short-axis views sets the stage for precise tracking of myocardial movement. The speckle-tracking system traces the endocardial and epicardial borders for at least 5 cardiac cycles. The LV myocardium is then automatically divided into six segments in both long-axis (anterior basal, anterior mid, anterior apex, posterior basal, posterior mid, and posterior apex segments) and short-axis (anterior, lateral, posterior, inferior, septal, and anterior septum segments) images as per American Society of Echocardiography guidelines. The speckle-tracking software then tracks the movement of acoustic markers within the myocardium to calculate strain curves for each segment in longitudinal, circumferential, and radial directions. These strain curves display regional variations in myocardial deformation during systole. The peak systolic strain values for each segment (regional strain value) are assessed as a percentage. The strain value across all segments represents the global strain, which represent the global deformation of the myocardium during cardiac contraction and relaxation (Table 3-5).

Strain analysis:

Analysis:

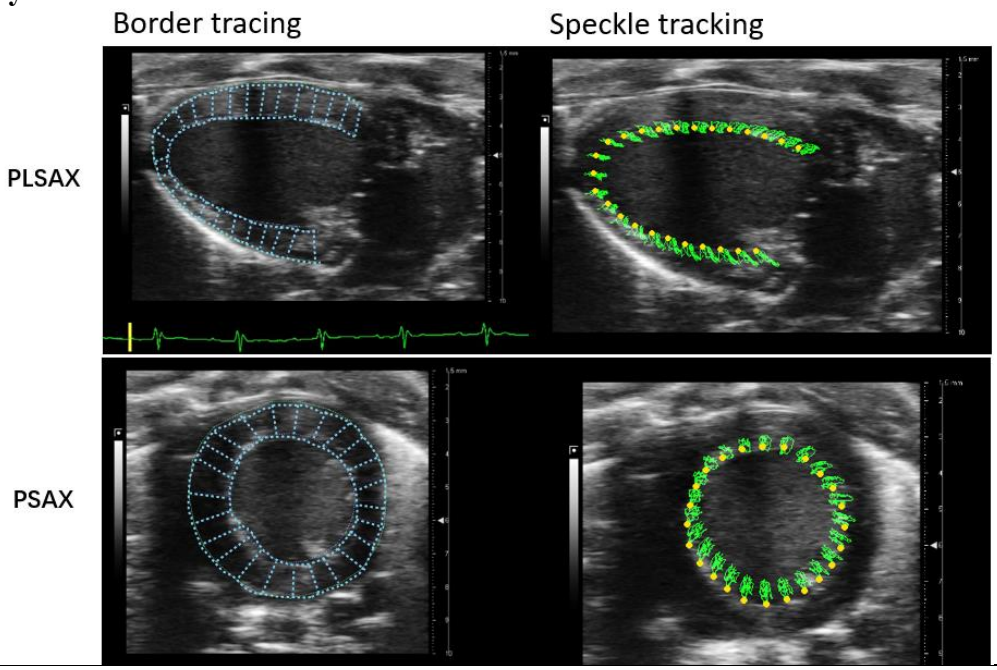

Schemic diagram:

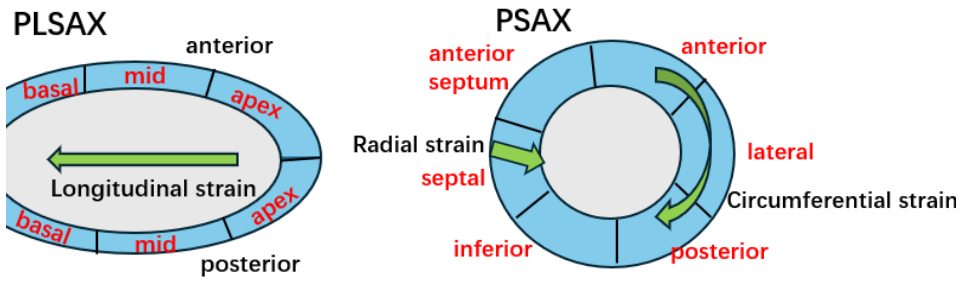

Data acquisition: strain curves

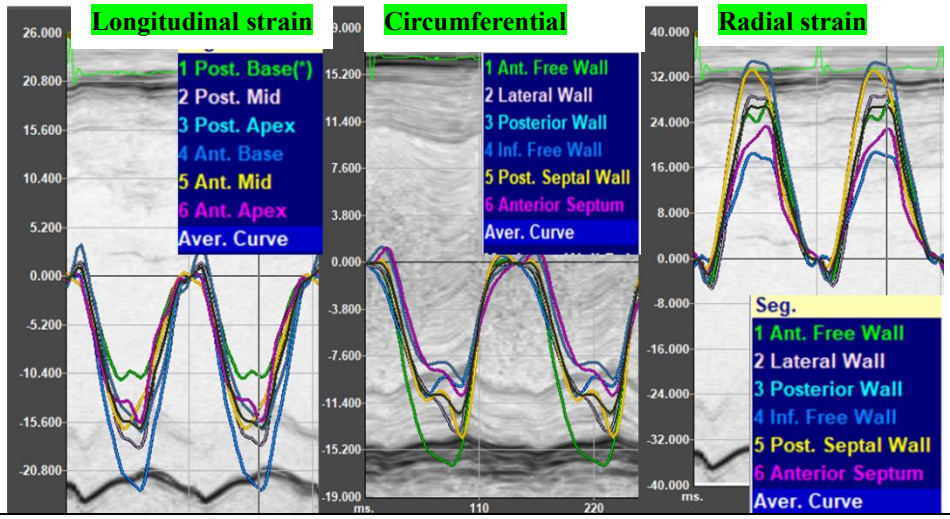

Table 3-5. Strain analysis. The acquisition of global and regional strain values in longitudinal, circumferential, and radial planes from both long- and short-axis views. The endocardial and epicardial borders are tracked semi-automatically for 5 cardiac cycles. The LV myocardium

is automatically divided into six segments for regional strain value assessment. Global strain values are derived across all segments.

3.2.4. Statistical analysis

Data collected from various ultrasound techniques were presented as mean and standard deviation (±SD). Analysis of statistical significance for two groups or more was performed using a one-way ANOVA followed by Tukey's post-hoc test with Geisser-Greenhouse correction applied. Pearson's correlation analysis and Bland-Altman analysis was applied between 4D-US with conventional ultrasound modes, and MRI was regarded as a reference. The correlation coefficient (R^2) demonstrates the strength of a relationship between two variables. When R^2 falls between 0.00 and 0.10, the correlation is considered negligible. R^2 values from 0.00 to 0.09, 0.10 to 0.39, 0.40 to 0.69, 0.70 to 0.89 and 0.90 to 1.00 indicate a negligible, weak, moderate, strong and very strong correlation, respectively. Bland-Altman analysis was applied to evaluate differences between 4D-US with conventional ultrasound modes, and MRI was regarded as a reference. Data were presented as % bias and 95% level of agreement (LOA). Bland-Altman percentage bias was calculated as (100*(B-A)/Average vs Average), in which "B" represented measurements from 4D-US, Simpson's multi-plane, SAX M-mode, PSLAX B-mode or PSLAX M-mode, and "A" represented measurements from MRI. For all statistical tests, $p \leqslant 0.05$ was considered significant.

3.3. Results

3.3.1. Study 1: Comparison of 4D-ultrasound to conventional ultrasound techniques for the assessment of cardiac function in an MI mouse model

After the comprehensive MRI, 4D-US, and conventional ultrasound assessments were conducted on 17 Balb/c mice with MI, representative images of the evaluation of cardiac function utilizing all imaging modalities were depicted in Figure 3-6. The results revealed that all conventional ultrasound methods measured LV volumes that strongly correlated with MRI findings. Specifically, EDV showed a correlation coefficient (R^2) greater than 0.60 across all methods, and ESV exhibited a value exceeding 0.76 (Table 3-6).

Interestingly, when comparing the ejection fractions obtained from different ultrasound modalities with MRI measurements, varying degrees of correlation were observed. Notably, 4D-US demonstrated the highest correlation with an R^2 value of 0.82, followed closely by Simpson's method at $R^2 = 0.79$. These outperformed other conventional ultrasound techniques: SAX M-mode ($R^2 = 0.40$), PSLAX B-mode ($R^2 = 0.40$), and PSLAX M-mode ($R^2 = 0.31$), as indicated in Table 3-6.

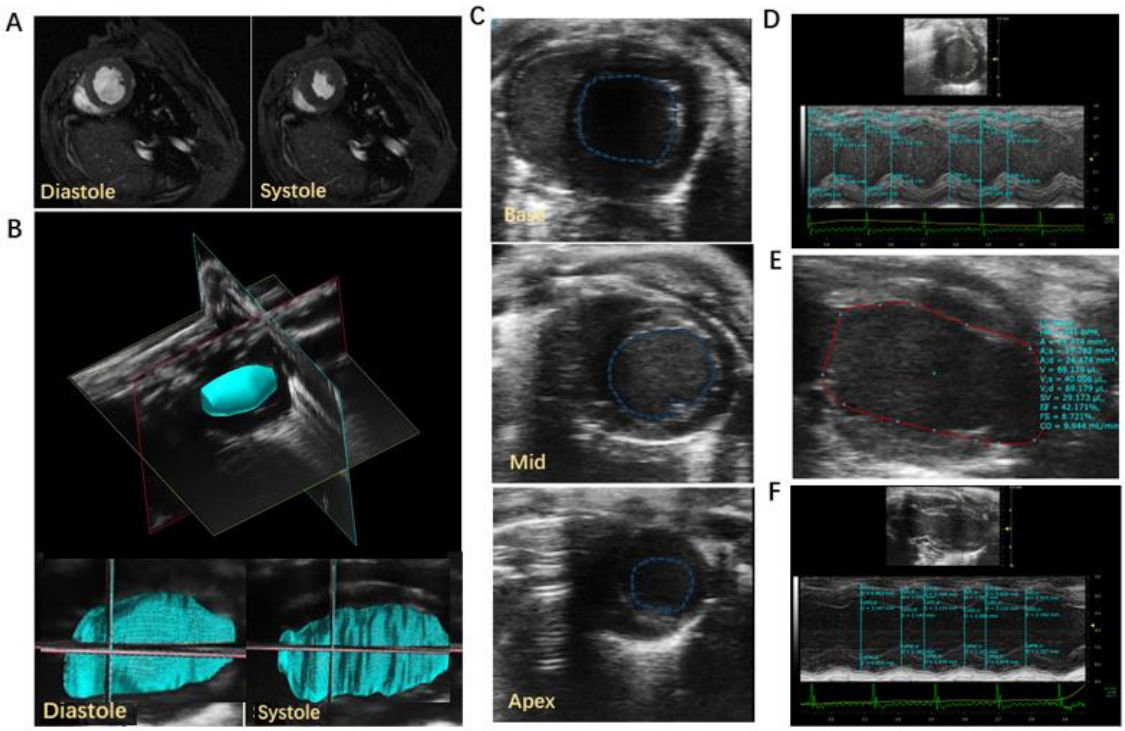

Figure 3-6. Representative images using cardiac MRI, 4D-US, and traditional ultrasound techniques. A: Mid-ventricular MRI images of an infarct heart during end-diastole (left) and end-systole (right). B: 4D-US images of an infarcted heart (top) and tracing of 4D-US reconstruction during end-diastole (left) and end-systole (right). C: Simpson's multiplane mode from base (top) to apex (bottom). D: SAX M-mode. E: PSLAX B-mode. F: PSLAX M-mode. MRI, magnetic resonance imaging; 4D-US, 4-dimensional ultrasound; SAX M-mode, 1-dimensional motion-mode in short axis; PSLAX B-mode, 2-dimensional brightness mode in single-plane parasternal long-axis view; PSLAX M-mode, 1-dimensional motion-mode in long axis.

Table 3-6. Correlation of MRI with 4D ultrasound and other conventional ultrasound techniques in cardiac function assessment of infarcted mouse hearts.

Measurement Method	Mean	Error	Percent Error	Correlation	R^2	P-value
End diastolic volume (µl)						
MRI	72.7 ± 22.5	-	-	-	-	-
4D-mode	70.8 ± 22.1	2.8 ± 1.6	3.8 ± 2.0	Y = 0.9774*X - 0.3215	0.9869	<0.0001
Simpson's multiplane	68.1 ± 22.8	5.9 ± 4.6	8.2 ± 6.7	Y = 0.9342*X + 0.1204	0.9292	<0.0001
SAX M-mode	65.0 ± 17.9	12.9 ± 9.5	18.5 ± 15.6	Y = 0.6136*X + 20.41	0.5968	<0.0001
PSLAX B-mode	63.4 ± 20.3	10.5 ± 4.1	15.3 ± 7.1	Y = 0.8648*X + 5.057	0.919	<0.0001
PSLAX M-mode	62.4 ± 19.1	13.1 ± 6.6	18.0 ± 7.6	Y = 0.7494*X + 7.914	0.7774	<0.0001
End systolic volume (µl)						
MRI	38.3 ± 18.7	-	-	-	-	-
4D-mode	38.2 ± 19.4	2.6 ± 2.1	7.8 ± 6.3	Y = 1.025*X - 1.049	0.9707	<0.0001
Simpson's multiplane	37.8 ± 18.5	4.4 ± 2.4	12.8 ± 6.9	Y = 0.9532*X + 1.311	0.9272	<0.0001
SAX M-mode	35.6 ± 17.6	8.1 ± 3.7	22.8 ± 8.1	Y = 0.7298*X + 9.617	0.7621	<0.0001
PSLAX B-mode	35.1 ± 16.5	5.8 ± 3.4	16.0 ± 7.7	Y = 0.8387*X + 2.984	0.8985	<0.0001
PSLAX M-mode	34.2 ± 14.7	8.1 ± 6.1	21.2 ± 10.5	Y = 0.6411*X + 9.680	0.7586	<0.0001
Ejection fraction (%)						
MRI	49.6 ± 11.1	-	-	-	-	-
4D-mode	48.8 ± 11.3	3.6 ± 3.2	7.3 ± 6.1	Y = 0.9262*X + 2.851	0.8222	<0.0001
Simpson's multiplane	47.3 ± 10.1	4.8 ± 2.6	10.1 ± 5.7	Y = 0.8056*X + 7.383	0.7868	0.0003
SAX M-mode	43.3 ± 14.6	10.9 ± 6.8	23.0 ± 14.8	Y = 0.8295*X + 2.218	0.3957	0.0068
PSLAX B-mode	45.7 ± 12.5	8.7 ± 5.7	17.2 ± 9.6	Y = 0.7428*X + 8.929	0.4035	0.0042
PSLAX M-mode	45.5 ± 11.7	9.4 ± 5.3	21.2 ± 12.2	Y = 0.5919*X + 16.17	0.3121	0.0198

All the ultrasound modalities demonstrated a strong correlation with MRI when assessing EDV and ESV. Only 4D-US and Simpson's strongly correlated with MRI on EF assessment, $p < 0.05$. Negligible correction: R^2: 0.00 and 0.09; weak correction: R^2: 0.10 to 0.39, moderate correction: R^2: 0.40 to 0.69; strong correction: R^2: 0.70 to 0.89; very strong correction: R^2: 0.90 to 1.00.

The Bland-Altman analysis of EDV, ESV and EF was conducted to assess differences between selected ultrasound modality (4D-US, Simpson's multi-plane, SAX M-mode, PSLAX B-mode, and PSLAX M-mode) and MRI. The agreements of measurements for EDV, ESV and EF between MRI and ultrasound imaging techniques were depicted in Figures 3-7, 3-8, and 3-9, respectively. The results demonstrated that higher agreement in EDV measurement was achieved between 4D-US with MRI (Figure 3-7A: bias, 1.97 µl; 95% CI, -3.09 to 7.06), followed by Simpson's multi-plane with MRI (Figure 3-7B: bias, 4.67 µl; 95% CI, -7.07 to 16.40), compared with other conventional ultrasound modes: SAX M-mode (Figure 3-7C: bias, 7.69 µl; 95% CI, -20.72 to 35.71), PSLAX B-mode (Figure3-7D: bias, 9.33 µl; 95% CI, -3.47 to 22.12), and PSLAX M-mode (Figure 3-7E: bias, 10.31 µl; 95% CI, -10.55 to 31.16). Similarly, better agreements were achieved in ESV measurement of 4D-US (Figure 3-8A: bias, 0.08 µl; 95% CI, -6.50 to 6.67) and Simpson's (Figure 3-8B: bias, 0.48

µl; 95% CI, -0.70 to 10.40) with MRI assessment when comparing with other conventional ultrasound modes: SAX M-mode (Figure 3-8C: bias, 0.73 µl; 95% CI, -17.18 to 18.63), PSLAX B-mode (Figure 3-8D: bias, 3.19 µl; 95% CI, -8.70 to 15.08), and PSLAX M-mode (Figure 3-8E: bias, 4.06 µl; 95% CI, -14.60 to 22.71). In EF evaluation, a higher level of agreement was also noticed for 4D-US when compared with MRI (Figure 3-9A: bias, 0.81%; 95% CI, -8.70 to 10.29), followed by Simpson's multi-plane (Figure 3-9B: bias, 2.25%; 95% CI, -7.79 to 12.28), compared with other conventional ultrasound modes: SAX M-mode (Figure 3-9C: bias, 6.23%; 95% CI, -16.32 to 28.79), PSLAX B-mode (Figure 3-9D: bias, 3.82%; 95% CI, -15.55 to 23.18), and PSLAX M-mode (Figure 3-9E: bias, 4.05%; 95% CI, -16.98 to 25.08).

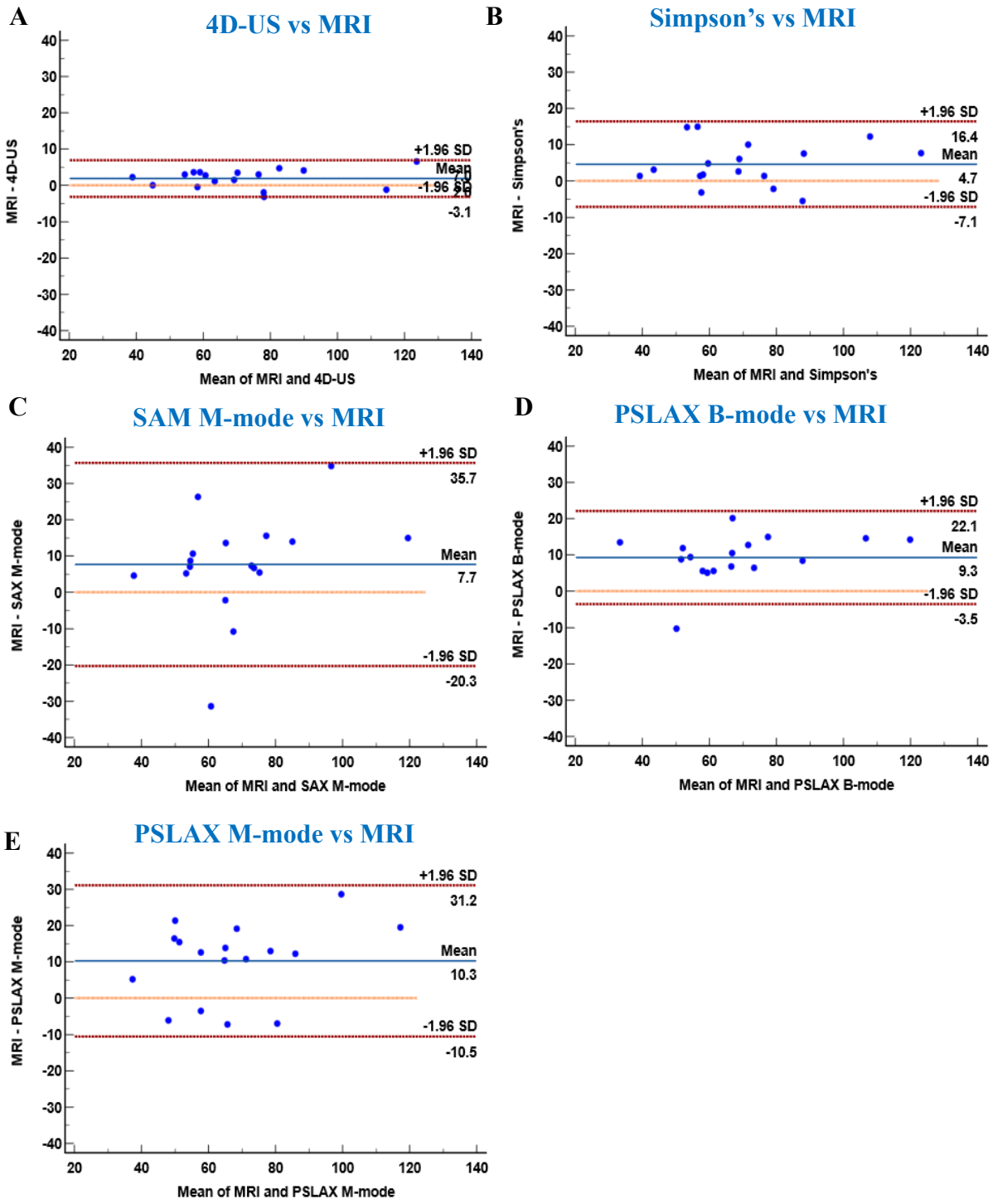

Figure 3-7. Bland–Altman analysis of EDV determined by MRI and 4D-US (A) or Simpson's multi plane (B), SAX M-mode (C), PSLAX B-mode (D) and PSLAX M-mode (E). Each plot displays the differences between the two measurement methods against their mean values. The mean (bias) is represented by the solid blue line, and the mean ± 1.96 SD by the dashed red lines. N=17.

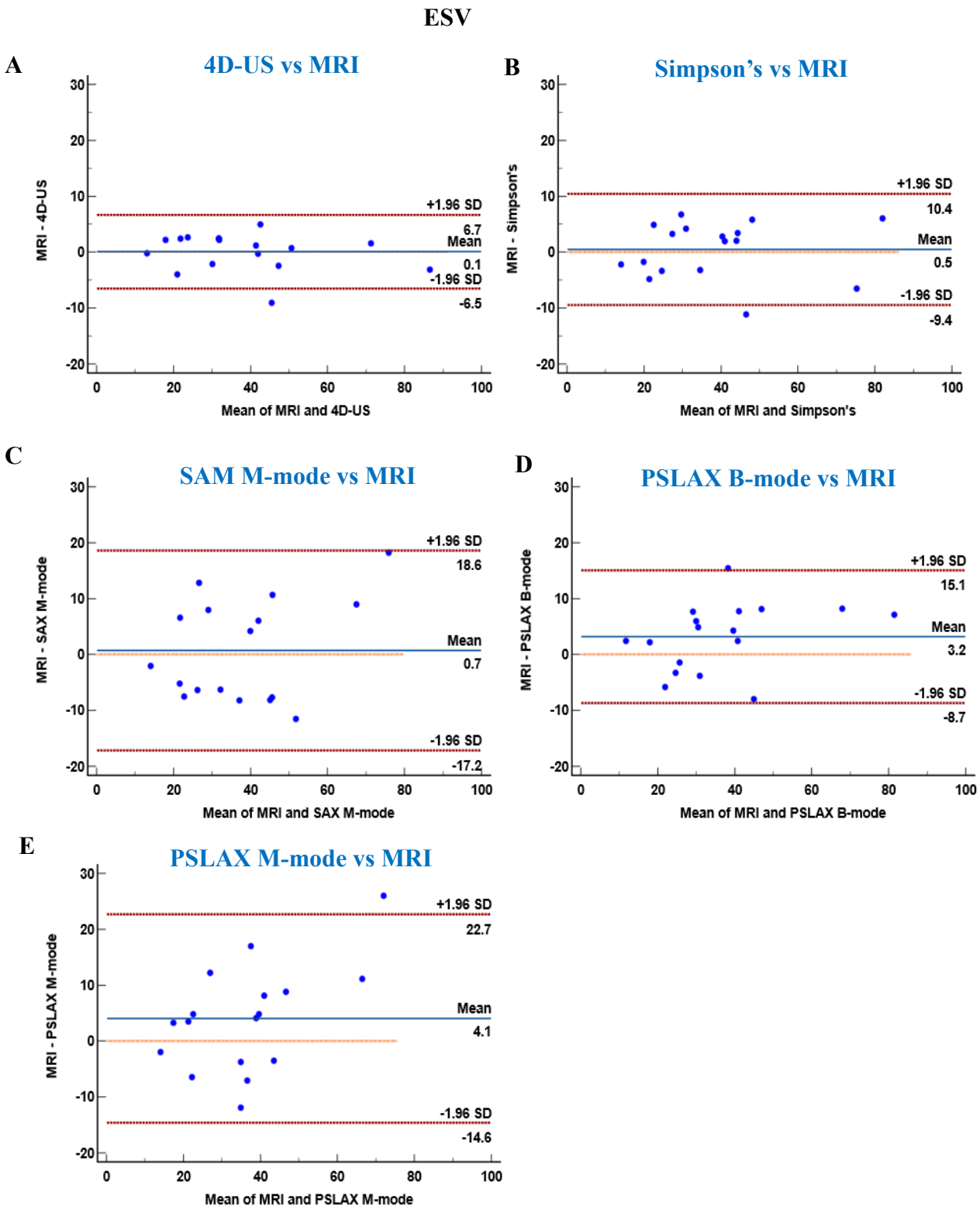

Figure 3-8. Bland–Altman analysis of ESV determined by MRI and 4D-US (A) or Simpson's multi plane (B), SAX M-mode (C), PSLAX B-mode (D) and PSLAX M-mode (E). Each plot displays the differences between the two measurement methods against their mean values. The mean (bias) is represented by the solid blue line, and the mean ± 1.96 SD by the dashed red lines. N=17.

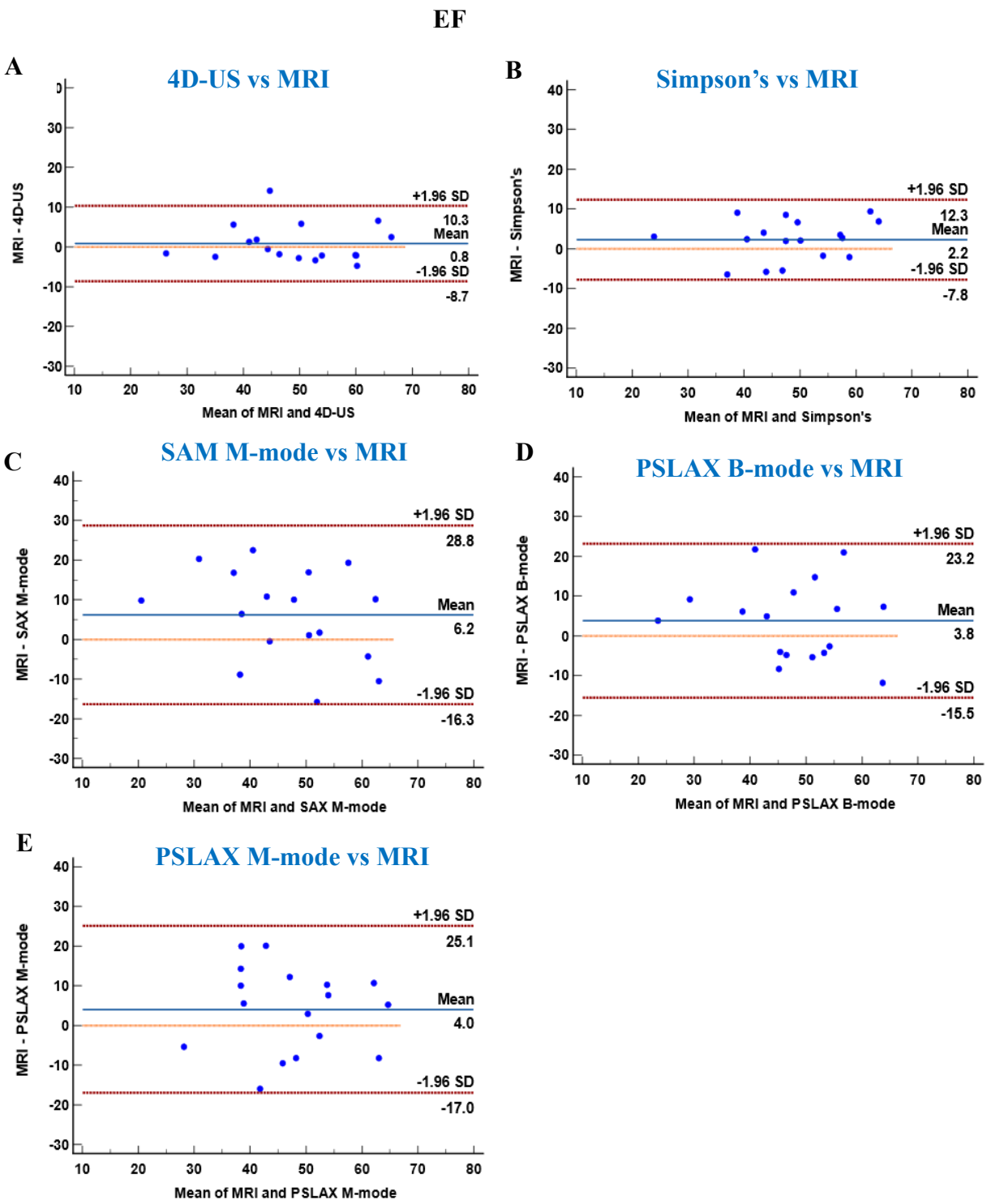

Figure 3-9. Bland–Altman analysis of EF determined by MRI and 4D-US (A) or Simpson's multi plane (B), SAX M-mode (C), PSLAX B-mode (D) and PSLAX M-mode (E). Each plot displays the differences between the two measurement methods against their mean values. The mean (bias) is represented by the solid blue line, and the mean ± 1.96 SD by the dashed red lines. N=17.

3.3.2. Study 2: Global and regional strain analysis in an MI mouse model

6 control mice (received open-chest surgery without LAD ligation) and 17 infarcted mice underwent strain analysis using STE in longitudinal, circumferential, and radial planes after 2 weeks post -MI. Speckle tracking images were acquired in the PSLAX and PSAX views of representative mice from both control and MI cohorts, as shown in Figure 3-10. The motion of the myocardium exhibited remarkable consistency from frame to frame in control mice (Figure 3-10 A, B). Conversely, MI mice displayed varying degrees of myocardial motion with distinct alterations in deformation dynamics across different segments of LV (Figure 3-10 C, D). These findings demonstrate the impact of MI on regional contractile function and deformation within the heart.

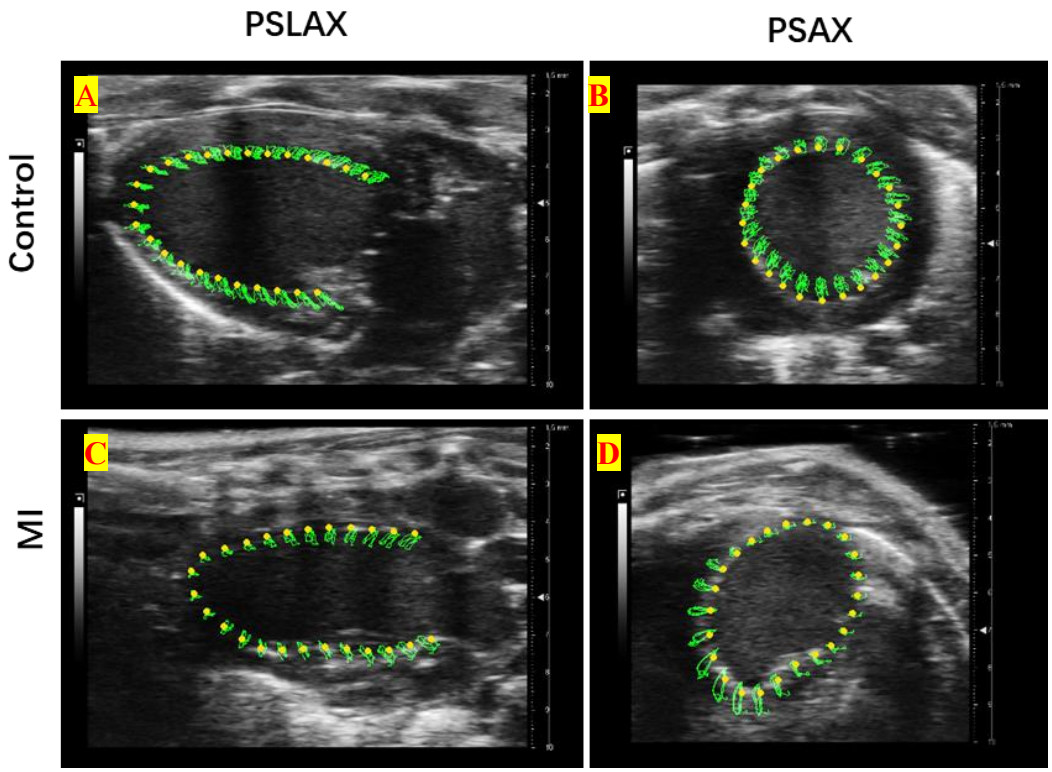

Figure 3-10. STE in control and MI mice in PSLAX and PSAX views. The green lines form patterns that indicate how the myocardium moves. The control mouse exhibited a consistency in cardiac motion, whereas MI mice displayed distinct alterations in cardiac deformation across segments of LV.

The global strain values were significantly lower in the MI group compared to the control group, with a statistical significance of $p < 0.01$. This observation was consistent across multiple planes, including longitudinal, circumferential, and radial

orientations, as depicted in Figure 3-11. The differences in global strain values between control and MI groups indicate impaired cardiac function and altered mechanical properties of the heart following MI.

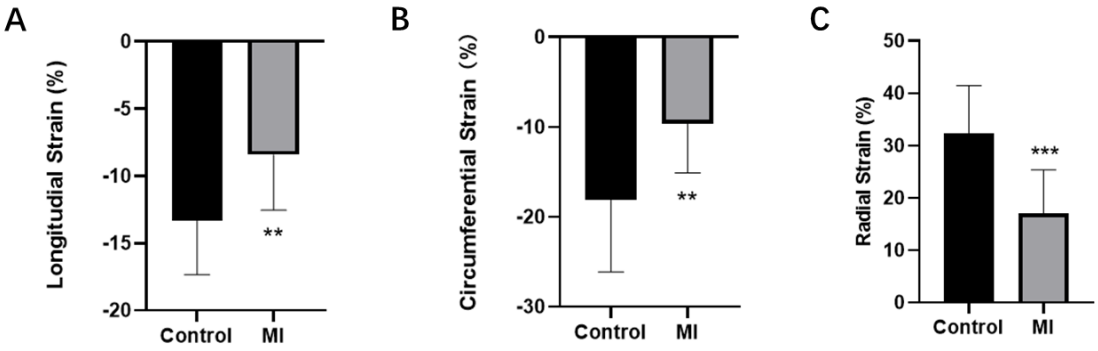

Figure 3-11. Comparison of global strain measurements in control and MI groups. Significant differences in global strain values between control and MI groups in longitudinal (A), circumferential (B) and radial (C) planes. One-way ANOVA followed by Tukey's post-hoc test with Geisser-Greenhouse correction. Control group: n=6; MI group: n=17. *$P < 0.05$; **$P < 0.01$; ***$P < 0.0001$.

For regional strain analysis, strain curves obtained from a representative control and MI mouse were presented in Figure 3-12. The multi-coloured lines depicted the non-coordinated movements of all six segments of the myocardium in longitudinal, circumferential and radial planes, demonstrating the inconsistent mechanical behavior and functional characteristics of the myocardium following MI.

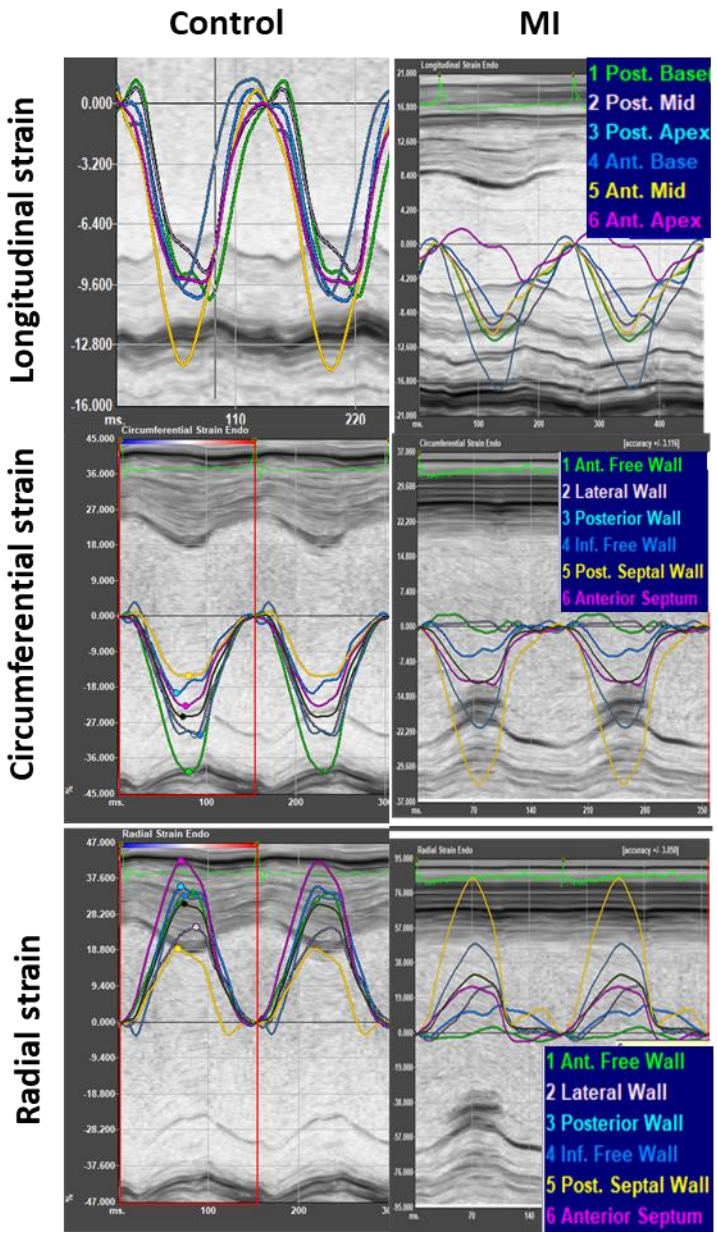

Figure 3-12. Strain curves obtained from a representative control and MI mouse. The lines in various colors indicate the uncoordinated movements of all six segments in longitudinal, circumferential and radial planes in MI mouse.

The RLS analysis revealed a significant decrease in all segments of the MI hearts when compared with the control group, except for the Posterior Mid and Posterior Base segments ($P < 0.001$). This observation indicated the significant impact of MI on cardiac function across multiple regions. Furthermore, it was evident that the RCS and RRS values in the MI group were markedly lower in both the Anterior Free wall and Lateral regions compared to those in the control group (all $P < 0.001$). Notably, additional analysis demonstrated that RRS values in both the Posterior and Inferior

segments were also significantly reduced in MI mice as compared to control mice (Figure 3-13). This further demonstrated the impairment of myocardial contractility following MI, particularly affecting specific areas of the heart.

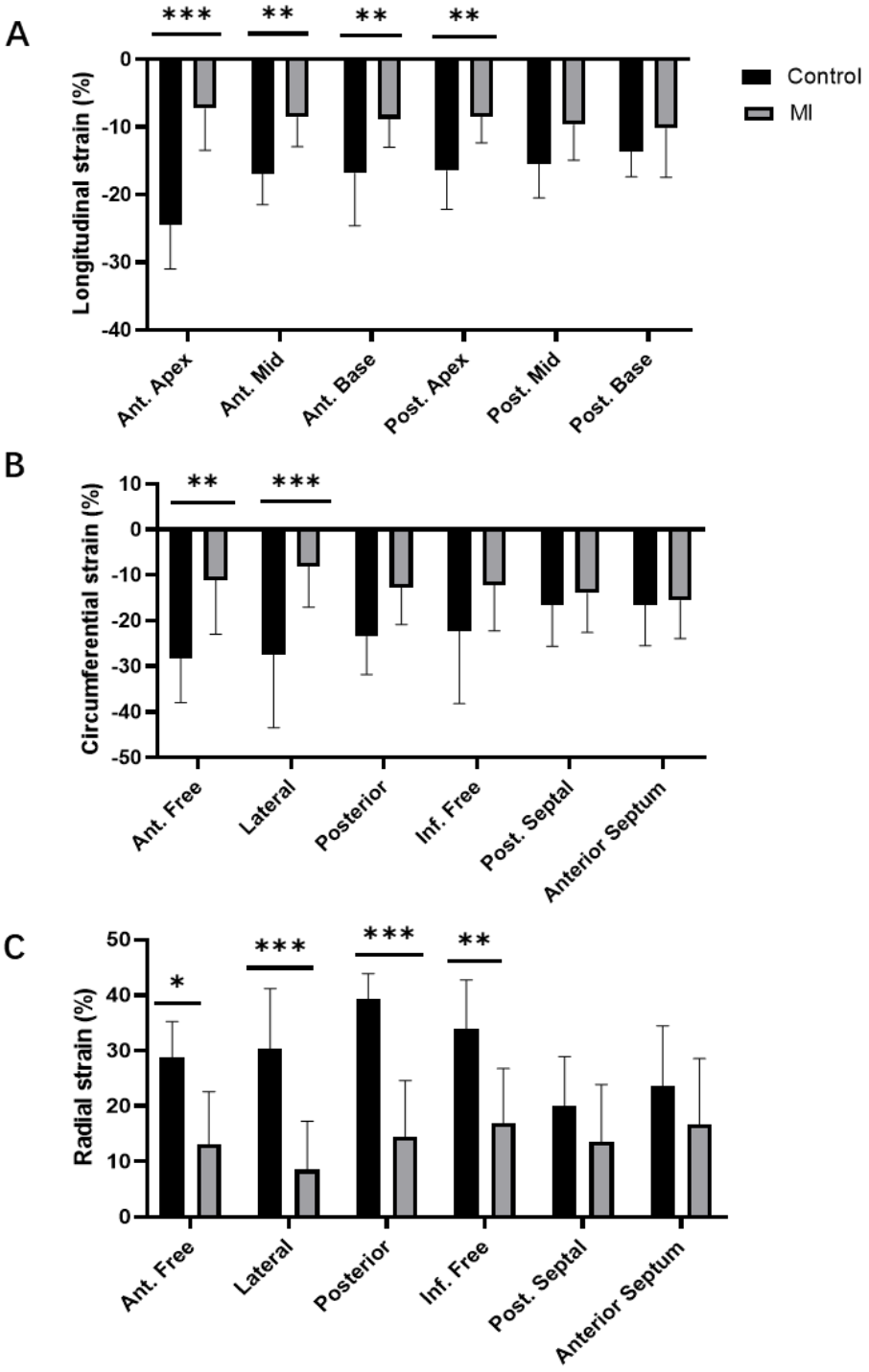

Figure 3-13. Comparison of regional strain measurements in control and MI groups. Significant differences were observed in regional strain between control and MI groups in longitudinal (A), circumferential (B), and radial (C) planes. Ant(B), anterior basal; Ant(M), anterior mid; Ant(A), anterior apical; Post(A), posterior apical; Post(M), posterior mid;

Post(B), posterior basal. One-way ANOVA followed by Tukey's post-hoc test with Geisser-Greenhouse correction. Control group: n=6; MI group: n=17. *$P < 0.05$; **$P < 0.01$; ***$P < 0.0001$.

3.3.3. Study 3: Validation of ATTR-CM mouse model using strain analysis

The 2D ultrasound acquisitions of 7 control mice and 11 ATTR-CM mice were subjected to Simpson's method to assess LV volumes and EF. The analysis revealed no significant differences in EDV (Figure 3-14A), ESV (Figure 3-14B), and EF (Figure 3-14C) between these two groups at both 9- and 12-month post-seeding. The data implies that, when evaluating the cardiac function using the most prevalently utilized ultrasound technique, Simpson's method, no distinct variations of cardiac function were witnessed between the control group and the ATTR-CM group at either time point. This indicates that advanced ultrasound techniques, such as strain analysis, may provide additional insights into the progression of cardiac pathology in this experimental model.

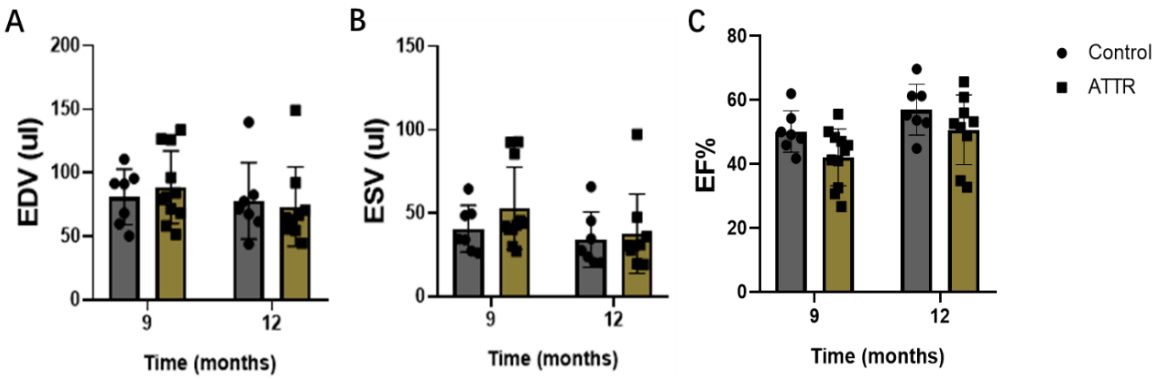

Figure 3-14. Comparison of LV volumes and EF between ATTR-CM and control groups derived from Simpson's measurements. There were no significant differences in EDV (A), ESV (B) and EF (C) between these two groups. EDV, end diastolic volume; ESV, end systolic volume; EF, ejection fraction. One-way ANOVA followed by Tukey's post-hoc test with Geisser-Greenhouse correction. Control group: n=6; ATTR-CM group: n=17.

Global/regional strain analysis was then performed in longitudinal, circumferential, and radial planes at 9- and 12-months post-seeding. The results indicated no significant differences in GLS between the control and ATTR-CM mice at two points (Figure 3-15A). Several clinical reference criteria that are commonly used for the diagnosis of ATTR-CM were used here to evaluate the progression of this disease in the ATTR-CM model. In longitudinal, RELAPS was calculated based on RLS that the average apical strain is divided by the sum of average basal strain and average

midwall strain. Clinically, RELAPS value > 0.87 indicates relatively preserved apical strain compared to basal and midwall strain, presenting as the pattern of 'apical sparing' [358]. At 9 months, significant RELAPS values were observed in four out of eleven mice (36%) in the ATTR-CM group. One ATTR-CM mouse with distinct RELAPS value died during an ultrasound scan at 9 months. By 12 months, three out of ten (30%) ATTR-CM mice exhibited the pattern of 'apical sparing' (Figure 3-15B).

Septal apical to basal longitudinal strain (SAB) is another deformation parameter for diagnosing ATTR-CA clinically, which is the calculation of the septal apical value divided by the basal value. A SAB value greater than 2.1 has been considered significant [359]. Similar to the RELAPS findings, 36% and 30% of mice in the ATTR-CM group exhibited higher SAB values at 9 and 12 months, respectively. However, it is worth mentioning that one control mouse displayed a higher SAB value (>2.1), primarily due to an artifact caused by shadowing on the septal basal region (Figure 3-15C). These data emphasized the potential of RLS analysis in diagnosing cardiac abnormalities associated with ATTR-CM in this experimental model in light of the clinical references. This suggests that not all ATTR-CM mice have exhibited detectable cardiac function alterations despite having confirmed the deposition of TTR via SPECT-CT scan and demonstrates the superiority of strain analysis for cardiac function assessment over LVEF.

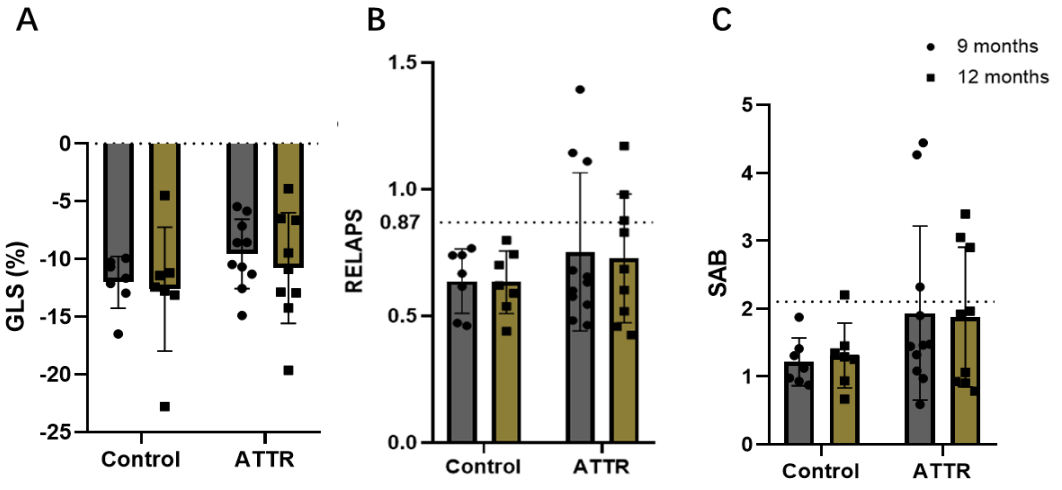

Figure 3-15. Comparison of GLS, RELAPS, and SAB between control and ATTR-CM groups over time. No difference was observed between these two groups in the GLS assessment. 36% and 30% of mice exhibited higher RELAPS values (> 0.87) in the ATTR-CM group at 9 months and 12 months post-seeding, respectively. GLS, global longitudinal strain. RELAPS, relative apical sparing. SAB, septal apical to base longitudinal strain.

In the RLS analysis, speckle-tracking images from the representative mice in the control group revealed a consistent and uniform motion of the myocardium across all segments, indicating normal cardiac function (Figure 3-16A). Conversely, the ATTR-CM mouse exhibited irregular and non-uniform motion patterns (Figure 3-16B). The segmental longitudinal curves demonstrated relatively consistent strains in the control mouse (Figure 3-16C), while the ATTR-CM mouse displayed non-coordinated movements across all six segments of the myocardium (Figure 3-16D).

Further quantitative analysis of segmental strain values showed consistent strain values in control mice (Figure 3-16E). In contrast, reduced strain values were observed in both basal and midwall segments while preserved values were observed in apical segments in ATTR-CM mice (Figure 3-16F). This distinct pattern of strain distribution highlighted by these results pointed to a localized impairment in cardiac function within certain regions of the heart among ARRT-CM mice. This observation has significant implications for understanding the pathophysiology of ATTR-CM and may offer valuable insights into potential targeted therapeutic interventions aimed at addressing region-specific cardiac dysfunction.

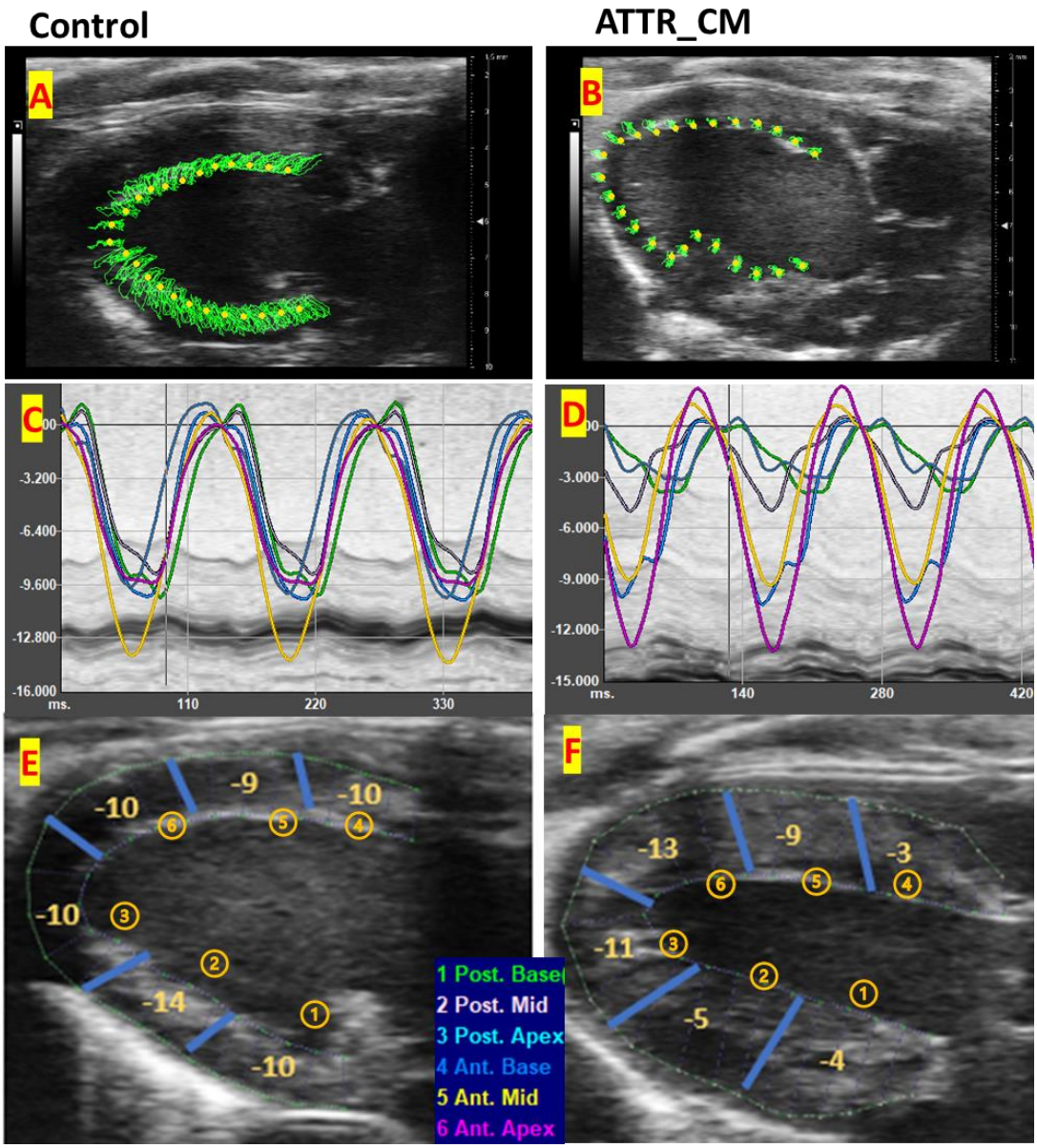

Figure 3-16. Regional longitudinal strain analysis in control and ATTR-CM mice. Speckle tracking images in control (A) and ATTR-CM mice (B) in longitudinal. The longitudinal deformation curve displayed uniform motion of the heart muscle in control mice (C) and the uncoordinated movement of all the segments in ATTR-CM mice (D). Regional strain remained relatively consistent in control mice (E); however, ATTR-CM mice exhibited reduced strain values in both basal and midwall segments while maintaining preserved values in apical segments (F). RLS, regional longitudinal strain.

CS and RS were subsequently assessed from basal, midpapillary, and apical short-axis views to determine their potential as useful diagnostic indicators in ATTR-CM. In previous studies, due to inadequate visualization of both basal and apical views for myocardial segment tracking, researchers analyzed CS and RS from a midpapillary LV short-axis view to maintain sample size [360]. However, given the predominant

signs characterized by reduced basal and midwall strains but preserved apical value observed in LS analysis in ATTR-CM mice, further investigation into strain values in circumferential and radial directions at the basal and apical regions is needed. Ultrasound images were acquired with care by experienced researchers to ensure adequate visualization of the myocardium in basal, midpapillary, and apical planes.

Representative speckle tracking images from both control and ATTR-CM mice were shown in Figure 3-17. In the control mice, consistent circular patterns of speckle tracking lines within the heart chambers across all three levels (basal, midwall, and apical) were observed, indicating uniform myocardial deformation throughout the cardiac cycle (Figure 3-17A, C, E). Conversely, in ATTR-CM mice, irregular patterns were noted in the speckle tracking lines, particularly in the basal and midwall views (Figure 3-17B, D, F). This observation suggests regional variations in myocardial strain distribution within these pathological hearts.

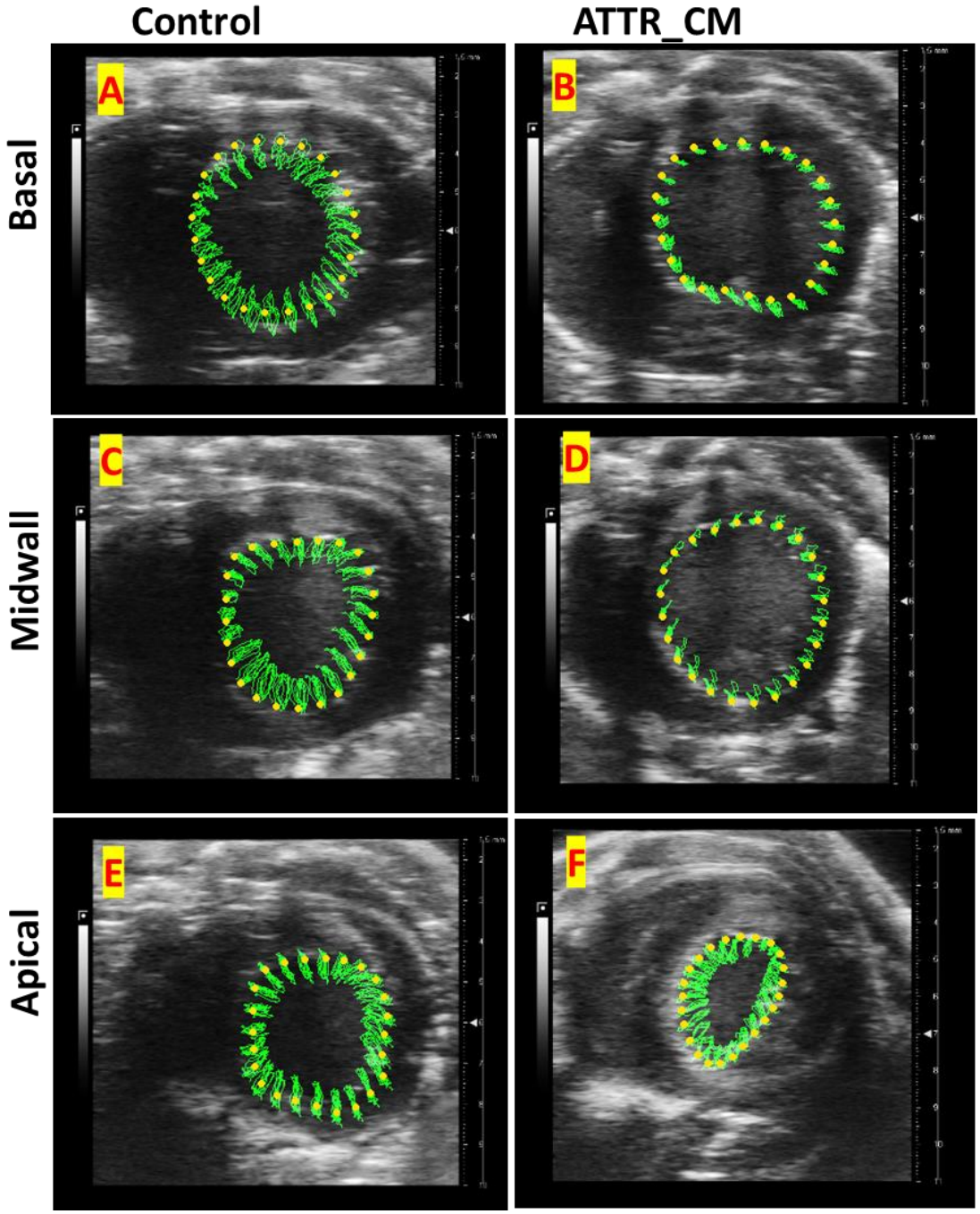

Figure 3-17. STE in control and ATTR-CM mice in PSAX view at basal, midwall and apical planes. Consistent circular patterns of speckle tracking lines at basal (A), midwall (C) and apical (E) planes were observed in control mice, whereas irregular patterns were noted ATTR-CM mice particularly in the basal (B) and midwall (D) planes.

GCS and GRS at the basal, midwall, and apical planes demonstrated no statistically significant differences observed between the control group and the ATTR-CM group over time (Figure 3-18). The lack of significant differences in these measures indicated a consistent pattern of myocardial mechanics in both cohorts globally. These findings prompted further investigation into regional circumferential and radial

strain values at basal, midwall and apical regions to elucidate potential differences between healthy and diseased myocardium.

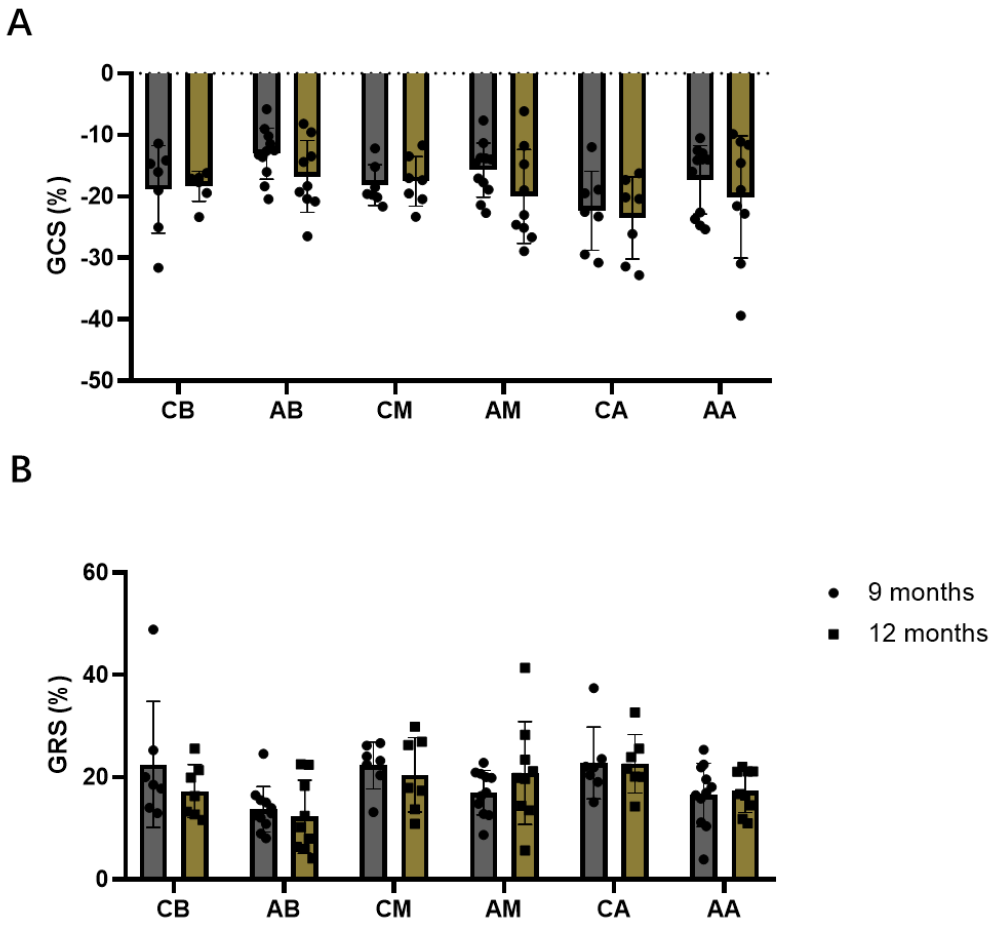

Figure 3-18. GRS and GRS measurements in control and ATTR-CM groups at 9 and 12 months. There were no significant differences between these two groups during these time points. CB, control_basal. AB, ATTR_basal. CM, control_midwall. AM, ATTR_midwall. CA, control_apical. AA, ATTR_apical. GCS, global circumferential strain. GRS, global radial strain.

RCS and RRS were then quantified from basal, midwall and apical planes by automatically dividing the myocardium into six segments. As shown in the circumferential and radial deformation curves (Figure 3-19), a synchronized motion of the myocardium was consistently observed across all three planes in the control mouse. In contrast, an asynchronous movement of all segments was noted in ATTR-CM mice across three planes. This abnormal pattern of myocardial motion suggested a disruption in cardiac function associated with this pathological condition.

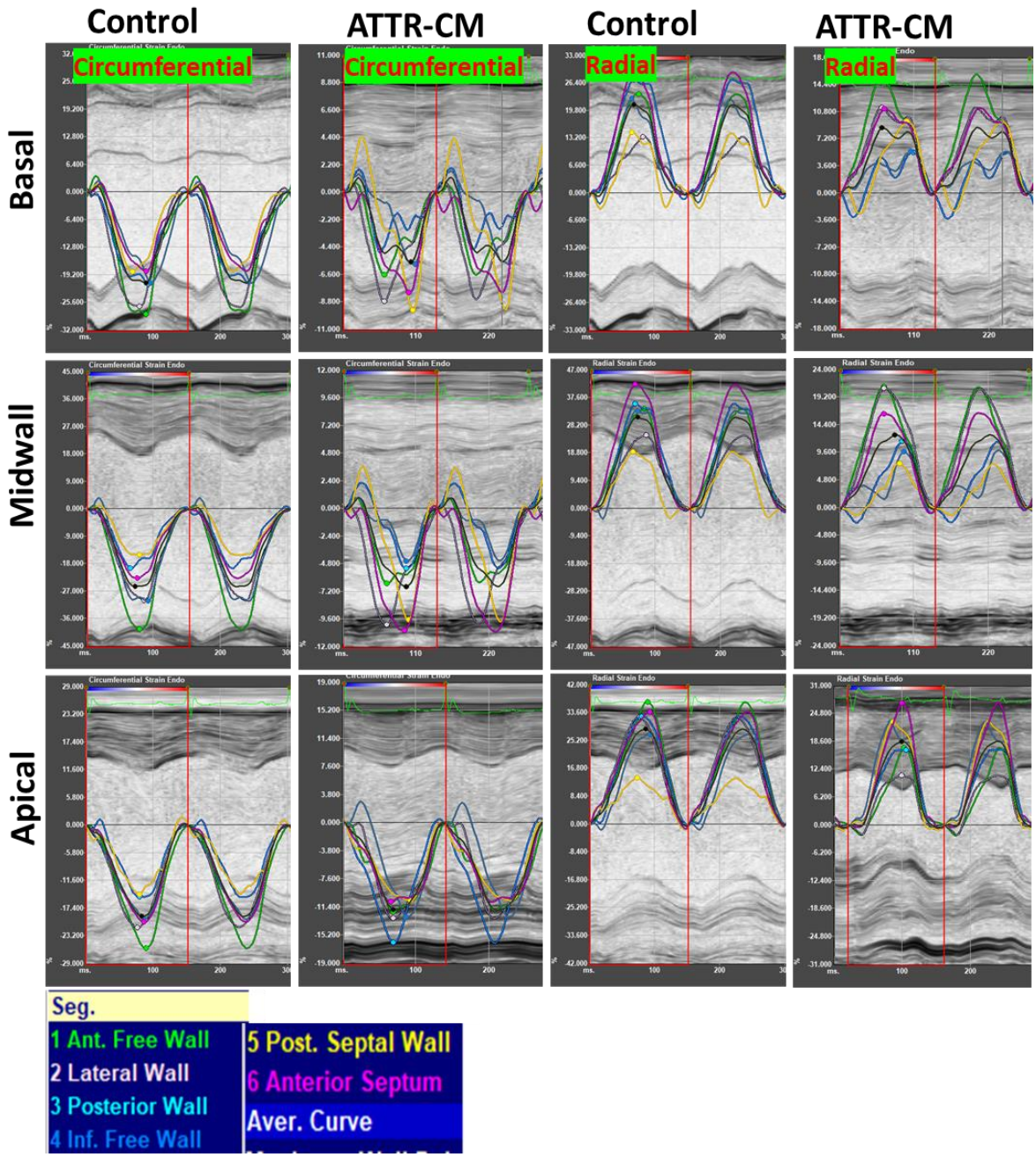

Figure 3-19. The circumferential and radial speckle-tracking deformation curves. These curves displayed uniform motion of the heart muscle in control mice, and the uncoordinated movement of all the segments in ATTR-CM mice in PSAX view at basal, midwall and apical levels.

The 18-segment bull's eye figures were generated based on RCS and RRS values obtained from the basal, midwall, and apical planes from representative mice in control and ATTR-CM groups. These figures provided a comprehensive visualization of the regional differences in cardiac function between the two groups. It was evident that the control mice consistently exhibited RCS values in six segments at the basal, midwall, and apical planes, indicating uniform myocardial performance across these

regions (Figure 3-20A). In contrast, the ATTR-CM mice displayed distinct variations in their RCS values. Specifically, there was a notable difference with respect to 5 out of 6 segments at the basal layer and 2 out of 6 segments (Posterior vs. Inf Free wall) at the midwall when compared to control mice (Figure 3-20B). This observation suggested regional disparities in myocardial function within the hearts of ATTR-CM mice in circumferential. In RRS-derived 18-segment bull's eye figures, 4 out of 6 segments at the basal layer in ATTR-CM mice exhibited lower values compared to those of control mice. However, RRS values at midwall and apical views remained comparable between both groups (Figure 3-20C, D). These findings highlighted specific areas within the heart where the reduced regional strain was particularly pronounced in ATTR-CM mice compared to controls.

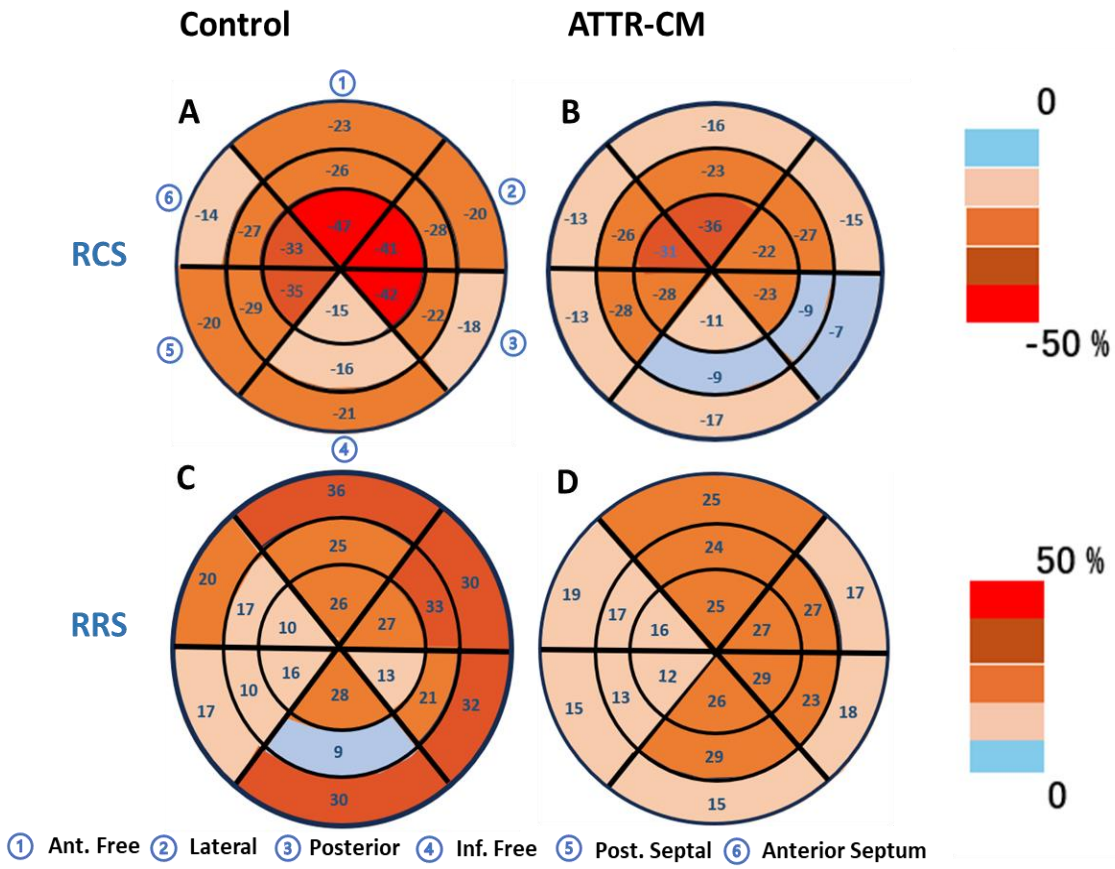

Figure 3-20. 18-segment bull's eye plots depicted RCS and RRS in control and ATTR-CM mice. In the RCS assessment, compared to the control mice, reduced strain values were observed in four out of six basal segments and two out of six midwall segments in ATTR-CM mice (A, B). Regarding RRS analysis, no significant differences were found at the midwall and apical views; however, lower strain values were observed in four out of six segments at the basal layer in ATTR mice (C, D). RCS, regional circumferential strain. RRS, regional radial strain.

3.4. Discussion

3.4.1. Comparison of 4D-US with conventional ultrasound techniques for assessing cardiac function in an MI model

Echocardiography, including M-mode and 2D B-mode, has long been an invaluable imaging modality in clinical and preclinical studies for assessing cardiac function post-MI. However, LV remodeling may compromise the accuracy of these ultrasound techniques due to infarct expansion and regional dilatation after MI. Thus, advances in ultrasound imaging systems now present an opportunity to assess cardiac function more precisely in animal models of heart disease, especially those with irregularly shaped ventricles. The optimal approach for volumetric and EF analysis is to employ real-time volumetric 3D imaging to detect all regions of the ventricular wall and

exhibit greater resilience to changes in heart shape [361]. 4D-US has been developed due to its capability of acquiring 3D images of the heart over time, with time serving as the fourth dimension.

The purpose of this study was to validate the reliability of 4D-US in assessing cardiac function post-MI compared to other conventional ultrasound techniques (Simpson's method, PSAX M-mode, PSLAX B-mode and PSLAX M-mode), using MRI as the standard reference. The findings revealed that 4D-US exhibited the strongest agreement with MRI data for evaluating EDV, ESV and EF, followed by Simpson's method. In contrast, other conventional ultrasound methods demonstrated lower reliability and weaker agreement with MRI assessment.

Several factors contribute to the differences in cardiac function assessment between 4D-US and conventional ultrasound techniques post-MI. Firstly, the conventional ultrasound faces challenges given that abnormal left ventricular geometry and asynchronous wall motion occur post-infarct. In traditional ultrasound methods, the assumption of a spherical heart shape modeled as stacks of elliptical discs is challenged by the progressive post-infarct remodeling observed in mice MI models. This results in limitations on geometric assumptions and inaccurate estimations of LV volumes and EF [362, 363]. Secondly, the number of long- or short-axis slices for data analysis also affects the accuracy of traditional ultrasound compared to 4D-US. The M-mode ultrasound provides a one-dimensional visualization of the heart, capturing the movement of two opposing myocardial walls over time, such as the anteroseptal and the posterior wall, from parasternal perspectives [364]. The Bland-Altman analysis showed that SAX M-mode measurement tended to overestimate EF at low values and underestimate high EF, possibly since the mid-papillary level of the heart may not include akinetic scar tissue or hyperkinetic basal myocardium. Similarly, PSLAX B-mode measured cardiac function by tracing the endocardial border around the LV cavity from a single plane but not detecting the other part of the myocardium. In contrast, Simpson's method involved measurements at three parallel slices in PSAX view, which included the infarct regions. 4D-US multi-slices were acquired in 0.2 mm steps following the transducer movement in the PSAX view, allowing for a more detailed and accurate analysis of cardiac function by dividing the entire heart into numerous slices [362].

Thirdly, the conventional ultrasound is impacted by through-plane motion and is sensitive to transducer alignment, resulting in underestimation or overestimation of the ventricular function. For example, the standard M-mode line placement in the parasternal view does not typically include the infarct area, which is usually located in the mid to apical anterolateral segments with sparing of mid to basal inferior and virtually all septal segments after LAD occlusion in mice. Owing to the orientation of the mouse heart in the chest, M-mode ultrasound scans through the LV via the anteroseptal and inferoposterior segments frequently lead to non-visualization of small anterolateral infarcts on PLSAX views [366]. However, in 4D imaging, the LV parameters were acquired by direct operator-defined edge-tracing from 3D geometries via Vevo 4D imaging software, which was less dependent on the angle of acquisition and imaging windows [329, 365].

The imaging acquisition and analysis time for Simpson's, SAX M-mode, PSLAX B-mode, and PSLAX M-mode were 3 ± 1 min, 2 ± 1 min, 2 ± 1 min, and 2 ± 1 min, respectively. The time consumption for the advanced 4D-US technique (20±5 min) exceeded that of traditional ultrasound methods. In correlation analyses of ultrasound techniques with MRI when assessing EF, 4D-US strongly correlated ($R^2 = 0.82$) and followed by moderate correlation of Simpson's multi-plane with MRI ($R^2 = 0.79$). In agreement analysis, the results demonstrated that 4D-US (Bias: 0.81%) and Simpson's (Bias: 2.25%) had lower percentage bias by Bland-Altman analysis than the other conventional ultrasound modes compared to MRI for the evaluation of EF. Therefore, assessing cardiac volumes and LVEF using 4D-US with minimal geometric assumptions yields results consistent with MRI. The capability of 4D-US to visualize the entire heart renders it particularly advantageous for diagnostic imaging in comparison to conventional ultrasound techniques that only capture a portion of the heart. As such, 4D-US holds promises for detecting wall motion abnormalities or changes in myocardial structures associated with heart disease.

Collectively, this study presents compelling evidence for the utility of 4D-US in the comprehensive noninvasive assessment of functional implications of MI. It revealed a significantly reduced variance in measurements when utilizing advanced 4D-US and Simpson's method, indicating the reliability of both techniques for assessing cardiac function post-MI. However, the advanced 4D-US approach offers additional

advantages. On the other hand, Simpson's multiplane technique is less time-consuming and user-friendly, making it the preferred ultrasound modality for basic cardiac functional evaluation in most research studies.

3.4.2. STE offers a comprehensive global and regional evaluation of myocardial deformation following MI

After MI, ventricular remodeling of the myocardium occurs following ischemic injury, leading to replacement of damaged tissue with permanent fibrotic scars. Excessive and extensive fibrosis results in progressive reduction of cardiac function, alteration of ventricular wall stiffness, and ultimately contribute to the development of HF [367]. Conventional ultrasound techniques such as 1D M-mode and 2D B-mode have been extensively employed in research settings for the assessment of global cardiac function due to their non-invasiveness, widespread availability, cost-effectiveness, and relatively short image acquisition and post-processing times [368]. However, their capabilities are limited in representing regional myocardial function. They lack the sensitivity to capture subtle changes in the heart structure and performance with preserved EF that may manifest early during MI. In this study, an advanced echocardiographic technique employing speckle-tracking based strain analysis was utilized for the noninvasively quantitative assessment of regional myocardial function, providing crucial diagnostic and prognostic insights alongside the global assessment of LVEF and volume measurements.

In the global strain analysis, GLS, GCS and GRS are effective parameters for evaluating global LV functions. In this study, all three parameters showed significant differences between MI and control mice, aligning with Sjøli’s finding. Sjøli's study also highlighted the significant prognostic value of global strain in comparison to LVEF for predicting final infarct size post-thrombolysis, emphasizing the clinical applicability of global strain analysis and its potential in MI regenerative therapies [369]. Diao's research further supported these findings by demonstrating a positive correlation between global strain analysis derived from STE and infarction size quantified by MRI in patients with MI [370]. In a separate study, researchers have validated the utility of GLS for identifying unrecognized MI in patients with preserved LVEF, with a prevalence of 18% in a community cohort of older adults

[371]. These results provide compelling evidence for the reliability and accuracy of global strain analysis as a non-invasive method for evaluating myocardial damage following MI. Nevertheless, advanced STE-derived strain analysis exhibits not only superior sensitivity compared to conventional echocardiography in detecting global alterations in cardiac function but also enables region-specific functional assessments post-MI.

The LV was automatically segmented into six regions when analyzing regional strain values, unveiling an inhomogeneous distribution of regional myocardial strains within the ventricle after MI. RLG values presented a marked decrease in MI mice compared to controls across all three anterior segments and the posterior-apical segment. This may be attributed to reduced myocardial contractility and increased fibrosis in the segments consistent with the infarcted region induced by LAD ligation. However, it is noteworthy that Bauer's study revealed a substantial reduction in RLG values across all six segments compared to baseline, indicating not only diminished myocardial performance within the infarcted regions but also in remote areas from the designated infarct. This broader impairment suggests potential global myocardial stunning and hypoperfusion or ongoing ventricular remodeling post-MI as contributing factors [368]. The difference between these two studies' results may be attributed to the variations in several key aspects, such as the location of infarcts, duration of infarct and infarct size induced by LAD ligation.

In the analysis of RCS, a significant decrease in two segments (Ant. Free and Lateral) in MI mice compared to control mice, indicating a small to moderate infarct size induced by LAD ligation. However, including these two segments, there was also a significant decrease observed in the other two segments (Posterior and Inf. Free) in the RRS analysis. In line with Sun *et al.'s* research findings, a marked reduction in both RCS and RLS was demonstrated within the LAD territory following MI [372]. Nevertheless, Sun also noted that no significant changes in RRS were observed in the adjacent and remote zones over time in this study, which was somewhat inconsistent with my results.

In anatomy, the orientation of myocardial fibers profoundly impacts the application of strain analysis. Myocardial fibers are longitudinally arrayed in the sub-

endocardium and LS assesses sub-endocardial function, and CS can provide information regarding mid-myocardial function and reflects myocardial wall shortening resulting from the inward movement of the overall endocardial circumference. At the same time, RS measures myocardial thickening from the endocardium to the epicardium (transmural) in the radial direction [373]. Clinical trials demonstrated that in the early stage of MI, patients with smaller infarcts and preserved EF exhibited reduced LS and RS, whereas CS remained relatively stable or minimally compromised, given that initially, the function of the midmyocardial and epicardial regions might remain relatively unaffected. In contrast, a more extensive transmural infarction was concomitant with an additional decrease in CS [374]. A study revealed a reduction in RS within the peri-infarct and distal regions subsequent to LAD ligation in a rat MI model, similar to the decrease in the infarct area. This suggests that early and chronic myopathic processes in the peri-infarct and distal areas after MI may be an unrecognized but important factor contributing to adverse LV remodeling and progression following MI [375]. RRS may yield additional insights in detecting subtle changes and monitoring the progression of MI. For example, RS can be used as an indicator to identify transmurality with 70% sensitivity and 71% specificity in the clinic [376]. This could be one possible reason to explain that larger regions of myocardial deformation in the radial direction compared to the circumferential direction in my study.

However, it is worth noting that less reliability of RS was observed compared to LS and CS in the clinic, partially due to the limited imaging acquisition window of ultrasound or poor-quality ultrasound images. Clinical practice has demonstrated intraobserver reproducibility based on LS, CS, and RS analysis. The highest was witnessed with LS (9 ± 13.6 %), followed by CS (13.3 ± 8.3 %), and the lowest was observed in RS (26.3 ± 30.1 %) [377]. In clinics, LR is prevalently recognized as the most frequently employed and highly reliable parameter for the assessment of cardiac function in MI, featuring a sensitivity of 97% and a specificity of 93% [378]. However, additional caution is needed when applying RS in cardiac function assessment. Taken together, the regional strain analysis presented in this study revealed that the measurement of LS, CS, and RS could effectively differentiate between infarcted and non-infarcted myocardium in an MI mouse model, with RS providing additional benefits on condition that the quality of ultrasound images was

ensured.

3.4.3. STE provides comprehensive and robust evidence for validating the ATTR-CM model

In comparison to LVEF, STE for myocardial strain assessment exhibited superior prognostic capability for adverse outcomes, particularly in the early stages of heart disease with EF still preserved. When observed from the apex, there is a clockwise rotation of the LV apex and a counterclockwise rotation of the base. This biomechanical process contributes to amplifying the 15% myocyte shortening into 40% radial LV wall thickening, resulting in a >60% change in LVEF in a normal heart. This functional pattern is commonly observed in hypertrophic and restrictive patterns of cardiomyopathy [379]. Bellavia *et al.* also reported similar findings, that CM strain values are reduced in comparison to those of healthy individuals, even when the EF is completely normal (>60%) [380]. In this study, LVEF demonstrated no significant differences between ATTR-CM mice with control mice. Hence, I conducted a comprehensive evaluation of global and regional LS, CS, and RS to detect cardiac functional impairment and follow disease progression noninvasively in the ATTR-CM model.

The GLS, GCS, and GRS in ATTR-CM mice exhibited no statistically significant differences compared to the control mice. In RLS analysis, the presence of 'apical sparing' is a distinctive clinical feature observed in cardiac amyloidosis where left ventricular LS impairment is more pronounced in basal and mid-segments compared to apical segments [381]. This study has validated that RLS can serve as an effective indicator for distinguishing animal models with and without cardiac dysfunction related to ATTR-CM, utilizing established clinical references such as REPLAS and SAB. Along with confirmation of TTR deposition by DPD scans, a consistent 'apical sparing' pattern was observed in four out of eleven ATTR-CM mice at 9 months and three out of ten ATTR-CM mice at 12 months post-seeding. Hence, RLS-derived REPLAS and SAB analysis represent distinctive, easily identifiable, and specific parameters for predicting cardiac functional impairment in the ATTR-CM model compared to more conventional parameters.

In RCS analysis, the findings demonstrated a reduction in strain values in certain

basal and midwall segments. In contrast, apical strain values remained preserved in ATTR-CM mice, aligning consistently with the RLS outcome. LS reflects the function of longitudinally oriented subendocardial muscle fibers, while CS primarily represents the circumferentially oriented fibers in the mid myocardial wall [382]. In a clinical study, cardiac MRI revealed that the subendocardial myocardium was the initial site of involvement in cardiac amyloidosis, with a predominant impact on longitudinal fibers [383]. In ATTR-CM, misfolded TTR proteins form insoluble fibers, which fill the interstitial spaces within the myocardium, resulting in rigidity and stiffness. The deposition of TTR leads to increased myocardial fibrosis, subsequently affecting the mechanical function of the heart [384]. In cardiac imaging, the myocardium appears hypertrophied and thickened due to TTR deposition, as demonstrated in our ultrasound image (Figure 3-12F). In clinical practice, patients diagnosed with cardiac amyloidosis underwent MRI, and the images showed a doubling of LV wall thickness in basal and mid-segments compared to standard reference ranges. However, the increase in wall thickness at the apex was only 26%. This finding suggested that amyloid deposition at the apex may be relatively lower than at other regions [382]. Additionally, Nakano *et al.* demonstrated that the infiltration of LV myocardial amyloid in ATTR-CM hearts initiated from the basal region and progressed towards the apex, resulting in subsequent thickening of the LV wall [350]. Hence, the results suggest that the reduced myocardial deformation in longitudinal and circumferential directions at basal and midwall segments may be attributed to the increased myocardial fibrosis. Conversely, in the apex, reduced extracellular protein deposition leads to decreased resistance to deformation, resulting in increased myocyte contraction and relatively preserved apical strain.

In a clinical study, patients with ATTR-CM were categorized into two distinct subgroups based on the varying deposition patterns of amyloid: wild-type and mutated. The findings revealed that individuals with wild-type ATTR exhibited lower LV basal and mid-wall RS values, while left ventricular LS did not exhibit significant differences between the two groups. Consequently, it was suggested that RRS might provide additional insights into the distribution of cardiac amyloid protein in the myocardium and could be valuable in evaluating sequential changes in amyloid depositions [385]. In my study, the representative ATTR-CM mouse demonstrated a decreasing trend in basal segments when assessing RS values, while no significant

variance was observed in midwall segments. This finding is somewhat inconsistent with clinical observations. Several possible reasons were considered. Firstly, as shown in Figure 3-E, the RRS assessment of a control mouse revealed lower values than the standard reference for three midwall segments (Inf. Free, Post. Septal, Anterior Septum), which may be attributed to poor image quality; hence, no significant differences were observed between these two mice on this layer. Secondly, at the time point of ultrasound acquisition, TTR deposition appeared to be less pronounced in midwall compared to basal regions in this ATTR-CM mouse. Thirdly, aligning with the phenomenon known as 'apical sparing', it is possible that preserved apical contractility compensates for impaired basal and medial segments within ATTR-CM mice; consequently leading to lesser decreases in strain values within midwall segments [386].

There are certain limitations to STE for strain analysis, especially in circumferential and radial directions. High-quality images are indispensable for accurate quantification. Shadowing artifacts, which are prevalent in ultrasound, especially after surgery, can have a significant impact on the ability to delineate endo/epicardial boundaries, leading to reduced measurement accuracy or rendering analysis unfeasible in certain cases. Studies have shown that the inter-observer variance in the interpretation of ultrasound data ranged from 100% to 43% agreement, with the lowest image quality [387]. Additionally, inherent beat-to-beat variability in contraction can also impact reproducibility and lead to variability in results.

Another limitation of this study is the lack of histological results showing the morphological alterations of the cardiac structure as well as the deposition of TTR in ATTR-CM model. By utilizing techniques such as Congo red staining and immunohistochemistry, further study can effectively identify amyloid deposits within cardiac tissue samples. Electron microscopy can be employed to visualize ultrastructural amyloid fibrils with high resolution and detail. Furthermore, integrating histological findings of amyloid deposits with areas of increased uptake in DPD scans could offer a direct correlation that confirms the presence and extent of amyloid infiltration.

3.5. Conclusion

In this project, advanced 4D-ultrasound has shown promising feasibility for measuring cardiac function in an MI model. In comparison to conventional ultrasound modalities, 4D-ultrasound has demonstrated the highest agreement and correlation with MRI assessment when evaluating EDV, ESV and EF. Furthermore, strain analysis derived from STE has proven effective in differentiating between infarcted and non-infarcted myocardium in an MI mouse model. This capability holds significant promise for evaluating therapeutic effects in future studies focused on regenerative therapies. Besides, STE-derived RLS analysis offers more optimal parameters for assessing adverse cardiac function in the ATTR-CM animal model and can function as a reliable predictor for future investigations on novel treatments. RCS and RRS can provide supplementary information in terms of both diagnosis and prognosis of ATTR-CM given their accessibility across 18 segments when high-quality images are ensured. In summary, this study highlighted the potential of advanced imaging techniques such as 4D-ultrasound and STE-derived strain analysis to significantly impact preclinical research related to cardiac function assessment and therapeutic evaluation.

Chapter 4 Optimization of injectable biomaterial patches for minimal invasive delivery of therapeutic grafts

Graphic abstract

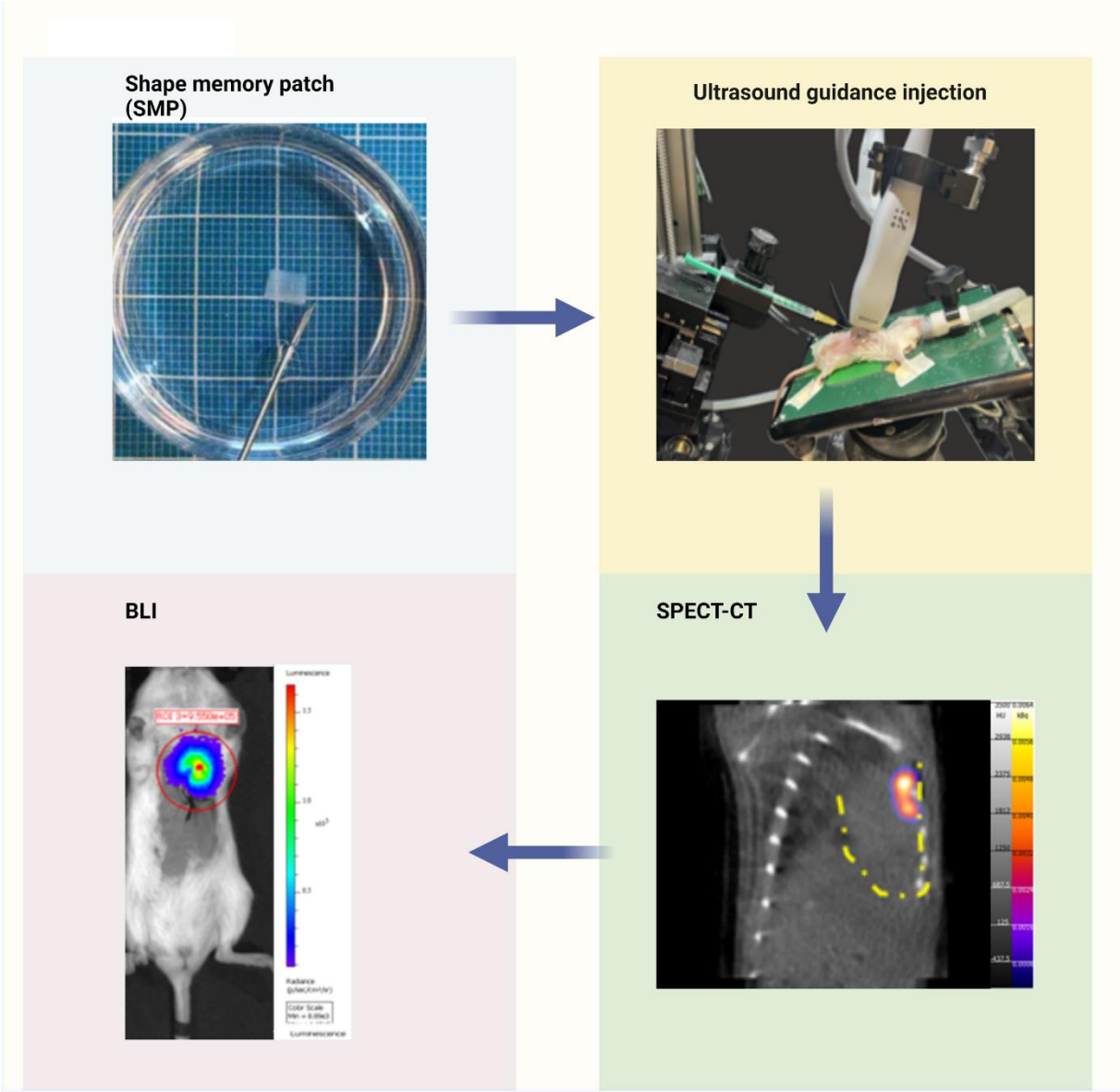

Abstract

Cardiac regenerative therapies can be enhanced through biomaterials that increase on-target retention of therapeutics. Cardiac patches which incorporate pluripotent stem-cell derived cardiomyocytes within a biomaterial are already being surgically grafted onto the myocardium of patients, but this procedure required highly invasive surgery. Here this study undertook preclinical testing of a collapsible shape-memory patch (SMP) which can be injected through a needle before returning to its original shape. This approach could allow minimally- invasive injection of large cardiac patches onto the heart, but validation of delivery success is required before this route can be effectively utilized.

In this study, we loaded SMP with bioluminescent mesenchymal stem cells and the radionuclide ^{111}Indium to allow *in vivo* detection of cell and biomaterial location using BLI and SPECT, respectively. Patches were then surgically implanted or injected closed chest under ultrasound guidance onto the epicardium of mouse hearts. Serial *in vivo* imaging was used to determine successful patch delivery and if the patch remained stably grafted on the epicardium.

BLI and SPECT/CT of mice (n=4) shortly after surgical placement of our first-generation patch demonstrated that the biomaterial and cells were positioned on the epicardium. However, subsequent scans indicated the patch frequently detached from the heart by 24 to 72 hours. This result was confirmed at sacrifice. Patch formulation was modified through a chitosan coating which has previously been shown to offer a tough adhesive to wet surfaces. *In vivo* BLI and SPECT/CT of the human embryonic stem cells (epi-hESCs) loaded second-generation SMP (n=5) showed that cells and patches remained attached to the heart for at least 7 days.

This study demonstrated how multimodal *in vivo* imaging can be used to inform on-graft location and optimize biomaterial formulation for enhanced on-target therapeutic retention. This approach will now allow us evaluation of the efficacy of minimally invasive ultrasound-guided delivery of biomaterial patches to the heart.

4.1 Introduction

After MI, the injured CMs undergo replacement by fibrotic tissue, which contributes to the progression of ventricular dysfunction and ultimately HF. CMs have a low turnover rate estimated at 0.5–1% per year in adult human hearts, and the limited rate of cardiomyogenesis fails to compensate for the significant cell loss after injury [388]. Currently, allogeneic heart transplantation remains the only effective intervention for this condition, but the limited availability of donors poses a significant obstacle. The ability for self-renewal and differentiation into organ-specific cell types makes stem cells promising candidates for replacing cells in tissues with limited intrinsic renewal capacity, particularly the heart [389]. Therefore, novel regenerative therapies, such as stem cell transplantation, have generated significant attention in research.

Over the past two decades, a wide array of stem cell therapies for heart repair have been developed [390]. However, the therapeutic efficacy of stem cell-based treatments remains limited due to inadequate donor cell retention at the target site caused by leakage of cell suspension at the injection site, exposure to ischemic and inflammatory environments, mechanical washout from incessantly beating myocardium, and flushing by the coronary vasculature [391]. The statistics indicate that the acute (< 24 h) cell retention in the heart is typically below 10%, irrespective of cell type, while long-term engraftment of cells is even lower [232]. Most of the cell displacement and death occur within the initial few days post-delivery with a lack of integration into host tissues [391].

Novel biomaterials such as cardiac patches are being developed as a cell delivery construct to overcome issues related to low cell retention and viability to enhance cardiac regenerative therapies [392]. In a clinical case, a cardiac patch incorporating iPSC-CMs was surgically implanted into a patient's heart. Significant improvement in clinical symptoms was observed, with no major adverse events after six months, indicating excellent tolerance of the patch [393]. However, this procedure requires highly invasive surgery that can lead to complications such as hemorrhage, respiratory failure, arrhythmia, or postoperative pain in patients [394]. Thus, it is of great significance to determine a superior approach for delivering these cell-based biomaterials to the patient in a manner that ensures patients' safety, cell viability, and therapeutic efficacy. Currently, intravenous injection (IV) and transendocardial

delivery are two commonly utilized minimally invasive routes for the delivery of therapeutic biomaterials. IV administration reduces potential procedure, cost, and time, but the biological distribution and clearance of the injected material remain important issues. Transendocardial delivery can achieve targeted delivery of stem cells and biomaterials but requires complex procedures and a high-standard 3D electromechanical mapping system [395].

Ultrasound-guided delivery has great potential to enhance clinical applicability due to its minimally invasive nature and ease of operation. Prendiville *et al.* demonstrated that ultrasound-guided transthoracic intracardiac injection can effectively and reliably deliver drugs to specific areas of the myocardium. The technique offers the advantages of avoiding surgical complications, delivering drugs to the myocardium at multiple predetermined time intervals, and enabling rapid post-anesthesia recovery in mice [396]. However, there is a lack of comprehensive studies on the ultrasound-guided delivery of biomaterials, specifically cardiac patches onto the heart for regenerative therapy.

In recent years, an increasing number of intelligent injectable patches have been developed, offering new possibilities for the treatment of heart diseases. The shape memory patch (SMP) exhibits outstanding flexibility due to its mechanical elasticity and shape-memory properties, which can revert to its original shape without compromising cell viability and function [397]. For instance, Dai's group has designed an injectable mesh-like conductive hydrogel patch for the elimination of atrial fibrillation, demonstrating excellent biocompatibility and stability following implantation for one month [398]. In Fan's group, a self-unfolding graphene oxide PVA microneedle patch was designed and fabricated for the treatment of MI through minimally invasive surgery. The patch exhibited a good shape memory effect and rapid shape recovery ability. It effectively promoted neovascularization, attenuated myocardial fibrosis, and restored cardiac function, underscoring its promising prospects for application in MI treatment [399].

In 2019, our collaborators at Professor Molly Stevens' Lab at Imperial College London developed an alginate-derived SMP based on the method originally published by Bencherif *et al.* from David Mooney's lab [397]. The material properties of the

patch indicated its potential for *ex vivo* adhesion to biological tissues and as a cell delivery system for *in vivo* tissue engineering. In collaboration with Sanjay Sinha's Lab at the University of Cambridge, we demonstrated that this SMP effectively maintained cell viability and showed great potential for delivering functional cells to the heart. *In vitro* studies successfully seeded the patches with 20,000 epicardial cells derived from human embryonic stem cells (epi-hESCs) per mm^2, sustaining their viability and proliferation for over 4 days. An *in vivo* study on Balb/C mice confirmed sustained survival of mouse mesenchymal stem cells (mMSCs) loaded in this SMP for more than 8 days when subcutaneously implanted into the dorsal area of the mice [400]. For further study, our lab collaborated with researchers from the University of Cambridge and Imperial College London to conduct preclinical testing of this alginate-based SMP that can be delivered via needle injection under ultrasound guidance onto the pericardium of the heart. This delivery approach holds significant potential for minimally invasive administration of large cardiac patches onto the heart; however, validation of successful delivery is essential prior to practical application.

To validate the ultrasound guidance delivery system and facilitate clinical translation, it is imperative to develop and employ robust imaging and tracking modalities to closely monitor the patches post-implantation *in vivo*. However, the inherent similarity of alginate patches to soft tissue poses a challenge for their visualization within the body using conventional biomedical imaging techniques [245]. Dr. Patrick, a lecturer in our lab, has developed a novel, rapid, and straightforward method for direct cross-linking of alginate with the nuclear imaging radio-metal ^{111}Indium chloride ($^{111}InCl_3$). This enables SPECT-CT imaging for non-invasive assessment of alginate-based graft stability, localization, and interactions between biomaterials and tissues [245]. SMP will then function as a vehicle for loading and transplanting stem cells to the heart. Subsequently, tracking and monitoring the location and viability of transplanted cells becomes the primary focus, with highly sensitive *in vivo* imaging technology playing an important role. BLI has become a prevalent method for evaluating survival and proliferation, as well as monitoring the localization of transplanted cells over time in various research studies owing to its exceptional sensitivity, relative user-friendly nature, and cost-effectiveness of instrumentation [401, 402].

The successful clinical application of the cardiac patch for regenerative therapy hinges on several critical factors, one of which is the secure adhesion of the patch to the myocardial surface. In previous studies, suturing or adhesive glue was utilized for affixing patches to the heart. However, suturing may lead to additional damage, bleeding, and inflammation in the heart, especially given the thinner myocardium of the LV and its increased susceptibility to rupture during the acute stage of MI [403]. While fibrin glue may create an undesirable gap between the heart and patch, potentially impeding cell migration [404]. Therefore, alternative strategies must be developed to address these limitations and enhance the adherence of patches in living organisms. Chitosan, a biopolymer derived from chitin, has gained significant attention as a promising natural adhesive candidate owing to its unique properties. The presence of NH_2 groups in Chitosan molecules facilitates enhanced ionic interactions with negatively charged adhesives, making it an ideal choice for applications requiring strong bonding on wet surfaces. This characteristic is particularly crucial in biomedical and tissue engineering fields, where the ability to form covalent bonds with negatively charged tissue and cell surfaces is essential [405].

1.2. Aims

The aim of this study was to develop a collapsible SMP that can unfold and attach to the heart after ultrasound-guided injection, preserving cell viability and delivering functional cells effectively. SPECT-CT and BLI techniques were employed for real-time monitoring and tracking of the cardiac patch as well as transplanted stem cells, respectively.

This project consists of three studies:

Study 1: Testing the minimally invasive injection of SMP via ultrasound-guided administration. In this study, the alginate SMP was radiolabeled with $^{111}InCl_3$ by direct cross-linking and delivered to the hearts of Balb/C mice, followed by SPECT-CT scans conducted over a 4-day period for patch localization.

Study 2: Modifying the formulation of the alginate SMP to improve its attachment to the heart, including alginate patch combined with bio-adhesive surgical mesh (1st generation with surgical mesh) and alginate patch with chitosan coating (2nd generation). Surgical implantation was applied to test the attachment of SMPs.

Study 3: Evaluating the efficiency of 2nd generation SMP for delivering and preserving stem cells *in vivo*. Two cohorts of mice were implanted with $^{111}InCl_3$ labelled 2nd generation SMP seeded with luciferase-expressing mMSCs or epi-hESCs, followed by BLI and SPECT-CT to evaluate cell viability and patch localization.

4.3 Methodology

4.3.1 Cryogelation to create shape memory patch

SMPs were synthesized by Daniel Hachim from the Stevens Group, Imperial College London. For the 1st generation of SMPs, the cryo-gelation method was employed for the cross-linking of methacrylate alginate patches through free radical polymerization, according to Bencherif *et al.* [397]. Basically, to prepare alginate for cryogelation, methacryloyl groups were added to the main chains to create methacrylated (MA)-alginate. Macroporous 3D alginate cryogels were then formed through cryogelation at −20 °C using a free-radical cross-linking mechanism. During this process, most of the solvent (water) freezes, concentrating the dissolved solutes in small semi-frozen regions called nonfrozen liquid microphase. Free-radical cryopolymerization and gelation occur in these regions over time. After complete polymerization and subsequent incubation at room temperature with water washing to remove unreacted precursors, the ice crystals melt, formatting large, interconnected pores (Figure 4-1). For the 2nd generation SMP, the patches were incubated in 1% chitosan for 24 hours to facilitate tough adhesion to wet surfaces, according to Li *et al.* [406].

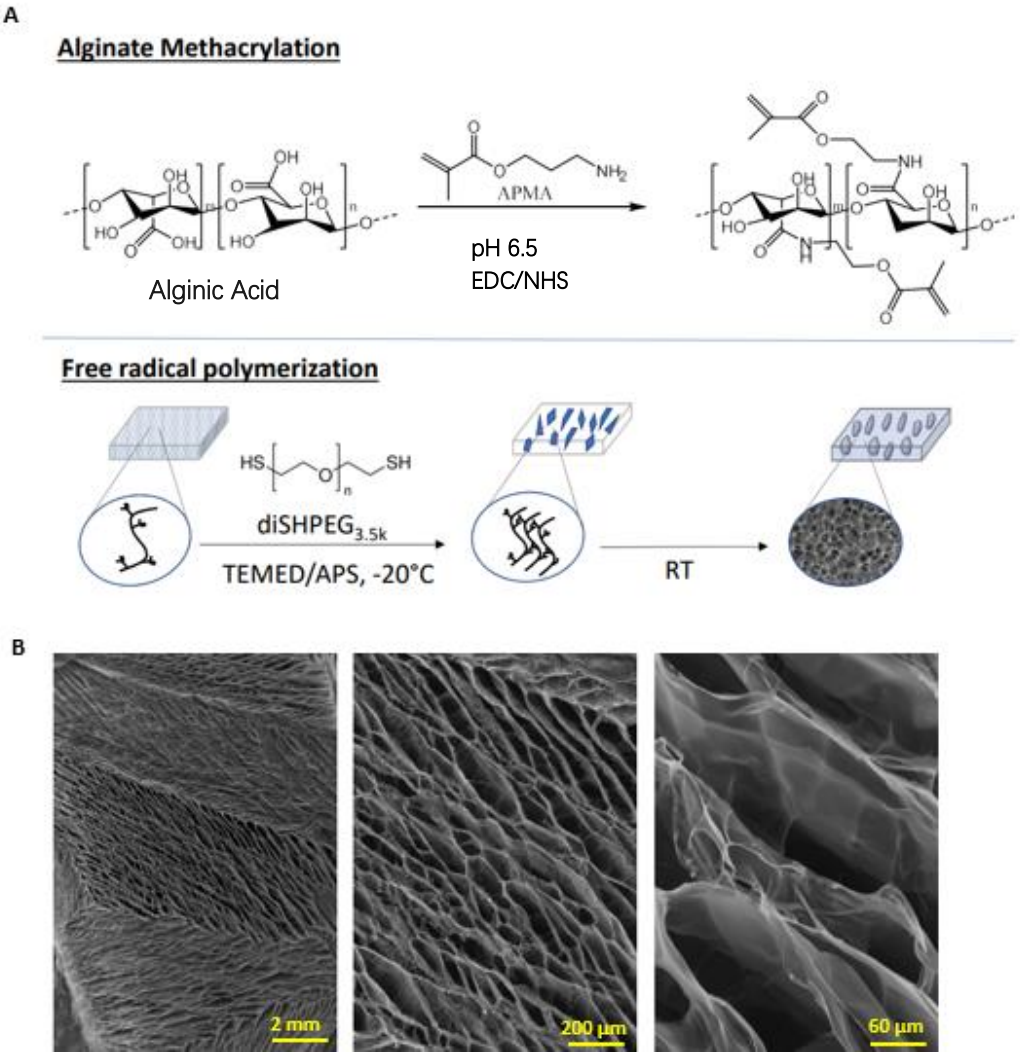

Figure 4-1. Shape-memory alginate cardiac patches synthesized via cryogelation process. (A) Process of alginate methacrylation and cryogelation. (B) Images of patch pore size.

4.3.2 Radiolabeling of shape memory patches with $^{111}InCl_3$

$^{111}InCl_3$ was obtained from Curium Pharma, University College of London Hospital (UCLH). Dry alginate SMPs were incubated with 5 MBq of $^{111}InCl_3$ for 10 minutes to facilitate cross-linking. Subsequently, they underwent three rounds of incubation in distilled water for 30 minutes each to remove unbound metal salts, as described by Patrick *et al.* [245]. The binding and retention of $^{111}InCl_3$ by 1st generation SMPs were assessed through dialysis against various solutions, including saline (0.9% w/v), HEPES, and DTPA as a negative control. A volume of 30 µl of each buffer was combined with 5 µl of $^{111}InCl_3$ (5MBq), and the mixture was applied onto alginate patches (size: 4x4 mm). The patches were then left to dry on the bench guard for 90

minutes for radioactivity detection by a dose calibrator. Following a similar procedure, the retention of $^{111}InCl_3$ by both 1st and 2nd generation SMPs was compared using two different washing solutions: saline and PBS.

4.3.3 Ultrasound guidance injection

Vevo 3100 ultrasound imaging systems (FUJIFILM VisualSonics, Toronto, Canada) with VisualSonic MX550S linear array transducer was used for all image acquisition. Adult female Balb/C mice weighing 20-25 g were used for ultrasound-guided injection of SMPs. Mice were anesthetized using a 2% isoflurane and oxygen mixture delivered by a nose cone. The hair was removed, and animals were maintained at 37 °C via a heating pad. Mice were placed on the operation pad in a supine position. The ECG and heart rate were monitored via surface ECG limb electrodes. The heart rate was maintained between 400 and 500 bpm during imaging by adjusting isoflurane concentration. The base-to-apex axis was parallel to the transducer. A baseline cardiac assessment was performed before starting the injection protocol to ensure optimal transducer position. Carefully advance the needle through the mouse's chest wall while closely monitoring the position of the beveled needle tip. Stop advancing when the needle tip approaches the target epicardium. Once the tip is in the desired place, push the syringe plunger to deliver the SMPs (3x3 mm). Withdraw the needle promptly after administration. Maintain the mouse under anesthesia for several minutes to verify preserved ventricular function and absence of complications during echocardiographic assessment (Figure 4-2).

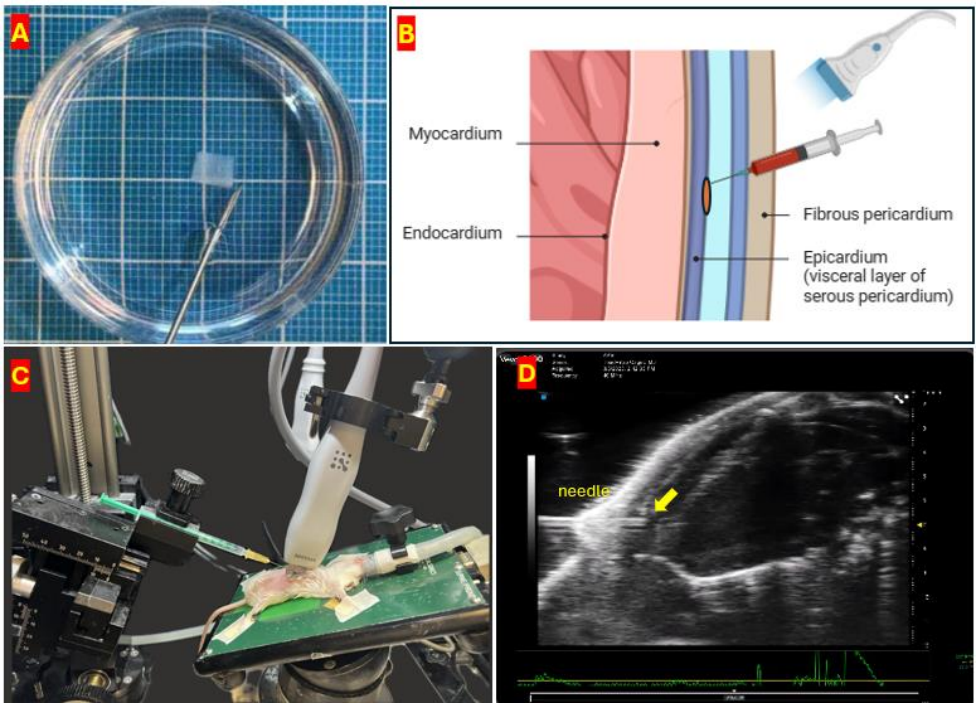

Figure 4-2. Ultrasound guidance injection of SMP. (A) A SMP pre-injection. (B) Schematic diagram of ultrasound-guided epicardial injection. (C) Setup for ultrasound-guided injection and animal preparation. (D) Representative ultrasound image in the parasternal long-axis plane for guidance during injection. The yellow arrow indicates the proximity of the needle tip to the target epicardium. Created with Biorender.

4.3.4 *In vivo* SPECT-CT scan

The mice were anesthetized with a 2% isoflurane and oxygen mixture during SPECT/CT scanning using a Nano SPECT/CT preclinical animal scanner (Mediso, Hungary). The body temperature was maintained at 37 °C using a heated bed, and breathing was monitored with a breathing pad. CT images were acquired in helical scan mode using a 55 kVp X-ray source, with an acquisition time of 3:45 minutes. SPECT images were acquired in helical mode with a scan time of 30 minutes. CT images were automatically reconstructed in voxel size 124 x 124 x 124 μm via Nucline software (Mediso, Hungary), and SPECT images were reconstructed in a 256 × 256 matrix using HiSPECT (Scivis GmbH, Bioscan) reconstruction software package. Images were fused using VivoQuant software (Bioscan, France). For *in vivo* activity analysis, 3D ROIs were manually delineated around the SMPs, kidneys and bladder with anatomical reference from CT data using VivoQuant software (Invicro).

4.3.5 Luciferase-expressing stem cells seeding and bioluminescent imaging

In vitro, luciferase-expressing mMSCs were cultured on seven 2nd generation SMPs at a density of $5x10^5$ cells overnight. BLI was employed to evaluate cell viability on days 0, 1, and 3 *in vitro* using an IVIS SPECTRUM (Perkin Elmer) optical imaging system. 10 µl of luciferin was added to mMSCs-loaded 2nd generation SMPs. These seven SMPs were imaged 20 minutes after luciferin was applied. Small binning, variable exposure, and F/stop adjustments were selected to prevent saturation. A grey-scale reference image was obtained under low-light conditions. Regions of interest (ROIs) were identified on the bioluminescent images, and radiance (photons) was measured using a data-acquisition PC running LivingImage software (Perkin Elmer).

Epi-hESCs were generated by Laure Gambardella from the Singha Lab, University of Cambridge, using their established protocol [407]. These cells were transfected with a lentivirus constitutively expressing firefly luciferase. A pro-survival cocktail was used to suspend the cells before seeding, which consisted of Matrigel 10% v/v, ZVAD-FMK 100mM, Pinacidil 1.25 ng/ml, IGF-1 100 ug/ml 50 ul x2 and Bcl-XL (TAT-BH4). 10 µl of media containing $2x10^5$ epi-hESC were cultured on 2nd generation SMPs (4x4 mm) for 24 hours before implantation.

For *in vivo* studies, 4 x 10^5 mMSCs were added to 2nd generation SMPs (4x4 mm), allowed to attach for 24 hours and then 2 MBq $^{111}InCl_3$ was added to radiolabel the SMPs. These SMPs were then surgically implanted into 5 Balb/C mice. When epi-hESCs were seeded on 2nd generation SMPs, dry SMPs were first loaded with $^{111}InCl_3$, then partially dried and loaded with 2 x 10^5 epi-hESCs to increase both binding of the radiotracer and cell viability. These SMPs were then surgically implanted into 5 immunocompromised NSG mice. *In vivo* BLI was performed on days 0, 1, 3 and 7. Mice received an intraperitoneal injection of luciferin at a dose of 150 mg/kg after being anesthetized with a 2% isoflurane and oxygen mixture for imaging.

4.3.6 Surgical implantation of SMPs

To conduct surgical implantation of SMPs, a similar procedure described in Chapter 2 was performed. Briefly, the animals were anesthetized with a 2% isoflurane and oxygen mixture. The animals were intubated with a 21-gauge catheter, and respiration

was maintained at 120 breaths/min with a tidal volume of 200 µl. Thoracotomy was performed by making a 1 cm longitudinal incision approximately 2 mm away from the left midclavicular line using surgical scissors. After dissection of muscle and ribs, four metal chest retractors were inserted to spread and maintain the operating window to approximately 8–10 mm in width, and a clear view of the heart including of the left auricle should be achieved. After allowing a few seconds for the heart surface to dry, SMP (3x3 mm) was carefully picked up using fine tweezers and placed onto the heart (Figure 4-3A). For the 1st generation SMP with surgical mesh, the mesh was amended to 4 x 6 mm to cover the 1st generation SMP (Figure 4-3B). 2nd generation SMP was delivered in a manner similar to 1st generation SMP (Figure 4-3C). Close observation was conducted for 5 minutes after implantation before closing the chest. Then the isoflurane administration was discontinued while maintaining O_2 until the mouse had fully recovered. Once a normal breathing pattern was observed, the endotracheal intubation was slowly removed. The animals were then kept in a heating chamber to ensure full recovery.

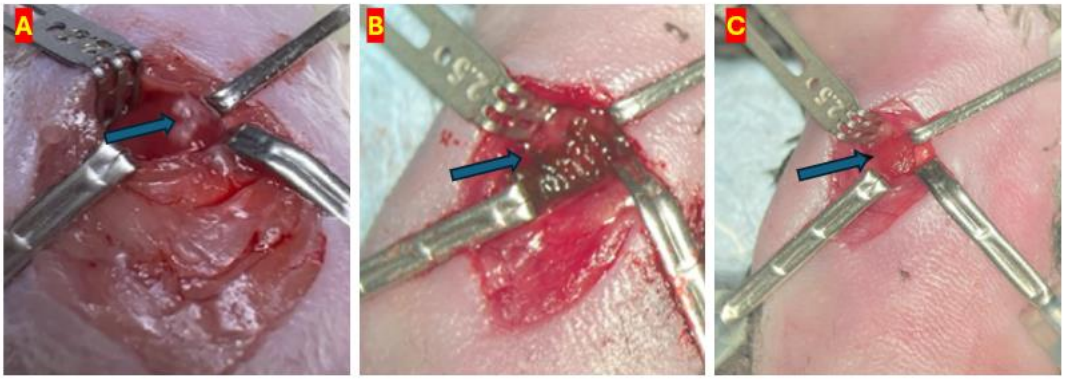

Figure 4-3. Surgical implantation of SMPs. (A) 1st generation SMP. (B) 1st generation SMP covered with surgical mesh. (C) 2nd generation SMP. Blue arrows indicate the locations of SMPs.

4.3.7 Autoradiography

After 7 days post-patch implantation, the animals were sacrificed, and autoradiography was performed following the protocol described by Patrick *et al.,* 2020 [245]. Briefly, the blood was flushed out with 5 ml PBS and the hearts were excised, flash frozen, and cropped into 1 mm thin sections along the short axis. The heart sections were then mounted on microscope slides, photographed, and exposed to GP 20 × 25 cm^2 phosphor screens for 2 h (VWR international LTD, U.K.). After

that, the screens were scanned by a Typhoon 9410 Trio + Phosphorimager (GE Healthcare, U.K). The images were processed and analyzed by ImageJ (NIH, USA).

4.3.8 Statistical analysis

Data is presented as mean and standard deviation (±SD). For all statistical tests, $p \leq 0.05$ was considered significant. Analysis of statistical significance for two or more groups was performed using a one-way ANOVA followed by Tukey's post-hoc test with Geisser-Greenhouse correction applied.

4.3.9 Contributions

This complex and multidisciplinary project involved several researchers across different universities. Cardiac patches were synthesized within Prof. Stevens' group at Imperial. Cell culture, patch seeding and radiolabeling were performed by colleagues at UCL and Prof. Sinha's group at Cambridge. My contributions were as follows.

- Ultrasound and surgical implantation of patches + animal welfare
- Ultrasound imaging of cardiac function
- SPECT/CT imaging of patch location
- Analysis of SPECT/CT data and interpretation of data
- BLI and analysis
- Animal dissection, *ex vivo* imaging and tissue collections

4.4 Results

Ultrasound injections are challenging and require extensive validation to ensure cells/biomaterials are being injected accurately. Our group has previously used radiolabeling of alginate hydrogels to optimize the on-target delivery of hydrogels by encapsulating MSCs to mouse hearts. In our previous study, alginate gels, patches and beads can be crosslinked using a mixture of $CaCl_2$ and picomolar quantities of $^{111}InCl_3$ to allow detection using SPECT/CT. It is important to state that the stability of this labelling process is not high. However, the high sensitivity of SPECT allows for serial tracking of labelled alginates over several weeks *in vivo*, with $^{111}InCl_3$ lost from the patch rapidly cleared via the kidneys through well-characterized

mechanisms. We showed here that the performed SMPs could be labelled $^{111}InCl_3$, and after washing free indium, the radioactivity of the patches remained detectable for at least 7 days *in vitro*. Patch injecting through ultrasound guidance adds extra complexity as the patch needs to be carefully loaded into the bore of the needle, and a sufficient volume of liquid needs to be administered with the patch to force it out of the needle and allow it to deploy in situ. Radiolabeling allowed a gamma counter to be used to rapidly determine whether the patch had been expelled from the needle or remained in the bore, in which case a repeat injection could be immediately undertaken.

1.2.1. Retention of $^{111}InCl_3$ on 1st generation SMP after dialysis using saline, HEPES, and DTPA

First-generation SMPs were labeled with 5 µl of $^{111}InCl_3$ (5 MBq) mixed with 30 µl of saline, HEPES or DTPA to determine the optimal buffer for enhanced retention of radioactivity. Three groups of 1st generation SMPs (n=3) were assessed for radioactivity levels after drying on the bench guard for 90 minutes (initial) and at 1- and 2-hours post-labeling. The initial radioactivity was measured as 2.63 ± 0.07 MBq in the saline group, 2.67 ± 0.01 MBq in the HEPES group, and 2.70 ± 0 .02 MBq in the DTPA group. As depicted in Figure 4-4, the saline group exhibited a significantly higher percentage of radioactivity retention on the 1st generation SMP at both 1- and 2 hours post-labeling. Therefore, alginate SMP dialyzed against saline exhibited enhanced binding and retention of $^{111}InCl_3$ over HEPES and DTPA, with a retention of 53.42% ± 5.97 SD at 2 hours post-labeling.

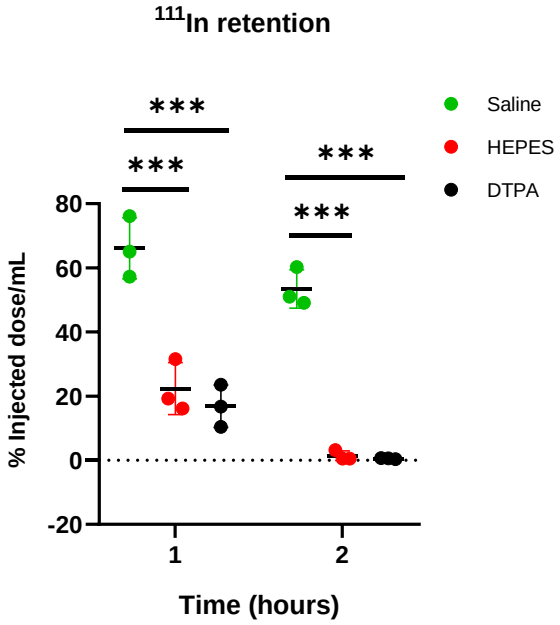

Figure 4-4. Retention of $^{111}InCl_3$ after dialysis using saline, HEPES and DTPA. Alginate SMP dialyzed against saline exhibited significant higher retention of $^{111}InCl_3$ than HEPES and DTPA. *$P < 0.05$; **$P < 0.01$; ***$P < 0.001$. n=3.

4.4.2 Comparison of retention of $^{111}InCl_3$ on 1st and 2nd generation SMPs after dialysis using saline and PBS

2nd generation of SMP was synthesized with a 1% chitosan-coated alginate for 24 hours. A mixture of 10 µl saline or PBS and 5 µl of $^{111}InCl_3$ (5 MBq) was used to label the first and second generations of SMPs (n=3). The radioactivity was measured at 2-, 6- and 24 hours post-labelling. As depicted in Figures 4-5, 2nd generation SMP dialyzed against PBS exhibited enhanced binding and retention of $^{111}InCl_3$ over saline or the first-generation groups, with a retention of 31.37% ± 5.53 SD, 16.98% ± 4.34 SD and 12.97% ± 3.53 SD at 2-, 6- and 24-hours post-labeling, respectively.

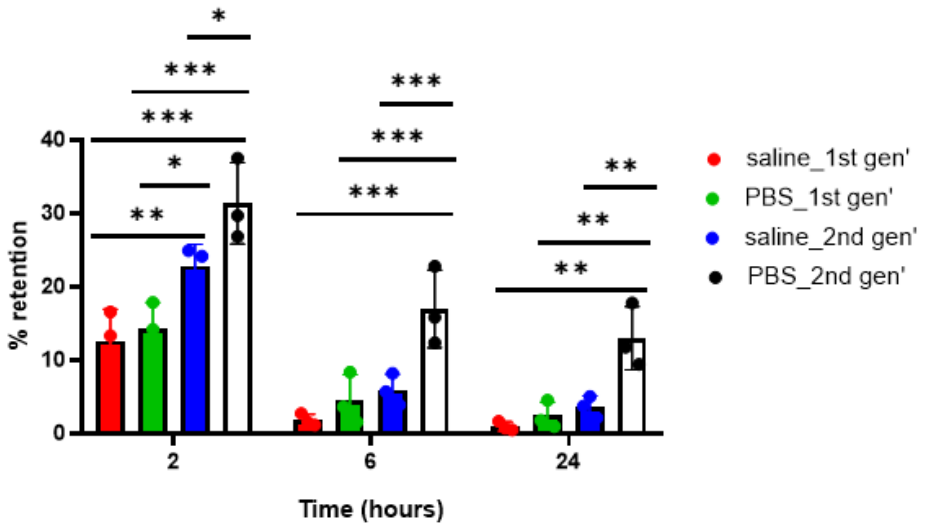

Figure 4-5. Comparison of percentage of retention of $^{111}InCl_3$ on 1st and 2nd generation SMPs after dialysis using saline and PBS. PBS washed 2nd generation SMP displayed significant higher retention of $^{111}InCl_3$ over time. *$P < 0.05$; **$P < 0.01$; ***$P < 0.001$. n=3.

4.4.3 Testing the minimally invasive injection of SMPs via ultrasound-guided administration

Following ultrasound-guided injection of 1st generation SMP to the anterior wall of a cohort of four animals, SPECT-CT imaging was conducted at day 0 (1-hour post-injection), 1, and 4. The initial scan revealed the absence of signals in two mice (mice 1 & 4), while the remaining two exhibited radiotracer signals localized to their cardiac surface (mice 2 & 3), with only one mouse displaying a signal on the anterior wall (mouse 2) (Figure 4-6). Subsequent SPECT-CT scans were conducted on mice 2 and 3 on day 1 and day 4. As illustrated in Figure 4-7, the SMP had detached from the heart between day 1 and day 4 in mouse 3, while consistent signals within the same region were observed in mouse 2 from day 1 to day 4.

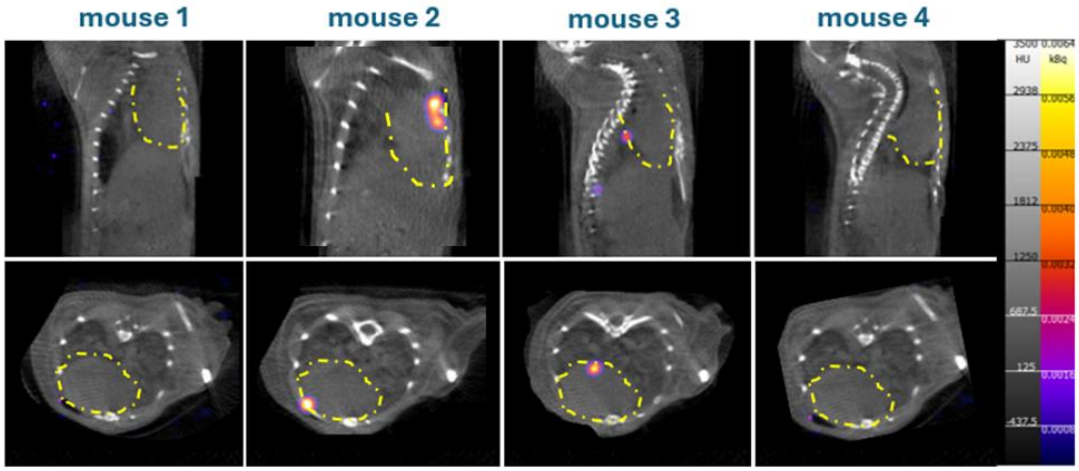

Figure 4-6. *In vivo* SPECT-CT of 1st generation SMP at 1-hour post-injection in sagittal (top) and transversal (bottom) views. The yellow dashed lines delineate the contours of the hearts. Both mouse 2 and mouse 3 exhibited radiotracer signals localized in the cardiac region, with mouse 2 displaying a distinct signal on the anterior wall.

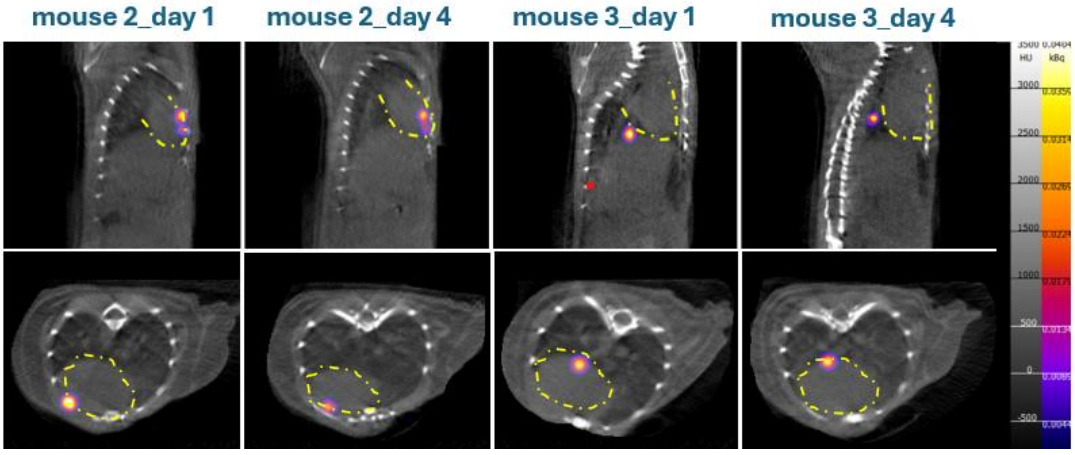

Figure 4-7. *In vivo* SPECT-CT of 1st generation SMP on day 1 and 4 in two representative mice in sagittal (top) and transversal (bottom) views. The contours of the hearts are delineated by yellow dashed lines. The patch detached from the heart in mouse 3 by day 1, while it remained at a consistent location in mouse 2 until day 4.

As the ultrasound-guided injection of 1st generation SMP did not consistently attach to the heart over time, it was crucial to investigate if the delivery route (ultrasound-guided injection) was the main factor contributing to this result or if the patches were less adhesive than anticipated in the *in vivo* environment. Therefore, I tested the ability of radiolabeled 1st generation SMPs to attach to the heart by surgically implanting them onto the epicardium of five mice and used SPECT-CT imaging to determine their locations. The representative mouse in Figure 4-8 demonstrated the open-chest surgical implantation of 1st generation SMP, where the patch initially adhered to the anterior wall of the heart (Figure 4-8A). Five minutes later, visual observation indicated that it had shifted towards the apex due to cardiac motion (Figure 4-8B). The 1-hour post-implantation *in vivo* SPECT-CT scan displayed sagittal and transversal views, revealing that the patch localized to the posterior aspect of the heart (Figure 4-8 C&D). Within 24 hours of implantation, SPECT-CT imaging indicated that all five mice exhibited detachment of the 1st generation SMPs. These findings were confirmed at sacrifice, where tweezers could be used to easily remove the patch found at inferior or posterior wall of the heart (Figure 4-8E).

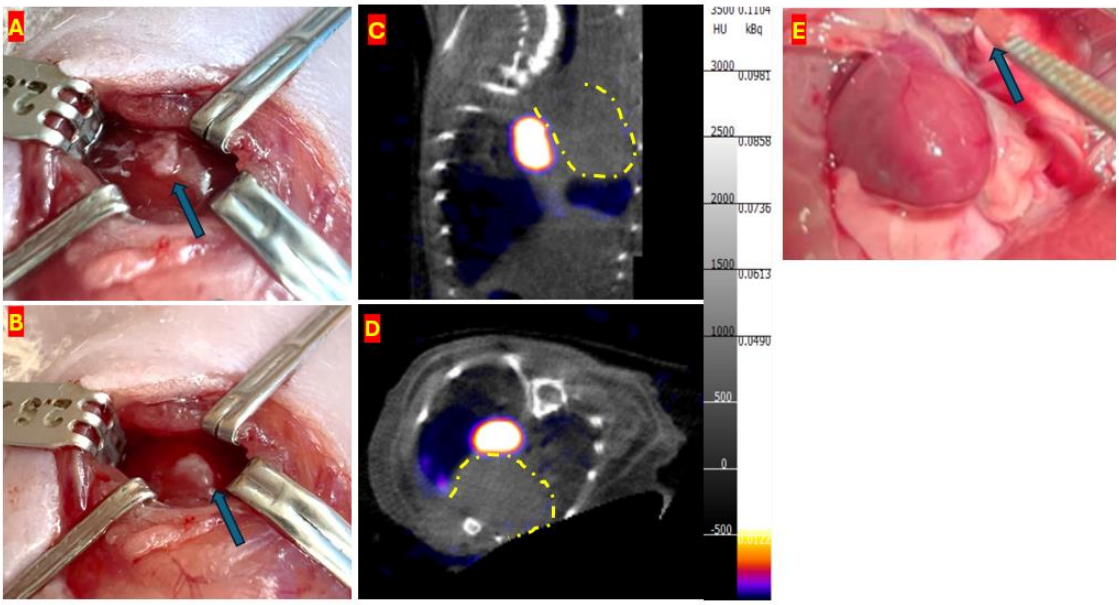

Figure 4-8. Surgical implantation of 1st generation SMP. (A) The initial location of the patch implantation at the first minute. (B) Five minutes after the implantation, the patch migrated towards the apex of the heart. (C) & (D) Sagittal and transversal views of SPECT-CT imaging revealed that one-hour post-surgery, the patch was located at the posterior of the heart. (E) Upon sacrificing the animal, it was confirmed that the patch had detached from the heart. The yellow dashed lines outline the shape of the heart, while blue arrows point to the location of the SMP.

4.4.4 Modifying the cardiac patch to enhance its attachment to the heart

Due to the weak adherence of the 1st generation SMP itself to tissues, two methods were investigated to enhance its attachment to the heart surface.

1. The employment of a surgical mesh for encapsulating the 1st generation SMP and maintaining its position (1st generation SMP with surgical mesh).
2. The modification of the 1st generation SMP with a 1% chitosan coating that provides a strong adhesion to wet surfaces (2nd generation SMP) is based on previous work from the Mooney lab [623].

Two groups of mice (n=4) underwent open-chest surgery to implant either the 1st generation SMP covered with surgical mesh or the 2nd generation SMP. SPECT-CT scans were conducted on days 1, 3 and 7. Diverse outcomes were observed in four mice from the 1st generation SMP + surgical mesh group. Mouse 1 exhibited initial patch movement towards the base of the heart on day 1 scan, followed by localization at the back of the heart near the apex on day 7. Mouse 2 demonstrated stable attachment at a consistent location over time. Mouse 3 and mouse 4 showed frequent detachment from day 1 to day 7. Mice in the 2nd generation SMP group displayed the enhanced patch attachment. The patch moved slightly downward towards the apex in mouse 1 from day 1 to day 3 and remained at that position until day 7. The remaining three mice exhibited stable attachment over time after implantation. Representative mice from each cohort were depicted in Figures 4-9.

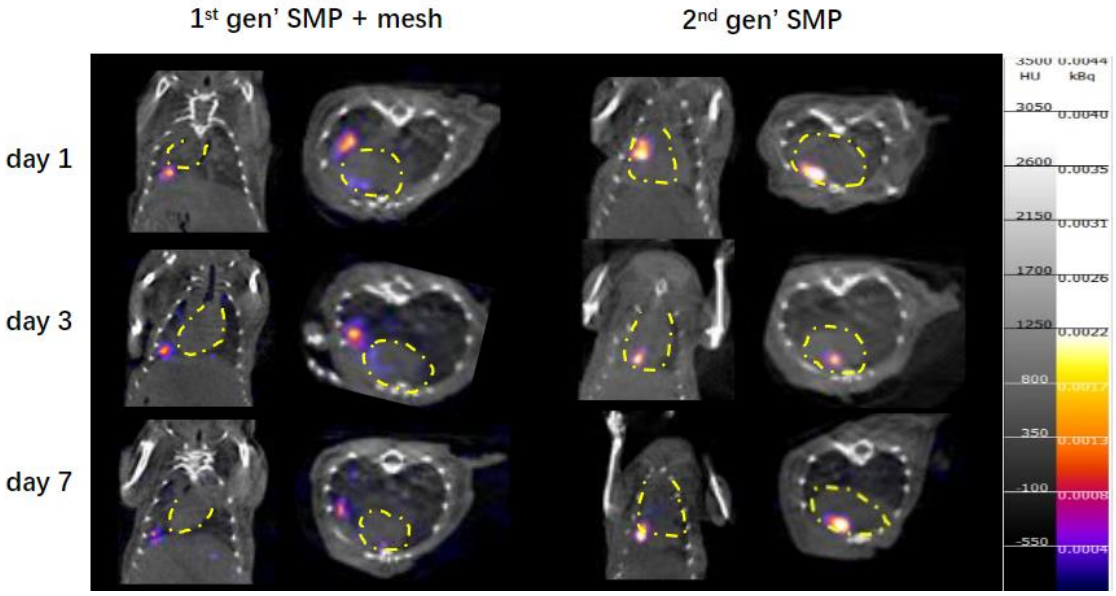

Figure 4-9. *In vivo* SPECT-CT imaging of 1st generation SMP with mesh covering (left) and 2nd generation SMP (right). The mouse implanted with 1st generation SMP with mesh covering showed patch detachment from day 1, whereas the mouse implanted with 2nd generation SMP demonstrated stable attachment over time.

4.4.5 Comparison of the stability of $^{111}InCl_3$ radiolabeling on 1st and 2nd generation SMPs

The above data has demonstrated that SPECT-CT imaging can serve as a sensitive imaging modality for direct visualization of the $^{111}InCl_3$ radiolabeled both 1st and 2nd generation SMPs. Based on this, this imaging technique can be used as a reliable and robust method to track the implanted biomaterial in the following several days. It is important to further investigate whether chitosan coating exerts an influence on the stability of $^{111}InCl_3$ radiolabeling, both *in vivo* and *in vitro*, particularly given the observed enhanced attachment of chitosan-coated alginate SMP compared to non-coated alginate SMP. Following $^{111}InCl_3$ labelling, a gamma counter was utilized to quantify the radioactivity of 1st and 2nd generation SMPs (n=3) at 2-, 6- and 24-hour intervals post-labeling. The radioactivity remained on both types of patches after 24 hours and 2nd generation SMP retained more percentage of $^{111}InCl_3$ than 1st generation SMP at all the time points (Figure 4-10A). *In vivo* study, SPECT-CT imaging was conducted over a week after implantation of 1st and 2nd generation SPMs onto the heart of two cohorts of mice (n=4). Serial *in vivo* SPECT-CT imaging confirmed a higher retention of radioactivity on 2nd generation SMP compared to 1st generation

(Figure 4-10B).

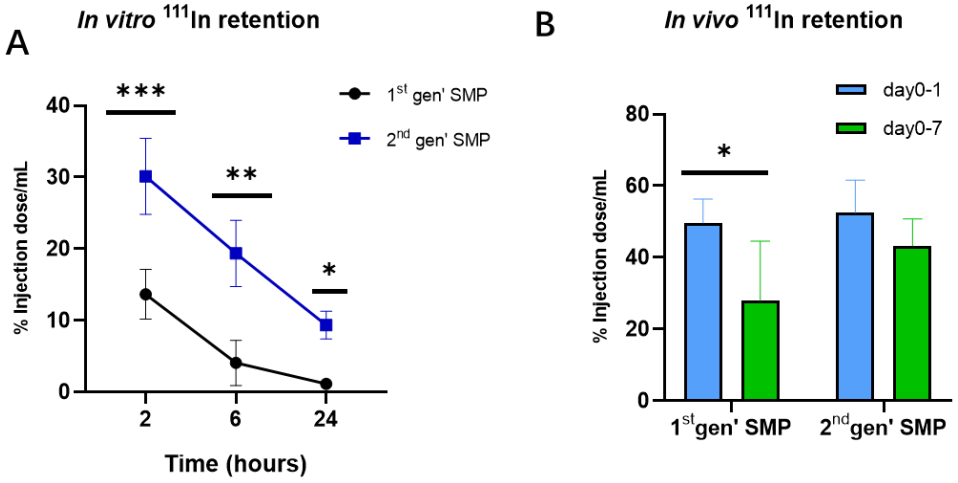

Figure 4-10. Comparison of the retention of $^{111}InCl_3$ radiolabeling on 1st and 2nd generation SMPs. An *in vitro* gamma counts of radioactivity remaining on the patch showed that 2nd generation SMP retained higher $^{111}InCl_3$ than 1st generation SMP (A). Serial *in vivo* SPECT confirmed that a higher percentage of radioactivity was retained on 2nd generation SMP than 1st generation SMP (B). *$P < 0.05$; **$P < 0.01$; ***$P < 0.001$.

4.4.6 Evaluating the efficiency of 2nd generation SMP for delivering and preserving stem cells *in vivo*

The above results demonstrated that 2nd generation SMP displayed an enhanced and stable attachment to the heart compared to 1st generation SMP alone or combined with surgical mesh. The further study was to assess the efficacy of 2nd generation SMP in preserving stem cells both *in vitro*. Seven 2nd generation SMPs (5x3 mm) were loaded with $5x10^5$ mMSCs, and the cell viability was monitored for three days using bioluminescence as an indicator. As depicted in Figure 4-11, mMSCs maintained viability for a minimum of three days *in vitro* on most of the patches. Notably, Patch 7 exhibited a significant difference in the signal intensity between day 0 and day 3, suggesting a potential proliferative phase of the cells on the patch.

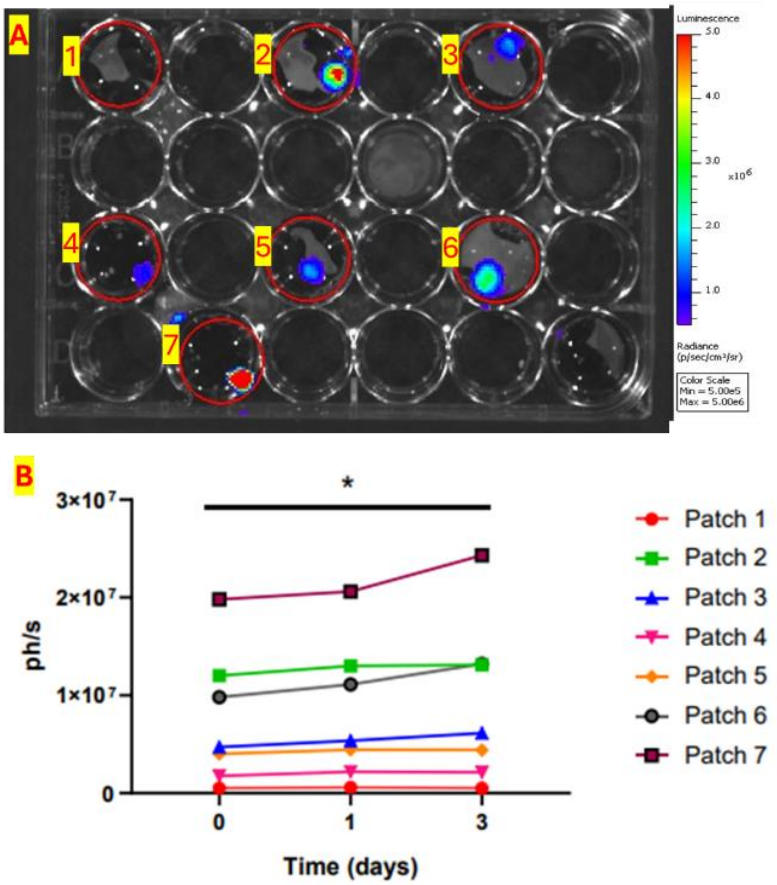

Figure 4-11. *In vitro* bioluminescent imaging and quantification of seven 2nd generation SMPs loaded with mMSCs. *$P < 0.05$.

A subsequent study was then carried out to test the efficiency of 2nd generation SMP in preserving the seeded stem cells *in vivo*. This involved surgically implanting patches labeled with $^{111}InCl_3$ and loaded with mMSCs into five mouse hearts. SPECT-CT and BLI were performed on days 0, 1, 3, and 7 to monitor the patch localization and transplanted cell survival *in vivo*, respectively. SPECT-CT images of two representative mice on days 0, 1, and 7 are presented in Figure 4-12. On day 0, one hour after the implantation, two out of five mice showed attachment of the patches to their hearts at the implanted points, while the other three showed displacement. By day 7, all five mice demonstrated that the patches were adhered to the chest wall.

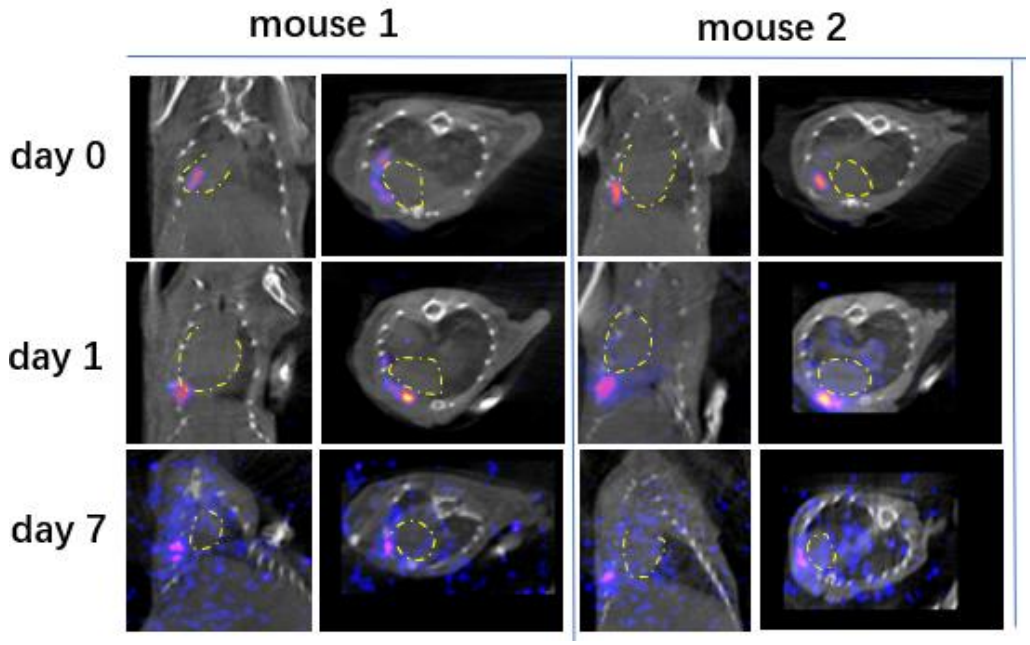

Figure 4-12. SPECT-CT images of two representative mice performed on day 0, 1 and 7 following mMSC-loaded SMPs implantation.

BLI was performed for the assessment of cell viability on the patches *in vivo* over time, indicating that only one out of five mice exhibited detectable BLI signals from day 0 to day 7 (Figure 4-13 A-D). *Ex vivo* BLI performed immediately after euthanasia revealed signals on the chest wall in most mice (Figure 4-13 E&F). Decreased bioluminescent signal intensity indicated lower cell viability over 7 days in most mice (Figure 4-13 G).

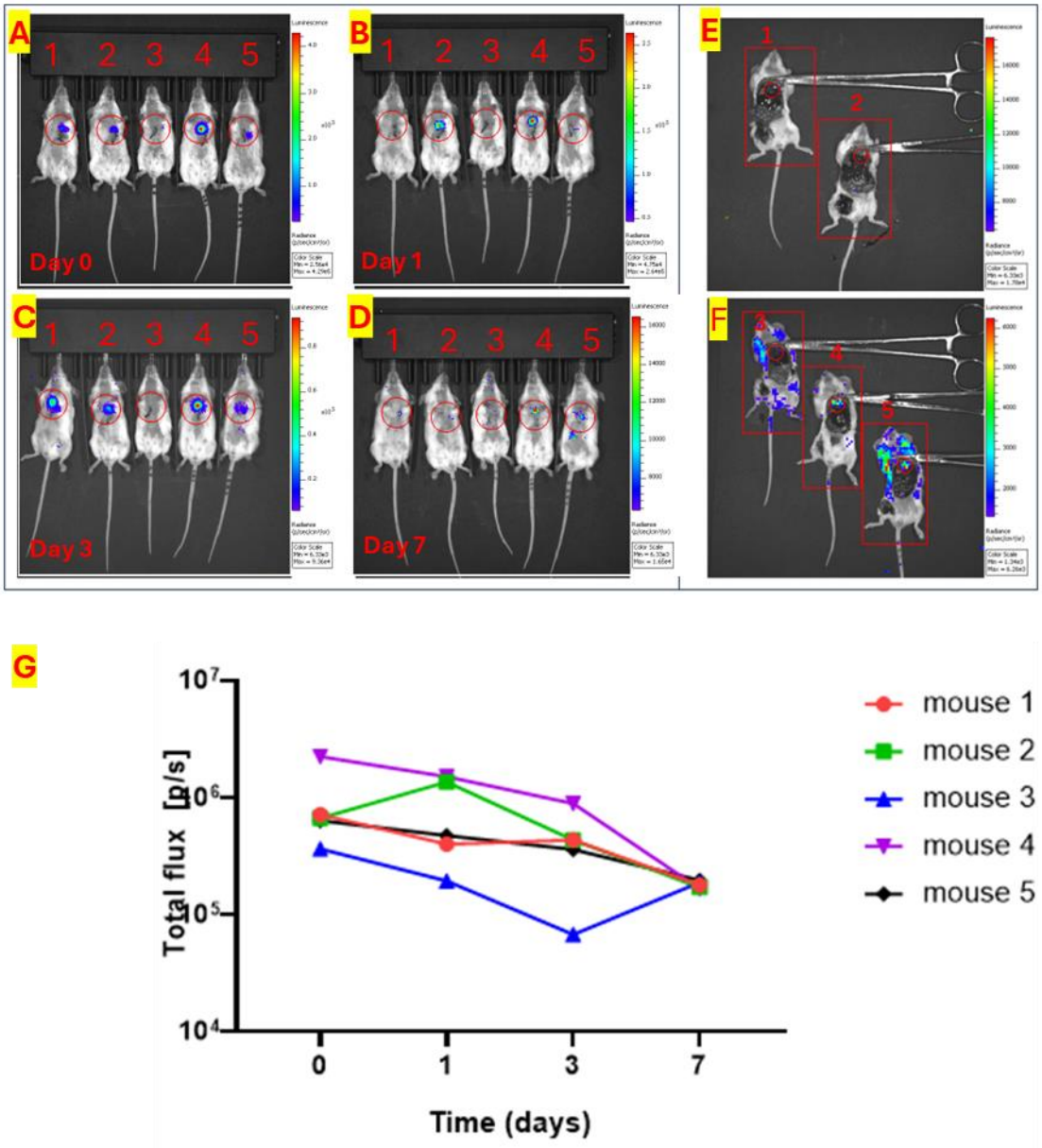

Figure 4-13. *In vivo* BLI evaluation of mMSCs viability on the 2nd generation SMP after surgical implantation to the heart over 7 days and *ex vivo* BLI on day 7. Only one mouse displayed detectable BLI signal for 7 days *in vivo* (A-D). *Ex vivo* BLI demonstrated BLI signals on the chest walls of most mice (E-F). Bioluminescent signal intensity decreased in four out five mice implanted with 2nd generation SMPs loaded with mMSCs over a 7-day period (G).

As mMSCs tested in the previous *in vivo* study did not survive on 2nd generation SMP could be that this allogenic transplant led to the rejection of the grafted cells by the immune system. Hence, we used immunocompromised NSG mice for this follow-up study and epi-hESCs to identify whether cell survival could be enhanced. 2nd generation SMPs (4x4 mm) were loaded with $4x10^5$ epi-hESCs and implanted in six NSG mice. SPECT-CT and *in vivo* BLI were performed on days 0, 1, 3, and 7.

According to SPECT-CT imaging, all six mice showed stable attachment of 2nd generation SMPs onto the hearts throughout the 7 days (Figure 4-14).

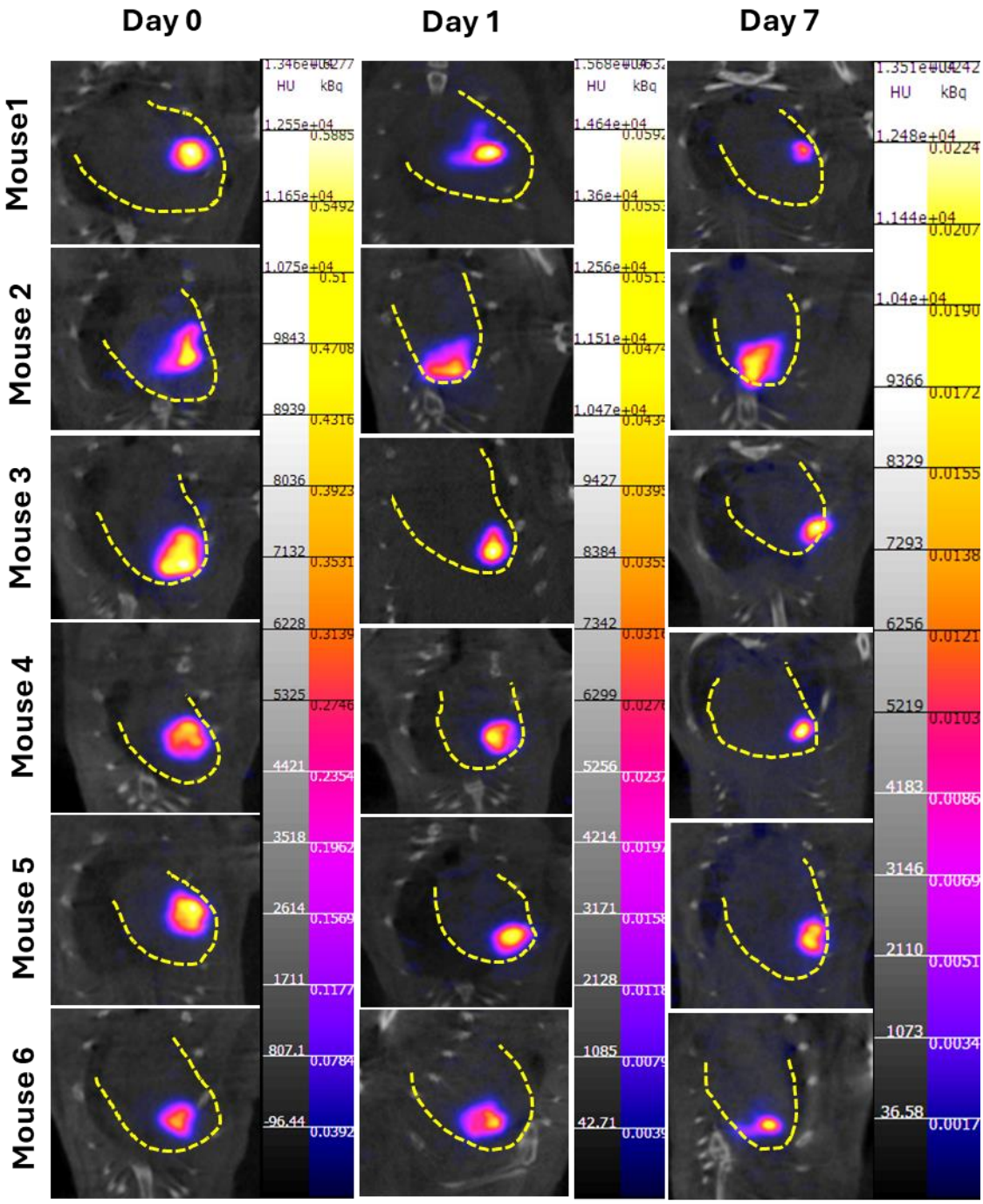

Figure 4-14. SPECT-CT images of 6 mice performed on day 0, 1 and 7 following epi-hESCs loaded 2nd generation SMP implantation.

BLI assessment of cell viability on the patches *in vivo* over 7 days demonstrated detectable bioluminescent signals within 1hour post-implantation of 2nd generation SMP. The signal increased by day 1 and remained detectable for 7 days (Figure 4-15). *Ex vivo* BLI conducted immediately after euthanasia revealed signals on the chest wall in two mice, as depicted in Figure 4-16.

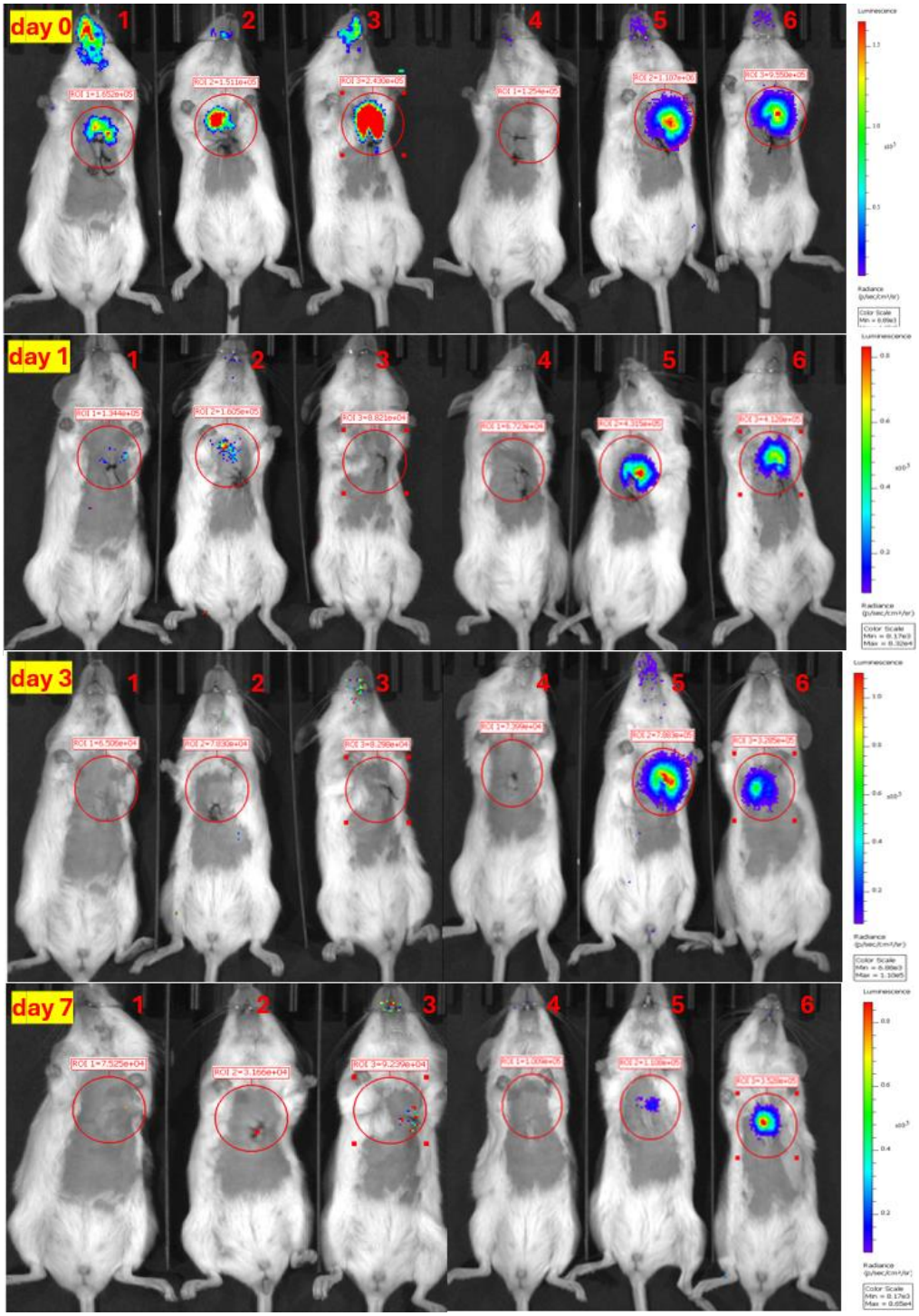

Figure 4-15. *In vivo* BLI evaluation of the viability of seeded epi-hESCs on 2nd generation SMPs over 7 days.

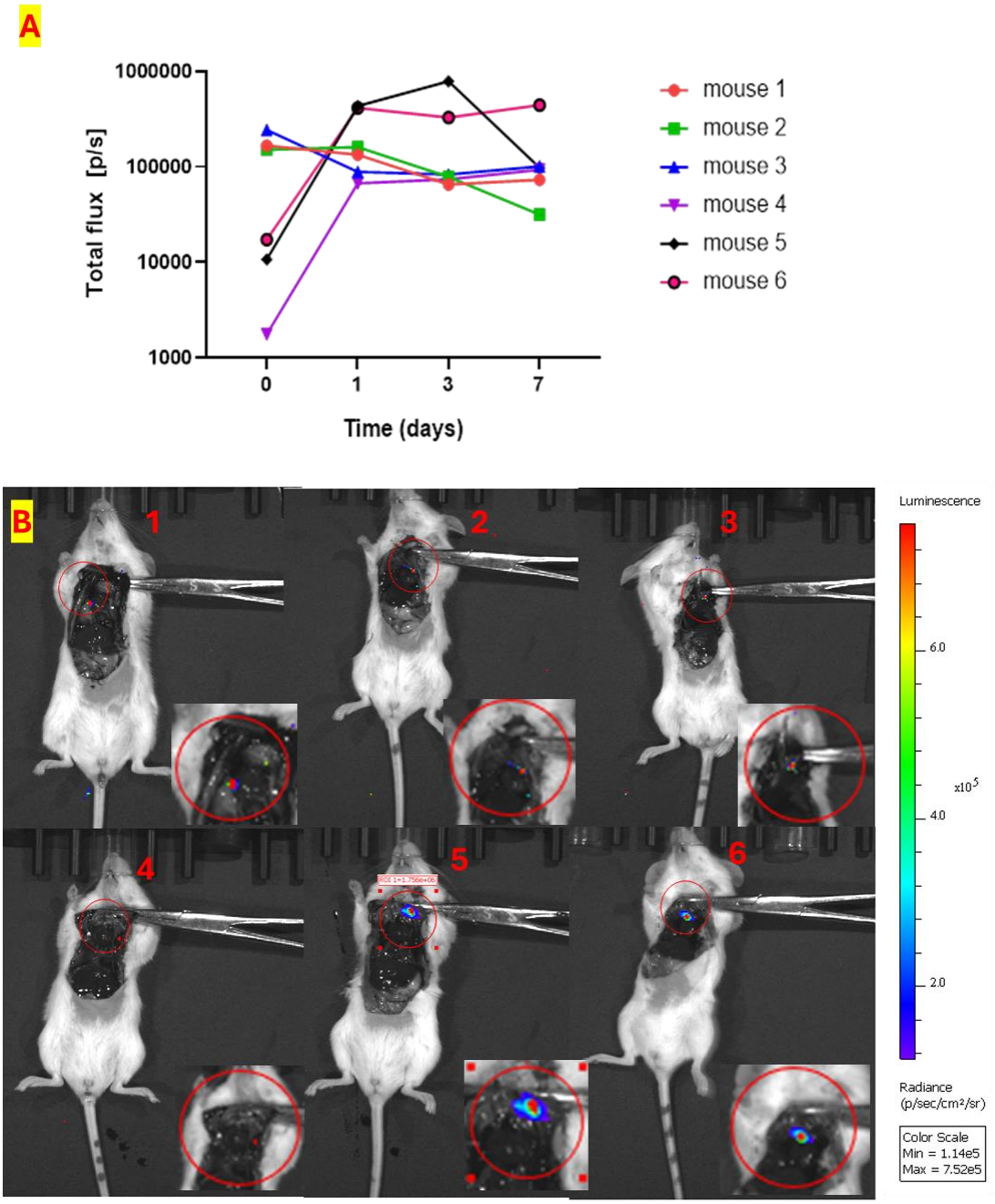

Figure 4-16. Bioluminescent signal intensity measurement in six NSG mice implanted with 2nd generation SMPs loaded with epi-hESCs over 7days. The bioluminescent signal was evident from 1 hour post implantation. The signal increased by day 1 and remained detectable for 7 days. *Ex vivo* BLI of epi-hESCs on 2nd generation SMPs after 7 days of implantation revealed detectable BLI signals on the chest wall in most of six mice.

4.5 Discussion

Over the past 20 years, cell therapies for heart disease have rapidly progressed from utilizing simple infusion of autologous mononuclear cells through to patient-specific iPSC-derived CMs, endothelial cells and epicardial cells. To date, the therapeutic

efficacy of stem cell-based therapies in preclinical and clinical settings remains limited, primarily due to the substantial loss (≈95–99%) of delivered cells within the initial 24-hour period, low graft retention, inadequate cellular proliferation and a small graft size [408]. This can be attributed to factors such as mechanical washout, apoptosis resulting from a hostile microenvironment (e.g., hypoxia and nutrient deprivation), and immune-mediated rejection by the host [135]. Tissue-engineered constructs can enhance cell retention by providing a cell attachment scaffold and allowing cell-cell contact/communication to be established before delivery. The utilization of tissue-engineered constructs/biomaterials incorporating stem cells for the treatment of MI has been reported to exhibit significant therapeutic efficacy [409]. However, most of these constructs require invasive surgery to expose the heart to allow their attachment, which limits their applicability to most HF patients. Hence, in this study, we tested a collapsible SMP, which could be loaded with therapeutic cells and injected into the heart via minimally invasive ultrasound guidance.

4.5.1 Ultrasound-guidance injections enable minimally invasive delivery of therapeutic biomaterials to the heart

Ultrasound is widely accepted in clinics due to its low cost, ease of use, and time efficiency. Currently, it shows great potential for delivering regenerative biomaterials. However, ultrasound-guided injections pose a significant challenge, especially when delivering a patch to the epicardium, making it difficult to confirm the successful delivery of biomaterials to the targeted region. Our previous research has demonstrated that radiolabeled hydrogels can be injected into the myocardium under ultrasound guidance, and SPECT-CT can be used to evaluate the efficacy of targeted delivery. In this study, I adapted this method to quantify the targeted delivery of injectable SMPs and utilize continuous *in vivo* data to optimize the biomaterials for developing more effective treatments. This work highlights that the combination of ultrasound guidance injection system and SPECT-CT imaging provides a reliable platform to achieve targeted minimally invasive delivery of biomaterials and improves tissue-engineered treatments for the heart and other organs.

4.5.2 SPECT/PET-CT imaging enables non-invasive monitoring and localization of implanted SMP

A major promise of ultrasound-guidance delivery of SMP lies in its potential to enable precise and targeted delivery of active drugs, molecules, or stem cells to specific sites, thereby maximizing therapeutic efficacy. However, a comprehensive assessment of the distribution of therapeutics is a crucial aspect of evaluating the efficacy of ultrasound-guided delivery prior to its clinical application [410]. In small animal models, biodistribution assessments are frequently conducted via *ex vivo* tissue analysis subsequent to the administration of the treatment and sacrificial euthanasia of the subjects. To enable the widespread clinical translation of tissue-engineered constructs, a fundamental challenge arises in the non-destructive monitoring of implants within living organisms and longitudinal evaluation of their *in vivo* performance. Therefore, there is a pressing necessity to develop techniques for monitoring and assessing implant biomaterials, which can be used to significantly reduce the number of animals. Additionally, longitudinal imaging also provides more reliable results, as intersubject variability is higher than test-retest intrasubject measurements [411, 412].

Non-invasive monitoring of therapeutics can be achieved through the utilization of advanced imaging modalities routinely employed in clinical practice, such as SPECT/PET-CT imaging. The proposed approaches facilitate rapid clinical implementation as they can utilize combinations of clinically approved radiotracers and materials and bypass prolonged validation and approval processes, leading to quicker acceptance by clinicians [244]. For instance, in a recent study, Nosrati *et al.* demonstrated the feasibility of simultaneous SPECT imaging using ^{123}I and ^{125}I for concurrent assessment of a drug and its carrier through dual radionuclide imaging. In their study, fenofibrate concentrations in plasma samples were quantified via SPECT imaging with ^{123}I-labeled fenofibrate and ^{125}I-labeled triolein over 24 hours in a rat model. The findings indicated that SPECT-CT imaging of dual-labeled drug delivery systems is an excellent modality for evaluating novel formulations and elucidating their pharmacokinetics and biodistribution *in vivo* [413]. Qiao *et al.* demonstrated the noninvasive monitoring of reparative fibrosis post-MI in a rat model using ^{68}Ga-labeled fibroblast activation protein inhibitor 04 (^{68}Ga-FAPI-04) via PET-CT imaging.

This approach holds significant value for comprehending the dynamic process of myocardial fibrosis following MI and providing additional insights for evaluating novel therapeutic interventions [414]. In my study, the SPECT-CT imaging technique was performed by utilizing the positive charge of the nuclear imaging radio-metal $^{111}InCl_3$, as a crosslinker for alginate monomers, thus binding it into the structure of the patch. Although this interaction is not long-lasting, the SPECT-CT images have shown it to be sufficient for longitudinal monitoring of the location of SMPs for at least 7 days. The results suggest that SPECT-CT imaging is effective in accurately localizing the implanted SMP with minimal interference from background signals at various time intervals, thus providing valuable insights for further optimizing the SMP for improved attachment to the heart.

4.5.3 Chitosan-coating promotes enhanced attachment of SMP to the heart

SPECT-CT imaging promptly revealed that ultrasound-guided injection of the first-generation SMP was ineffective, partly due to the relatively large volume of liquid required to propel the patch through the needle, ultimately washing it away from the target site. Another potential reason for the non-adherence of the patch after delivery may be attributed to its adhesive properties, which were efficacious *ex vivo* but not sustained under *in vivo* conditions. Hence, I undertook a multi-step iterative process for optimizing patch attachment. First, an open-chest surgical procedure was performed to directly visualize the attachment of the SMP, and it was observed that most 1st generation SMPs detached from the hearts within the first few hours, indicating a weakness in their attachment. Second, surgical mesh or chitosan coating was applied to enhance the adhesive of 1st generation SMPs. Bio-adhesive surgical mesh is extensively utilized in surgical procedures, demonstrating an adhesive with a well-balanced combination of strength and biodegradability to facilitate proper healing and long-term repair. The submicron protein layer does not occlude the mesh pores, thereby preserving the macro-porosity essential for tissue integration during the healing process [415]. Hence, we selected the surgical mesh to augment 1st generation SMP attachment. Initially, it demonstrated a stable fixation of SMP onto the heart surface; however, the mesh exhibited poor adhesion to the heart surface over time due to the presence of body fluid. Upon becoming wet, the double-sided adhesive nature of the mesh caused it to adhere to the chest wall or lungs due to

cardiac and pulmonary motion, leading to detachment of the SMPs, as observed in SPECT-CT imaging. We then developed 2nd generation SMP by applying a chitosan coating. Chitosan, a widely utilized natural biopolymer derived from chitin, possesses intrinsic properties such as high biocompatibility, biodegradability, and non-toxicity. Chitosan-based adhesives exhibit promising prospects owing to their unique adhesive properties and compatibility with biological systems [416, 417]. After chitosan coating, the surface-modified SMP exhibited sustained adhesion following implantation for 7 days, as depicted in the SPECT-CT images. Thus, chitosan coating effectively enhanced the stability of SMP after implantation in the heart, irrespective of cardiac motion or tissue fluid. In this study, we also observed that chitosan-coating modification improved the retention of radioactivity for $^{111}InCl_3$ compared to 1st generation SMP both in *vivo* and *in vitro*, enabling prolonged and stable tracking of biomaterial.

4.5.4 2nd generation SMP improves the cell viability and retention

The ultimate aim of employing SMP is to facilitate the retention, engraftment and migration of therapeutic cells, thereby enhancing the regeneration of damaged myocardial tissue. After chitosan-modified SMP displayed enhanced attachment to the tissue surface, the viability of stem cells seeded on 2nd generation SMP was evaluated. Firstly, mMSCs were selected as a test cell line based on their ease of isolation and rapid *in vitro* expansion [418]. *In vitro* BLI results demonstrated that 2nd generation SMP maintained cell viability of mMSCs for a minimum of three days. For *in vivo* studies, 4 x 10^5 mMSCs were added to 4x4 mm SMPs, allowed to attach for 24 hours and then 5 MBq on $^{111}InCl_3$ was added to label the patch. However, *in vivo* BLI revealed that only one out of five mice exhibited strong BLI signals over 7 days.

Additionally, SPECT-CT images indicated detachment and degradation of the mMSCs-seeded SMPs over the same period. The possible reason could be that by adding a large number of highly proliferative mMSCs to the patches, the adhesive nature of the chitosan coating was masked, leading to patch detachment. Further, the addition of $^{111}InCl_3$ onto seeded patches followed by several washing steps could have affected cell viability/adhesion just prior to administration, which, coupled with the

allogeneic nature of the transplant, resulted in poor *in vivo* cell survival.

For further study, we assessed the cell viability of epi-hESCs to determine whether SMP could offer enhanced cellular survival of epi-hESCs compared to mMSCs. Epi-hESCs were suspended with a pro-survival cocktail before seeding, which consisted of Matrigel 10% v/v, ZVAD-FMK 100mM, Pinacidil 1.25 ng/ml, IGF-1 100ug/ml 50ulx2 and Bcl-XL (TAT-BH4). Then dry SMPs were first loaded with $^{111}InCl_3$ then partially dried and loaded with 2 x 10^5 epi-hESCs to increase both binding of the radiotracer and cell viability. Epi-hESCs seeded on 2nd generation SMPs and surgical implanted onto the epicardium of six NSG mice retained bioluminescent signal over 7 days *in vivo*. This highlights that a pro-survival cocktail before seeding allows donor cells to be retained on target.

Epi-hESCs demonstrated remarkable survival *in vivo* for at least 7 days, and the 2nd generation SMP effectively maintained cell viability over an extended period, highlighting the significance of additional modifications using a pro-survival cocktail to suspend the cells for further enhanced cell retention. However, the low proliferation of these cells may not be sufficient to bring effective therapy. It is essential to consider alternative approaches to enhance the proliferation and migration of cells. The ideal scaffold for cell loading should have interconnected porosity with pore sizes suitable for 3D cell culture [419]. Our biomaterial, SMP, has a three-dimensional porous structure that allows efficient exchange of oxygen, nutrients, and wastes for the encapsulated cells. However, following chitosan coating, the pores within the alginate may become narrower and are filled with the coating, thereby reducing space for cell growth, proliferation and migration. Given cells' sensitivity to their surrounding environment, this condition could lead to a decrease in cell viability [420]. Therefore, further modification may be required to precisely define the thickness and structure of the chitosan-coated alginate patch to facilitate expansive cell proliferation. Additionally, the limited access to essential nutrients and oxygen following the implantation may have a significant impact, as adequate nutrient supply is crucial for supporting cellular metabolic activities. Therefore, supplementing survival factors to the patches after stem cell seeding may enhance cell viability and proliferation. Jiang *et al.* developed a bioengineered cardiac patch containing multiple growth and angiogenic factors, including vascular endothelial

growth factor, platelet-derived growth factor, insulin-like growth factor-1, basic fibroblast growth factor, angiogenin, and angiopoietin-2. *In vitro* studies demonstrated that the patch enhanced the maturation of hiPSC-CMs. *In vivo* studies showed that the regenerative engraftment of the patch at the infarct zone induced a decreased infarct size and increased cell retention and neovascularization [421].

Currently, numerous studies employ biomaterials such as hydrogels or cardiac patches to enhance cell viability and retention. Panda *et al.* demonstrated that alginate hydrogel encapsulation improved MSCs retention in an MI model [422]. Pok and colleagues developed a novel cardiac scaffold derived from heart matrix/chitosan hydrogels, maintaining >80% viability and higher cell retention [423]. In a separate study, researchers compared four biomaterials loaded with hMSCs: alginate or chitosan hydrogels and alginate or collagen patches, with saline mixture injection as a control. The results demonstrated that all four biomaterials retained 50–60% of cells immediately following transplantation, compared to 10% for the saline control. At 24 hours, cell viability of all biomaterials surpassed that of the saline control, with alginate and chitosan hydrogels improving by about 8 and 14 times, respectively, while collagen and alginate patches improved by 47 and 59 times, respectively [391]. However, these studies did not track the specific biomaterials utilized in regenerative medicine and their interaction with stem cells. In my project, SPECT-CT imaging was applied to precisely visualize the distribution of biomaterials and BLI was used to monitor the transplanted stem cells. This reliable multimodal imaging platform can be applied to inform on-graft location and optimize biomaterial formulation for enhanced on-target therapeutic retention.

4.6 Limitations

This study has several limitations that should be acknowledged. First, the ultrasound-guided injection technique has not yet been validated as a reliable method for effectively delivering the cardiac patch to the heart. While SPECT-CT offers a promising approach to track, monitor, and confirm the delivery location, further refinement of the delivery method is necessary. Additionally, future research should prioritize implanting the cardiac patch into disease models, such as MI models. The structural changes in diseased hearts, compared to healthy ones, may introduce additional challenges for ultrasound-guided injection due to altered morphology.

Furthermore, this study lacks histological data to evaluate cell retention and migration—critical factors for assessing the regenerative potential of the cardiac patch. Addressing these gaps in future studies will be pivotal for advancing the clinical translation of this approach.

4.7 Conclusion

In conclusion, dual-imaging modalities such as SPECT-CT imaging combined with BLI provide a robust and reliable platform for optimizing and evaluating the delivery of stem cells-loaded biomaterials to the heart. Chitosan coating has significantly enhanced SMP attachment to the heart as well as radioactivity retention. Our findings suggest that chitosan-coated SMP could be an effective strategy for stem-cell-based MI therapy. Future research could investigate the potential of using ultrasound to guide the delivery of SMP loaded with therapeutics or stem cells containing multiple growth/survival factors for treating MI, as well as explore how epi-hESCs loaded SMP contribute to regenerative therapy in a murine model of MI.

Chapter 5 Testing AAV9 mediated activation of the YAP pathway as a route to cardiac regeneration

Graphic abstract

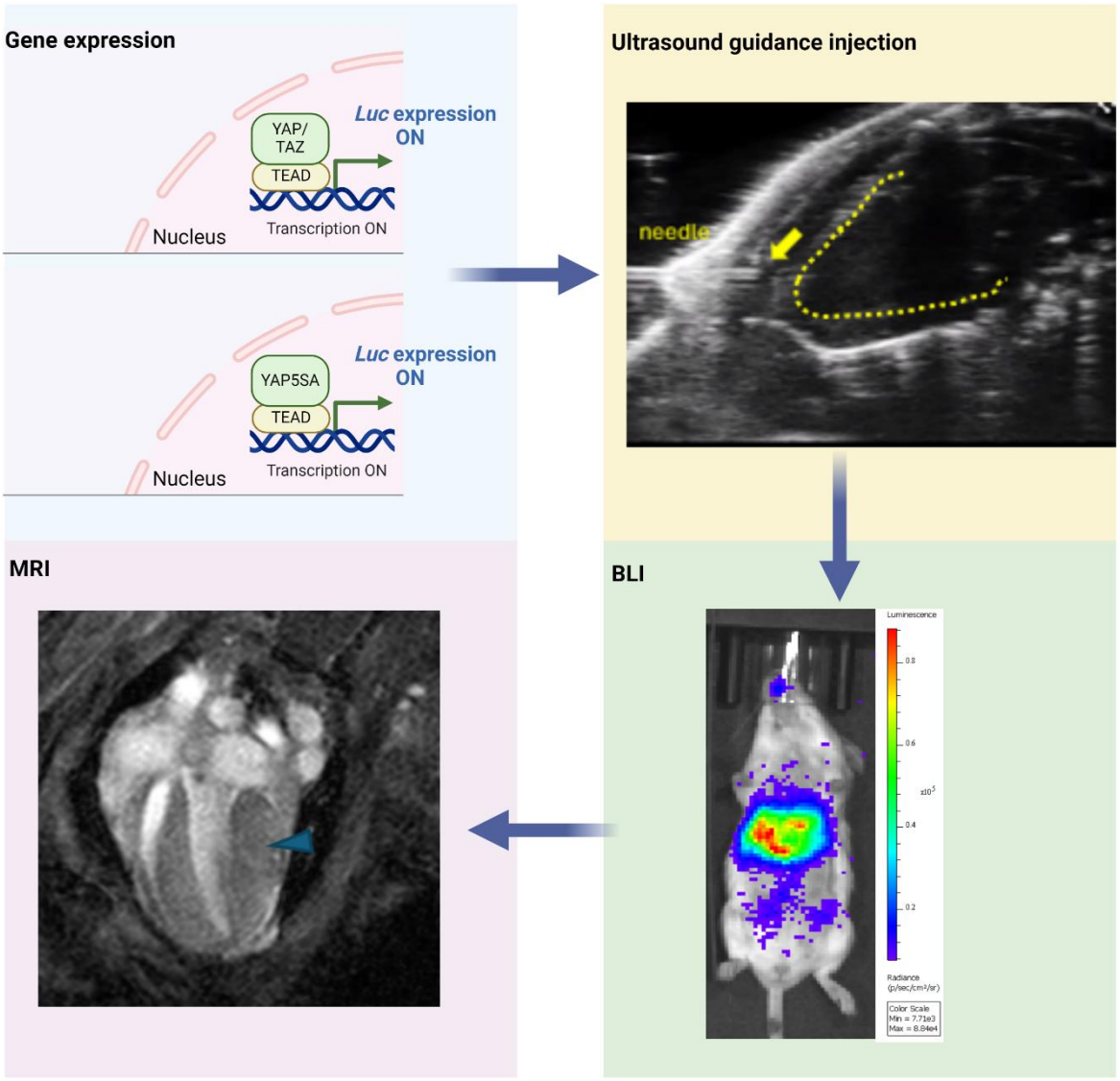

Abstract

Gene transfer is a promising strategy for myocardial infarction treatment, but its clinical application faces challenges related to gene expression regulation, therapeutic monitoring, and adverse side effects. The Hippo signaling pathway, upregulated in ischemic heart failure, contributes to adverse cardiac remodeling and dysfunction. Activating the transcriptional coactivator Yes-associated protein (YAP) or its downstream effectors may improve the outcomes of post-myocardial infarction (MI). This study aimed to develop a multimodal imaging platform integrating bioluminescence imaging (BLI), magnetic resonance imaging (MRI), and ultrasound to monitor gene expression dynamics and assess therapeutic efficacy.

AAV9 vectors encoding firefly luciferase and YAP variants (YAPREP and YAP5SA) were delivered via ultrasound-guided intramyocardial injections to 26 mice (YAPREP: n = 11; co-injection of YAPREP+YAP5SA: n = 15). BLI tracked YAP activation on days 4 and 12. Subgroups underwent MI (YAPREP_MI: n = 7; YAPREP+YAP5SA_MI: n = 8), and sham groups conducted open-chest operation (YAPREP: n = 4; YAPREP+YAP5SA: n = 7). MRI and ultrasound were assessed cardiac structure and function on days 2, 14, and 28. BLI monitored signal pathway activation on days 4, 7, 14, 21, and 28.

BLI confirmed YAP pathway activation, with YAPREP+YAP5SA group peaking on day 4 post-injection before declining to YAPREP levels by day 12. Post-MI, no significant increase in BLI signal was observed in either group. MRI and ultrasound revealed focal wall thickening and impaired cardiac function with no significant global functional recovery, though strain analysis indicated regional improvements. BLI signal intensity correlated with lateral wall thickness.

This study developed a multimodal *in vivo* imaging system capable of real-time gene expression monitoring and functional assessment. Although YAP activation did not improve global cardiac function post-MI, regional functional improvements and the platform's potential for optimizing gene therapy strategies highlight its value in cardiac disease research.

5.1. Introduction

Gene transfer has emerged as a revolutionary therapeutic approach to address the limitations of conventional therapies for MI, such as pharmacological and surgical interventions, which are unable to reverse the pathophysiology associated with MI and regenerate the lost myocardium [424]. As presented in the main introduction to this thesis, cardiac regeneration can potentially be achieved through at least three strategies. One approach involves deriving new CMs from ESCs or iPSCs, which can be delivered to the heart using injectable hydrogels or cardiac patches as carriers. However, this method is limited by low cell survival rates and the potential for arrhythmias. Alternatively, directly reprogramming FBs into CMs is another innovative approach to cardiac regeneration. Despite its potential, this approach faces challenges due to the low reprogramming efficiency. A third method seeks to activate the intrinsic proliferative capacity of CMs by introducing specific genes or microRNAs [425].

Currently, an increasing number of studies are focusing on regulating the proliferation of endogenous mature CMs through gene transfer [426]. This can be achieved by stimulating various molecules, including cell cycle regulators, non-coding RNAs, transcription, and metabolic factors [427]. The homeodomain transcription factor Meis1 is crucial for regulating the CM cell cycle and normal cardiac development. In a study by Mahmoud *et al.,* the researchers examined the impact of deleting Meis1 in mouse CMs. The results demonstrated an extended postnatal proliferative window for CMs and reactivated CM mitosis without harming cardiac function [428]. Su *et al.* demonstrated that adenoviral gene therapy vectors expressing insulin-like growth factors (IGF) -I and -II efficiently transduced CMs, enhancing cell migration and angiogenic outgrowth [429].

Non-coding RNAs, including microRNAs (miRNAs) (≈22 peptides), long non-coding RNAs (lncRNAs) (> 200 nucleotides), and circular RNAs (circRNAs), are functional RNA molecules that do not encode proteins but participate in cardiac regeneration in heart diseases [430]. Eulalio *et al.* identified a comprehensive array of human miRNAs that elicit CM proliferation *in vitro*. Notably, miR-199a-3p stands out as one of the most potent inducers of CM proliferation and represents one of the pioneering miRNAs demonstrated to activate rather than inhibit the cardiac cell cycle

[431]. Tao *et al.* verified that miRNR-199a-3p promoted CM proliferation by directly targeting and inhibiting CD151 expression, a known endogenous inhibitor of the cell cycle [432]. Other miRNAs, such as miRNA-1825 and miRNA302-367, are essential regulators of CM proliferation [430]. lncRNAs are important in CM differentiation via associated regulators such as CARMEN and H19. CARMEN expression was upregulated during pathological remodeling in both mouse and human hearts, and it played a crucial role in maintaining the cardiac phenotype of differentiated CMs [433]. H19 is vital in regulating CM apoptosis and proliferation. The knockdown of H19 in a dilated cardiomyopathy rat model demonstrated reduced CM apoptosis and improved the structure and function of the LV [434]. Furthermore, circRNAs have become increasingly important in cardiac regeneration and repair. Chen *et al.* demonstrated that circRNAs-CDR1 regulated the proliferation and apoptosis of human CMs via the miR-135a/HMOX1 and miR-135b/HMOX1 Axes [434]. In another study, circRNA Hipk3 was reported to induce cardiac regeneration in a mouse MI model by binding to Notch1 and miR-133a [435].

Over the past decade, numerous studies have shown encouraging outcomes regarding gene transfer that stimulated the proliferation of endogenous CMs for treating MI. Mauro Giacca's group demonstrated that the expression of human microRNA-199a in infarcted pig hearts could stimulate cardiac repair. One month after the delivery of human microRNA-199a to the MI models, the treated animals exhibited significant improvements in global and regional contractility. The decreased scar size and increased muscle mass were also observed in treated animals. These functional and morphological findings were associated with CM de-differentiation and proliferation. Nevertheless, at a longer follow-up, 7 out of 10 pigs suffered from sudden arrhythmic death due to the prolonged and uncontrol expression of the microRNA [436]. In another study, YAP5SA partially reprogrammed chromatin accessibility through the daily injection of tamoxifen (40 μg/g) for four consecutive days to induce adult CMs to revert to a primitive, fetal-like cell state. One week after induction, the number of CMs increased by 40%, and the CMs of the YAP5SA lineage were coupled with the existing CMs. However, it has been reported that some mice overexpressing YAP5SA died due to HF within four days of the last dose [437]. Taken together, the mechanisms by which gene transfer regulate the renewal of CMs remain unclear. More crucially, for strategies intended to regenerate cardiac tissue by stimulating

myocyte proliferation to succeed, it is important to explore, understand and control genes for regular expression *in vivo.*

In previous studies, several signal pathways have been identified as crucial regulators that facilitate the proliferation of CMs during development or neonatal regeneration. These findings further suggest that these pathways hold great potential as pro-proliferative and pro-regenerative mechanisms to stimulate myocardial growth in adult hearts [438]. The Hippo-YAP signaling pathway is one of the most significant signal pathways known to regulate CMs proliferation in both neonatal and adult stages [439]. Initially identified in Drosophila, this signaling pathway plays a pivotal role in stem cell biology, developmental organ growth regulation, and the progression of diverse diseases [440]. At the core of the Hippo pathway lies the intricate regulation of a kinase cascade that ultimately leads to phosphorylation and subsequent deactivation of the transcriptional coactivator YAP. Upon the Hippo pathway kinase deactivation, nonphosphorylated YAP/TAZ is capable of translocating to the nucleus and interacting with TEAD to promote target gene expression, which is involved in cell proliferation, differentiation, growth, and death [441, 442].

Given that Hippo signaling is upregulated in ischemic HF among patients, which may contribute to adverse cardiac remodeling and dysfunction, the inhabitation of the Hippo pathway may confer therapeutic benefits for individuals with ischemic HF [443]. For example, Lin *et al.* demonstrated that cardiac-specific YAP activation after MI alleviated myocardial injury, enhanced cardiac function, and improved survival [444]. Under the negative effects of the Hippo pathway, the activated YAP interacted with FoxO1 in the nucleus of CMs, demonstrating the protective effect against IR injury by promoting the survival of CMs [445]. These findings imply that therapeutically activating YAP or its downstream targets could be a strategy to enhance outcome after MI.

The efficacy of gene therapy relies heavily on the viral vector employed. AAVs have gained significant attention in myocardial gene therapy due to their capacity for more stable and long-lasting transgene expression compared to commonly used adenoviruses, and their ability to transduce non-dividing cells like CMs [446].

Previous research has indicated that AAV9 stands out as the most potent vector for cardiac gene transfer among serotypes 1-9, primarily owing to its rapid onset of gene expression [190]. Additionally, achieving optimal gene delivery to the heart remains a challenge. The site and administration method significantly impact the delivery's effectiveness and can act as a crucial determinant of treatment outcome. Gene delivery routes, such as catheter-based angioplasty, IC infusion, and coronary sinus retroperfusion are frequently used [181]. These delivery routes enable rapid systemic dissemination but demonstrate suboptimal transference efficiency [447]. Localized direct delivery of genes to target tissues is considered more efficacious than systemic administration by minimizing undesired side effects on non-target tissues. Also, the ideal gene transfer method should cause minimal trauma [448]. Ultrasound guidance injection has demonstrated significant promise in a minimally invasive and targeted method for delivering therapeutic agents directly to the targeted area, thereby minimizing potential systemic side effects.

Before embarking on gene therapies, it is essential to consider several factors. Firstly, verifying vector delivery to the intended target site post-gene injection is crucial. It raises questions about how we can accurately confirm the presence of the vector at the desired location and distinguish whether non-target tissues also exhibit vector delivery or gene expression. Secondly, understanding the duration and magnitude of gene expression becomes vital in determining the most effective route, timing, and dosage for gene delivery. The ability to control these variables will significantly impact treatment outcomes by ensuring sustained therapeutic levels without adverse effects. Thirdly, efficient tracking and monitoring of gene expressions are essential for assessing treatment efficacy over time. Lastly, evaluating the adequacy of gene expression levels in eliciting a therapeutic response remains a critical challenge. To address these inquiries, non-invasive and highly sensitive biomedical imaging modalities such as BLI exhibit their potential. This advanced technique allows for monitoring the transfected cells that constitutively express the firefly luciferase gene, enabling precisely differentiate between targeted and non-targeted cells and tracking the dynamic changes in gene expression within specific tissues or organs.

YAPREP is a YAP-sensitive promoter, driving luciferase expression. It is a specialized DNA sequence employed in research to monitor the activity of Yes-

associated protein (YAP); a transcriptional coactivator integral to the Hippo signaling pathway. The YAP promoter contains TEAD-binding elements and exerts its transcriptional effects by forming complexes with TEAD (TEA domain) transcription factors. The interaction between YAP and TEAD facilitates the activation of downstream target genes, including the luciferase reporter gene. When the Hippo pathway is inactive, such as during stress or injury—YAP/TAZ translocates to the nucleus, binding to TEAD on the promoter. This event activates transcription of the luciferase gene, culminating in the production of luciferase enzyme. In turn, this enzyme emits light when exposed to its substrate (luciferin), thereby enabling detection of YAP activity through bioluminescence imaging. The YAP5SA variant, a constitutively active form of YAP, characterized by mutations in all phosphorylation sites of LATS1/2 from serine to alanine, exhibits constant activity and has considerable potential in targeting the genesis of new CMs by facilitating CM proliferation in cardiac disorders.

This study focuses on monitoring YAP pathway activity using BLI, where the luciferase signal serves as a direct indicator of YAP transcriptional activity. The activation of the YAP pathway will be assessed using the established activator YAP5SA. To develop a reliable method for evaluating gene transfer therapies, this study employed AAV9-mediated induction of YAP5SA, targeting the Hippo signaling pathway to regulate endogenous CM proliferation. Before examining the therapeutic potential of this gene therapy, this study aimed to assess and monitor gene expression levels in vivo through BLI, following delivery to the hearts of animal models with or without MI.

5.2 Aims

This comprehensive study is structured into four sections:

- The study aimed to assess the efficacy of ultrasound-guided gene delivery as a rapid and reliable method to precisely transport therapeutic genes to targeted areas.
- An imaging platform was established to monitor the activation of the YAP pathway using a YAP-sensitive luciferase, then test the activation of the YAP pathway with the known activator, YAP5SA.

- This study integrated BLI, Simpson's ultrasound, and MRI to monitor gene expression and CM proliferation over time while providing extensive structural and functional characterization of a mouse MI model after gene delivery.
- Advanced ultrasound techniques such as STE were applied to effectively evaluate regional cardiac function, offering further insights into the mechanisms underlying AAV9-mediated YAP transfer for cardiac regeneration following MI.

5.3 Methodology

This complex and multidisciplinary project involved several researchers across different universities. Three different AAVs were used in this study (Figure 5-1A):

- CMV-LUC = constitutively active firefly luciferase as a positive control to report on-target transduction efficiency and expression levels
- YAP-REP-LUC (YAPREP) = luciferase under the control of a YAP responsive promotor containing multiple TEAD transcription factor binding sites, to report activity of the YAP pathway. In this experimental setting, YAP/TAZ proteins (transcriptional co-activators) translocate into the nucleus and bind to TEAD transcription factors. This activates the YAP-sensitive promoter, leading to luciferase (Luc) expression (Figure 5-1B).
- CMV-YAP(5SA) (YAP5SA) = CMV driven mutant form of constitutively active YAP, which stimulates cell proliferation. In this experimental setting, the activity of the CMV-YAP(5SA) construct, which expresses constitutively active YAP5SA. YAP5SA enters the nucleus and interacts with TEAD transcription factors, driving continuous transcription of the luciferase gene under YAP-sensitive promoters, resulting in Luc expression (Figure 5-1C).

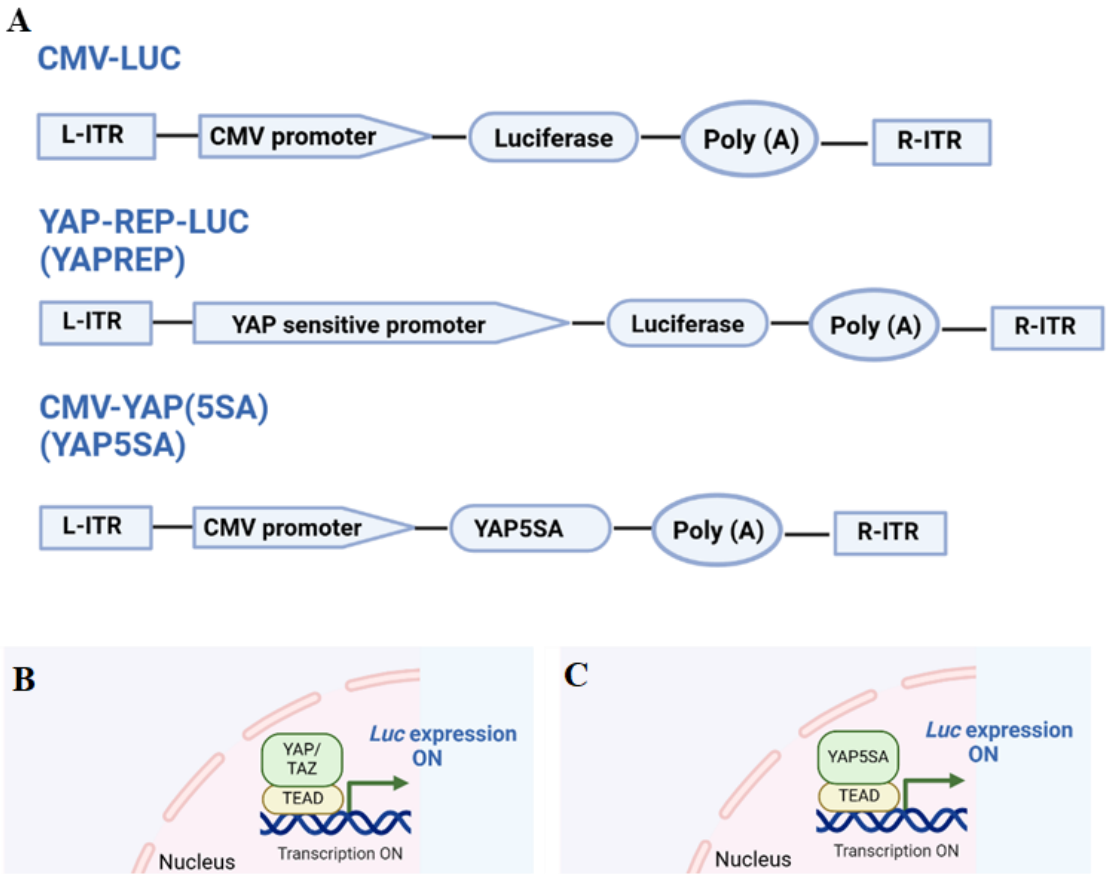

Figure 5-1. AAV9 constructs utilized in this study and schematic of luciferase expression activation by YAP/TAZ and YAP5SA-TEAD complexes. ITR: AAV inverted terminal repeat. Created with Biorender.

AAVs were synthesized in collaboration with Prof. Mauro Giacca's team at Kings College London and the International Centre for Genetic Engineering and Biotechnology, Trieste, Italy. Prof. Daniel Stuckey performed an ultrasound guidance injection of AAV-CMV/YAPREP/YAP5SA and acquired MRI imaging.

My contributions were as follows.

- BLI and analysis
- Surgical-induced MI model and animal welfare
- Ultrasound imaging of cardiac function/morphology
- Analysis of MRI and US data and interpretation of data
- Animal dissection, *ex vivo* imaging and tissue collections

5.3.1 Ultrasound guidance injection of AAV9

As demonstrated in Chapter 4, section 4.3.3, a similar method was performed to deliver AAV9-mediated gene transfer via ultrasound guidance. Adult female BALB/C mice weighing 20-25 g (n=26) were used for ultrasound-guided injection after anesthetized using a 2% isoflurane and oxygen mixture delivered by a nose cone. After removing hair, animals were kept at 37 °C using a heating pad, with mice positioned supine on an operation pad for monitoring ECG and heart rate via limb electrodes. Imaging required maintaining heart rate between 400-500 bpm by adjusting isoflurane concentration, with careful positioning of needles ensured prior to injections. The base-to-apex axis was aligned parallel to the transducer. A baseline cardiac assessment was conducted prior to initiating the injection protocol to confirm optimal transducer positioning. The needle was carefully advanced through the mouse's chest wall, with continuous monitoring of the beveled tip's position. Advancement was halted as the needle tip approached the target myocardium. Once the tip was appropriately positioned, the AAV vectors were delivered by gently pressing the syringe plunger. The needle was promptly withdrawn following administration. The mouse was kept under anesthesia for several minutes post-injection to assess ventricular function and ensure no complications occurred during echocardiographic evaluation.

5.3.2 Surgical induced myocardial infarction mouse model

As depicted in Chapter 2, section 2.3.1.2, a mouse MI model was established following the protocol. Basically, the animal first was intubated and then transferred to an operation pad in supine with the body temperature maintained at 37 °C using a heating pad. After the thoracotomy, the heart was fully exposed with left auricle can be seen in the surgical view. LAD was ligated 1-2mm below the tip of the left auricle. The ribs and skin were sutured to close the chest.

5.3.3 Bioluminescent imaging

Mice received an intraperitoneal injection of luciferin at a dose of 150 mg/kg after being anesthetized with a 2% isoflurane and oxygen mixture for imaging. BLI was performed using small binning, variable exposure, and F/stop adjustments to prevent

saturation. A grey-scale reference image was obtained under low-light conditions. Manually or automatically position the ROI over the area of interest (heart), where the bioluminescence signal is localized. The ROI size and position are the same across all images unless adjusting for significant signal spread. Measure the total photon flux (photons/second) emitted within the ROI using a data-acquisition PC running LivingImage software (Perkin Elmer).

5.3.4 Ultrasound assessment of cardiac function

Simpson's multiplane ultrasound was performed one day prior to MI conduction. As depicted in Chapter 3, section 3.3.3, mice were anesthetized and positioned in a supine position on the operating pad and kept at a temperature of 37 °C using a heating pad. Surface ECG limb electrodes were used to monitor the ECG and heart rate. The heart rate was maintained between 400 and 500 bpm during imaging by adjusting the concentration of isoflurane. The Vevo 3100 ultrasound imaging system (FUJIFILM VisualSonics, Toronto, Canada) with VisualSonic MX550S linear array transducer was utilized for all image acquisitions. Ultrasound images were acquired in PSLAX and PSAX views. In PSAX view, LV was analyzed at three parallel slices: (i) at the base level, (ii) at papillary muscle levels, and (iii) at the apex level. Measurements of LVEDL and LVESL are then performed from the PSLAX view. EDV and ESV were then calculated through a modified Simpson's rule.

Strain analysis was conducted across multiple dimensions, including longitudinal, circumferential, and radial measurements. This was performed by semi-automatically tracing the endocardium and epicardium borders in long-axis view for GLS and RLS, and in short-axis view for GCS, RCS, GRS and RRS. The myocardium was divided into six segments. The regional strain peak values were derived from the segmental myocardium and the global strain values were the average of all the segments.

5.3.5 MRI acquisition and assessment of cardiac function and morphology

Cine-MRI was performed in the short-axis view to acquire nine slices from the apex to the base of the LV as depicted in Chapter 3, section 3.3.2. The software Image J was used to analyze the cardiac function from cine images. EDV was obtained by segmentation of the LV endocardium in all end-diastole slices. Similarly, ESV was

obtained from endocardial segmentation in all end-systole slices. EF was calculated by EDV and ESV. Lateral and septal wall thickness was measured on the slice above the infarction.

5.3.6 Data analysis

Data is presented as mean and standard deviation (±SD). For all statistical tests, $p \leq 0.05$ was considered significant. Analysis of statistical significance for two or more groups was performed using a one-way ANOVA followed by Tukey's post-hoc test with Geisser-Greenhouse correction applied.

5.4. Results

5.4.1. Time course of AAV9 expression in mouse heart

To investigate whether BLI could be used to monitor luciferase-expressing AAV-mediated gene delivery to the heart *in vivo*, CMV-LUC (MOI 0.8*1011vg in 40µl) were injected into the anterolateral wall of five Balb/C mouse hearts under ultrasound guidance, with an additional 25µl injected into the hindlimb of one mouse. To monitor temporal gene expression dynamics, BLI was performed from day 1 to day 74 (Figure 5-2). Luciferase expression was detectable as soon as one day after delivery and was predominantly localized to the left midthoracic region of the mice (Figure 5-3A). Co-registration of 3D BLI and 3D whole body micro-CT on day 15 suggested the signals derived from the heart (Figure 5-3B). Quantitative analysis of luciferase expression is presented in Figure 5-3C, demonstrating detectable BLI signals on day one that reached a plateau by day 15 and remained sustained for a duration of 74 days. The highest BLI signal intensity was observed at the hindlimb injection site due to its superficial location and more excellent on-target retention than the contracting heart. One mouse was sacrificed on day three while the remaining four were sacrificed on day 74; their hearts were sectioned into three slices for *ex vivo* BLI analysis. *Ex vivo* BLI of heart sections exhibited a robust signal, particularly near the injection site. Some signals were also present on the chest wall (Figure 5-3D). These findings demonstrated that ultrasound can efficiently deliver AAV-mediated genes to the myocardium, and that BLI can be used to determine the site of AAV delivery and monitor gene expression long-term, and that CMV-Luciferase expression levels in mouse hearts were high and remained stable from 15 to at least 74 days.

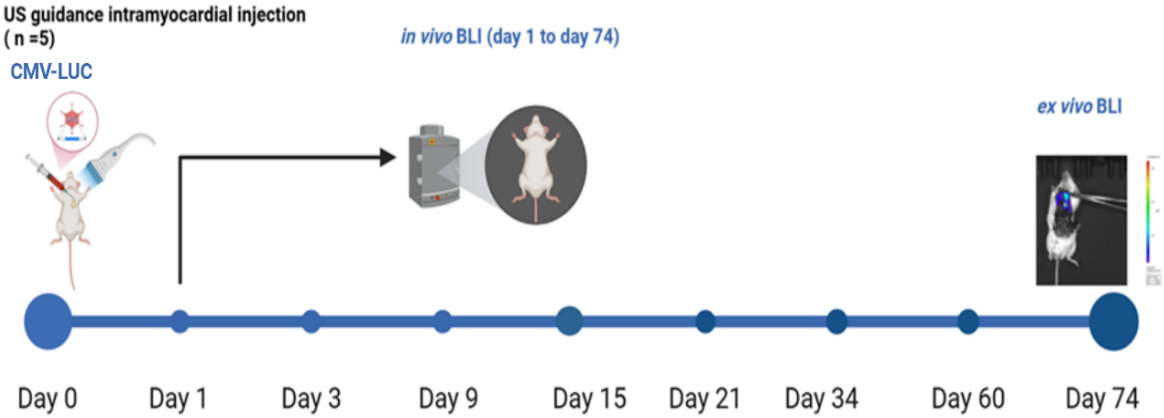

Figure 5-2. Experimental timeline schematic for monitoring CMV-Luciferase expression.

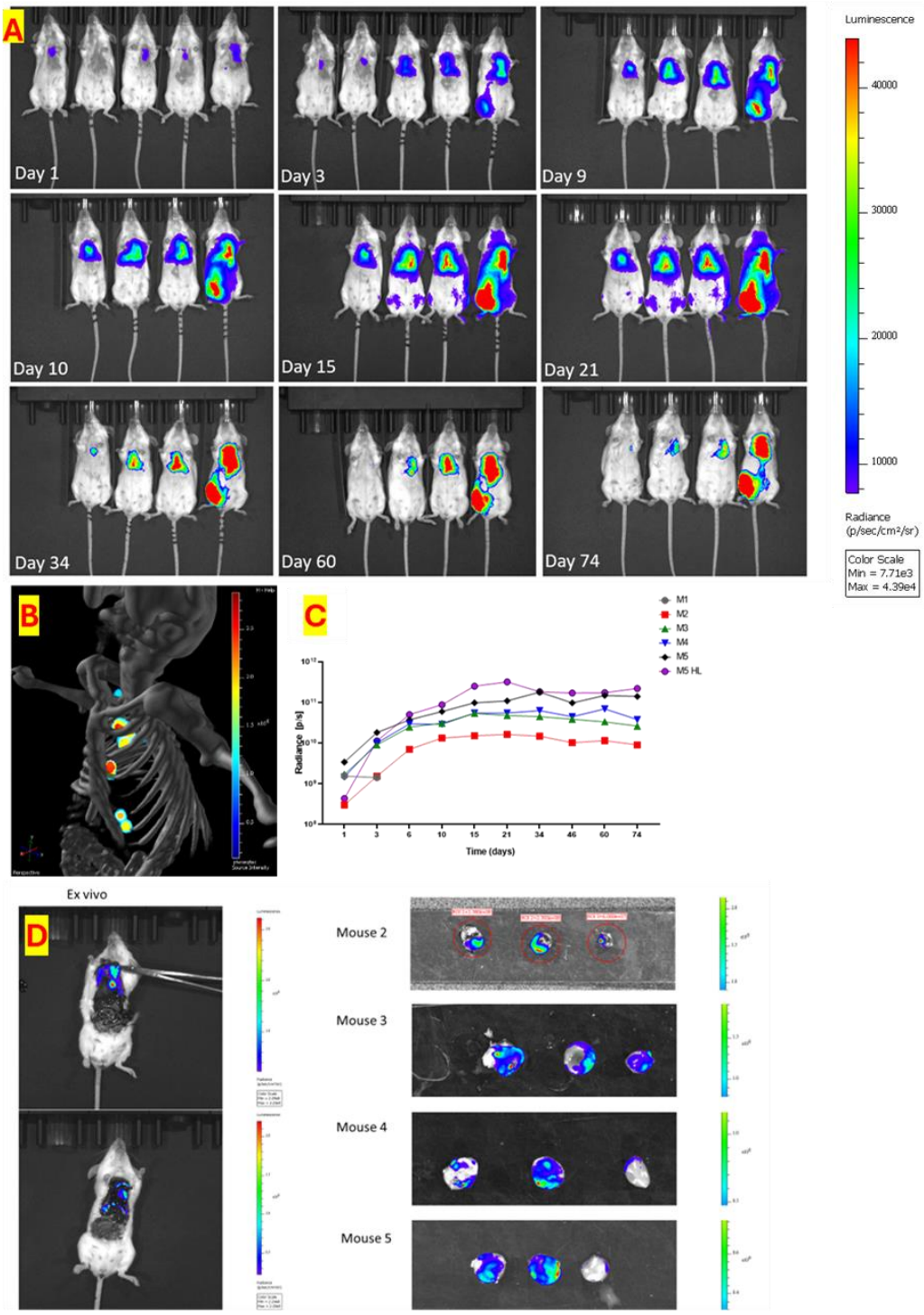

Figure 5-3. Bioluminescent imaging of CMV-LUC injected mice. Bioluminescent images were obtained from day 1 to day 74 following ultrasound-guided intramyocardial injection of CMV-LUC (A) (n = 5). 3D BLI and 3D micro-CT co-registration was performed on a representative mouse on day 15 (B). Luciferase expression exhibited predominant localization in the heart, reaching a stable level within 15 days post-injection and maintaining this level throughout the 74-day period (C). *Ex vivo* BLI demonstrated high-intensity signals near the injection site on heart slices (D).

5.4.2. *In vivo* bioluminescent imaging of YAP pathway activation before and after MI

To investigate whether BLI could be used to monitor the activation of the YAP pathway *in vivo*, luciferase-expressing AAV9 combined with a YAP responsive promotor (YAPREP-40µl) were injected into the anterolateral wall of 11 mice. Co-injection of YAPREP (40µl) with YAP5SA (40µl) was performed in another 15 mice into the anterolateral wall (Figure 5-4A). BLI was conducted on day 4 and day 12 following the injection. The YAPREP group showed signal slightly higher than background, indicating either a low level of leakiness of the promoter or representation basal YAP expression. The BLI signal from the YAPREP+YAP5SA group was significantly higher than the YAPREP group and was maximal at the earliest scan point, 4 days post-injection, as shown in Figure 5-4 B, C. Then there was a rapid decrease in the BLI signal intensity by 12 days post-injection in YAPREP+YAP5SA group. These data suggest that it is possible to use BLI and YAPREP to monitor the activation of the Hippo-YAP pathway serially in live mice and that activation from YAP5SA occurs rapidly after administration and is transient.

On the fourteenth day after the injection, a subset of mice underwent surgery to induce MI to determine whether BLI could be used to visualize the activation of the YAP pathway which is known to occur post MI. The following groups, YAPREP (n=4, animals underwent open-chest surgery without LAD ligation), YAPREP_MI (n=7), YAPREP+YAP5SA (n=7, animals underwent open-chest surgery without LAD ligation), and YAPREP+YAP5SA_MI (n=8) underwent BLI at 4-, 7-, 14-, 21- and 28-days post-surgery/sham (Figure 5-4A). No significant increase in BLI signal intensity was observed after MI in either the YAPREP_MI group or the YAPREP+YAP5SA_MI group (Figure 5-5). The data suggested that in this experimental setting, BLI may not be sensitive enough to detect the activation of the YAP pathway, which is expected following MI, although alternative explanations are presented in the Discussion.

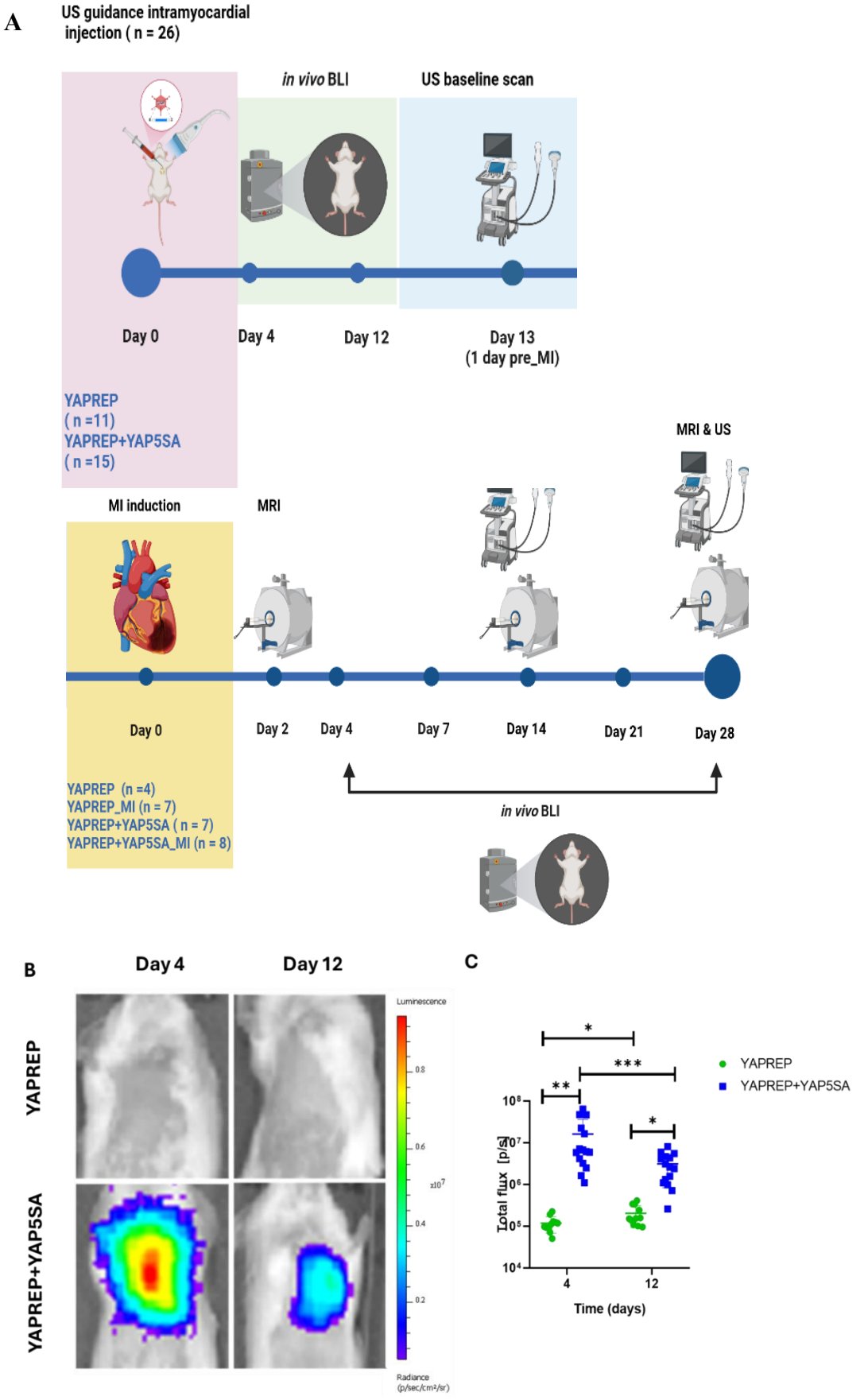

Figure 5-4. Experimental timeline schematic of study (A). BLI representative images (B) and signal intensity measurement (C) following injections of YAPREP and YAPREP+YAP5SA.

The YAPREP group displayed a relatively constant and low BLI signal intensity post-injection from day 4 to day 12. The YAP5SA group reached its maximum at the earliest scan point (day 4) and then decreased rapidly by day 12 post-injection. YAPREP group: n = 11; YAPREP+YAP5SA group: n = 15. One-way ANOVA followed by Tukey's post-hoc test with Geisser-Greenhouse correction applied.

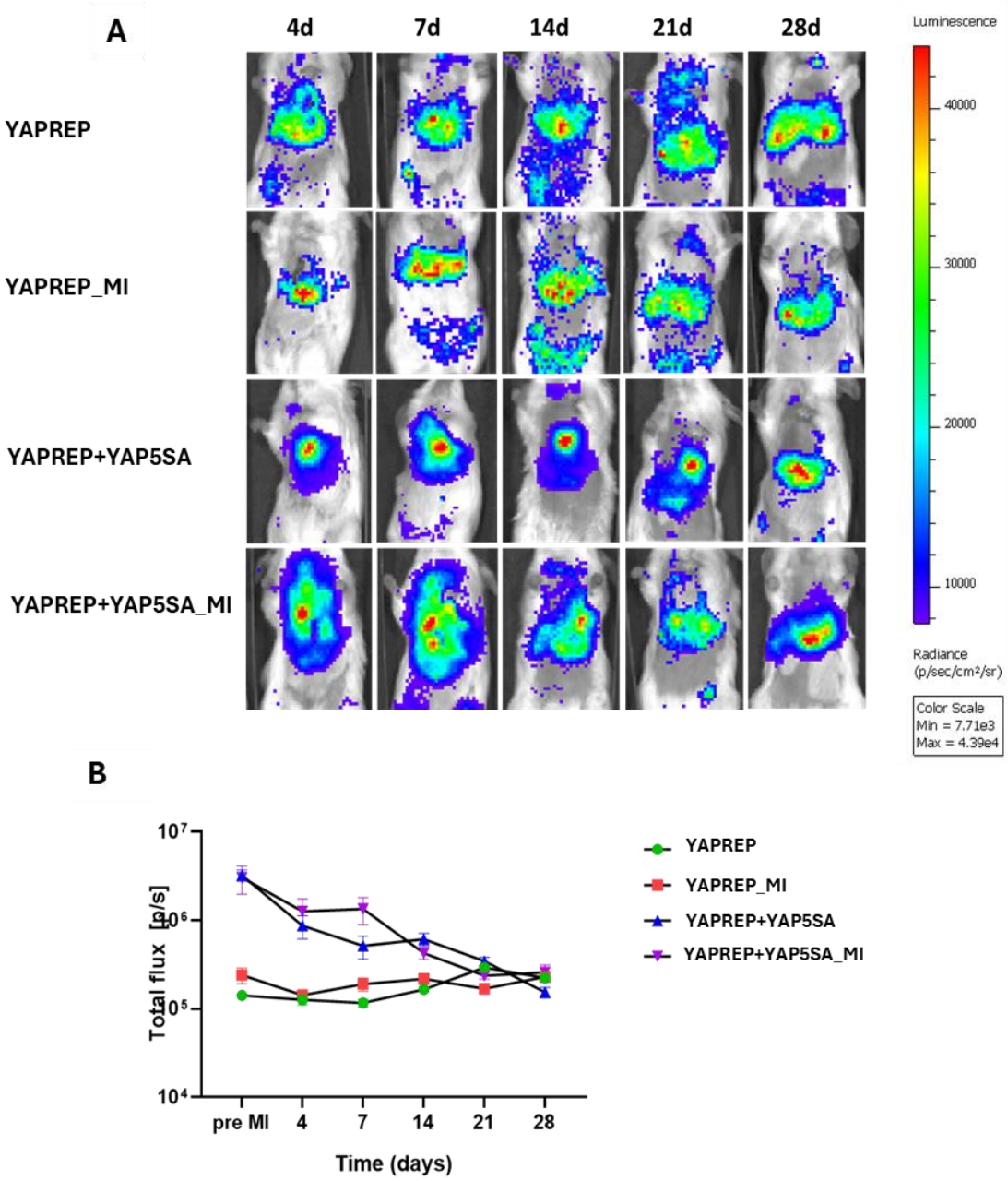

Figure 5-5. BLI representative images and signal intensity measurement following MI induction. The YAPREP and YAPREP_MI groups displayed a relatively constant and low BLI signal intensity from baseline. The YAPREP+YAP5SA and YAPREP+YAP5SA_MI groups decreased over time until attaining a similar level to that other two groups. YAPREP group: n = 4; YAPREP_MI group: n = 7; YAPREP+YAP5SA group: n = 7; YAPREP+YAP5SA_MI group: n = 8.

5.4.3. Ultrasound assessment of cardiac function and left ventricular wall thickness before MI

Ultrasound was performed 13 days post injection to determine baseline measures of cardiac function and wall thickness before MI was induced. Simpsons multi-plane was used to assess EDV, ESV, and EF. EDV ($p < 0.01$) (Figure 5-6A) and EF ($p < 0.001$) (Figure 5-6C) significantly decreased in the YAPREP+YAP5SA group compared to those in the YAPREP group. These data suggest that the YAP5SA may have a detrimental effect on cardiac function in normal heart even before undergoing MI surgery.

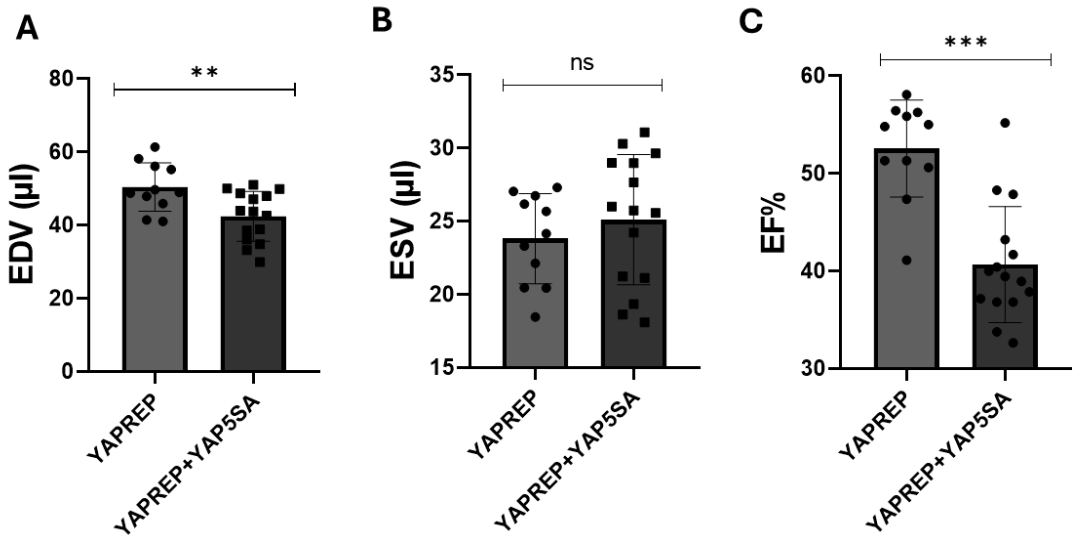

Figure 5-6. Ultrasound measurements of cardiac function prior to MI. EDV (A) and EF (C) showed significant decreases in the YAPREP+YAP5SA group (n = 15) compared to the YAPREP group (n = 11), $^{**}p < 0.01$, $^{**}p < 0.001$. One-way ANOVA followed by Tukey's post-hoc test with Geisser-Greenhouse correction applied.

Representative long-axis and short-axis ultrasound images of the LV acquired at end-diastolic are shown in Figure 5-7A, illustrating geometrical differences between the two groups. The myocardium was divided into six segments in both long- and short-axis views. In the long-axis view, there was a notable increase in anterior wall thickness within the YAPREP+YAP5SA group compared to the YAPREP group, primarily affecting all three anterior segments: Ant. Base, Ant. Mid, and Ant. Apex (blue arrow). In the short-axis view, a significant increase in wall thickness was observed in two segments within the YAPREP+YAP5SA group when compared to the YAPREP group (green arrow): lateral wall (Figure 5-7B) and anterior free wall

(Figure 5-7C) ($p < 0.001$). These data suggest that injections of YAPREP+YAP5SA induced wall thickening at the site of injection, which might exert a detrimental impact on cardiac function.

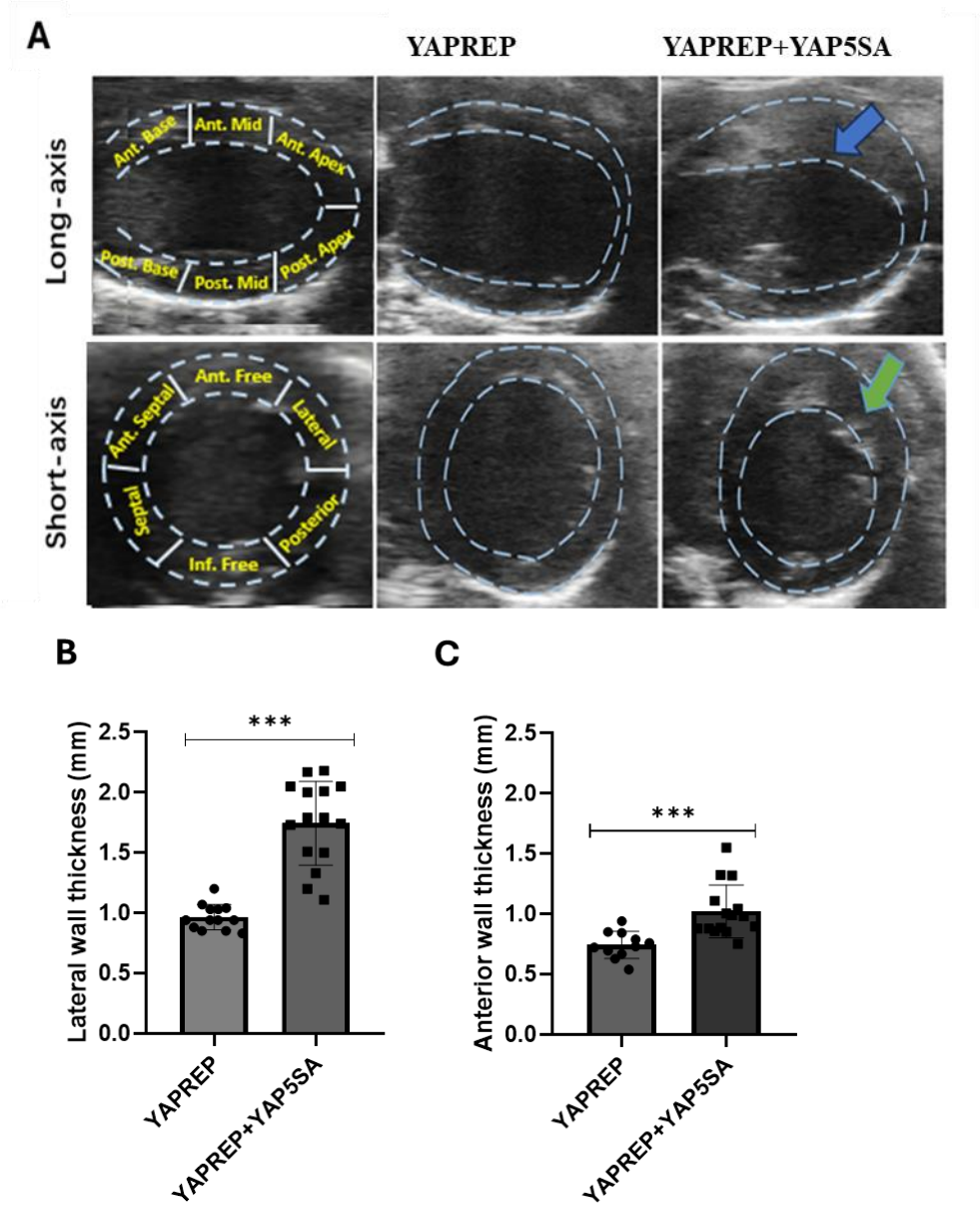

Figure 5-7. Ultrasound evaluation of wall thickness prior to MI in both long- and short-axis views. In the long-axis view, a notable increase in anterior wall thickness was observed in the YAPREP+YAP5SA group (n = 15) compared to the YAPREP group (n = 11) (blue arrow). In the short-axis view, there were significant increases in wall thickness within the lateral wall and anterior free wall segments of the YAPREP+YAP5SA group compared to the YAPREP group (green arrow) (A). Representative segmental measurements were obtained from the lateral wall (B), as well as from the anterior free wall in a short-axis view (C), ***$p < 0.001$. One-way ANOVA followed by Tukey's post-hoc test with Geisser-Greenhouse correction applied.

5.4.4. MRI assessment of cardiac function and infarction size post MI

MRI was performed on days 2, 14, and 28 post-MI. As expected, MI resulted in increased EDV and ESV and reduced EF in the YAPREP_MI and YAPREP+YAP5SA_MI groups by 14 days post-MI compared with both non-infarcted groups. By 28 days post-MI, EDV and ESV had further elevated ($p < 0.05$) (Figure 5-8 A-C). LGE-MRI revealed no significant differences in infarct size between the YAPREP_MI and YAPREP+YAP5SA_MI groups over 28 days, as depicted in Figure 5-8 D and E. This suggests that the activation of YAP may not yield a therapeutic effect for treating MI.

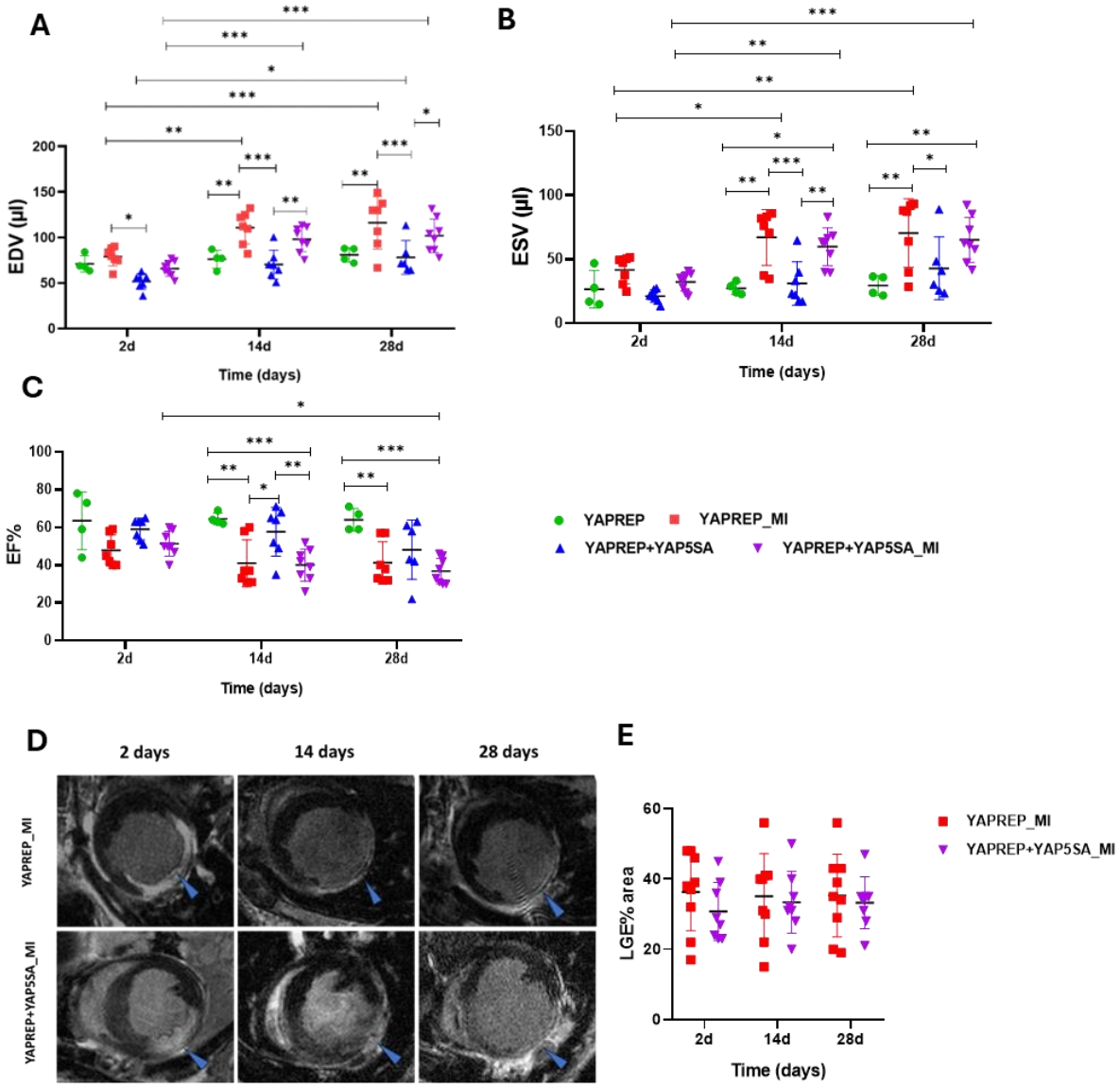

Figure 5-8. MRI assessment of cardiac function and infarct size post-MI. YAPREP_MI, YAPREP+YAP5SA, and YAPREP+YAP5SA_MI groups showed a significant increase in

EDV (A) and ESV (B) across the 28 days compared to the YAPREP group. EF decreased in both MI groups over time (C). The infarct size showed no significant change between MI groups over time (D, E). Blue arrows indicated the infarct regions. *$p < 0.05$, **$p < 0.01$, **$p < 0.001$. One-way ANOVA followed by Tukey's post-hoc test with Geisser-Greenhouse correction applied.

5.4.5. MRI assessment of cardiac wall thickening and asymmetry post MI

As there were no significant changes observed in cardiac function assessment between the YAPREP_MI and YAPREP+YAP5SA_MI groups over time, to gain a more comprehensive understanding of potential morphological changes induced by YAPREP+YAP5SA injection beyond functional alterations, further analysis was conducted to quantify LV mass, lateral wall thickness, and septal wall thickness. LV mass was significantly higher in both MI groups than the YAPREP group at all time points ($p < 0.001$), reflecting post-MI hypertrophy and remodeling. LV mass in the YAPREP+YAP5SA group without MI was also higher than the YAPREP group at all time points ($p < 0.01$), suggesting continued wall thickening induced by YAP5SA (Figure 5-9A). At two days post-MI, both YAPREP+YAP5SA and YAPREP+YAP5SA_MI groups exhibited increased LVM/EDV compared to the YAPREP group ($p < 0.01$); however, this increase was reduced over 28 days. By day 28, the LVM/EDV in the YAPREP+YAP5SA and YAPREP+YAP5SA_MI groups were significantly higher than that in the YAPREP_MI group ($p < 0.05$) (Figure 5-9B).

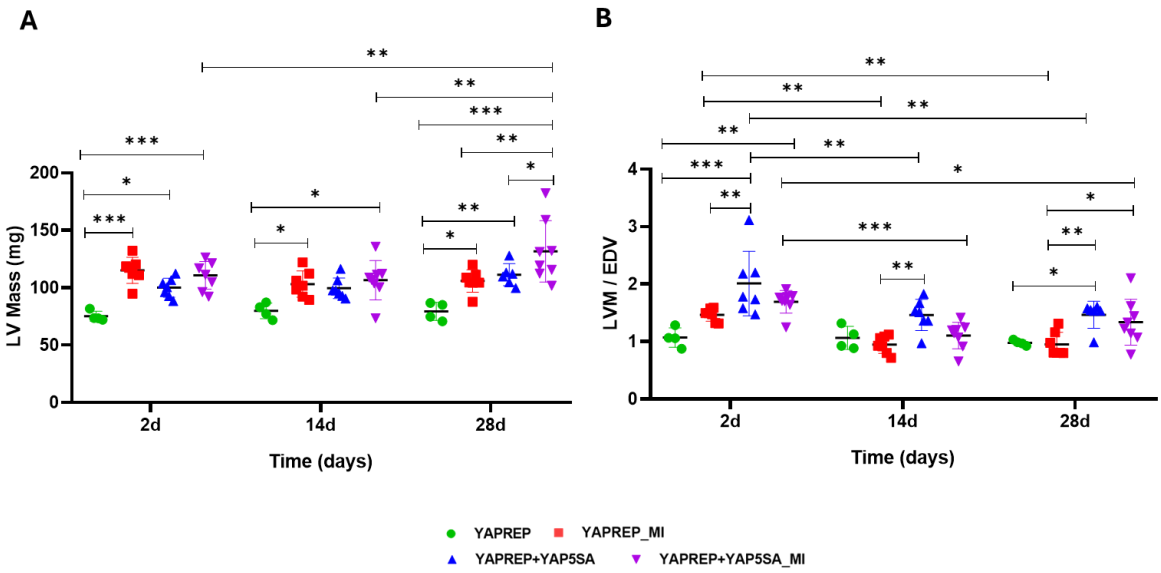

Figure 5-9. MRI assessment of LV mass and LVM/EDV. Both MI and YAPREP+YAP5SA groups showed an increase in LV mass compared to the YAPREP group over time. By day

28 days of post-MI, LV mass was significantly higher in YAPREP+YAP5SA_MI than in the other three groups (A). LVM/EDV showed an increase in YAPREP+YAP5SA, and YAPREP+YAP5SA_MI groups compared to YAPREP at two days post-MI, then reduced over 28 days. By day 28, the LVM/EDV in the YAP5SA-MI and YAP5SA groups was significantly higher than that in the YAPREP_MI group (B). *$p < 0.05$, **$p < 0.01$, **$p < 0.001$. One-way ANOVA followed by Tukey's post-hoc test with Geisser-Greenhouse correction applied.

The lateral wall (indicated by a blue arrow) and septal wall (indicated by a yellow arrow) thickness were measured in basal slices above the site of coronary occlusion to assess cardiac hypertrophy/hyperplasia and ventricular remodeling over 28 days following MI as depicted in Figure 5-10A. MRI measurement at two days post-MI revealed a significant increase in lateral wall thickness in the YAPREP+YAP5SA and YAPREP+YAP5SA_MI groups compared to the YAPREP and YAPREP_MI groups ($p < 0.001$). Subsequently, on 14 and 28 days, a reduction in lateral wall thickness was observed in the YAPREP+YAP5SA group (Figure 5-10B). By day 28, the YAPREP+YAP5SA_MI group showed significantly higher lateral wall thickness than the other three groups ($p < 0.05$). Septal wall thickness demonstrated no significant differences between groups by day 28, except for YAPREP+YAP5SA_MI, where the septum thickened over time by 28 days post-MI ($p < 0.05$) (Figure 5-10C). The thickening fraction of the lateral wall [Lateral THK% = $(THK_{-dia}-THK_{-sys})/THK_{-dia}$] was higher in YAPREP_MI than both the YAPREP+YAP5SA and YAPREP+YAP5SA_MI groups at all points ($p < 0.05$), possibly owing to increased contraction from the viable myocardial region to compensate for the reduced contraction within the distal infarct. The lack of increased contractility in the YAP5SA and YAP5SA_MI groups further highlighted the poor contractility of the myocardium at the site of YAP5SA injection (Figure 5-10D). The thickening fraction of septal walls (Septal THK%) was not different between groups (Figure 5-10E).

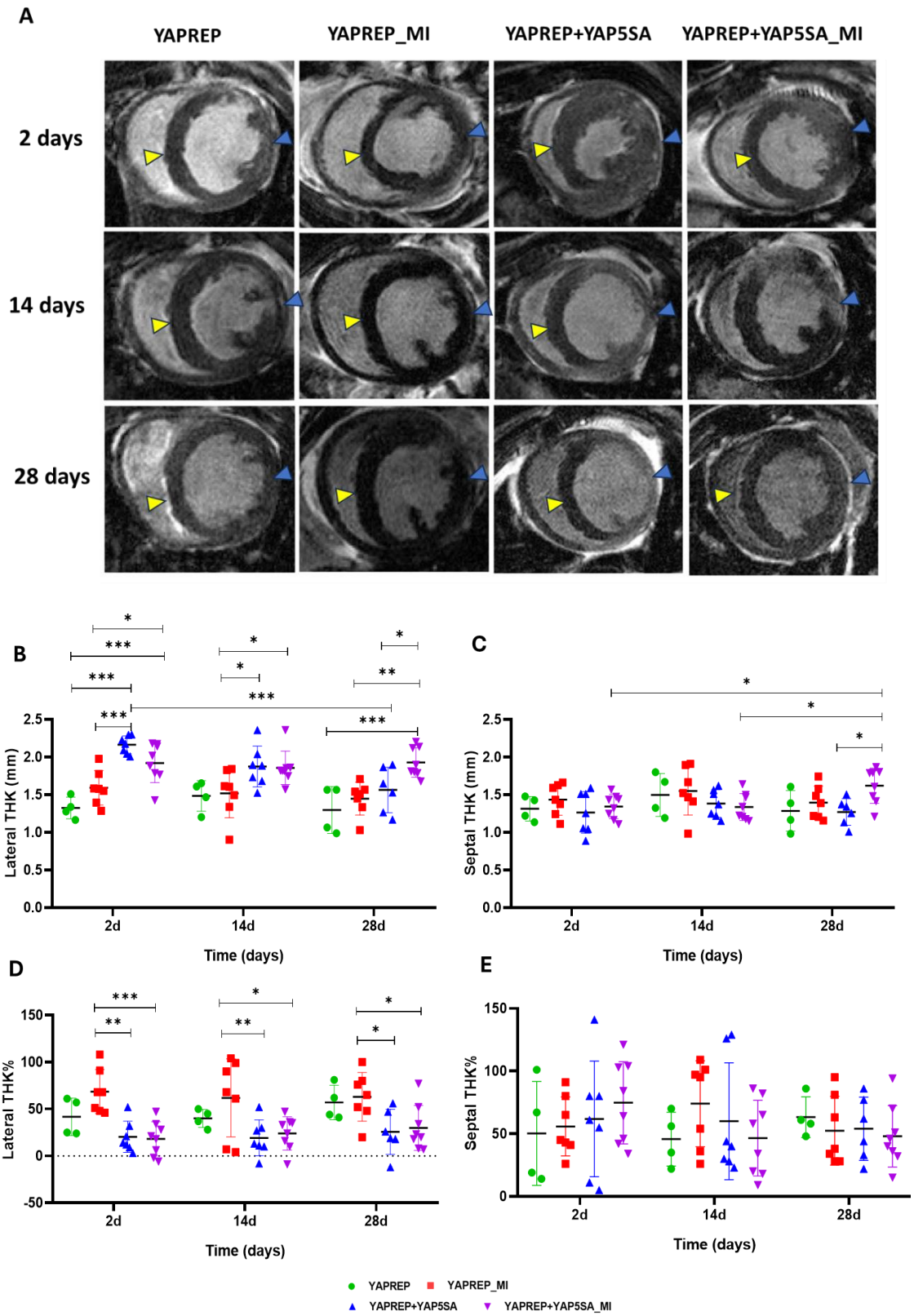

Figure 5-10. MRI assessment of lateral wall and septal wall thickness, thickening fraction of lateral and septal walls post-MI. Representative images of the lateral wall (indicated by a blue arrow) and the septal wall (indicated by a yellow arrow) from MRI in the four groups (A).The lateral wall thickness increased in both YAPREP+YAP5SA, and YAPREP+YAP5SA_MI groups compared to the other two groups over 28 days (B). Septal wall thickness significantly increased solely in the YAPREP+YAP5SA_MI group over time

(C). The lateral THK% was significantly decreased in the YAPREP+YAP5SA and YAPREP+YAP5SA_MI groups compared to the YAPREP_MI group within 28 days post-MI (D). *$p < 0.05$, **$p < 0.01$, **$p < 0.001$. One-way ANOVA followed by Tukey's post-hoc test with Geisser-Greenhouse correction applied.

Lateral-to-septal asymmetry refers to the difference in function or size between the lateral wall and the septum of the LV in the heart. A significant increase in lateral-to-septal asymmetry was presented in the YAPREP+ YAP5SA and YAPREP+YAP5SA_MI groups compared to the YAPREP and YAPREP_MI groups at all points ($p < 0.01$), further highlighting the regional wall thickening within the injection site. This asymmetry reduced over time as the anterior wall thinned in groups injected with YAPREP+YAP5SA ($p < 0.05$) (Figure 5-11A). The myocardial contraction fraction (MCF), representing the ratio of left ventricular stroke volume to myocardial volume, is a valuable indicator for evaluating both pathological and physiological hypertrophy and myocardial contractile efficiency. Compared to the YAPREP group, both MI and YAPREP+YAP5SA groups exhibited a reduced MCF ($p < 0.001$). By day 28, MCF significantly decreased in the YAPREP+YAP5SA, and YAPREP+YAP5SA_MI groups compared to the YAPREP_MI group ($p < 0.05$). The data further indicated reduced contractile efficacy after YAP5SA injection likely due to a myocardial architecture disruption (Figure 5-11B).

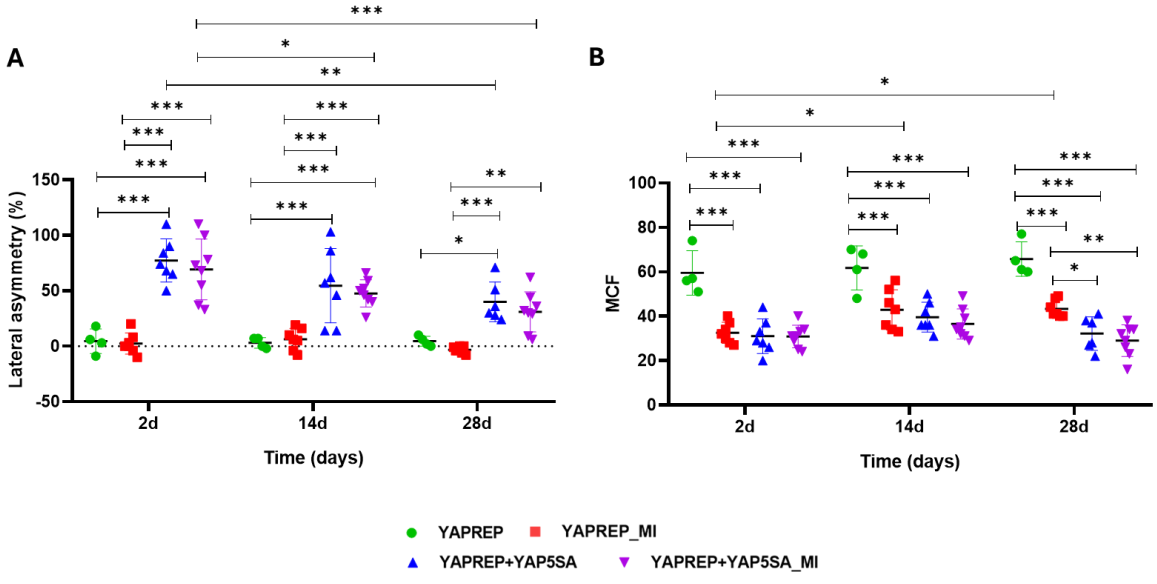

Figure 5-11. The lateral to septal asymmetry and MCF measurements between groups. The lateral asymmetry significantly increased in the YAPREP+YAP5SA and YAPREP+YAP5SA_MI groups, followed by a substantial decrease overtime (A). MCF significantly reduced in the YAP5SA group and both MI groups over 28 days (B). *$p < 0.05$, **$p < 0.01$, **$p < 0.001$. One-way ANOVA followed by Tukey's post-hoc test with Geisser-Greenhouse correction applied.

5.4.6. Strain analysis in the evaluation of cardiac function

The global strain parameters were evaluated through PSLAX (GLS) and PSAX views at the middle slices (GCS and GRS). GLS was significantly increased by day 28 only in the YAPREP+YAP5SA group compared to baseline ($p < 0.01$) (Figure 5-12A). GCS was significantly lower in the YAPREP_MI group compared to the YAPREP group by day 28 ($p < 0.05$) (Figure 5-12C). There were no significant differences among groups over time in GRS measurement (Figure 5-12E). All global strain parameters showed a significant but weak correlation with EF (Figure 5-12B, D, F).

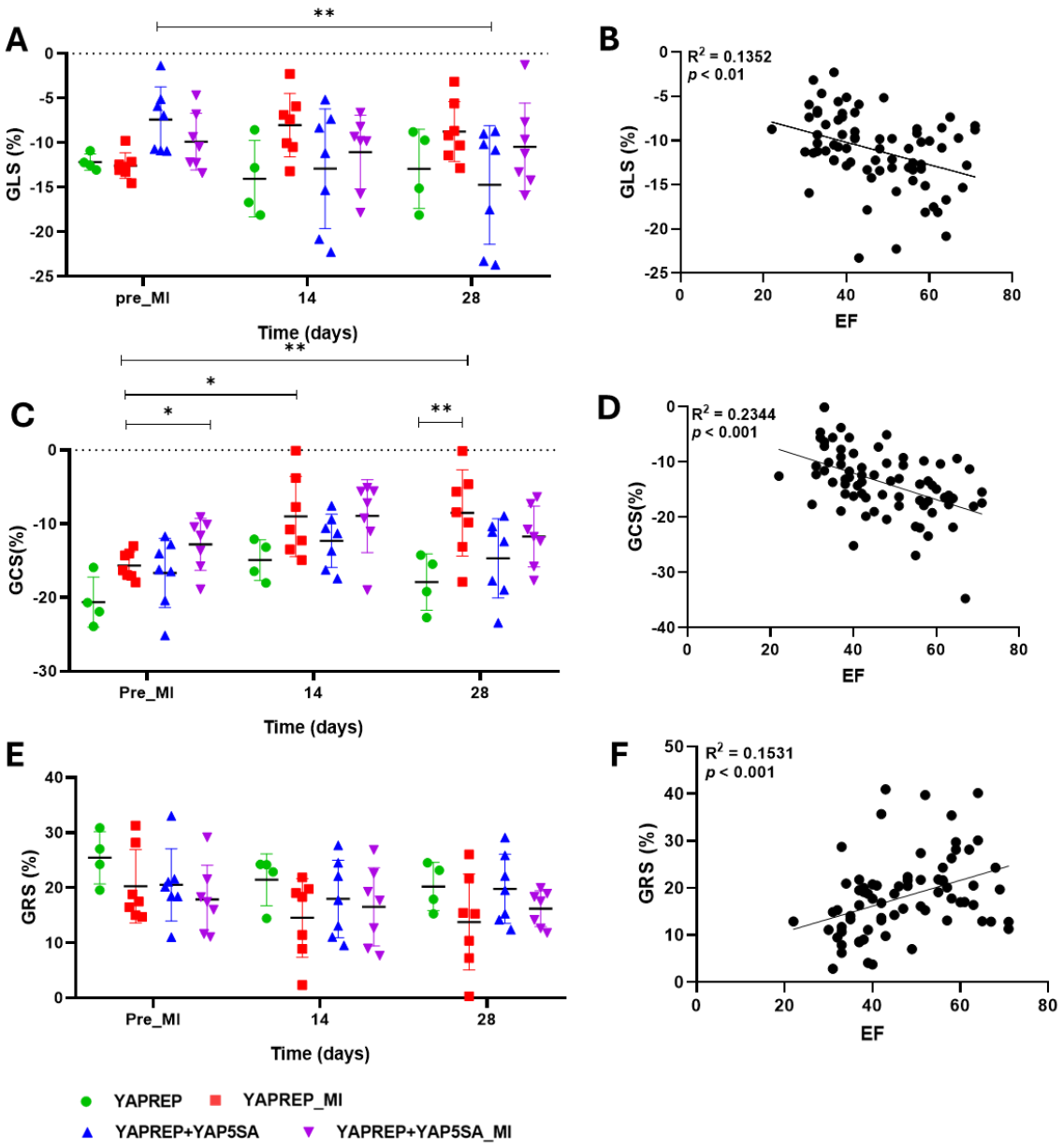

Figure 5-12. Global strain analysis for the assessment of cardiac function. GLS showed a significant increase in the YAPREP+YAP5SA group overtime (A). Only the YAPREP_MI group presented a marked decrease in GCS values over time by 28 days (C). Global strain analysis revealed a weak correlation with EF (B, D, F). *$p < 0.05$, **$p < 0.01$, **$p < 0.001$. One-way ANOVA followed by Tukey's post-hoc test with Geisser-Greenhouse correction applied.

Regional strain analysis was performed on a segmental basis to evaluate the regional contractile function of the LV myocardium. Based on our previous study, specific regions of interest for regional strain analysis after MI include the anterior mid (Ant. Mid), anterior apex (Ant. Apex), and posterior apex (Post. Apex) in the long-axis view, as well as the anterior free (Ant. Free) and lateral segments in the short-axis view. In

the long-axis view, RLS values in the YAPREP+YAP5SA group increased in the three regions of interest over time ($p < 0.05$) (Figure 5-13A). In the Ant. Apex, RLS value in the YAPREP+YAP5SA_MI group was significantly higher than the control MI group at day 28 ($p < 0.05$), potentially suggesting an improvement in cardiac function in the apex due to YAP5SA transfer (Figure 5-13B). A similar trend was identified in the Post. Apex segment but did not reach significance (Figure 5-13C).

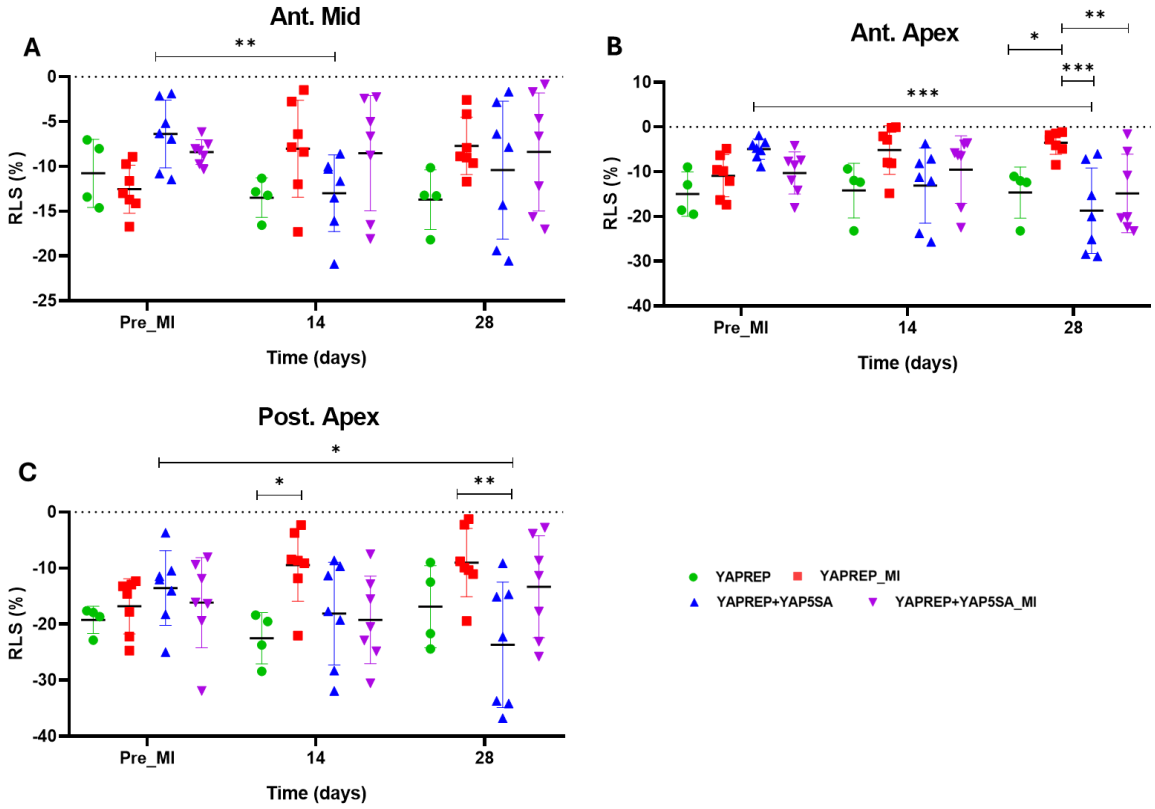

Figure 5-13. RLS assessment based on three interest segments. Ant. Mid (A), Ant. Apex (B) and Post. Apex (C). The YAPREP+YAP5SA group had significantly increased RLS values in all three interest segments over time. YAPREP_MI group showed notably lower RLS values in Ant. Apex segment compared to the other three groups by day 28. *$p < 0.05$, **$p < 0.01$, **$p < 0.001$. One-way ANOVA followed by Tukey's post-hoc test with Geisser-Greenhouse correction applied.

In the short-axis view, the RCS and RRS were evaluated at Ant. Free and lateral segments. Prior to MI, the RCS values of the Ant. Free wall and the RRS strain values of the Ant. Free and lateral wall diminished contractile function following the administration of YAPREP+YAP5SA. After MI, both MI groups showed a continuous decrease in the RCS values of the Ant. Free wall over time (Figure 5-14A). Only the YAPREP_MI group had decreased RCS values of the lateral wall by day 28, indicating functional impairment after injury (Figure 5-14B). In the measurement of

RRS, the strain value in the Ant. Free wall decreased over time in the YAPREP_MI group. It significantly decreased only in the YAPREP+YAP5SA_MI group by day 14. In contrast, in the lateral wall, only the YAPREP_MI group showed a significant decrease in RRS values from baseline to day 28 post MI. Taken together, the YAPREP+YAP5SA_MI group demonstrated a smaller region of myocardium with impaired cardiac function than the YAPREP_MI group, suggesting that there may be potential therapeutic effects at a regional level due to the YAP activation.

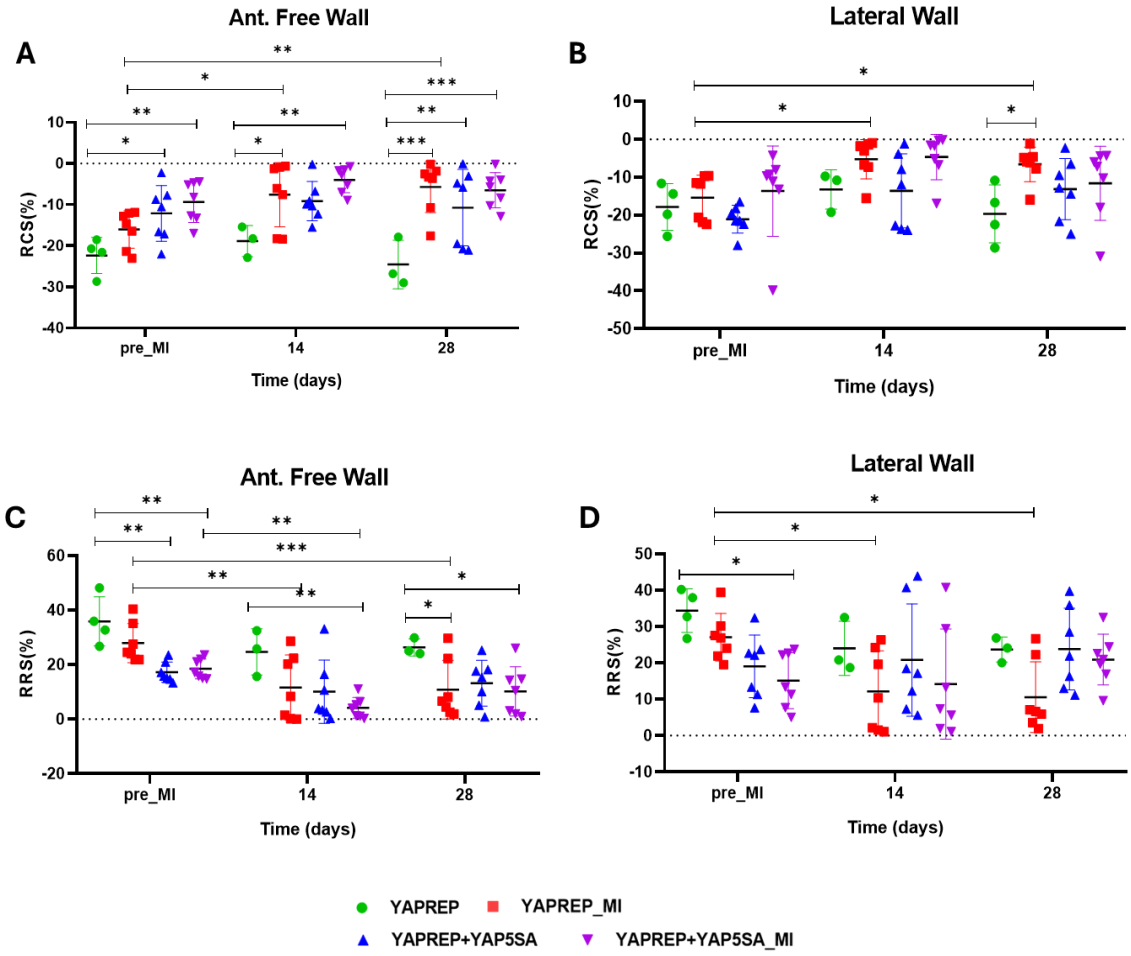

Figure 5-14. Regional circumferential and radial strain assessment based on two interest segments: Ant. Free and Lateral wall. *$p < 0.05$, **$p < 0.01$, **$p < 0.001$. One-way ANOVA followed by Tukey's post-hoc test with Geisser-Greenhouse correction applied.

5.4.7. Correlation of myocardial wall thickness with BLI signal intensity

Given that we identified an increased BLI signal and a thickening of the myocardium at the site of YAPREP+YAP5SA injection, we next investigated whether there was a correlation between myocardial tissue thickness and BLI signal intensity. We

correlated the BLI signal intensity obtained on day 12 post-injection with the measurements of lateral and septal wall thickness measured on day 2 post-MI. Figure 5-15A showed a significant correlation between lateral wall thickness and BLI signal intensity, whereas no notable correlation was found between septal wall thickness and BLI signal (Figure 5-15B). Furthermore, there was a significant correlation between the BLI signal and the ratio of lateral to septal wall thickness (L/S) (Figure 5-15C). These data suggest that the level of YAP pathway activation detected by BLI is directly correlated with the level of wall thickening identified by MRI.

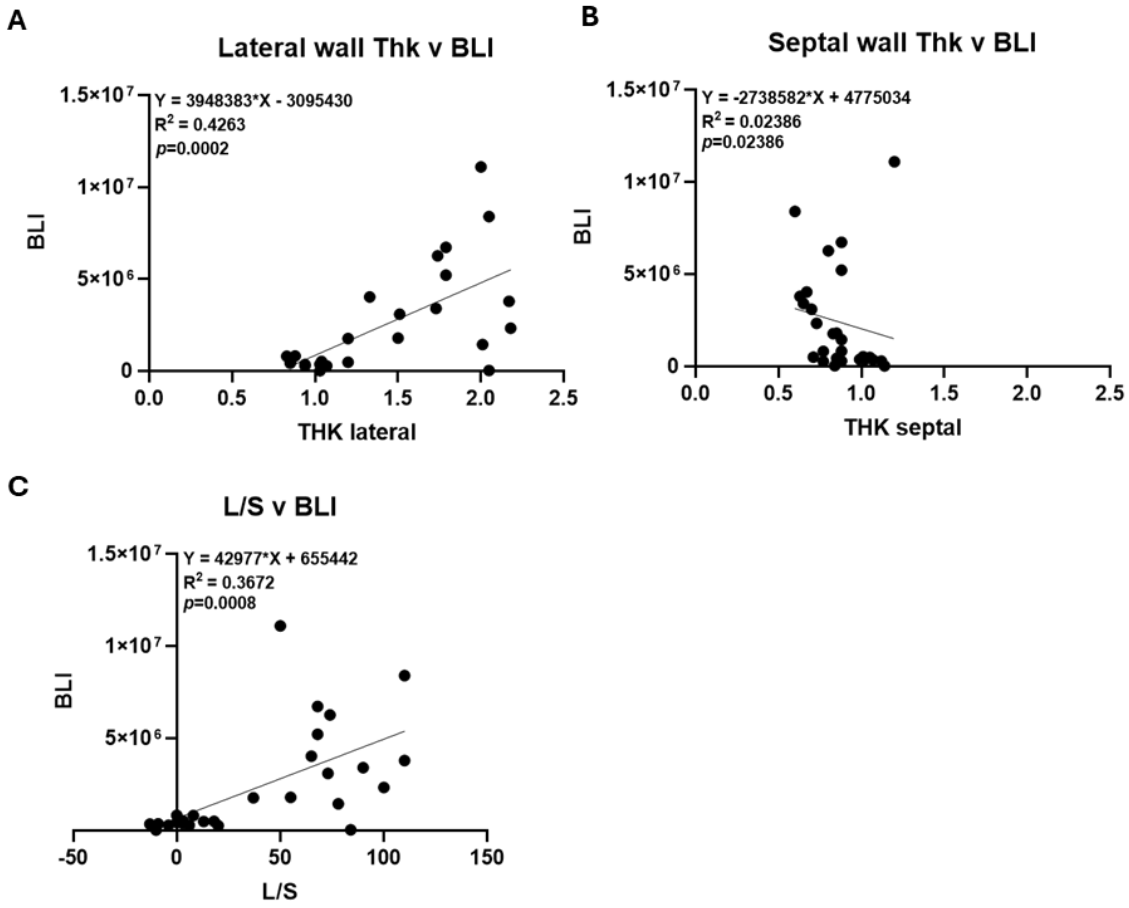

Figure 5-15. Correlation of myocardial wall thickness with BLI signal intensity. L/S: the ratio of lateral to septal wall thickness.

5.5. Discussion

AAV-mediated gene transfer is an attractive technique for the treatment of cardiac diseases. Lawrence *et al.* demonstrated that AAV9 exhibited exclusive targeting of the heart with a dosage approximately five times lower than that through tail vein injection while exhibiting limited exposure to extracardiac tissues such as the liver and muscle [449]. Boink *et al.* have developed a dual AAV system to efficiently deliver the skeletal muscle sodium channel 1 for the potential treatment of arrhythmias [450]. Ni's group has carried out a gene therapy using AAV-9, combined with the atrial natriuretic factor promoter, to establish a research platform for investigating the pathogenesis of atrial diseases [451]. Additionally, AAV-mediated gene therapy is an attractive prospect for cardiac regeneration, especially as current treatments do not address the central issue associated with MI - the massive loss of CMs due to the limited self-renewal capacity of the heart. Although several studies demonstrated early improvements in cardiac function after MI through YAP pathway activation, ultimately, several animals died of cardiac arrhythmia, likely due to the generation of arrhythmic foci and myofiber disarray arising from the uncontrolled and disorganized proliferation. Therefore, achieving a regulatory gene expression is of great significance for optimal therapeutics. As the YAP signal pathway continues to be examined in preclinical studies, the development of an imaging platform to noninvasively and efficiently monitor YAP expression, distribution and kinetics *in vivo* is required to modulate gene expression.

The Hippo signaling pathway modulates heart size by regulating cell proliferation during heart development [452]. During MI, cellular stress activates the Hippo signaling pathway and inactivates YAP1/TAZ, leading to CM apoptosis, fibrosis, increased infarction size, and subsequent impairment of cardiac function. Heallen and colleagues have demonstrated that inhibiting Hippo components or expressing a constitutively active form can potentially extend the period of CMs proliferation, leading to improved heart function after injury [453]. However, the mechanism underlying this process remains to be determined. Further understanding how YAP regulates CM proliferation through the Hippo pathway in cardiac injury is crucial for treating heart disease.

In this study, we minimally invasively deliver YAP pathway activatable luciferase-expressing AAV9 vectors to monitor the activity of the YAP pathway in normal physiological conditions; after activation by MI; and after direct stimulation using the mutant active form of YAP(YAP5SA). This approach aimed to establish a platform that can be utilized to test, monitor, and optimize activators of myocyte proliferation *in vivo* and provide insights into how to control and regulate CM proliferation.

5.5.1. Serially *in vivo* tracking of gene expression from AAV9 delivered luciferase

BLI has demonstrated remarkable success in providing semiquantitative measurements of various biological processes due to the strong correlation between the detected bioluminescence signal and cell numbers, both *in vitro* and *in vivo* [272]. In the first part of our study, we administered a cytomegalovirus promoter (CMV-LUC) into the anterolateral wall of five mice hearts to determine whether it was possible to serially track gene expression of AAV-delivered luciferase *in vivo*. The BLI signal was detected at the earliest imaging point and showed a continuous increase in signal until day 15. Subsequently, it plateaued until the end of the experiment on day 74. The high number of photons emitted allowed rapid image acquisition of novel 3D BLI to be performed with co-registration to 3D whole body micro-CT, and *ex vivo* BLI. These data determined that the strong BLI signal corresponded with the injection site in the heart, although some signals did derive from the chest wall. Further confirmed that luciferase delivered by AAVs can be serially followed *in vivo* and that expression level plateau at ~15 days, informing the optimal timeline for using a reporter system to monitor interventions to stimulate the YAP or other signaling pathways.

5.5.2. AAV9 delivered YAP driven luciferase does not generate a detectable increase in BLI signal after MI

After the AAV9-mediated YAPREP delivery, initial observations in control mice before MI revealed a low signal above background. The CMV-LUC BLI data showed stable gene expression plateauing after 15 days. Based on this, mice were subjected to infarction 21 days after being injected with YAPREP or YAPREP+YAP5SA. However, a series of BLI measurements from 4 days to 28 days post-MI demonstrated

that no significant increases in signal intensity were detected. A possible reason could be potential leakage from the injection site contributing to insufficient distribution and uptake of YAPREP within the target tissue. MI surgery procedure may result in the elimination of transfected cells.

5.5.3. YAP driven luciferase was activated by co-injection of YAP activator YAP5SA

In the second part of our study, we tested if BLI can be used to monitor CM proliferation stimulated by YAP activators (YAP5SA) in control mice. The results revealed that the BLI signal peaked at the earliest time point, day four after the injection in the YAPREP+YAP5SA group, followed by a swift decline by day 12 post-injection, indicating a rapid and transient activation. These data suggest cardiac-targeted gene transduction can be achieved by AAV9, which possesses a high tropism for the myocardium, along with the cardiac-specific promoters, and AAV9-YAPREP can be used as an *in vivo* readout of gene expression via BLI. To our knowledge, only one previous study has employed a similar approach where intramyocardial delivery of plasmid DNA for luciferase on a HIF1α promotor was conducted to monitor activation on gene expression in a mouse MI model, with BLI signal detectable for up to 4 weeks [454].

These data demonstrated the potential of BLI to serially monitor changes in gene expression pathways, and MRI and ultrasound to directly visualize the wall thickening *in vivo*. This would not be feasible using only endpoint readouts obtained through histology analysis alone. Traditionally, *in vitro* laboratory analysis of biopsies or autopsy tissue has been the primary approach for assessing the biological distribution and pharmacokinetics of gene therapy. However, this approach provides limited insights into the optimal type, dosage, administration route, and timing for gene delivery. This limitation is particularly evident *in vivo* due to challenges associated with real-time assessment of cellular activity within the heart [454]. Hence, *in vivo* BLI enhances the reproducibility of results by enabling repeatable detection and quantification, ultimately reducing the need for experimental animals, aligning with the principles of replacement, reduction, and refinement (3Rs). However, BLI has limited tissue penetrance (3–5 mm), so it cannot be extensively utilized in large

animal models or clinical settings. Nevertheless, given that most basic cardiovascular research relies on rodent models, BLI offers valuable insights for validating and optimizing novel therapies in small animals during preclinical studies of heart disease [272].

5.5.4. AAV9 delivered YAP activator YAP5SA induced morphological changes in the myocardium near the site of injection

Ultrasound conducted 13 days post-injection revealed a significant increase in Ant. Free and lateral wall thickness in the short-axis view and anterior wall in the long-axis view in the YAPREP+YAP5SA group compared to the YAPREP group, as depicted in Figure 5-7, suggesting a highly proliferative stage of YAP5SA activated CMs. Conversely, the wall thickness of Ant. Free and lateral wall segments significantly decreased in the YAPREP+YAP5SA group during the subsequent 28 days. This result could potentially be explained by the density-dependent growth inhibition demonstrated in an *in vitro* study. Mugahid *et al.* observed a density-dependent growth inhibition in YAP5SA-expressing cells, as evidenced by a decrease in cell growth rate with increasing cell density. The authors also noted a significant increase in cell death rate upon reaching high cell density and a larger YAP5SA-expressing cell size than control cells at low-density cultures [455]. Papizan and Olson demonstrated that YAP was released from inhibition and dephosphorylated at low cell density, facilitating its nuclear entry and activation of genes promoting growth. Conversely, at high cell density, YAP remained sequestered within the cytoplasm, where its ability to stimulate growth was inhibited [456]. Another study demonstrated that YAP5SA significantly enhanced the self-renewal and proliferation of human embryonic stem cells. However, a decline in the expression levels of YAP was observed in the YAP5SA group during prolonged culture (14 days post-transfection) [457]. Further statistics revealed that YAP expression retained its peak level only for a short term and subsequently gradually declined to approximately 60% of the maximal value in adult hearts [458].

Consistent with the ultrasound assessment of wall thickness, the BLI signal intensity peaked at the first measured time point (day four post-injection), followed by a significant decrease by day 12, indicating that YAP5SA-expressing cells achieved

their maximum density at or more likely before day four and subsequently underwent cellular atrophy. This finding further demonstrated the capability of *in vivo* BLI to monitor pathway activation, providing a valuable tool for the next generation of gene therapies, with our data indicating very early activation of YAP, which may have resulted in uncontrolled wall thickening.

5.5.5. Over-activated YAP affects cardiac remodeling progression and cardiac function

Although YAP5SA could initiate CM proliferation as demonstrated above, researchers did observe that an overactivated YAP gave rise to a deterioration of cardiac function. Von Gist *et al.* demonstrated that the overexpression of YAP in mice led to hemorrhaging and substantial myocardial hypertrophy, resulting in cardiac dysfunction [459]. These changes exacerbated cardiac injury and potentially contributed to chronic HF onset [160]. In our study, pre-MI ultrasound acquisition revealed a decrease in EDV and EF (Figure 5-7), and an increase in anterior-lateral wall thickness in YAP5SA group (Figure 5-8). This suggests that YAP5SA induced uncontrolled wall thickness at the injection site and was detrimental to cardiac function even prior to MI. This finding highlights the importance of accurately controlling gene delivery-mediated activation of proliferative pathways. In contrast, Monroe's team observed a significant increase in ventricular wall thickness and enhanced EF in hearts expressing tamoxifen-induced YAP5SA compared to control hearts. In this study, tamoxifen (40 μg/g) was administered once daily for four consecutive days [437]. The potential explanation of the difference is that in Monroe's study, they assessed cardiac function at an early point (one day after the fourth tamoxifen injection). In contrast, the ultrasound assessment in our study was conducted on day 12 post-injection. It is also possible that tamoxifen did not stimulate YAP5SA to the same levels are induced by direct administration of AAV9.

Initial MRI measurements of regional wall thickness and thickening at the anterior-lateral wall in basal slices proximal to LAD ligation revealed a significantly increased wall thickness in YAP5SA injected mice, resulting in a highly asymmetrical LV (Figure 5-9B). However, the thickening fraction in these regions was significantly reduced, suggesting that the thickened tissue displayed poor contractility (Figure 5-

10D). Further, the thickened tissue of the YAPREP+YEP5SA group became thinner after 28 days, indicating that overexpression of YAP ultimately led to atrophy of new myocytes. Meanwhile, other parameters further demonstrated the deteriorated cardiac function induced by over-expression of YAP. LVM/EDV has been characterized as an effective indicator of LV remodeling primarily utilized by cardiac MRI. The elevated LVM/EDV correlated with augmented myocardial fibrosis and dysfunction, offering insights into the changes in LV geometry and the type of hypertrophy [460]. In our study, LVM/EDV was elevated in the YAPREP+YAP5SA groups upon the initial MRI scan; nevertheless, it decreased after 28 days, possibly suggesting concentric hypertrophy initially and then a transition to eccentric hypertrophy at the late stage, as manifested by ventricular enlargement in MRI images, indicating that long-term overexpression of YAP led to poor myocardial contraction (Figure 5-10B). MCF has shown potential advantages over LVEF as another parameter that measures LV systolic function, which is described as the volume of myocardium required to eject a certain volume of blood. It represents the relationship between stroke volume and myocardial capacity, reflecting the efficiency of myocardial contraction [461]. In pathological cases, reduced MCF indicates abnormal shortening of the heart muscle due to ventricular dysfunction and geometry changes [462]. As depicted in Figure 5-11B, MCF exhibited a significant decrease in the YAP5SA group over time, which further highlighted that YAP5SA-induced hyperplasia was non-contractile and not contributing to contraction.

5.5.6. YAP pathway activation prior to induction of myocardial infarction did not result in an improved outcome

Following MI, MRI scans were conducted at 2-, 14- and 28-day intervals to assess changes in cardiac function and morphology. As expected, MI-induced increased EDV and ESV, a reduced EF and an infarct size of 30.12 ± 8.08% in the YAPREP group. YEP5SA did not prevent these changes, as shown in Figure 5-8, suggesting that YAP activation did not enhance cardiac function. Likewise, Windmuller and Morrisey's research has shown similar results. They depicted that continuous expression of miR302-367, a small RNA molecule targeting the Hippo/YAP pathway, increased CM proliferation in the adult murine heart. In moderation, this elevated YAP activity facilitated functional regeneration and enhanced cardiac function

following MI. However, long-term YAP activity induced a dedifferentiated phenotype and organ-wide dysfunction, ultimately causing HF [463].

The lack of notable therapeutic effects in our study could potentially be attributed to several factors: First, YAP-activated proliferation may solely occur at specific regions of the heart after MI, potentially limiting comprehensive treatment for the entire heart in the short term. Del Re *et al.* demonstrated that four days after MI, YAP was detected predominantly in the nuclei of CMs in the border zone (tissue adjacent to the scar), suggesting that a subpopulation of YAP was selectively activated at the injury site during MI [464]. Similar results demonstrated in Morikawa' s study that YAP expression increased in the border zone to regenerate the lost heart tissue [465]. Hence, to apply AAV-mediated YAP-expressing gene therapy targeted at the border zone, further studies could be carried out in a reperfused MI model that enlarges the size of the border zone, which is more clinically relevant. Second, MI surgery procedures potentially resulted in a high proportion of transfected CMs being lost. To test the above, further experiments were planned where CMV-LUC is administrated to mice 15 days before MI. As expected, luciferase expression should have plateaued by this point, and baseline BLI can be performed. The mice will then undergo surgery-induced MI, and BLI will be repeated serially to determine whether MI with infarct in the anterior-lateral wall can reduce the constitutively expressed luciferase. MRI, *ex vivo* BLI and histology will be undertaken to confirm injection site and infarct size.

For the segmental wall thickness measurement, however, in the YAPREP+YEP5SA_MI group, the anterior-lateral and septal walls remained thicker (Figure 5-10B). Additionally, our results revealed that MI significantly increased septal wall thickness only within the YAP5SA_MI group over 28 days (Figure 5-10C). This probably could be explained by the impact of YAP-mediated changes on cell size. Mugahid *et al.* co-cultured YAP5SA-expressing cells with wildtype cells and observed that YAP exhibited non-cell autonomous effects on cell size through the secretion of solute factors by YAP5SA-expressing cells, increasing the size of naïve cells [455]. Moreover, the substantial elevation in LV mass at day 28 post-MI observed in the YAP5SA_MI group compared to the other three groups suggests that YAP5SA induced CMs proliferation and enlargement in areas remote from the infarct and the site of injection (Figure 5-7A). LVM/EDV was elevated in the

YAPREP+YAP5SA_MI groups at two days post-MI, and then decreased after 28 days, possibly indicating concentric hypertrophy in the early stage of MI, which was confirmed by MRI-acquired images showing an increase in wall thickness without an increase in chamber size. However, the shift towards eccentric hypertrophy at the late stage of MI, shown as the ventricular enlargement, indicated potential maladaptive changes associated with sustained YAP overexpression. Additionally, MCF exhibited a significant decrease in the YAP5SA_MI group over time, further highlighting that YAP5SA-induced wall thickening did not contribute to contraction to improve cardiac function.

These studies highlight the importance of regulating gene expression effectively to ensure that cellular processes occur in a coordinated and balanced manner. Lin *et al.* demonstrated that in a mouse model expressing the activated form of human YAP specifically in CMs (YAP^{GOF}) under the control of doxycycline, long-term cardio protection was sustained. This was evidenced by the maintenance of heart size in doxycycline-treated YAP^{GOF} mice at a 4.5-month time point and attenuation of hypertrophic remodeling post-MI, leading to improved cardiac function and reduced infarct size 4 weeks after treatment [444]. In this study, researchers applied constitutively active YAP combined with Doxycycline induction. Doxycycline modulates YAP expression in a dose- and time-dependent manner [457]. Notably, they performed the induction of the combination one-week post-MI, thereby avoiding the immediate post-MI phase characterized by predominant cell death and targeting proliferative effects of YAP. The optimal timepoint for YAP activation after MI was also investigated in another study. Xin *et al.* demonstrated that the regenerative capacity of newborn mouse hearts was found to be diminished after day 7. To potentially extend the cardiac regeneration window, they induced the anti-phosphorylated activated form of YAP (YapS112A). In this study, ligation of the LAD artery was performed 7 days following YAP activation. Observations revealed a significant reduction in LV fibrosis and a marked improvement in myocardial tissue among mice overexpressing YAP. However, in our study, we injected YAP5SA to upregulate YAP expression nearly two weeks prior to MI, potentially missing the optimal therapeutic window.

Overall, the findings indicated that YAP overexpression can induce abnormal cardiac

remodeling rather than beneficially promoting proliferation of CMs, in which the timing of YAP induction following MI may play a crucial role in determining cardiac repair and regeneration. It is suggested that delayed induction of YAP post-MI, coupled with transient YAP expression, may hold significant potential for enhancing cardiac recovery after MI.

5.5.7. Ultrasound-guided gene delivery is a robust, and reproducible approach for conducting gene transfer

A high level of CM transduction is required to achieve long-term efficacy in gene therapy for heart disease. While several vector delivery techniques have been developed, direct intramural injection has emerged as the preferred approach in numerous preclinical studies, owing to its ability to achieve strong specificity and sustained transgenic expression [141]. In our study, we employed ultrasound-guided injections to achieve a rapid and minimally invasive procedure compared to alternative methods such as catheter delivery systems and IV injection. The ultrasound-guided injections were successfully performed in all animals without any mortality. As reported, AAV9 demonstrated highly efficient gene transfer to the LV free wall of rodents following direct intramyocardial injection and maintained stability for up to 1 year [449]. Consistent with our BLI findings, ultrasound-guided intramyocardial injection exhibited rapid onset and relative stability for a minimum of 74 days.

Ultrasound-guided direct intramyocardial injection offers several advantages, including avoiding non-cardiac tissue transduction and subsequent toxicity, titer dilution, and post-intravenous systemic neutralization. Also, the use of minimally invasive injection methods can avoid traumatic thoracotomy and more closely mimic the human transcutaneous approach employed in clinical practice. However, it is essential to consider the limitations associated with intramuscular injections when evaluating treatment options. For example, transduction is confined to the vicinity of the injection site, potentially limiting comprehensive treatment for the entire heart. Another significant limitation arises from the development of acute inflammation at the injection sites due to needle-induced injury, which may trigger an adaptive

immune response against the vector and/or transgene products, thereby restricting the efficacy of the therapy [141, 466].

In this study, ultrasound was not only used as a delivery approach but also enabled the assessment of alterations in cardiac morphology and quantification of global cardiac function through parameters such as EDV, ESV and EF. Moreover, an advanced ultrasound technique, STE, was employed to evaluate regional myocardial function by measuring regional wall thickening and thinning, providing detailed information regarding the activation of the Hippo-YAP pathway which will be discussed below.

5.5.8. Strain analysis for the assessment of deformation in infarcted segments

Recent research has demonstrated that STE can detect early prehypertensive myocardial deformation even if EF remains unaltered [467]. As confirmed in our study, Figure 5-12 depicted a significant relationship between LV global strain parameters and LVEF through linear regression analysis (all $p < 0.01$). In the long-axis view, RLS exhibited a notable decrease in Ant.Mid, Ant.Apex, and Post.Apex within the YAPREP_MI group after 28 days post-MI procedure, although only reached statistically significant in Post. Apex segment: These regions corresponded to infarct areas on the LV. In the YAPREP+YAP5SA group, RLS significantly increased in these segments over time and by day 28, RLS values were significantly higher in the YAPREP+YAP5SA group than that in the YAPREP_MI group in both apical segments. Part of newly formed myocytes may migrate distally to apex at the late stage, which was supposed to be the damaged region. These new myocytes may have compensatory effect on myocardial contraction, which can be confirmed by the improved RLS values in YAPREP+YAP5SA_MI group compared to YAPREP_MI group.

In the short-axis view, RCS and RRS values on Ant. Free wall showed significant decreases in the YAPREP+YAP5SA group compared to the YAPREP group prior to MI, indicating YAP over-expression induced cardiac wall thickening impaired the cardiac contractility. After MI, the MI and YAPREP+YAP5SA groups presented decreased RCS and RRS values in the Ant. Free wall, while only the YAPREP_MI group displayed decreased strain values in the lateral wall. These findings imply that

the YAP5SA_MI group exhibited a smaller area of myocardium with compromised cardiac function compared to the YAPREP_MI group, suggesting that the newly generated myocytes had limited impacts on enhancing cardiac contraction since only regional cardiac function displayed indications of improvement, and no notable enhancement was witnessed in global cardiac function.

However, significant variability of strain values was observed in RCS and RRS measurement in contrast to RLS, especially in YAPREP+YAP5SA and YAPREP+YAP5SA_MI groups. Several possible reasons could explain the results. First, in the YAPREP+YAP5SA and YAPREP+YAP5SA_MI groups, circumferential tracking is more susceptible to wall thickening caused by the over-expression of YAP, which influences acoustic properties. Also, the increased relative wall thickness induced a concentric geometry change and limited myocardial compressibility. Consequently, the RCS and RRS in the Anterior Free and Lateral walls decreased. Second, the orientation of myocardial fibers contributes to the difference. The subendocardial and subepicardial fiber layers are longitudinally oriented and arranged in counter-directional helical loops. The midwall fibers are circumferentially oriented. This architecture determines the systolic longitudinal shortening and torsion of the LV, and the thickening of the myocardium in the radial direction, which in turn causes the shift of the endocardium towards the LV cavity [468, 469]. LS can be quantified by directly estimating the cardiac deformation along the beam direction from parasternal long-axis views. The reliability of LS assessments exceeds that of RS primarily because LS provides the most accurate representation of myocardial deformation at the endocardium level, and the apical window enables tracing of all left ventricular segments [470, 471]. In addition, due to its distance from the epicardial coronary artery, the subendocardial fiber layer is more sensitive to myocardial ischemia, and LS seems more sensitive and effective at recognizing abnormal movements [468]. However, CS and RS, assessed in a parasternal short-axis view, cannot be directly derived from displacement and strain estimated along the beam direction [472]. Josef and his colleagues have shown a relatively lower resolution for displacement and strain components perpendicular to the beam propagation direction compared to those estimated along the beam direction [472, 473]. Thomas *et al.* demonstrated that RS in short-axis view has been the most challenging strain component to measure as RS mainly represents mid-myocardial

layers, showing more significant variability and less reproducibility compared to assessment of CR and LS [474]. The RS was assessed by manually delineating the endo- and epicardial LV boundaries in an early-systolic frame, followed by automatic calculation of time-derived radial strain. This method is operator-dependent and relies on the accurate identification of a suitable ultrasound cardiac window. However, challenges may arise due to suboptimal image quality or rib artifacts, making it difficult to trace the epicardial border. This may explain the abnormal trend of RRS in the Ant. Free wall in the YAPREP+YAP5SA_MI group evaluated by day 14 post-MI, as shown in Figure 5-14C.

Hence, strain analysis has the potential to detect subtle changes in LV function and myocardial deformation. The findings from this study indicate that the evaluation of regional cardiac performance through strain analysis reflects cardiac functional changes at an earlier stage than EF. This is based on the results, which showed that the assessment of LS demonstrated improvements at the apex, while the evaluations of CS and RS detected improvements in the lateral wall. This suggests that strain analysis could be a superior predictor of patient outcomes compared to EF measurements.

5.5.9. Correlation of BLI signal intensity with myocardial wall thickness

Our data demonstrated that a significant but weak correlation was observed between lateral wall thickness and BLI signal intensity ($R^2 = 0.43$, $P < 0.01$). In contrast, no notable correlation was found between septal wall thickness and BLI signal (Figure 5-15B). Furthermore, there was a significant correlation between the BLI signal and the ratio of lateral to septal wall thickness (L/S) ($R^2 = 0.34$, $P < 0.01$). The correlation analyses confirmed that BLI exhibited a significant advantage due to its direct reflection of myocyte regeneration, suggesting a direct correlation between activation of the YAP pathway and wall thickness. Overall, these findings validated the highly efficient expression of AAV9-mediated YAP5SA in cardiac tissue, suggesting that BLI can serve as a reliable platform for long-term monitoring of cardiac gene expression.

5.5.10. Alternative regulatory mechanisms of YAP pathway following myocardial infarction

Further investigations into the interplay between the YAP pathway and other key molecular factors involved in tissue repair and remodeling after MI are crucial for advancing our understanding of cardiac regeneration. Exploring the intricate crosstalk between YAP signaling, various cell types, and the ECM holds great potential for uncovering novel therapeutic targets and strategies to enhance post-MI healing.

Macrophage polarization, regulated by YAP expression, may play an important role in determining treatment. Research conducted by Miyamura and colleagues had previously demonstrated that the YAP-activating hepatocytes proliferated without cellular stress. However, after liver injury, YAP5SA-expressing hepatocyte fate changes from proliferation to migration/apoptosis. The YAP-activating hepatocytes were eliminated with the participation of Kupffer cells, the sinusoid-resident macrophages, via the mechanism from senescence surveillance [172]. Following MI, the death of CM initiates an acute inflammatory response via the recruitment of macrophages to the damaged area. This process is crucial for activating repair mechanisms that prevent additional CM loss, reduce the formation of a dense fibrotic scar, and maintain the structural integrity of the heart tissue. Mia group has investigated the roles of YAP/TAZ in regulating the polarization of macrophages after MI. YAP/TAZ-deficient mice exhibited enhanced cardiac remodeling and improved function post-MI, as indicated by reduced cardiac fibrosis, decreased cardiac hypertrophy, and improved angiogenesis. In contrast, mice with overexpressed active YAP variant (YAP5SA) displayed reverse effects, with macrophage polarization leading to increased fibrosis and detrimental cardiac remodeling after MI [475]. Korpela *et al.* also reported that the therapeutic efficacy of AAV2 gene transfer was compromised by inflammatory responses, leading to a significant reduction in successful transduction and long-term gene expression [446]. In line with these results, our study similarly revealed that the overexpression of YAP had a negative impact on facilitating the recovery of cardiac function after MI in the YAP5SA_MI group based on the fact that we delivered YAP5SA prior to MI occurring, indicative of the significance of YAP expression in modulating the inflammatory and healing

responses after MI potentially by influencing the polarization of macrophage.

In theory, cells not only perceive their extracellular environment through biochemical signals but also respond to physical and mechanical stimuli within the ECM [476]. Myocardial fibrosis, a fundamental pathological aspect of structural remodeling in MI, is primarily characterized by increased collagen deposition in the interstitium and perivascular regions of the myocardium, leading to increased ventricular stiffness, diastolic dysfunction, arrhythmia, and potentially sudden death. The rigidity of ECM has been acknowledged as a crucial mediator influencing cardiac cell behavior [477, 478]. The study conducted by Arshi *et al.* demonstrated that the stiffness of the ECM regulated the maturation of differentiated cardiac myocytes and influenced the induction and proliferation of CMs from undifferentiated progenitor cells [479]. Recently, evidence suggested a direct correlation between diverse nuclear transcription factors and mechano-regulated cellular activities. Specifically, YAP is recognized as the prototypical mechano-sensor responsible for transducing mechanical signals, such as ECM stiffness and cell morphology, into biological outcomes [480]. The study conducted by Dupont and colleagues demonstrated that mechanical signaling through changes in cell shape and alterations in cytoskeletal tension affected the activity of the Hippo-YAP signal pathway. The findings noted that YAP1/TAZ exhibited nucleus translocation and increased transcriptional activity in a stiff ECM, whereas they underwent cytoplasmic sequestration in a soft ECM, resulting in reduced YAP1/TAZ activity. These results support the hypothesis that YAP1/TAZ activity is crucial for cell differentiation following cardiac ECM remodeling and/or fibrosis after MI [160, 481]. The study conducted by Bassat *et al.* involved the application of agrin, derived from neonatal ECM to adult mice following MI. This intervention effectively promoted cardiac regeneration and enhanced cardiac repair, potentially through ECM softening that may induce the dedifferentiation of mature CMs [482].

The post-MI remodeling process consists of three distinct phases: the inflammatory phase (first three days), the proliferative phase (3–14 days), and the maturation phase (2 weeks–2 months). Initially, there is a peak recruitment of immune cells around three days after MI. Subsequently, the recovery phase occurs within 3–7 days of MI, during which macrophages play a crucial role in mediating ECM-related fibrosis and

scar formation [483, 484]. In our study, the BLI signal demonstrated a small increase in both YAPREP_MI and YAP5SA_MI groups from day 4 to day 7 post-MI, as depicted in Figure 5-3B. This observation suggests that YAP nuclear translocation and enhanced transcriptional activity may occur during the proliferative phase (3 to 14 days) of post-MI remodeling. However, it was not significantly enhanced in BLI signal intensity and was insufficient to improve cardiac function.

5.5.11. General discussion and conclusion

AAV9-mediated YAP transaction and activation was not employed here as a realistic therapeutic option, but to determine whether high-level activation of the YAP could be monitored *in vivo* and to identify how cardiac function would be affected in control and infarcted mice. The acute wall thickening and subsequent wall thinning confirmed a strong induction of changes to the myocardium, presumably through cell proliferation, although histology will be required to confirm this. However, the detrimental effects on cardiac function even without MI highlight the need for tight control of these therapies. Gabisonia's group's research on the expression of human microRNA-199a in infarcted pig hearts has sparked significant interest and potential implications for cardiac repair [436]. In addition to the notable improvements in global and regional contractility seen one-month post-treatment, the decreased scar size and increased muscle mass observed in treated animals may be attributed to CM de-differentiation and proliferation induced by microRNA-199a expression. However, concerns regarding long-term safety have emerged with several animals died of cardiac arrhythmia likely owing to the generation of arrhythmic foci and myofiber disarray arising from uncontrolled and disorganised proliferation. Although no electrophysical monitoring was performed in the mice investigated here, we had no deaths after YAP5SA administration.

We elected to administer both the YAPREP and the YAP5SA within the same injection to guarantee co-localization of the reporter and the activator. Nevertheless, more substantial benefits for cardiac functional recovery post-MI might have emerged if YAP5SA had been administered at the time of or after MI. In cases where the mice had wall thickening before the surgery, the injury could have been exacerbated, masking any proliferation-mediated improvements in function.

Delivering YAPREP 15 days before YAP5SA, or any other local or systemic YAP activator, might also contribute to a more stable reporting system, as our CMV-LUC data indicated that the expression increased tenfold from day 3 to day 15. Taken together, time and dose-dependent control over YAP activation in CMs is imperative to harness its short-term beneficial effects while minimizing potential adverse consequences, thereby optimizing post-injury cardiac function improvement.

5.6 Limitations

This study has several limitations, as it did not include any histological, PCR and single-cell RNA sequencing analysis. *Ex vivo* BLI was also not performed to confirm AAV9 injection. One key reason for this occasion was the decision to collect cardiac tissue for PCR analysis immediately after euthanasia. Since *ex vivo* BLI requires fresh tissue and is time-sensitive, this approach was not feasible without compromising the quality of samples needed for PCR. Additionally, the luciferase injection could have interfered with downstream PCR results, introducing potential confounding effects. Histological analysis is crucial for a comprehensive examination of cardiac tissue structure and can elucidate the impacts of YAP5SA and YAPREP on heart morphology. PCR techniques can measure the expression levels of specific genes that are involved in the pathways affected by YAP5SA and YAPREP. Single-cell RNA sequencing analysis can provide detailed understanding of how YAP constructs affect different cell types within the heart at the single-cell level. Table 5-1 summarises how these techniques can contribute to optimization. By integrating these techniques, further study will gain a comprehensive understanding of how YAP5SA and YAPREP affect the heart at multiple levels, from molecular signalling to tissue structure and function. This will guide the optimization of their use, such as adjusting the dosage, timing, and combination with other therapies to maximize therapeutic benefits while minimizing adverse effects.

Table 5-1. Summary of possible techniques to optimize the use of YAP5SA and YAPREP in cardiac therapy.

Histology:	
Myocardial Hypertrophy:	Hematoxylin and eosin (H&E) staining: CM size, myocardial wall thickness
Fibrosis:	Masson's Trichrome Staining: detect collagen deposition, fibrosis
Apoptosis and Necrosis:	TUNEL Assay: apoptotic cells
Immunohistochemistry	Antibodies against cleaved caspase-3: apoptosis levels Staining for makers such as troponin: integrity of CMs
Angiogenesis:	CD31 or VEGF Staining: level of angiogenesis
Quantitative PCR (qPCR) and RT-PCR:	
Proliferation and Hypertrophy Markers:	Cyclin D1, PCNA (Proliferating Cell Nuclear Antigen): cell proliferation ANP (Atrial Natriuretic Peptide), BNP (Brain Natriuretic Peptide), and β-MHC (Beta-Myosin Heavy Chain): cardiac hypertrophy
Fibrosis Markers:	Collagen I and III, TGF-β1 (Transforming Growth Factor-Beta 1), CTGF (Connective Tissue Growth Factor)
Apoptosis and Survival Markers:	Bcl-2, Bax, and Caspase-3
Hippo Pathway Components:	LATS1/2, MST1/2
Single-Cell RNA Sequencing (scRNA-seq): cell types	
Cell-Type Specific Effects:	Identify how different populations of cells (e.g., cardiomyocytes, fibroblasts, endothelial cells) are responding to YAP5SA or YAPREP expression

5.7 Conclusion

AAV-mediated gene therapies present new possibilities for treating MI. The imaging platform established here, which integrates BLI with ultrasound and MRI techniques, provides a reliable and safe method for serially monitoring the gene therapy process and evaluating its therapeutic outcomes. While this study did not observe significant therapeutic effects from YAP5SA-induced wall thickening—primarily due to the detrimental effects of uncontrolled activation—we successfully established a robust platform for tracking gene delivery and expression over time.

Chapter 6 General discussion

Current treatment for MI primarily focusses on alleviating symptoms and disease progression and are unable to regenerate cardiac tissue lost due to the ischemic event. Hence, regenerative strategies such as stem cell transplantation, biomaterial application, and gene transfer have demonstrated significant promise, but have yet to become routine therapies for heart disease owing to a number of limitations. For example, an effective regenerative therapy requires a minimal invasive delivery approach to deliver therapeutics in a targeted and controlled manner. Additionally, the capacity to serially track and monitor the implants/stem cells *in vivo* can yield important information on how effective the treatment is and how it can be improved. These challenges can be addressed by using multimodal biomedical imaging techniques such as MRI, ultrasound, SPECT-CT and optical imaging to provide comprehensive understanding of the behavior and efficacy of implanted materials, cells or genes within living organisms, and to assess therapeutic effects both globally and regionally. Given the imaging is routinely performed in patients with heart disease, multimodal imaging could provide clinically relevant data in clinical trials of regenerative therapies.

6.1. Animal models of myocardial infarction for regenerative therapies

However, these novel imaging methods must first be developed and tested preclinically. Animal models are essential tools for evaluation of efficacy of therapeutic interventions prior to clinical use. In Chapter 2, an MI mouse model was successfully established with optimised surgical procedures. The surgical protocol demonstrated a PL model with characteristics of ultrasound-friendly, less trauma, minimized lung damage, and more severe and sustained cardiac impairment. On the other hand, the IR 45 minutes model showed sufficient cardiac functional impairment. Although alternative species and models do offer systems for testing therapies, the mouse as a lower order species with relevant anatomy which can be imaged *in vivo* is more appropriate for initial testing than larger animals and offers greater cost efficiency for comparing multiple variables.

Previous studies have highlighted the variability in infarct size and cardiac function in conventional MI models [87, 286]. By refining the conventional MI induction surgery, this study provides a more reliable and reproducible PL model. This is crucial for preclinical research, where consistency and reproducibility are key to validating experimental treatments. Also, the comparison between PL and IR models

offers valuable insights into the different impacts of permanent ligation versus ischemia-reperfusion on cardiac function. The findings suggest that the PL model is suitable for testing experimental treatments aimed at reducing long-term cardiac dysfunction, while the IR models, particularly the IR 45 minutes model, are useful for studying the mechanisms of ischemia-reperfusion injury and potential interventions.

However, this study was conducted with a relatively small sample size (n=6 per group), which may limit the applicability of the findings. Larger studies are needed to confirm these results and provide more robust statistical power. Also, there was a higher variability in EF within the IR models, particularly the IR 45 minutes group. This variability could be due to differences in individual responses to ischemia-reperfusion injury and may affect the reproducibility of the results. Future research should involve larger cohorts to enhance the statistical power and reliability of the results.

6.2. Novel ultrasound imaging for cardiac function assessment

Conventional echocardiography, although a valuable tool for assessing cardiac function in preclinical studies, has limitations in accurately measuring cardiac dysfunction and providing sufficient regional information in cases of heart diseases, particularly those involving abnormally shaped ventricles. In Chapter 3, advanced ultrasound techniques 4D ultrasound were validated through the comparison of 4D ultrasound with conventional ultrasound modes such as M-mode and 2D B-mode. The results showed that 4D ultrasound exhibited the highest correlation and agreement with MRI for assessing LV volumes and EF. Simpson’s multiplane demonstrated comparable reliability to 4D ultrasound for cardiac functional assessment.

Although 4D-US offers improved spatial and temporal resolution for visualizing the heart's structure in a 3D perspective, as well as capturing full-heart motion throughout the entire cardiac cycle compared to traditional echocardiography, its complex data acquisition processes and time-consuming offline data analysis limit its accessibility and widespread adoption in preclinical research settings [485]. Simpson’s multiplane system offers user-friendly operation, reduced time requirements, and mature software for analysis. Due to the interest in observing not only the cardiac functional

changes following experimental therapies but also the morphological changes and infarct size, the combination of Simpson's multiplane with MRI was chosen to evaluate therapeutic effects in this thesis.

Chapter 3 then demonstrated that strain analysis effectively differentiated between infarcted and non-infarcted myocardium, offering a deeper understanding of cardiac mechanics and enables the detection of subtle abnormalities that may not be captured by EF alone. Global strain analysis has manifested a significant correlation with EF, as presented in Chapters 3 and Chapter 5. Furthermore, regional strain analysis provides more benefits than global strain as it enables the evaluation of cardiac function segmentally. In Chapter 3, regional strain assessment has successfully distinguished the injured region after MI. In Chapter 5, regional strain analysis indicated that AAV-mediated gene transfer, YAP5SA, potentially induced an improvement of cardiac contractility post-MI, mainly localized to the apical region, which was not detected through MRI and ultrasound assessment, as well as global strain analysis.

Additionally, this study has successfully validated the ATTR-CM model according to clinical diagnostic parameters and LS analysis was confirmed as a reliable approach to monitor and track the progression of ARRT-CM over time. While RCS and RRS analysis can provide additional segmental information in cardiac functional assessment in both MI and ATTR-CM models, their accuracy and reliability may be compromised when compared to LS measurements.

This study highlights several key advancements in cardiac ultrasound techniques, including 4D-ultrasound and strain analysis. These modalities show promise as feasible and noninvasive methods for evaluating myocardial deformation, ultimately enhancing the development and assessment of cardiac regenerative therapies.

6.3. Enhancing stem cell delivery using imaging guidance

Chapter 4 demonstrated the potential of a collapsible SMP for minimally invasive cardiac regenerative therapy. In this study, a SMP was developed and tested *in vivo* by implanting the patch by minimally invasive ultrasound guidance injection. This delivery approach can precisely position the patch within the heart. In addition, the use of ^{111}In radiolabeling facilitated detailed tracking of the patch's location through

SPECT-CT imaging post-injection, demonstrating a considerable number of patches had fallen off from the heart within a short timeframe following implantation. This prompted the modification of the patch aimed at enhancing the attachment of the patch to ensure sustained adherence to the heart tissue, in which a 1% chitosan solution was applied, resulting in a remarkable improvement in the stability and secure attachment of the patch onto the cardiac surface. Further investigation was carried out to examine whether the chitosan-coated patch could improve cell retention and survival both *in vivo* and *in vitro*. Coupled with BLI, cell viability was serially quantified, and it was demonstrated that the second-generation SMP maintained the viability of epi-hESCs both *in vivo* and *in vitro*. Taken together, this chapter demonstrated an efficient way for biomaterial delivery achieved by ultrasound guidance injection, allowing for precise and localized administration of therapeutic agents to specific organs and minimizing off-target effects and enhances the overall efficacy of treatment. Additionally, this study highlighted the significance of monitoring biomaterials and stem cells *in vivo* achieved by SPECT-CT imaging and BLI. This non-invasive imaging platform enables the visualization of the distribution and retention of biomaterials within the body but also real-time tracking of seeded stem cells, providing direct evidence for optimizing biomaterials and evaluating therapeutic effects in preclinical studies. The combination of ultrasound-guided injection for biomaterial delivery with non-invasive monitoring through SPECT-CT imaging and BLI represents a powerful toolset for advancing biomedical research.

6.4. Imaging gene therapy

In Chapter 5, we aimed to validate the multimodal imaging system comprising BLI, MRI, STE and Simpson's ultrasound can be used to track, monitor and evaluate AAV-mediated gene transfer targeted at the Hippo-YAP signal pathway in a MI mouse model. The results demonstrated that BLI serves as a highly sensitive modality for serial monitoring of gene expression over time after ultrasound guidance injection. Additionally, both MRI and ultrasound images revealed morphological changes induced by the AAV9-delivered YAP activator YAP5SA in the myocardium near the site of injection. Notably, we observed an increased thickness of the lateral wall that correlated with BLI intensity. Following the injection of YAP5SA, there was no significant improvement in global cardiac function observed after MI. This may be

attributed to various factors such as the timing and dosage of gene delivery. However, upon conducting regional strain analysis, potential improvements were identified in apical regions. Therefore, for future studies, it is essential to optimize the therapeutics by exploring AAV9-mediated YAPREP/YAP5SA delivery with different time points post-MI and dosages. The multimodal imaging system established herein provides a powerful toolset for comprehensive evaluation of gene transfer therapy in MI. The ability to real-time monitor gene expression dynamics, tissue remodeling, and cardiac function through multiple imaging modalities offers a robust tool for evaluating and optimizing gene therapies.

In summary, this work addresses the primary challenges faced by current studies, specifically the invasive or non-targeted delivery of biomaterials, and the deficiency in *in vivo* sequential tracking and monitoring of implants/stem cells/genes. The integration of multimodal imaging techniques proposed in this work encompasses minimally invasive delivery through ultrasound-guided injection, and sequential tracking and monitoring of delivered biomaterials and cellular therapies *in vivo* via SPECT-CT and BLI, as well as morphological and functional changes via MRI, STE and Simpson's ultrasound.

References

1. Feng, L., et al., *Prevalence of depression in myocardial infarction: A PRISMA-compliant meta-analysis.* Medicine (Baltimore), 2019. **98**(8): p. e14596.
2. Golforoush, P., D.M. Yellon, and S.M. Davidson, *Mouse models of atherosclerosis and their suitability for the study of myocardial infarction.* Basic Research in Cardiology, 2020. **115**(6).
3. Nadarajah, R., et al., *Inequalities in care delivery and outcomes for myocardial infarction heart failure, atrial fibrillation, and aortic stenosis in the United Kingdom.* Lancet Reg Health Eur, 2023. **33**: p. 100719.
4. Carmeliet, E., *Cardiac ionic currents and acute ischemia: from channels to arrhythmias.* Physiol Rev, 1999. **79**(3): p. 917-1017.
5. Martin, T.P., et al., *Preclinical models of myocardial infarction: from mechanism to translation.* Br J Pharmacol, 2022. **179**(5): p. 770-791.
6. Frangogiannis, N.G., *The inflammatory response in myocardial injury, repair, and remodelling.* Nat Rev Cardiol, 2014. **11**(5): p. 255-65.
7. Tariq, U., et al., *Role of Biomaterials in Cardiac Repair and Regeneration: Therapeutic Intervention for Myocardial Infarction.* ACS Biomater Sci Eng, 2022. **8**(8): p. 3271-3298.
8. Hadjipanayi, E., V. Mudera, and R.A. Brown, *Close dependence of fibroblast proliferation on collagen scaffold matrix stiffness.* J Tissue Eng Regen Med, 2009. **3**(2): p. 77-84.
9. Wu, W.Q., et al., *Collagen biomaterial for the treatment of myocardial infarction: an update on cardiac tissue engineering and myocardial regeneration.* Drug Deliv Transl Res, 2019. **9**(5): p. 920-934.
10. Frangogiannis, N.G., Pathophysiology of Myocardial Infarction. Compr Physiol, 2015. 5(4): p. 1841-75
11. Portillo Esquivel, L.E. and B. Zhang, *Application of Cell, Tissue, and Biomaterial Delivery in Cardiac Regenerative Therapy.* ACS Biomater Sci Eng, 2021. **7**(3): p. 1000-1021.
12. Flynn, A., et al., *Trends in Door-to-Balloon Time and Mortality in Patients With ST-Elevation Myocardial Infarction Undergoing Primary Percutaneous Coronary Intervention.* Archives of Internal Medicine, 2010. **170**(20).
13. Eltzschig, H.K. and T. Eckle, *Ischemia and reperfusion—from mechanism to translation.* Nature Medicine, 2011. **17**(11): p. 1391-1401.
14. Bacmeister, L., et al., *Inflammation and fibrosis in murine models of heart failure.* Basic Research in Cardiology, 2019. **114**(3).
15. Reimer, K.A., R.S.V. Heide, and V.J. Richard, *Reperfusion in acute myocardial infarction: Effect of timing and modulating factors in experimental models.* The American Journal of Cardiology, 1993. **72**(19): p. G13-G21.
16. Scholz, K.H., et al., *Patient delay and benefit of timely reperfusion in ST-segment elevation myocardial infarction.* Open Heart, 2021. **8**(1): p. e001650.
17. Yellon, D.M. and D.J. Hausenloy, *Myocardial Reperfusion Injury.* New England Journal of Medicine, 2007. **357**(11): p. 1121-1135.
18. Hashmi, S., & Al-Salam, S., *Acute myocardial infarction and myocardial*

ischemia-reperfusion injury: a comparison. International Journal of Clinical and Experimental Pathology, 2015. **8(8), 8786.**

19. Prasad, A., et al., *Reperfusion Injury, Microvascular Dysfunction, and Cardioprotection.* Circulation, 2009. **120**(21): p. 2105-2112.
20. Burgoyne, J.R., et al., *Redox signaling in cardiac physiology and pathology.* Circ Res, 2012. **111**(8): p. 1091-106.
21. Hausenloy, D.J. and D.M. Yellon, *Myocardial ischemia-reperfusion injury: a neglected therapeutic target.* J Clin Invest, 2013. **123**(1): p. 92-100.
22. Rodriguez-Sinovas, A., et al., *Reperfusion injury as a therapeutic challenge in patients with acute myocardial infarction.* Heart Fail Rev, 2007. **12**(3-4): p. 207-16.
23. Braunwald, E., *The treatment of acute myocardial infarction: the Past, the Present, and the Future.* Eur Heart J Acute Cardiovasc Care, 2012. **1**(1): p. 9-12.
24. Miura, T. and T. Miki, *Limitation of myocardial infarct size in the clinical setting: current status and challenges in translating animal experiments into clinical therapy.* Basic research in cardiology, 2008. **103**: p. 501-513.
25. Murphy, E. and C. Steenbergen, Mechanisms underlying acute protection from cardiac ischemia-reperfusion injury. Physiol Rev, 2008. 88(2): p. 581-609.
26. Mukherjee, P., et al., *Role of animal models in biomedical research: a review.* Lab Anim Res, 2022. **38**(1): p. 18.
27. Heusch, G., *Critical Issues for the Translation of Cardioprotection.* Circulation Research, 2017. **120**(9): p. 1477-1486.
28. Bhindi, R., et al., *Rat models of myocardial infarction.* Thrombosis and Haemostasis, 2006. **96**(11): p. 602-610.
29. Camacho, P., et al., *Large Mammalian Animal Models of Heart Disease.* Journal of Cardiovascular Development and Disease, 2016. **3**(4).
30. Riehle, C. and J. Bauersachs, *Small animal models of heart failure.* Cardiovasc Res, 2019. **115**(13): p. 1838-1849.
31. Ponzoni, M., J.G. Coles, and J.T. Maynes, *Rodent Models of Dilated Cardiomyopathy and Heart Failure for Translational Investigations and Therapeutic Discovery.* Int J Mol Sci, 2023. **24**(4).
32. Thomas, D., et al., *Noninvasive assessment of myocardial viability in a small animal model: comparison of MRI, SPECT, and PET.* Magn Reson Med, 2008. **59**(2): p. 252-9.
33. Zhang, Y., et al., *Research methods for animal models of atherosclerosis (Review).* Mol Med Rep, 2021. **24**(6).
34. Poznyak, A.V., et al., *Animal models of human atherosclerosis: current progress.* Braz J Med Biol Res, 2020. **53**(6): p. e9557.
35. Lee, Y.T., et al., *Mouse models of atherosclerosis: a historical perspective and recent advances.* Lipids Health Dis, 2017. **16**(1): p. 12.
36. Tang, Y.P., et al., *To develop a novel animal model of myocardial infarction: A research imperative.* Animal Models and Experimental Medicine, 2018. **1**(1): p. 36-39.
37. Khalifa, A.A., R.M. Rashad, and W.F. El-Hadidy, *Thymoquinone protects against cardiac mitochondrial DNA loss, oxidative stress, inflammation and apoptosis in isoproterenol-induced myocardial infarction in rats.* Heliyon,

2021. **7**(7).
38. Shukla, S.K., S.B. Sharma, and U.R. Singh, *beta-Adrenoreceptor Agonist Isoproterenol Alters Oxidative Status, Inflammatory Signaling, Injury Markers and Apoptotic Cell Death in Myocardium of Rats.* Indian J Clin Biochem, 2015. **30**(1): p. 27-34.
39. Salerno, N., et al., *A Mouse Model of Dilated Cardiomyopathy Produced by Isoproterenol Acute Exposure Followed by 5-Fluorouracil Administration.* J Cardiovasc Dev Dis, 2023. **10**(6).
40. Ellison, G.M., et al., *Adult c-kit(pos) cardiac stem cells are necessary and sufficient for functional cardiac regeneration and repair.* Cell, 2013. **154**(4): p. 827-42.
41. Viswanatha Swamy, A.H., et al., *Cardioprotective effect of ascorbic acid on doxorubicin-induced myocardial toxicity in rats.* Indian J Pharmacol, 2011. **43**(5): p. 507-11.
42. Takemura, G. and H. Fujiwara, *Doxorubicin-induced cardiomyopathy from the cardiotoxic mechanisms to management.* Prog Cardiovasc Dis, 2007. **49**(5): p. 330-52.
43. Xinyong, C., et al., *The role of toll-like receptors in myocardial toxicity induced by doxorubicin.* Immunol Lett, 2020. **217**: p. 56-64.
44. Kelishomi, R.B., et al., *Morphine is protective against doxorubicin-induced cardiotoxicity in rat.* Toxicology, 2008. **243**(1-2): p. 96-104.
45. Ahmed Elshaer, A.E.S., Mohammed Mohsen Elalfy, Alyaa Mohammed Ghoneem, Amira Kamal Elhawary, Mohammed Ahdy Attia, *Comparative Study Among Three Different Models for Induction of Acute Myocardial Infarction in Rats.* European Heart Journal Supplements, 2021. **23**.
46. Klocke, R., et al., *Surgical animal models of heart failure related to coronary heart disease.* Cardiovasc Res, 2007. **74**(1): p. 29-38.
47. Selye, H., et al., *Simple techniques for the surgical occlusion of coronary vessels in the rat.* Angiology, 1960. **11**: p. 398-407.
48. Loukas, M., et al., *The normal and abnormal anatomy of the coronary arteries.* Clinical Anatomy, 2009. **22**(1): p. 114-128.
49. De Villiers, C. and P.R. Riley, *Mouse models of myocardial infarction: comparing permanent ligation and ischaemia-reperfusion.* Disease Models & Mechanisms, 2020. **13**(11): p. dmm046565.
50. Rochitte, C.E. and C.F. Azevedo, *The myocardial area at risk.* Heart, 2012. **98**(5): p. 348- 50.
51. Luther, D.J., C.K. Thodeti, and J.G. Meszaros, *Injury Models to Study Cardiac Remodeling in the Mouse: Myocardial Infarction and Ischemia–Reperfusion*. 2013, Humana Press. p. 325-342.
52. Lindsey, M.L., et al., *Reperfused vs. nonreperfused myocardial infarction: when to use which model.* American Journal of Physiology-Heart and Circulatory Physiology, 2021. **321**(1): p. H208-H213.
53. Strauss, M.H. and A.S. Hall, *Angiotensin receptor blockers may increase risk of myocardial infarction: unraveling the ARB-MI paradox.* Circulation, 2006. **114**(8): p. 838-54.
54. Lee, K., et al., *Evidence-Based Optimal Medical Therapy and Mortality in Patients With Acute Myocardial Infarction After Percutaneous Coronary*

Intervention. J Am Heart Assoc, 2023. **12**(10): p. e024370.
55. Saito, Y., et al., *Treatment strategies of acute myocardial infarction: updates on revascularization, pharmacological therapy, and beyond.* J Cardiol, 2023. **81**(2): p. 168-178.
56. Armstrong, P.W., D. Collen, and E. Antman, *Fibrinolysis for acute myocardial infarction: the future is here and now.* Circulation, 2003. **107**(20): p. 2533-7.
57. Tajabadi, M., et al., *Regenerative strategies for the consequences of myocardial infarction: Chronological indication and upcoming visions.* Biomed Pharmacother, 2022. **146**: p. 112584.
58. Cantor, W.J., et al., *Routine early angioplasty after fibrinolysis for acute myocardial infarction.* N Engl J Med, 2009. **360**(26): p. 2705-18.
59. Collet, C., et al., *State of the art: coronary angiography.* EuroIntervention, 2017. **13**(6): p. 634-643.
60. Keeley, E.C. and L.D. Hillis, *Primary PCI for myocardial infarction with ST-segment elevation.* N Engl J Med, 2007. **356**(1): p. 47-54.
61. Bravata, D.M., et al., *Systematic review: the comparative effectiveness of percutaneous coronary interventions and coronary artery bypass graft surgery.* Ann Intern Med, 2007. **147**(10): p. 703-16.
62. Bergmann, O., et al., *Evidence for cardiomyocyte renewal in humans.* Science, 2009. **324**(5923): p. 98-102.
63. Aly, R.M., *Current state of stem cell-based therapies: an overview.* Stem Cell Investig, 2020. **7**: p. 8.
64. Shafei, A.E., et al., *Mesenchymal stem cell therapy: A promising cell-based therapy for treatment of myocardial infarction.* Journal of Gene Medicine, 2017. **19**(12).
65. Orlic, D., J.M. Hill, and A.E. Arai, *Stem cells for myocardial regeneration.* Circ Res, 2002. **91**(12): p. 1092-102.
66. Lalit, P.A., et al., Induced pluripotent stem cells for post-myocardial infarction repair: remarkable opportunities and challenges. Circ Res, 2014. 114(8): p. 1328-45.
67. Sun, B., et al., New treatment methods for myocardial infarction. Front Cardiovasc Med, 2023. 10: p. 1251669.
68. Khodayari, S., et al., Inflammatory Microenvironment of Acute Myocardial Infarction Prevents Regeneration of Heart with Stem Cells Therapy. Cell Physiol Biochem, 2019. 53(5): p. 887-909.
69. Srinivas, G., P. Anversa, and W.H. Frishman, *Cytokines and myocardial regeneration: a novel treatment option for acute myocardial infarction.* Cardiol Rev, 2009. **17**(1): p. 1-9.
70. Ma, R., et al., *Electrical Stimulation Enhances Cardiac Differentiation of Human Induced Pluripotent Stem Cells for Myocardial Infarction Therapy.* Antioxid Redox Signal, 2018. **28**(5): p. 371-384.
71. Belien, H., et al., *Combining stem cells in myocardial infarction: The road to superior repair?* Med Res Rev, 2022. **42**(1): p. 343-373.
72. Lemcke, H., et al., *Recent Progress in Stem Cell Modification for Cardiac Regeneration.* Stem Cells Int, 2018. **2018**: p. 1909346.
73. Mathur, A. and J.F. Martin, *Stem cells and repair of the heart.* Lancet, 2004. **364**(9429): p. 183-92.

74. Menasche, P., *Skeletal myoblasts and cardiac repair.* J Mol Cell Cardiol, 2008. **45**(4): p. 545-53.
75. Si, Y.L., et al., MSCs: Biological characteristics, clinical applications and their outstanding concerns. Ageing Res Rev, 2011. 10(1): p. 93-103.
76. Liao, S.Y. and H.F. Tse, *Multipotent (adult) and pluripotent stem cells for heart regeneration: what are the pros and cons?* Stem Cell Res Ther, 2013. **4**(6): p. 151.
77. Cambria, E., et al., Translational cardiac stem cell therapy: advancing from first-generation to next-generation cell types. Npj Regenerative Medicine, 2017. 2.
78. Vasu, S., et al., *Biomaterials-based Approaches for Cardiac Regeneration.* Korean Circulation Journal, 2021. **51**(12): p. 943-960.
79. Emmert, M.Y., R.W. Hitchcock, and S.P. Hoerstrup, *Cell therapy, 3D culture systems and tissue engineering for cardiac regeneration.* Adv Drug Deliv Rev, 2014. **69-70**: p. 254-69.
80. Cianflone, E., et al., *Adult Cardiac Stem Cell Aging: A Reversible Stochastic Phenomenon?* Oxid Med Cell Longev, 2019. **2019**: p. 5813147.
81. van den Heuvel, N.H., et al., *Lessons from the heart: mirroring electrophysiological characteristics during cardiac development to in vitro differentiation of stem cell derived cardiomyocytes.* J Mol Cell Cardiol, 2014. **67**: p. 12-25.
82. Liu, Y.W., et al., *Human embryonic stem cell-derived cardiomyocytes restore function in infarcted hearts of non-human primates.* Nat Biotechnol, 2018. **36**(7): p. 597-605.
83. Thomson, J.A., et al., *Embryonic stem cell lines derived from human blastocysts.* Science, 1998. **282**(5391): p. 1145-7.
84. Harding, S.E., et al., *The human embryonic stem cell-derived cardiomyocyte as a pharmacological model.* Pharmacol Ther, 2007. **113**(2): p. 341-53.
85. Takahashi, K. and S. Yamanaka, *Induction of pluripotent stem cells from mouse embryonic and adult fibroblast cultures by defined factors.* Cell, 2006. **126**(4): p. 663-76.
86. Naftilan, A.J. and F.G. Schuening, *Stem cell therapy for cardiac disease: what can be learned from oncology.* Heart Fail Clin, 2011. **7**(3): p. 345-55.
87. Clavellina, D., W. Balkan, and J.M. Hare, *Stem cell therapy for acute myocardial infarction: Mesenchymal Stem Cells and induced Pluripotent Stem Cells.* Expert Opin Biol Ther, 2023. **23**(10): p. 951-967.
88. Cui, Z., B.F. Yang, and R.K. Li, *Application of Biomaterials in Cardiac Repair and Regeneration.* Engineering, 2016. **2**(1): p. 141-148.
89. Mummery, C.L., *Cardiology: solace for the broken-hearted?* Nature, 2005. **433**(7026): p. 585-7.
90. Kim, Y.S. and Y. Ahn, A long road for stem cells to cure sick hearts: update on recent clinical trials. Korean Circ J, 2012. 42(2): p. 71-9.
91. Lister, Z., K.J. Rayner, and E.J. Suuronen, *How Biomaterials Can Influence Various Cell Types in the Repair and Regeneration of the Heart after Myocardial Infarction.* Front Bioeng Biotechnol, 2016. **4**: p. 62.
92. Vasu, S., et al., *Biomaterials-based Approaches for Cardiac Regeneration.* Korean Circ J, 2021. **51**(12): p. 943-960.

93. Park, H., et al., *A novel composite scaffold for cardiac tissue engineering.* In Vitro Cell Dev Biol Anim, 2005. **41**(7): p. 188-96.
94. Yu, L. and J. Ding, *Injectable hydrogels as unique biomedical materials.* Chem Soc Rev, 2008. **37**(8): p. 1473-81.
95. Capuani, S., et al., *Advanced strategies to thwart foreign body response to implantable devices.* Bioeng Transl Med, 2022. **7**(3): p. e10300.
96. Ishihara, M., et al., *Biomaterials as cell carriers for augmentation of adipose tissue-derived stromal cell transplantation.* Biomed Mater Eng, 2018. **29**(5): p. 567-585.
97. Zheng, Z., et al., *Biotherapeutic-loaded injectable hydrogels as a synergistic strategy to support myocardial repair after myocardial infarction.* J Control Release, 2021. **335**: p. 216-236.
98. Tallawi, M., et al., *Strategies for the chemical and biological functionalization of scaffolds for cardiac tissue engineering: a review.* J R Soc Interface, 2015. **12**(108): p. 20150254.
99. Hasan, A., et al., *Injectable Hydrogels for Cardiac Tissue Repair after Myocardial Infarction.* Adv Sci (Weinh), 2015. **2**(11): p. 1500122.
100. Ahmed, E.M., Hydrogel: Preparation, characterization, and applications: A review. J Adv Res, 2015. 6(2): p. 105-21.189. Nasution, H., et al., *Hydrogel and Effects of Crosslinking Agent on Cellulose-Based Hydrogels: A Review.* Gels, 2022. **8**(9).
101. Gu, D., et al., *Hydrogels with smart systems for delivery of hydrophobic drugs.* Expert Opin Drug Deliv, 2017. **14**(7): p. 879-895.
102. De France, K.J., F. Xu, and T. Hoare, *Structured Macroporous Hydrogels: Progress, Challenges, and Opportunities.* Adv Healthc Mater, 2018. **7**(1).
103. Garbern, J.C., et al., *Delivery of basic fibroblast growth factor with a pH-responsive, injectable hydrogel to improve angiogenesis in infarcted myocardium.* Biomaterials, 2011. **32**(9): p. 2407-16.
104. Neeraj Kumar, R.G., Sadanand Pandey, Suprakas Sinha Ray, Hydrogel Nanocomposite Adsorbents and Photocatalysts for Sustainable Water Purification. Advanced Materials Interfaces, 2022. 10(2).
105. Reis, L.A., et al., *Hydrogels with integrin-binding angiopoietin-1-derived peptide, QHREDGS, for treatment of acute myocardial infarction.* Circ Heart Fail, 2015. **8**(2): p. 333-41.
106. Liao, X., et al., Injectable Hydrogel-Based Nanocomposites for Cardiovascular Diseases. Front Bioeng Biotechnol, 2020. 8: p. 251
107. Ho, T.C., et al., Hydrogels: Properties and Applications in Biomedicine. Molecules, 2022. 27(9).
108. Sargeant, T.D., et al., *An in situ forming collagen-PEG hydrogel for tissue regeneration.* Acta Biomater, 2012. **8**(1): p. 124-32.
109. Vasile, C., et al., *New Developments in Medical Applications of Hybrid Hydrogels Containing Natural Polymers.* Molecules, 2020. **25**(7).
110. Xu, G., et al., *Injectable biodegradable hybrid hydrogels based on thiolated collagen and oligo(acryloyl carbonate)-poly(ethylene glycol)-oligo(acryloyl carbonate) copolymer for functional cardiac regeneration.* Acta Biomater, 2015. **15**: p. 55-64.
111. Kong, P., et al., *Extracellular Matrix/Glycopeptide Hybrid Hydrogel as an*

Immunomodulatory Niche for Endogenous Cardiac Repair after Myocardial Infarction. Adv Sci (Weinh), 2023. **10**(23): p. e2301244.
112. Mousavi, A., et al., *Biohybrid oxidized alginate/myocardial extracellular matrix injectable hydrogels with improved electromechanical properties for cardiac tissue engineering.* Int J Biol Macromol, 2021. **180**: p. 692-708.
113. Hoeeg, C., A. Dolatshahi-Pirouz, and B. Follin, *Injectable Hydrogels for Improving Cardiac Cell Therapy-In Vivo Evidence and Translational Challenges.* Gels, 2021. **7**(1).
114. Li, Y., H.Y. Yang, and D.S. Lee, Advances in biodegradable and injectable hydrogels for biomedical applications. J Control Release, 2021. 330: p. 151-160.
115. Zhang, Y., et al., *Recent Advances in Cardiac Patches: Materials, Preparations, and Properties.* ACS Biomater Sci Eng, 2022. **8**(9): p. 3659-3675.
116. Sharma, D., et al., *Constructing Biomimetic Cardiac Tissues: A Review of Scaffold Materials for Engineering Cardiac Patches.* Emergent Mater, 2019. **2**: p. 181-191.
117. Omens, J.H., Stress and strain as regulators of myocardial growth. Prog Biophys Mol Biol, 1998. 69(2-3): p. 559-72.
118. Loh, Q.L. and C. Choong, *Three-dimensional scaffolds for tissue engineering applications: role of porosity and pore size.* Tissue Eng Part B Rev, 2013. **19**(6): p. 485-502.
119. Chang, T., et al., *Biomaterials based cardiac patches for the treatment of myocardial infarction.* Journal of Materials Science & Technology, 2021. **94**: p. 77-89.
120. Li, P., et al., *The Role of Hydrogel in Cardiac Repair and Regeneration for Myocardial Infarction: Recent Advances and Future Perspectives.* Bioengineering (Basel), 2023. **10**(2).
121. Mei, X. and K. Cheng, *Recent Development in Therapeutic Cardiac Patches.* Front Cardiovasc Med, 2020. **7**: p. 610364.
122. Tang, J., et al., *A Regenerative Cardiac Patch Formed by Spray Painting of Biomaterials onto the Heart.* Tissue Engineering Part C: Methods, 2017. **23**(3): p. 146-155.
123. Li, M., et al., *Recent fabrications and applications of cardiac patch in myocardial infarction treatment.* VIEW, 2022. **3**(2): p. 20200153.
124. Melhem, M., et al., *A Hydrogel Construct and Fibrin-based Glue Approach to Deliver Therapeutics in a Murine Myocardial Infarction Model.* J Vis Exp, 2015(100): p. e52562.
125. Sax, H., et al., *Prolonged Outbreak of Mycobacterium chimaera Infection After Open-Chest Heart Surgery.* Clin Infect Dis, 2015. **61**(1): p. 67-75.
126. Sy, J.C. and M.E. Davis, *Delivering regenerative cues to the heart: cardiac drug delivery by microspheres and peptide nanofibers.* J Cardiovasc Transl Res, 2010. **3**(5): p. 461-8.
127. Li, Q., et al., *Functional microspheres for tissue regeneration.* Bioactive Materials, 2023. **25**: p. 485-499.
128. Yang, J., et al., *Bio-Functional Hydrogel Microspheres for Musculoskeletal Regeneration.* Advanced Functional Materials, 2024. **n/a**(n/a): p. 2400257.
129. Li, Y., et al., *Elastic porous microspheres/extracellular matrix hydrogel*

injectable composites releasing dual bio-factors enable tissue regeneration. Nature Communications, 2024. **15**(1): p. 1377.
130. Alagarsamy, K.N., et al., Application of injectable hydrogels for cardiac stem cell therapy and tissue engineering. Rev Cardiovasc Med, 2019. 20(4): p. 221-230.
131. Webber, M.J., J.A. Kessler, and S.I. Stupp, *Emerging peptide nanomedicine to regenerate tissues and organs.* J Intern Med, 2010. **267**(1): p. 71-88.
132. Guo, H.D., et al., *Sustained delivery of VEGF from designer self-assembling peptides improves cardiac function after myocardial infarction.* Biochem Biophys Res Commun, 2012. **424**(1): p. 105-11.
133. Guo, H.D., et al., *Transplantation of marrow-derived cardiac stem cells carried in designer self-assembling peptide nanofibers improves cardiac function after myocardial infarction.* Biochem Biophys Res Commun, 2010. **399**(1): p. 42-8.
134. Nabel, E.G., et al., *Recombinant gene expression in vivo within endothelial cells of the arterial wall.* Science, 1989. **244**(4910): p. 1342-4.
135. Haneke, T. and M. Sahara, *Progress in Bioengineering Strategies for Heart Regenerative Medicine.* Int J Mol Sci, 2022. **23**(7).
136. Rissanen, T.T. and S. Yla-Herttuala, *Current status of cardiovascular gene therapy.* Mol Ther, 2007. **15**(7): p. 1233-47.
137. Ferrara, N. and K. Alitalo, *Clinical applications of angiogenic growth factors and their inhibitors.* Nature medicine, 1999. **5**(12): p. 1359-1364.
138. Simons, M., et al., *Pharmacological treatment of coronary artery disease with recombinant fibroblast growth factor-2: double-blind, randomized, controlled clinical trial.* Circulation, 2002. **105**(7): p. 788-93.
139. Rosengart, T.K., et al., *Six-month assessment of a phase I trial of angiogenic gene therapy for the treatment of coronary artery disease using direct intramyocardial administration of an adenovirus vector expressing the VEGF121 cDNA.* Annals of surgery, 1999. **230**(4): p. 466.
140. Favaloro, L., et al., *High-dose plasmid-mediated VEGF gene transfer is safe in patients with severe ischemic heart disease (Genesis-I). A phase I, open-label, two-year follow-up trial.* Catheter Cardiovasc Interv, 2013. **82**(6): p. 899-906.
141. Zouein, F.A. and G.W. Booz, *AAV-mediated gene therapy for heart failure: enhancing contractility and calcium handling.* F1000Prime Rep, 2013. **5**: p. 27.
142. Samuel, T.J., et al., *Correcting Calcium Dysregulation in Chronic Heart Failure Using SERCA2a Gene Therapy.* Int J Mol Sci, 2018. **19**(4).
143. Jessup, M., et al., *Calcium Upregulation by Percutaneous Administration of Gene Therapy in Cardiac Disease (CUPID): a phase 2 trial of intracoronary gene therapy of sarcoplasmic reticulum Ca2+-ATPase in patients with advanced heart failure.* Circulation, 2011. **124**(3): p. 304-13.
144. Sikkel, M.B., et al., *SERCA2a gene therapy in heart failure: an anti-arrhythmic positive inotrope.* British Journal of Pharmacology, 2014. **171**(1): p. 38-54.
145. Cutler, M.J., et al., *Targeted sarcoplasmic reticulum Ca2+ ATPase 2a gene delivery to restore electrical stability in the failing heart.* Circulation, 2012. **126**(17): p. 2095-104.
146. Chen, J.X., et al., *Inefficient reprogramming of fibroblasts into*

cardiomyocytes using Gata4, Mef2c, and Tbx5. Circ Res, 2012. **111**(1): p. 50-5.
147. Fu, J.D. and D. Srivastava, *Direct reprogramming of fibroblasts into cardiomyocytes for cardiac regenerative medicine.* Circ J, 2015. **79**(2): p. 245-54.
148. Ieda, M., et al., *Direct reprogramming of fibroblasts into functional cardiomyocytes by defined factors.* Cell, 2010. **142**(3): p. 375-386.
149. Qian, L., et al., *In vivo reprogramming of murine cardiac fibroblasts into induced cardiomyocytes.* Nature, 2012. **485**(7400): p. 593-598.
150. Inagawa, K., et al., *Induction of cardiomyocyte-like cells in infarct hearts by gene transfer of Gata4, Mef2c, and Tbx5.* Circulation research, 2012. **111**(9): p. 1147-1156.
151. Krenning, G., E.M. Zeisberg, and R. Kalluri, *The origin of fibroblasts and mechanism of cardiac fibrosis.* J Cell Physiol, 2010. **225**(3): p. 631-7.
152. Hirai, H., et al., *Accelerated direct reprogramming of fibroblasts into cardiomyocyte-like cells with the MyoD transactivation domain.* Cardiovasc Res, 2013. **100**(1): p. 105-13.
153. Christoforou, N., et al., *Transcription factors MYOCD, SRF, Mesp1 and SMARCD3 enhance the cardio-inducing effect of GATA4, TBX5, and MEF2C during direct cellular reprogramming.* PLoS One, 2013. **8**(5): p. e63577.
154. Nam, Y.J., et al., *Reprogramming of human fibroblasts toward a cardiac fate.* Proc Natl Acad Sci U S A, 2013. **110**(14): p. 5588-93.
155. Wang, J., et al., Non-Viral Gene Delivery Systems for Treatment of Myocardial Infarction: Targeting Strategies and Cardiac Cell Modulation. Pharmaceutics, 2021. 13(9).
156. Bicknell, K.A., C.H. Coxon, and G. Brooks, *Can the cardiomyocyte cell cycle be reprogrammed?* J Mol Cell Cardiol, 2007. **42**(4): p. 706-21.
157. Olson, E.N., *Gene regulatory networks in the evolution and development of the heart.* Science, 2006. **313**(5795): p. 1922-1927.
158. Payan, S.M., F. Hubert, and F. Rochais, *Cardiomyocyte proliferation, a target for cardiac regeneration.* Biochim Biophys Acta Mol Cell Res, 2020. **1867**(3): p. 118461.
159. Zhu, F., et al., *Adult cardiomyocyte proliferation: a new insight for myocardial infarction therapy.* Journal of Cardiovascular Translational Research, 2021. **14**: p. 457-466.
160. Chen, X., et al., *Molecular Mechanism of Hippo-YAP1/TAZ Pathway in Heart Development, Disease, and Regeneration.* Front Physiol, 2020. **11**: p. 389.
161. Pobbati, A.V., et al., *Identification of Quinolinols as Activators of TEAD-Dependent Transcription.* ACS Chem Biol, 2019. **14**(12): p. 2909-2921.
162. Ma, S., et al., *The Hippo Pathway: Biology and Pathophysiology.* Annu Rev Biochem, 2019. **88**: p. 577-604.
163. Singh, V.P., et al., *Hippo Pathway Effector Tead1 Induces Cardiac Fibroblast to Cardiomyocyte Reprogramming.* J Am Heart Assoc, 2021. **10**(24): p. e022659.
164. Dey, A., X. Varelas, and K.L. Guan, *Targeting the Hippo pathway in cancer, fibrosis, wound healing and regenerative medicine.* Nat Rev Drug Discov, 2020. **19**(7): p. 480-494.
165. Pobbati, A.V. and W. Hong, *Emerging roles of TEAD transcription factors and*

its coactivators in cancers. Cancer Biol Ther, 2013. **14**(5): p. 390-8.
166. Meng, Z., T. Moroishi, and K.L. Guan, *Mechanisms of Hippo pathway regulation.* Genes Dev, 2016. **30**(1): p. 1-17.
167. Boopathy, G.T.K. and W. Hong, *Role of Hippo Pathway-YAP/TAZ Signaling in Angiogenesis.* Front Cell Dev Biol, 2019. **7**: p. 49.
168. Juan, W.C. and W. Hong, *Targeting the Hippo Signaling Pathway for Tissue Regeneration and Cancer Therapy.* Genes (Basel), 2016. **7**(9).
169. Piccolo, S., S. Dupont, and M. Cordenonsi, *The biology of YAP/TAZ: hippo signaling and beyond.* Physiol Rev, 2014. **94**(4): p. 1287-312.
170. Werneburg, N., G.J. Gores, and R.L. Smoot, *The Hippo Pathway and YAP Signaling: Emerging Concepts in Regulation, Signaling, and Experimental Targeting Strategies With Implications for Hepatobiliary Malignancies.* Gene Expr, 2020. **20**(1): p. 67-74.
171. Dai, X., et al., *YAP activates the Hippo pathway in a negative feedback loop.* Cell Res, 2015. **25**(10): p. 1175-8.
172. Miyamura, N., et al., *YAP determines the cell fate of injured mouse hepatocytes in vivo.* Nat Commun, 2017. **8**: p. 16017.
173. Dong, J., et al., *Elucidation of a universal size-control mechanism in Drosophila and mammals.* Cell, 2007. **130**(6): p. 1120-33.
174. Camargo, F.D., et al., *YAP1 increases organ size and expands undifferentiated progenitor cells.* Curr Biol, 2007. **17**(23): p. 2054-60.
175. Kim, J., et al., *YAP/TAZ regulates sprouting angiogenesis and vascular barrier maturation.* J Clin Invest, 2017. **127**(9): p. 3441-3461.
176. Zheng, A., Q. Chen, and L. Zhang, The Hippo-YAP pathway in various cardiovascular diseases: Focusing on the inflammatory response. Front Immunol, 2022. 13: p. 971416.
177. Su, C.H., et al., *Nonviral gene therapy targeting cardiovascular system.* Am J Physiol Heart Circ Physiol, 2012. **303**(6): p. H629-38.
178. Sun, L., et al., *Construction of PR39 recombinant AAV under control of the HRE promoter and the effect of recombinant AAV on gene therapy of ischemic heart disease.* Exp Ther Med, 2012. **4**(5): p. 811-814.
179. Katz, M.G., et al., Gene therapy delivery systems for enhancing viral and nonviral vectors for cardiac diseases: current concepts and future applications. Hum Gene Ther, 2013. 24(11): p. 914-27.
180. Vassalli, G., et al., *Adeno-associated virus (AAV) vectors achieve prolonged transgene expression in mouse myocardium and arteries in vivo: a comparative study with adenovirus vectors.* Int J Cardiol, 2003. **90**(2-3): p. 229-38.
181. Tilemann, L., et al., *Gene therapy for heart failure.* Circ Res, 2012. **110**(5): p. 777-93.
182. Muller, O.J., H.A. Katus, and R. Bekeredjian, *Targeting the heart with gene therapy-optimized gene delivery methods.* Cardiovasc Res, 2007. **73**(3): p. 453-62.
183. Wright, M.J., et al., *In vivo myocardial gene transfer: optimization, evaluation and direct comparison of gene transfer vectors.* Basic Res Cardiol, 2001. **96**(3): p. 227-36.
184. Issa, S.S., et al., *Various AAV Serotypes and Their Applications in Gene*

Therapy: An Overview. Cells, 2023. **12**(5).
185. Hardcastle, N., N.M. Boulis, and T. Federici, *AAV gene delivery to the spinal cord: serotypes, methods, candidate diseases, and clinical trials.* Expert Opin Biol Ther, 2018. **18**(3): p. 293-307.
186. Miyake, K., et al., *Serotype-independent method of recombinant adeno-associated virus (AAV) vector production and purification.* J Nippon Med Sch, 2012. **79**(6): p. 394-402.
187. Zhang, H., et al., AAV-mediated gene therapy: Advancing cardiovascular disease treatment. Front Cardiovasc Med, 2022. 9: p. 952755.
188. Garcia-Olloqui, P., et al., Effect of heart ischemia and administration route on biodistribution and transduction efficiency of AAV9 vectors. J Tissue Eng Regen Med, 2020. 14(1): p. 123-134.
189. Sasaki, N., et al., *In Search of Adeno-Associated Virus Vectors With Enhanced Cardiac Tropism for Gene Therapy.* Heart Lung Circ, 2023. **32**(7): p. 816-824.
190. Zincarelli, C., et al., *Analysis of AAV serotypes 1-9 mediated gene expression and tropism in mice after systemic injection.* Mol Ther, 2008. **16**(6): p. 1073-80.
191. Westhaus, A., et al., *High-Throughput In Vitro, Ex Vivo, and In Vivo Screen of Adeno-Associated Virus Vectors Based on Physical and Functional Transduction.* Hum Gene Ther, 2020. **31**(9-10): p. 575-589.
192. Bulcha, J.T., et al., *Viral vector platforms within the gene therapy landscape.* Signal Transduct Target Ther, 2021. **6**(1): p. 53.
193. Prasad, K.M., et al., *A single direct injection into the left ventricular wall of an adeno-associated virus 9 (AAV9) vector expressing extracellular superoxide dismutase from the cardiac troponin-T promoter protects mice against myocardial infarction.* J Gene Med, 2011. **13**(6): p. 333-41.
194. Sahoo, S., T. Kariya, and K. Ishikawa, *Targeted delivery of therapeutic agents to the heart.* Nat Rev Cardiol, 2021. **18**(6): p. 389-399.
195. Campbell, N.G. and K. Suzuki, *Cell Delivery Routes for Stem Cell Therapy to the Heart: Current and Future Approaches.* Journal of Cardiovascular Translational Research, 2012. **5**(5): p. 713-726.
196. Rheault-Henry, M., et al., *Stem cell therapy for heart failure: Medical breakthrough, or dead end?* World J Stem Cells, 2021. **13**(4): p. 236-259.
197. Li, Q., et al., *Intracoronary administration of cardiac stem cells in mice: a new, improved technique for cell therapy in murine models.* Basic Res Cardiol, 2011. **106**(5): p. 849-64.
198. Gao, L.R., et al., *Intracoronary infusion of Wharton's jelly-derived mesenchymal stem cells in acute myocardial infarction: double-blind, randomized controlled trial.* BMC Medicine, 2015. **13**(1): p. 162.
199. Halkos, M.E., et al., *Intravenous infusion of mesenchymal stem cells enhances regional perfusion and improves ventricular function in a porcine model of myocardial infarction.* Basic Research in Cardiology, 2008. **103**(6): p. 525-536.
200. Bartolucci, J., et al., *Safety and Efficacy of the Intravenous Infusion of Umbilical Cord Mesenchymal Stem Cells in Patients With Heart Failure: A Phase 1/2 Randomized Controlled Trial (RIMECARD Trial [Randomized Clinical Trial of Intravenous Infusion Umbilical Cord Mesenchymal Stem Cells on Cardiopathy]).* Circ Res, 2017. **121**(10): p. 1192-1204.

201. Mitsutake, Y., et al., *Improvement of Local Cell Delivery Using Helix Transendocardial Delivery Catheter in a Porcine Heart.* Int Heart J, 2017. **58**(3): p. 435-440.
202. Wu, G., et al., *A new route of transendocardial stem cell injection: from femoral vein to left ventricle through atrial septa.* Eur Rev Med Pharmacol Sci, 2014. **18**(18): p. 2715-2719.
203. Kharbikar, B.N., P. Mohindra, and T.A. Desai, *Biomaterials to enhance stem cell transplantation.* Cell Stem Cell, 2022. **29**(5): p. 692-721.
204. Saludas, L., et al., *Hydrogel based approaches for cardiac tissue engineering.* Int J Pharm, 2017. **523**(2): p. 454-475.
205. Nelson, D.M., et al., *Intra-myocardial biomaterial injection therapy in the treatment of heart failure: Materials, outcomes and challenges.* Acta Biomater, 2011. **7**(1): p. 1-15.
206. He, S., et al., *Advances in Injectable Hydrogel Strategies for Heart Failure Treatment.* Adv Healthc Mater, 2023. **12**(19): p. e2300029.
207. Ye, L., et al., *Patching the heart: cardiac repair from within and outside.* Circulation research, 2013. **113**(7): p. 922-932.
208. Cannata, A., et al., *Gene Therapy for the Heart Lessons Learned and Future Perspectives.* Circ Res, 2020. **126**(10): p. 1394-1414.
209. Sanz, G., et al., *Determinants of prognosis in survivors of myocardial infarction: a prospective clinical angiographic study.* N Engl J Med, 1982. **306**(18): p. 1065-70.
210. Pujadas, S., et al., *MR imaging assessment of cardiac function.* J Magn Reson Imaging, 2004. **19**(6): p. 789-99.
211. Bruss, Z.S. and A. Raja, *Physiology, Stroke Volume*, in *StatPearls*. 2024: Treasure Island (FL).
212. Cikes, M. and S.D. Solomon, *Beyond ejection fraction: an integrative approach for assessment of cardiac structure and function in heart failure.* Eur Heart J, 2016. **37**(21): p. 1642-50.
213. Gargiulo, S., et al., *PET/CT imaging in mouse models of myocardial ischemia.* J Biomed Biotechnol, 2012. **2012**: p. 541872.
214. Santos, A., et al., *Cardiovascular imaging: what have we learned from animal models?* Front Pharmacol, 2015. **6**: p. 227.
215. Frantz, S., et al., Left ventricular remodelling post-myocardial infarction: pathophysiology, imaging, and novel therapies. Eur Heart J, 2022. 43(27): p. 2549-2561.
216. Li, M., et al., Multimodality reporter gene imaging: Construction strategies and application. Theranostics, 2018. 8(11): p. 2954-2973.
217. Doubrovin, M., V. Ponomarev, and R.G. Blasberg, *PET-based reporter gene imaging. Assessment of endogenous molecular-genetic events.* IEEE Eng Med Biol Mag, 2004. **23**(4): p. 38-50.
218. Yang, C., et al., *MRI Reporter Genes for Noninvasive Molecular Imaging.* Molecules, 2016. **21**(5).
219. Hong, H., Y. Yang, and W. Cai, *Imaging gene expression in live cells and tissues.* Cold Spring Harb Protoc, 2011. **2011**(4): p. pdb top103.
220. Abbas, F., et al., Molecular Imaging of Stem Cells. StemJournal, 2019. 1: p. 27-46.

221. Ruggiero, A., et al., Cell tracking in cardiac repair: what to image and how to image. Eur Radiol, 2012. 22(1): p. 189-204.
222. Lu, X., et al., MRI tracking stem cells transplantation for coronary heart disease. Pak J Med Sci, 2014. 30(4): p. 899-903.
223. Zhang, S.J. and J.C. Wu, Comparison of imaging techniques for tracking cardiac stem cell therapy. J Nucl Med, 2007. 48(12): p. 1916-9.
224. Guenoun, J., et al., Cationic Gd-DTPA liposomes for highly efficient labeling of mesenchymal stem cells and cell tracking with MRI. Cell Transplant, 2012. 21(1): p. 191-205.
225. Goodfellow, F., et al., Tracking and Quantification of Magnetically Labeled Stem Cells using Magnetic Resonance Imaging. Adv Funct Mater, 2016. 26(22): p. 3899-3915.
226. Moonshi, S.S., Y. Wu, and H.T. Ta, Visualizing stem cells in vivo using magnetic resonance imaging. Wiley Interdiscip Rev Nanomed Nanobiotechnol, 2022. 14(2): p. e1760.
227. Hermann, P., et al., Gadolinium (III) complexes as MRI contrast agents: ligand design and properties of the complexes. Dalton Transactions, 2008(23): p. 3027-3047.
228. Li, L., et al., Superparamagnetic iron oxide nanoparticles as MRI contrast agents for non-invasive stem cell labeling and tracking. Theranostics, 2013. 3(8): p. 595-615.
229. Kraitchman, D.L. and J.W. Bulte, Imaging of stem cells using MRI. Basic Res Cardiol, 2008. 103(2): p. 105-13.
230. Verma, V.K., et al., Fluorescent magnetic iron oxide nanoparticles for cardiac precursor cell selection from stromal vascular fraction and optimization for magnetic resonance imaging. Int J Nanomedicine, 2015. 10: p. 711-26.
231. Chelluri, L.K., et al., Effect of engineered superparamagnetic iron oxide nanoparticles in targeted cardiac precursor cell delivery by MRI. Biochem Biophys Res Commun, 2021. 541: p. 15-21.
232. Vandergriff, A.C., et al., Magnetic targeting of cardiosphere-derived stem cells with ferumoxytol nanoparticles for treating rats with myocardial infarction. Biomaterials, 2014. 35(30): p. 8528-39.
233. Tawagi, E., et al., In Vivo MRI Tracking of Degradable Polyurethane Hydrogel Degradation In Situ Using a Manganese Porphyrin Contrast Agent. J Magn Reson Imaging, 2023. 58(4): p. 1139-1150.
234. Hill, L.K., et al., Engineered Protein-Iron Oxide Hybrid Biomaterial for MRI-traceable Drug Encapsulation. Mol Syst Des Eng, 2022. 7(8): p. 915-932.
235. Marianne E. Mertens, A.H., Anne Bühren, Leon Olde-Damink, Diana Möckel, Felix Gremse, Josef Ehling, Fabian Kiessling, Twan Lammers, Iron Oxide-Labeled Collagen Scaffolds for Non-Invasive MR Imaging in Tissue Engineering. Advanced Functional Materials, 2013. 24(6): p. 754-762.
236. Mueller, R., et al., Imaging and Characterization of Sustained Gadolinium Nanoparticle Release from Next Generation Radiotherapy Biomaterial. Nanomaterials (Basel), 2020. 10(11).
237. Xiao, Y.D., et al., MRI contrast agents: Classification and application (Review). Int J Mol Med, 2016. 38(5): p. 1319-1326.
238. Mathiasen, A.B. and J. Kastrup, Non-invasive in-vivo imaging of stem cells

after transplantation in cardiovascular tissue. Theranostics, 2013. 3(8): p. 561-72.
239. Wu, C., et al., In vivo cell tracking via (1)(8)F-fluorodeoxyglucose labeling: a review of the preclinical and clinical applications in cell-based diagnosis and therapy. Clin Imaging, 2013. 37(1): p. 28-36.
240. Zaw Thin, M., et al., Multi-modal imaging probe for assessing the efficiency of stem cell delivery to orthotopic breast tumours. Nanoscale, 2020. 12(31): p. 16570-16585.
241. Villa, C., et al., In vivo tracking of stem cell by nanotechnologies: future prospects for mouse to human translation. Tissue Eng Part B Rev, 2011. 17(1): p. 1-11.
242. Collantes, M., et al., Non-invasive in vivo imaging of cardiac stem/progenitor cell biodistribution and retention after intracoronary and intramyocardial delivery in a swine model of chronic ischemia reperfusion injury. J Transl Med, 2017. 15(1): p. 56.
243. Zhou, R., et al., In vivo detection of stem cells grafted in infarcted rat myocardium. J Nucl Med, 2005. 46(5): p. 816-22.
244. Wolf, F., et al., MR and PET-CT monitoring of tissue-engineered vascular grafts in the ovine carotid artery. Biomaterials, 2019. 216: p. 119228.
245. Patrick, P.S., et al., Radio-metal cross-linking of alginate hydrogels for non-invasive in vivo imaging. Biomaterials, 2020. 243: p. 119930.
246. Patrick, P.S., et al., Lung delivery of MSCs expressing anti-cancer protein TRAIL visualised with (89)Zr-oxine PET-CT. Stem Cell Res Ther, 2020. 11(1): p. 256.
247. Sato, N., et al., (89)Zr-Oxine Complex PET Cell Imaging in Monitoring Cell-based Therapies. Radiology, 2015. 275(2): p. 490-500.
248. Gawne, P.J., et al., Direct Cell Radiolabeling for in Vivo Cell Tracking with PET and SPECT Imaging. Chem Rev, 2022. 122(11): p. 10266-10318.
249. Appel, A.A., et al., Imaging challenges in biomaterials and tissue engineering. Biomaterials, 2013. 34(28): p. 6615-30.
250. Gil, C.J., et al., In Vivo Tracking of Tissue Engineered Constructs. Micromachines (Basel), 2019. 10(7)
251. Gabrielson, K., et al., In Vivo Imaging With Confirmation by Histopathology for Increased Rigor and Reproducibility in Translational Research: A Review of Examples, Options, and Resources. ILAR J, 2018. 59(1): p. 80-98.
252. de Bournonville, S., S. Vangrunderbeeck, and G. Kerckhofs, Contrast-Enhanced MicroCT for Virtual 3D Anatomical Pathology of Biological Tissues: A Literature Review. Contrast Media Mol Imaging, 2019. 2019: p. 8617406.
253. Waarsing, J.H., et al., Detecting and tracking local changes in the tibiae of individual rats: a novel method to analyse longitudinal in vivo micro-CT data. Bone, 2004. 34(1): p. 163-9.
254. Klodowski, K., et al., Micro-imaging of implanted scaffolds using combined MRI and micro-CT. Comput Med Imaging Graph, 2014. 38(6): p. 458-68.
255. Kirschner, S., et al., In vivo micro-CT imaging of untreated and irradiated orthotopic glioblastoma xenografts in mice: capabilities, limitations and a comparison with bioluminescence imaging. J Neurooncol, 2015. 122(2): p. 245-54.

256. Ashton, J.R., J.L. West, and C.T. Badea, In vivo small animal micro-CT using nanoparticle contrast agents. Front Pharmacol, 2015. 6: p. 256.
257. Keklikoglou, K., et al., Micro-CT for Biological and Biomedical Studies: A Comparison of Imaging Techniques. J Imaging, 2021. 7(9).
258. Heimel, P., et al., Iodine-Enhanced Micro-CT Imaging of Soft Tissue on the Example of Peripheral Nerve Regeneration. Contrast Media Mol Imaging, 2019. 2019: p. 7483745.
259. Flechas Becerra, C., et al., X-Ray Visible Protein Scaffolds by Bulk Iodination. Adv Sci (Weinh), 2024. 11(10): p. e2306246.
260. Kleoniki Keklikoglou, S.F., Eva Chatzinikolaou, Patricia Wils, Jonathan Brecko, Jiří Kvaček, Brian Metscher, Christos Arvanitidis, Micro-computed tomography for natural history specimens: a handbook of best practice protocols. European Journal of Taxonomy, 2019. 522.
261. Shaikh, F.A., et al., Reporter gene imaging and its role in imaging-based drug development. Drug Discov Today, 2020. 25(3): p. 582-592.
262. Liu, M., et al., Using tyrosinase as a tri-modality reporter gene to monitor transplanted stem cells in acute myocardial infarction. Exp Mol Med, 2018. 50(4): p. 1-10.
263. Taghian, T., et al., Real-time MR tracking of AAV gene therapy with betagal-responsive MR probe in a murine model of GM1-gangliosidosis. Mol Ther Methods Clin Dev, 2021. 23: p. 128-134.
264. Anna V. Naumova, H.R., Vasily Yarnykh, Jennifer Deem, Chun Yuan, and Charles E. Murry, Ferritin Overexpression for Noninvasive Magnetic Resonance Imaging–Based Tracking of Stem Cells Transplanted into the Heart. Molecular Imaging., 2010. 9(4).
265. Inubushi, M. and N. Tamaki, Positron emission tomography reporter gene imaging in the myocardium: for monitoring of angiogenic gene therapy in ischemic heart disease. J Card Surg, 2005. 20(6): p. S20-4.
266. Acton, P.D. and R. Zhou, Imaging reporter genes for cell tracking with PET and SPECT. Q J Nucl Med Mol Imaging, 2005. 49(4): p. 349-60.
267. Terrovitis, J., et al., Ectopic expression of the sodium-iodide symporter enables imaging of transplanted cardiac stem cells in vivo by single-photon emission computed tomography or positron emission tomography. J Am Coll Cardiol, 2008. 52(20): p. 1652-60.
268. Lan, X., et al., Autoradiography study and SPECT imaging of reporter gene HSV1-tk expression in heart. Nucl Med Biol, 2010. 37(3): p. 371-80.
269. Wu, J.C., et al., Positron emission tomography imaging of cardiac reporter gene expression in living rats. Circulation, 2002. 106(2): p. 180-3.
270. Peeters, M., et al., Bioluminescence-mediated longitudinal monitoring of adipose-derived stem cells in a large mammal ex vivo organ culture. Sci Rep, 2015. 5: p. 13960.
271. Madsen, S.D., et al., Illuminating the Regenerative Properties of Stem Cells In Vivo with Bioluminescence Imaging. Biotechnol J, 2021. 16(3): p. e2000248.
272. de Almeida, P.E., J.R. van Rappard, and J.C. Wu, In vivo bioluminescence for tracking cell fate and function. Am J Physiol Heart Circ Physiol, 2011. 301(3): p. H663-71.
273. Oliveira, E.P., et al., Advances in bioinks and in vivo imaging of biomaterials

for CNS applications. Acta Biomater, 2019. 95: p. 60-72.
274. Degano, I.R., et al., Bioluminescence imaging of calvarial bone repair using bone marrow and adipose tissue-derived mesenchymal stem cells. Biomaterials, 2008. 29(4): p. 427-37.
276. Li, S.H., et al., Tracking cardiac engraftment and distribution of implanted bone marrow cells: Comparing intra-aortic, intravenous, and intramyocardial delivery. J Thorac Cardiovasc Surg, 2009. 137(5): p. 1225-33 e1.
277. Pei, Z., et al., Multimodality molecular imaging to monitor transplanted stem cells for the treatment of ischemic heart disease. PLoS One, 2014. 9(3): p. e90543.
278. Rieffel, J., U. Chitgupi, and J.F. Lovell, Recent Advances in Higher-Order, Multimodal, Biomedical Imaging Agents. Small, 2015. 11(35): p. 4445-61.
279. Qu, C., et al., Multimodality imaging in the assessment of bone marrow-derived mesenchymal stem cell therapy for doxorubicin-induced cardiomyopathy. Am J Cancer Res, 2022. 12(2): p. 574-584.
280. Yang, J.J., et al., Real-time tracking of adipose tissue-derived stem cells with injectable scaffolds in the infarcted heart. Heart Vessels, 2013. 28(3): p. 385-96.
281. Higuchi, T., et al., Combined reporter gene PET and iron oxide MRI for monitoring survival and localization of transplanted cells in the rat heart. J Nucl Med, 2009. 50(7): p. 1088-94.
282. Jernryd, V., et al., *The influence of ischemia and reperfusion time on outcome in heart transplantation.* Clin Transplant, 2020. **34**(5): p. e13840.
283. Chimenti, S., et al., *Myocardial infarction: animal models.* Methods Mol Med, 2004. **98**: p. 217-26.
284. Yellon, D.M. and D.J. Hausenloy, *Myocardial reperfusion injury.* N Engl J Med, 2007. **357**(11): p. 1121-35.
285. Wang, J., et al., *A simple and fast experimental model of myocardial infarction in the mouse.* Tex Heart Inst J, 2006. **33**(3): p. 290-3.
286. Lindsey, M.L., et al., *Guidelines for in vivo mouse models of myocardial infarction.* Am J Physiol Heart Circ Physiol, 2021. **321**(6): p. H1056-H1073.
287. Kainuma, S., et al., Influence of coronary architecture on the variability in myocardial infarction induced by coronary ligation in rats. PLoS One, 2017. 12(8): p. e0183323.
288. Schomig, A., et al., *Therapy-dependent influence of time-to-treatment interval on myocardial salvage in patients with acute myocardial infarction treated with coronary artery stenting or thrombolysis.* Circulation, 2003. **108**(9): p. 1084-8.
289. Christian, T.F., R.S. Schwartz, and R.J. Gibbons, *Determinants of infarct size in reperfusion therapy for acute myocardial infarction.* Circulation, 1992. **86**(1): p. 81-90.
290. Xu, Z., et al., A murine model of myocardial ischemia-reperfusion injury through ligation of the left anterior descending artery. J Vis Exp, 2014(86).
291. Preda, M.B. and A. Burlacu, Electrocardiography as a tool for validating myocardial ischemia–reperfusion procedures in mice. Comparative medicine, 2010. 60(6): p. 443-447.
292. Nugroho, J., et al., Modification on acute myocardial infarction model

through left anterior descending coronary artery ligation: An experimental study on rats (Rattus norvegicus) using readily available materials. Vet World, 2019. 12(9): p. 1448-1453.
293. Spindola-Franco, H., R. Grose, and N. Solomon, Dual left anterior descending coronary artery: angiographic description of important variants and surgical implications. Am Heart J, 1983. 105(3): p. 445-55.
294. Jariwala, P., K.P. Jadhav, and S. Koduganti, Dual left anterior descending artery: diagnostic criteria and novel classification. Indian J Thorac Cardiovasc Surg, 2021. 37(3): p. 285-294.
295. Michael, L.H., et al., Myocardial ischemia and reperfusion: a murine model. Am J Physiol, 1995. 269(6 Pt 2): p. H2147-54.
296. Buja, L.M., Myocardial ischemia and reperfusion injury. Cardiovasc Pathol, 2005. 14(4): p. 170-5.
297. Miura, T. and T. Miki, Limitation of myocardial infarct size in the clinical setting: current status and challenges in translating animal experiments into clinical therapy. Basic Res Cardiol, 2008. 103(6): p. 501-13.
298. Brodie, B.R., et al., Impact of time to treatment on myocardial reperfusion and infarct size with primary percutaneous coronary intervention for acute myocardial infarction (from the EMERALD Trial). Am J Cardiol, 2007. 99(12): p. 1680-6.
299. De Celle, T., et al., Long-term structural and functional consequences of cardiac ischaemia-reperfusion injury in vivo in mice. Exp Physiol, 2004. 89(5): p. 605-15.
300. Bayat, H., et al., Progressive heart failure after myocardial infarction in mice. Basic Res Cardiol, 2002. 97(3): p. 206-13.
301. Bohl, S., et al., Refined approach for quantification of in vivo ischemia-reperfusion injury in the mouse heart. Am J Physiol Heart Circ Physiol, 2009. 297(6): p. H2054-8.
302. Ueda, T., et al., Left Ventricular Ejection Fraction (EF) of 55% as Cutoff for Late Transition From Heart Failure (HF) With Preserved EF to HF With Mildly Reduced EF. Circ J, 2015. 79(10): p. 2209-15.
303. Garcia-Dorado, D., et al., Myocardial reperfusion in the pig heart model: infarct size and duration of coronary occlusion. Cardiovasc Res, 1987. 21(7): p. 537-44.
304. Zhang, J., et al., Animal Models and Techniques Used in Cardiovascular Research, in Cutting-edge Technologies in Biological Sensing and Analysis. 2024, River Publishers. p. 95-144.
305. Wang, B.J. and H.W. Chaudhry, Pop-Out Myocardial Infarction Induction in Mice, in Experimental Models of Cardiovascular Diseases: Methods and Protocols. 2024, Springer. p. 137-144.
306. Gao, E., et al., A novel and efficient model of coronary artery ligation and myocardial infarction in the mouse. Circ Res, 2010. 107(12): p. 1445-53.
307. Yue, X., et al., Investigation into the optimal surgical conditions for coronary artery ligation for establishing a myocardial infarction model in mice. Exp Ther Med, 2013. 6(2): p. 341-346.
308. Chen, J., Ceholski, D. K., Liang, L., Fish, K., & Hajjar, R. J. , Variability in coronary artery anatomy affects consistency of cardiac damage after

myocardial infarction in mice. . American Journal of Physiology-Heart and Circulatory Physiology, 2017. 313(2), H275-H282.
309. Salto-Tellez M, Y.L.S., El-Oakley RM, Tang TP, Almsherqi ZA, Lim SK. , Myocardial infarction in the C57BL/6J mouse: a quantifiable and highly reproducible experimental model. . Cardiovasc Pathol 2004. 13:91-7.
310. Chung, H., et al., Different contribution of extent of myocardial injury to left ventricular systolic and diastolic function in early reperfused acute myocardial infarction. Cardiovasc Ultrasound, 2014. 12: p. 6.
311. Miranda, A., et al., Time course of echocardiographic and electrocardiographic parameters in myocardial infarct in rats. An Acad Bras Cienc, 2007. 79(4): p. 639-48.
312. Erik Kjoller MD, D.-P., DMScb, Long-term prognostic importance of hyperkinesia following acute myocardial infarction. The American Journal of Cardiology, 1999. Volume 83, Issue 5.
313. Altamirano, F., Z.V. Wang, and J.A. Hill, Cardioprotection in ischaemia-reperfusion injury: novel mechanisms and clinical translation. J Physiol, 2015. 593(17): p. 3773-88.
314. Milavetz, J.J., et al., Time to therapy and salvage in myocardial infarction. J Am Coll Cardiol, 1998. 31(6): p. 1246-51.
315. Schomig, A., et al., Therapy-dependent influence of time-to-treatment interval on myocardial salvage in patients with acute myocardial infarction treated with coronary artery stenting or thrombolysis. Circulation, 2003. 108(9): p. 1084-8.
316. Christian, T.F., R.S. Schwartz, and R.J. Gibbons, Determinants of infarct size in reperfusion therapy for acute myocardial infarction. Circulation, 1992. 86(1): p. 81-90.
317. Matthay, M.A., et al., The Translational Value of Rodent Models of Sepsis. Am J Respir Crit Care Med, 2024. 209(5): p. 488-490.
318. Hausenloy, D.J. and D.M. Yellon, Myocardial ischemia-reperfusion injury: a neglected therapeutic target. Journal of Clinical Investigation, 2013. 123(1): p. 92-100.
319. Lin, H.A., et al., Characterization of Cardiac Dynamics in an Acute Myocardial Infarction Model by Four-Dimensional Optoacoustic and Magnetic Resonance Imaging. Theranostics, 2017. 7(18): p. 4470-4479.
320. Gehrmann, J., et al., Electrophysiological characterization of murine myocardial ischemia and infarction. Basic Res Cardiol, 2001. 96(3): p. 237-50.
321. Chan, D. and L.L. Ng, Biomarkers in acute myocardial infarction. BMC Med, 2010. 8: p. 34.
322. Wu, J., et al., Noninvasive estimation of infarct size in a mouse model of myocardial infarction by echocardiographic coronary perfusion. J Ultrasound Med, 2012. 31(7): p. 1111-21.
323. Ibrahim, E.H., et al., Diastolic Cardiac Function by MRI-Imaging Capabilities and Clinical Applications. Tomography, 2021. 7(4): p. 893-914.
324. Li, Y., et al., Quantification and MRI validation of regional contractile dysfunction in mice post myocardial infarction using high resolution ultrasound. Ultrasound Med Biol, 2007. 33(6): p. 894-904.
325. Yao, Y., et al., Evaluation of left ventricular volumes and ejection fraction by

99m Tc-MIBI gated SPECT and 18 F-FDG gated PET in patients with prior myocardial infarction. Journal of Nuclear Cardiology, 2021. 28: p. 560-574.
326. Benavides-Vallve, C., et al., New strategies for echocardiographic evaluation of left ventricular function in a mouse model of long-term myocardial infarction. PLoS One, 2012. 7(7): p. e41691.
327. Rutledge, C., et al., Commercial 4-dimensional echocardiography for murine heart volumetric evaluation after myocardial infarction. Cardiovascular Ultrasound, 2020. 18(1).
328. Damen, F.W., et al., High-Frequency 4-Dimensional Ultrasound (4DUS): A Reliable Method for Assessing Murine Cardiac Function. Tomography, 2017. 3(4): p. 180-187.
329. Dann, M.M., Clark, S. Q., Trzaskalski, N. A., Earl, C. C., Schepers, L. E., Pulente, S. M., ... & Mulvihill, E. E. , Quantification of Murine Myocardial Infarct Size using 2D and 4D High Frequency Ultrasound. . American Journal of Physiology-Heart and Circulatory Physiology., 2022.
330. Gopal, A.S., et al., Freehand three-dimensional echocardiography for determination of left ventricular volume and mass in patients with abnormal ventricles: Comparison with magnetic resonance imaging. Journal of the American Society of Echocardiography, 1997. 10(8): p. 853-861.
331. Thomas, J.D. and Z.B. Popovic, Assessment of left ventricular function by cardiac ultrasound. J Am Coll Cardiol, 2006. 48(10): p. 2012-25.
332. Bansal, M. and R.R. Kasliwal, How do I do it? Speckle-tracking echocardiography. Indian Heart J, 2013. 65(1): p. 117-23.
333. Chong, A., et al., Perioperative Applications of Deformation (Myocardial Strain) Imaging With Speckle-Tracking Echocardiography. Journal of Cardiothoracic and Vascular Anesthesia, 2014. 28(1): p. 128-140.
334. D'Hooge, J., Regional Strain and Strain Rate Measurements by Cardiac Ultrasound: Principles, Implementation and Limitations. European Journal of Echocardiography, 2000. 1(3): p. 154-170.
335. Lindsey, M.L., Kassiri, Z., Virag, J. A., de Castro Brás, L. E., & Scherrer-Crosbie, M., Guidelines for measuring cardiac physiology in mice.
American Journal of Physiology-Heart and Circulatory Physiology, 2018. 314(4), H733-H752.
336. Zacchigna, S., et al., Towards standardization of echocardiography for the evaluation of left ventricular function in adult rodents: a position paper of the ESC Working Group on Myocardial Function. Cardiovascular Research, 2021. 117(1): p. 43-59.
337. Kleijn, S.A., et al., Normal reference values of left ventricular strain using three-dimensional speckle tracking echocardiography: results from a multicentre study. Eur Heart J Cardiovasc Imaging, 2015. 16(4): p. 410-6.
338. Negishi, T. and K. Negishi, How to standardize measurement of global longitudinal strain. Journal of Medical Ultrasonics, 2022. 49(1): p. 45-52.
339. Mondillo, S., et al., Speckle-tracking echocardiography: a new technique for assessing myocardial function. J Ultrasound Med, 2011. 30(1): p. 71-83.
340. Abduch, M.C., et al., Cardiac mechanics evaluated by speckle tracking echocardiography. Arq Bras Cardiol, 2014. 102(4): p. 403-12.
341. Voigt, J.U., et al., Definitions for a common standard for 2D speckle tracking

echocardiography: consensus document of the EACVI/ASE/Industry Task Force to standardize deformation imaging. European Heart Journal - Cardiovascular Imaging, 2015. 16(1): p. 1-11.
342. Brown, J., C. Jenkins, and T.H. Marwick, Use of myocardial strain to assess global left ventricular function: a comparison with cardiac magnetic resonance and 3-dimensional echocardiography. American heart journal, 2009. 157(1): p. 102. e1-102. e5.
343. Vartdal, T., et al., Early prediction of infarct size by strain Doppler echocardiography after coronary reperfusion. Journal of the American College of Cardiology, 2007. 49(16): p. 1715-1721.
344. Edvardsen, T., T. Helle-Valle, and O.A. Smiseth, Systolic dysfunction in heart failure with normal ejection fraction: speckle-tracking echocardiography. Progress in cardiovascular diseases, 2006. 49(3): p. 207-214.
345. Martinez-Naharro, A., P.N. Hawkins, and M. Fontana, Cardiac amyloidosis. Clin Med (Lond), 2018. 18(Suppl 2): p. s30-s35.
346. Di Lisi, D., et al., Therapy of ATTR Cardiac Amyloidosis: Current Indications. Curr Probl Cardiol, 2023. 48(2): p. 101487.
347. Kittleson, M.M., et al., Cardiac Amyloidosis: Evolving Diagnosis and Management: A Scientific Statement From the American Heart Association. Circulation, 2020. 142(1): p. e7-e22.
348. Siddiqi, O.K. and F.L. Ruberg, Cardiac amyloidosis: An update on pathophysiology, diagnosis, and treatment. Trends Cardiovasc Med, 2018. 28(1): p. 10-21.
349. Ruberg, F.L., et al., Transthyretin Amyloid Cardiomyopathy: JACC State-of-the-Art Review. J Am Coll Cardiol, 2019. 73(22): p. 2872-2891.
350. Nakano, T., et al., Transthyretin Amyloid Cardiomyopathy: Impact of Transthyretin Amyloid Deposition in Myocardium on Cardiac Morphology and Function. J Pers Med, 2022. 12(5).
351. Rapezzi, C., et al., Cardiac amyloidosis: the great pretender. Heart Fail Rev, 2015. 20(2): p. 117-24.
352. Manolis, A.S., et al., Cardiac amyloidosis: An underdiagnosed/underappreciated disease. Eur J Intern Med, 2019. 67: p. 1-13.
353. Falk, R.H. and S.W. Dubrey, Amyloid heart disease. Prog Cardiovasc Dis, 2010. 52(4): p. 347-61.
354. Slamova, I., et al., Plasmin activity promotes amyloid deposition in a transgenic model of human transthyretin amyloidosis. Nature Communications, 2021. 12(1): p. 7112.
355. Scully, P.R., et al., DPD Quantification in Cardiac Amyloidosis: A Novel Imaging Biomarker. JACC Cardiovasc Imaging, 2020. 13(6): p. 1353-1363.
356. De Bruijn, S., et al., A special case of hypertrophic cardiomyopathy with a differential diagnosis of isolated cardiac amyloidosis or junctophilin type 2 associated cardiomyopathy. Acta Clin Belg, 2021. 76(2): p. 136-143.
357. Henein, M.Y., B. Pilebro, and P. Lindqvist, Disease progression in cardiac morphology and function in heart failure: ATTR cardiac amyloidosis versus hypertensive left ventricular hypertrophy. Heart Vessels, 2022. 37(9): p. 1562-1569.

358. Stypmann, J., et al., Echocardiographic assessment of global left ventricular function in mice. Lab Anim, 2009. 43(2): p. 127-37.
359. Pagourelias, E.D., et al., Echo Parameters for Differential Diagnosis in Cardiac Amyloidosis: A Head-to-Head Comparison of Deformation and Nondeformation Parameters. Circ Cardiovasc Imaging, 2017. 10(3): p. e005588.
360. Abadie, B., et al., Prevalence of ATTR-CA and high-risk features to guide testing in patients referred for TAVR. Eur J Nucl Med Mol Imaging, 2023. 50(13): p. 3910-3916.
361. Zhang, K., et al., A Comparison of Global Longitudinal, Circumferential, and Radial Strain to Predict Outcomes After Cardiac Surgery. J Cardiothorac Vasc Anesth, 2019. 33(5): p. 1315-1322.
362. Heinen, A., et al., Echocardiographic Analysis of Cardiac Function after Infarction in Mice: Validation of Single-Plane Long-Axis View Measurements and the Bi-Plane Simpson Method. Ultrasound Med Biol, 2018. 44(7): p. 1544-1555.
363. Kanno, S., et al., Echocardiographic evaluation of ventricular remodeling in a mouse model of myocardial infarction. Journal of the American Society of Echocardiography, 2002. 15(6): p. 601-609.
363. Russo, I., et al., A novel echocardiographic method closely agrees with cardiac magnetic resonance in the assessment of left ventricular function in infarcted mice. Scientific Reports, 2019. 9(1).
364. Stegmann, H., et al., 4D cardiac magnetic resonance imaging, 4D and 2D transthoracic echocardiography: a comparison of in-vivo assessment of ventricular function in rats. Lab Anim, 2019. 53(2): p. 169-179.
365. Soepriatna, A.H., et al., Cardiac and respiratory-gated volumetric murine ultrasound. The International Journal of Cardiovascular Imaging, 2017.
366. Kanno, S., et al., Echocardiographic evaluation of ventricular remodeling in a mouse model of myocardial infarction. J Am Soc Echocardiogr, 2002. 15(6): p. 601-9.
367. Talman, V. and H. Ruskoaho, Cardiac fibrosis in myocardial infarction-from repair and remodeling to regeneration. Cell Tissue Res, 2016. 365(3): p. 563-81.
368. Bauer, M., et al., Echocardiographic speckle-tracking based strain imaging for rapid cardiovascular phenotyping in mice. Circ Res, 2011. 108(8): p. 908-16.
369. Sjøli, B., et al., Comparison of Left Ventricular Ejection Fraction and Left Ventricular Global Strain as Determinants of Infarct Size in Patients with Acute Myocardial Infarction. Journal of the American Society of Echocardiography, 2009. 22(11): p. 1232-1238.
370. Diao, K.Y., et al., The Diagnostic Value of Global Longitudinal Strain (GLS) on Myocardial Infarction Size by Echocardiography: A Systematic Review and Meta-analysis. Sci Rep, 2017. 7(1): p. 10082.
371. Fent, G.J., et al., The utility of global longitudinal strain in the identification of prior myocardial infarction in patients with preserved left ventricular ejection fraction. Int J Cardiovasc Imaging, 2017. 33(10): p. 1561-1569.
372. Sun, J.P., et al., Alterations of regional myocardial function in a swine model of myocardial infarction assessed by echocardiographic 2-dimensional strain

imaging. J Am Soc Echocardiogr, 2007. 20(5): p. 498-504.
373. Brady, B., et al., Myocardial strain: a clinical review. Irish Journal of Medical Science (1971 -), 2023. 192(4): p. 1649-1656.
374. Takeuchi, M., et al., The assessment of left ventricular twist in anterior wall myocardial infarction using two-dimensional speckle tracking imaging. Journal of the American Society of Echocardiography, 2007. 20(1): p. 36-44.
375. Migrino, R.Q., et al., Myocardial dysfunction in the periinfarct and remote regions following anterior infarction in rats quantified by 2D radial strain echocardiography: an observational cohort study. Cardiovasc Ultrasound, 2008. 6: p. 17.
376. Becker, M., et al., Analysis of myocardial deformation based on ultrasonic pixel tracking to determine transmurality in chronic myocardial infarction. European heart journal, 2006. 27(21): p. 2560-2566.
377. Leischik, R., B. Dworrak, and K. Hensel, Intraobserver and interobserver reproducibility for radial, circumferential and longitudinal strain echocardiography. Open Cardiovasc Med J, 2014. 8: p. 102-9.
378. Ishii, K., et al., Exercise-induced post-ischemic left ventricular delayed relaxation or diastolic stunning: is it a reliable marker in detecting coronary artery disease? Journal of the American College of Cardiology, 2009. 53(8): p. 698-705.
379. Modesto, K. and P.P. Sengupta, Myocardial mechanics in cardiomyopathies. Prog Cardiovasc Dis, 2014. 57(1): p. 111-24.
380. Bellavia, D., et al., Detection of left ventricular systolic dysfunction in cardiac amyloidosis with strain rate echocardiography. Journal of the American Society of Echocardiography, 2007. 20(10): p. 1194-1202.
381. Belkin, R.N., et al., A novel two-dimensional echocardiographic finding in cardiac amyloidosis. Echocardiography, 2010. 27(10): p. 1171-1176.
382. Phelan, D., et al., Relative apical sparing of longitudinal strain using two-dimensional speckle-tracking echocardiography is both sensitive and specific for the diagnosis of cardiac amyloidosis. Heart, 2012. 98(19): p. 1442-8.
383. Sun, J.P., et al., Differentiation of hypertrophic cardiomyopathy and cardiac amyloidosis from other causes of ventricular wall thickening by two-dimensional strain imaging echocardiography. The American journal of cardiology, 2009. 103(3): p. 411-415.
384. Porcari, A., et al., Breakthrough advances enhancing care in ATTR amyloid cardiomyopathy. Eur J Intern Med, 2024.
385. Minamisawa, M., et al., Comparison of the standard and speckle tracking echocardiographic features of wild-type and mutated transthyretin cardiac amyloidoses. Eur Heart J Cardiovasc Imaging, 2016. 17(4): p. 402-10.
386. Di Nunzio, D., et al., Echocardiographic Findings in Cardiac Amyloidosis: Inside Two-Dimensional, Doppler, and Strain Imaging. Curr Cardiol Rep, 2019. 21(2): p. 7.
387. Hoffmann, R., et al., Reasons for interinstitutional observer variance in the interpretation of stress echocardiograms. Journal of the American College of Cardiology, 1996. 27(2S1): p. 404-404.
388. Breckwoldt, K., F. Weinberger, and T. Eschenhagen, *Heart regeneration.* Biochim Biophys Acta, 2016. **1863**(7 Pt B): p. 1749-59.

389. Smits, A.M., et al., *The role of stem cells in cardiac regeneration.* J Cell Mol Med, 2005. **9**(1): p. 25-36.
390. Ikada, Y., *Challenges in tissue engineering.* J R Soc Interface, 2006. **3**(10): p. 589-601.
391. Roche, E.T., et al., *Comparison of biomaterial delivery vehicles for improving acute retention of stem cells in the infarcted heart.* Biomaterials, 2014. **35**(25): p. 6850-6858.
392. Rane, A.A. and K.L. Christman, *Biomaterials for the treatment of myocardial infarction: a 5-year update.* J Am Coll Cardiol, 2011. **58**(25): p. 2615-29.
393. Miyagawa, S., et al., *Case report: Transplantation of human induced pluripotent stem cell-derived cardiomyocyte patches for ischemic cardiomyopathy.* Front Cardiovasc Med, 2022. **9**: p. 950829.
394. Kim, D., et al., *The Uncomfortable Truth: Open Thoracotomy versus Minimally Invasive Surgery in Lung Cancer: A Systematic Review and Meta-Analysis.* Cancers (Basel), 2023. **15**(9).
395. Collantes, M., et al., Non-invasive in vivo imaging of cardiac stem/progenitor cell biodistribution and retention after intracoronary and intramyocardial delivery in a swine model of chronic ischemia reperfusion injury. Journal of Translational Medicine, 2017. 15.
396. Prendiville, T.W., et al., Ultrasound-guided transthoracic intramyocardial injection in mice. J Vis Exp, 2014(90): p. e51566.
397. Bencherif, S.A., et al., Injectable preformed scaffolds with shape-memory properties. Proc Natl Acad Sci U S A, 2012. 109(48): p. 19590-5.
398. Dai, J., et al., Injectable Mesh-like Conductive Hydrogel Patch for Elimination of Atrial Fibrillation. Adv Healthc Mater, 2024: p. e2303219.
399. Fan, Z., et al., Near-Infrared Light-Triggered Unfolding Microneedle Patch for Minimally Invasive Treatment of Myocardial Ischemia. ACS Appl Mater Interfaces, 2021. 13(34): p. 40278-40289.
400. Mylonaki, I., et al., Stem cell viability and proliferation is maintained in vivo using an alginate patch designed for epicardial administration. Cytotherapy, 2020. 22(5, Supplement): p. S205.
401. Rojas, S.V., et al., Multimodal Imaging for In Vivo Evaluation of Induced Pluripotent Stem Cells in a Murine Model of Heart Failure. Artif Organs, 2017. 41(2): p. 192-199.
402. Kim, J.E., S. Kalimuthu, and B.C. Ahn, In vivo cell tracking with bioluminescence imaging. Nucl Med Mol Imaging, 2015. 49(1): p. 3-10.
403. Mei, X., et al., A fluid-powered refillable origami heart pouch for minimally invasive delivery of cell therapies in rats and pigs. Med, 2021. 2(11): p. 1253-1268.
404. Kasahara, H. and I. Hayashi, Polyglycolic acid sheet with fibrin glue potentiates the effect of a fibrin-based haemostat in cardiac surgery. J Cardiothorac Surg, 2014. 9: p. 121.
405. Patel, A.K., Chitosan: Emergence as potent candidate for green adhesive market. Biochemical Engineering Journal, 2015. 102: p. 74-81.
406. Li, J., et al., Tough adhesives for diverse wet surfaces. Science, 2017. 357(6349): p. 378-381.
407. Bargehr, J., et al., Epicardial cells derived from human embryonic stem cells

augment cardiomyocyte-driven heart regeneration. Nature Biotechnology, 2019. 37(8): p. 895-906.
408. Bargehr, J., et al., Epicardial cells derived from human embryonic stem cells augment cardiomyocyte-driven heart regeneration. Nat Biotechnol, 2019. 37(8): p. 895-906.
409. Zhu, K., et al., Conductive nanocomposite hydrogel and mesenchymal stem cells for the treatment of myocardial infarction and non-invasive monitoring via PET/CT. J Nanobiotechnology, 2022. 20(1): p. 211.
410. Aslund, A.K.O., et al., A comparative biodistribution study of polymeric and lipid-based nanoparticles. Drug Deliv Transl Res, 2022. 12(9): p. 2114-2131.
411. Cunha, L., et al., The role of molecular imaging in modern drug development. Drug Discov Today, 2014. 19(7): p. 936-48.
412. Willmann, J.K., et al., Molecular imaging in drug development. Nat Rev Drug Discov, 2008. 7(7): p. 591-607.
413. Nosrati, Z., et al., Simultaneous SPECT imaging with (123)I and (125)I - a practical approach to assessing a drug and its carrier at the same time with dual imaging. Int J Pharm, 2021. 606: p. 120884.
414. Qiao, P., et al., Noninvasive Monitoring of Reparative Fibrosis after Myocardial Infarction in Rats Using (68)Ga-FAPI-04 PET/CT. Mol Pharm, 2022. 19(11): p. 4171-4178.
415. Harman, M., et al., A Novel Bio-Adhesive Mesh System for Medical Implant Applications: In Vivo Assessment in a Rabbit Model. Gels, 2023. 9(5).
416. Mati-Baouche, N., et al., Chitosan as an adhesive. European Polymer Journal, 2014. 60: p. 198-212.
417. Jayabal, P., et al., Fabrication of a Chitosan-Based Wound Dressing Patch for Enhanced Antimicrobial, Hemostatic, and Wound Healing Application. ACS Appl Bio Mater, 2023. 6(2): p. 615-627.
418. Song, H., et al., Modification of mesenchymal stem cells for cardiac regeneration. Expert Opin Biol Ther, 2010. 10(3): p. 309-19.
419. Bushkalova, R., et al., Alginate-chitosan PEC scaffolds: A useful tool for soft tissues cell therapy. Int J Pharm, 2019. 571: p. 118692.
421. Jiang, Y., et al., Myocardial repair of bioengineered cardiac patches with decellularized placental scaffold and human-induced pluripotent stem cells in a rat model of myocardial infarction. Stem Cell Res Ther, 2021. 12(1): p. 13.
422. Panda, N.C., et al., Improved conduction and increased cell retention in healed MI using mesenchymal stem cells suspended in alginate hydrogel. Journal of Interventional Cardiac Electrophysiology, 2014. 41(2): p. 117-127.
423. Pok, S., et al., Use of myocardial matrix in a chitosan-based full-thickness heart patch. Tissue Eng Part A, 2014. 20(13-14): p. 1877-87.
424. Lee, S., et al., In vivo combinatory gene therapy synergistically promotes cardiac function and vascular regeneration following myocardial infarction. J Tissue Eng, 2020. 11: p. 2041731420953413.
425. Giacca, M., Cardiac Regeneration After Myocardial Infarction: an Approachable Goal. Current Cardiology Reports, 2020. 22(10): p. 122.
426. Leach, J.P. and J.F. Martin, Cardiomyocyte Proliferation for Therapeutic Regeneration. Current Cardiology Reports, 2018. 20(8): p. 63.
427. Lopez, A.E., et al., Gene Therapy: Targeting Cardiomyocyte Proliferation to

Repopulate the Ischemic Heart. J Cardiovasc Pharmacol, 2021. 78(3): p. 346-360.
428. Mahmoud, A.I., et al., Meis1 regulates postnatal cardiomyocyte cell cycle arrest. Nature, 2013. 497(7448): p. 249-253.
429. Su, E.J., et al., Gene therapy vector-mediated expression of insulin-like growth factors protects cardiomyocytes from apoptosis and enhances neovascularization. Am J Physiol Heart Circ Physiol, 2003. 284(4): p. H1429-40.
430. Abbas, N., F. Perbellini, and T. Thum, Non-coding RNAs: emerging players in cardiomyocyte proliferation and cardiac regeneration. Basic Research in Cardiology, 2020. 115(5): p. 52.
431. Eulalio, A., et al., Functional screening identifies miRNAs inducing cardiac regeneration. Nature, 2012. 492(7429): p. 376-381.
432. Tao, Y., et al., miR-199a-3p promotes cardiomyocyte proliferation by inhibiting Cd151 expression. Biochem Biophys Res Commun, 2019. 516(1): p. 28-36.
433. Ounzain, S., et al., CARMEN, a human super enhancer-associated long noncoding RNA controlling cardiac specification, differentiation and homeostasis. Journal of Molecular and Cellular Cardiology, 2015. 89: p. 98-112.
434. Zhang, Z., et al., Increased plasma levels of lncRNA H19 and LIPCAR are associated with increased risk of coronary artery disease in a Chinese population. Sci Rep, 2017. 7(1): p. 7491.
435. Si, X., et al., circRNA Hipk3 Induces Cardiac Regeneration after Myocardial Infarction in Mice by Binding to Notch1 and miR-133a. Mol Ther Nucleic Acids, 2020. 21: p. 636-655.
436. Gabisonia, K., et al., MicroRNA therapy stimulates uncontrolled cardiac repair after myocardial infarction in pigs. Nature, 2019. 569(7756): p. 418-422.
437. Monroe, T.O., et al., YAP Partially Reprograms Chromatin Accessibility to Directly Induce Adult Cardiogenesis In Vivo. Dev Cell, 2019. 48(6): p. 765-779 e7.
438. Ozhan, G. and G. Weidinger, Wnt/beta-catenin signaling in heart regeneration. Cell Regen, 2015. 4(1): p. 3.
439. Flinn, M.A., B.A. Link, and C.C. O'Meara, Upstream regulation of the Hippo-Yap pathway in cardiomyocyte regeneration. Semin Cell Dev Biol, 2020. 100: p. 11-19.
440. Xin, M., et al., Hippo pathway effector Yap promotes cardiac regeneration. Proc Natl Acad Sci U S A, 2013. 110(34): p. 13839-44.
441. Johnson, R. and G. Halder, The two faces of Hippo: targeting the Hippo pathway for regenerative medicine and cancer treatment. Nat Rev Drug Discov, 2014. 13(1): p. 63-79.
442. Mannaerts, I., et al., The Hippo pathway effector YAP controls mouse hepatic stellate cell activation. J Hepatol, 2015. 63(3): p. 679-88.
443. Huynh, K., Basic research: Inhibition of Hippo pathway signalling reverses systolic heart failure. Nat Rev Cardiol, 2017. 14(12): p. 697.
444. Lin, Z., et al., Cardiac-specific YAP activation improves cardiac function and survival in an experimental murine MI model. Circ Res, 2014. 115(3): p. 354-

63.
445. Shao, D., et al., A functional interaction between Hippo-YAP signalling and FoxO1 mediates the oxidative stress response. Nat Commun, 2014. 5: p. 3315.
446. Korpela, H., et al., AAV2-VEGF-B gene therapy failed to induce angiogenesis in ischemic porcine myocardium due to inflammatory responses. Gene Ther, 2022. 29(10-11): p. 643-652.
447. Mühlhauser, J., et al., Safety and efficacy of in vivo gene transfer into the porcine heart with replication-deficient, recombinant adenovirus vectors. Gene Therapy, 1996. 3(2): p. 145-153.
448. Merentie, M., et al., Efficacy and safety of myocardial gene transfer of adenovirus, adeno-associated virus and lentivirus vectors in the mouse heart. Gene Ther, 2016. 23(3): p. 296-305.
449. Bish, L.T., et al., Adeno-associated virus (AAV) serotype 9 provides global cardiac gene transfer superior to AAV1, AAV6, AAV7, and AAV8 in the mouse and rat. Hum Gene Ther, 2008. 19(12): p. 1359-68.
450. G.J.J. Boink, J.W., M. Klerk, V.M. Christoffels, H.L. Tan, D. Geerts, Sodium channel gene therapy with dual adeno-associated viral vectors. European Heart Journal, 2019. 40.
451. Ni, L., et al., Atrial-Specific Gene Delivery Using an Adeno-Associated Viral Vector. Circ Res, 2019. 124(2): p. 256-262.
452. Ulaganathan, T., et al., Pathological implications of cellular stress in cardiovascular diseases. Int J Biochem Cell Biol, 2023. 158: p. 106397.
453. Heallen, T., et al., Hippo signaling impedes adult heart regeneration. Development, 2013. 140(23): p. 4683-90.
454. Chen, I.Y., et al., Noninvasive imaging of hypoxia-inducible factor-1alpha gene therapy for myocardial ischemia. Hum Gene Ther Methods, 2013. 24(5): p. 279-88.
455. Mugahid, D., et al., YAP regulates cell size and growth dynamics via non-cell autonomous mediators. Elife, 2020. 9.
456. Papizan, J.B. and E.N. Olson, Hippo in the path to heart repair. Circ Res, 2014. 115(3): p. 332-4.
457. Choe, M.S., et al., Human embryonic stem cell-specific role of YAP in maintenance of self-renewal and survival. Cell Mol Life Sci, 2022. 79(11): p. 544.
458. Hou, N., et al., Activation of Yap1/Taz signaling in ischemic heart disease and dilated cardiomyopathy. Exp Mol Pathol, 2017. 103(3): p. 267-275.
459. von Gise, A., et al., YAP1, the nuclear target of Hippo signaling, stimulates heart growth through cardiomyocyte proliferation but not hypertrophy. Proc Natl Acad Sci U S A, 2012. 109(7): p. 2394-9.
460. Lembo, M., et al., Impact of left ventricular mass/end-diastolic volume ratio by three-dimensional echocardiography on two-dimensional global longitudinal strain and diastolic function in native hypertensive patients. J Hypertens, 2019. 37(10): p. 2041-2047.
461. Shimada, Y.J., et al., Myocardial Contraction Fraction Predicts Cardiovascular Events in Patients With Hypertrophic Cardiomyopathy and Normal Ejection Fraction. J Card Fail, 2019. 25(6): p. 450-456.
462. Jentzer, J.C., et al., Myocardial contraction fraction by echocardiography and

mortality in cardiac intensive care unit patients. Int J Cardiol, 2021. 344: p. 230-239.
463. Windmueller, R. and E.E. Morrisey, Hippo and Cardiac Hypertrophy: A Complex Interaction. Circ Res, 2015. 117(10): p. 832-4.
464. Del Re, D.P., et al., Yes-associated protein isoform 1 (Yap1) promotes cardiomyocyte survival and growth to protect against myocardial ischemic injury. J Biol Chem, 2013. 288(6): p. 3977-88.
465. Morikawa, Y., et al., Actin cytoskeletal remodeling with protrusion formation is essential for heart regeneration in Hippo-deficient mice. Sci Signal, 2015. 8(375): p. ra41.
466. Katz, M.G., et al., Gene delivery technologies for cardiac applications. Gene Ther, 2012. 19(6): p. 659-69.
467. Oboirien, I.O., et al., Echocardiographic Assessment of the Left Ventricle in Young Prehypertensive Nigerians. Cureus, 2023. 15(10): p. e46740.
468. Lairez, O., et al., Prediction of all-cause mortality from gated-SPECT global myocardial wall thickening: comparison with ejection fraction and global longitudinal 2D-strain. J Nucl Cardiol, 2014. 21(1): p. 86-95.
469. Russo, C., et al., Relationship of multidirectional myocardial strain with radial thickening and ejection fraction and impact of left ventricular hypertrophy: a study in a community-based cohort. Echocardiography, 2013. 30(7): p. 794-802.
470. Liao, S.S., et al., Value of segmental myocardial strain by 2-dimensional strain echocardiography for assessment of scar area induced in a rat model of myocardial infarction. Cardiovasc Ultrasound, 2012. 10: p. 17.
471. de Lucia, C., et al., Echocardiographic Strain Analysis for the Early Detection of Left Ventricular Systolic/Diastolic Dysfunction and Dyssynchrony in a Mouse Model of Physiological Aging. J Gerontol A Biol Sci Med Sci, 2019. 74(4): p. 455-461.
472. Ma, C., X. Wang, and T. Varghese, Segmental Analysis of Cardiac Short-Axis Views Using Lagrangian Radial and Circumferential Strain. Ultrason Imaging, 2016. 38(6): p. 363-383.
473. Korinek, J., et al., Two-dimensional strain--a Doppler-independent ultrasound method for quantitation of regional deformation: validation in vitro and in vivo. J Am Soc Echocardiogr, 2005. 18(12): p. 1247-53.
474. Helle-Valle, T.M., et al., Usefulness of radial strain mapping by multidetector computer tomography to quantify regional myocardial function in patients with healed myocardial infarction. Am J Cardiol, 2010. 106(4): p. 483-91.
475. Mia, M.M., et al., YAP/TAZ deficiency reprograms macrophage phenotype and improves infarct healing and cardiac function after myocardial infarction. PLoS Biol, 2020. 18(12): p. e3000941.
476. Mohri, Z., A. Del Rio Hernandez, and R. Krams, The emerging role of YAP/TAZ in mechanotransduction. J Thorac Dis, 2017. 9(5): p. E507-E509.
477. Xie, J., et al., Substrate stiffness-regulated matrix metalloproteinase output in myocardial cells and cardiac fibroblasts: implications for myocardial fibrosis. Acta Biomater, 2014. 10(6): p. 2463-72.
478. Garoffolo, G., et al., Reduction of Cardiac Fibrosis by Interference With YAP-Dependent Transactivation. Circ Res, 2022. 131(3): p. 239-257.

479. Arshi, A., et al., Rigid microenvironments promote cardiac differentiation of mouse and human embryonic stem cells. Sci Technol Adv Mater, 2013. 14(2).
480. Dupont, S., Regulation of YAP/TAZ Activity by Mechanical Cues: An Experimental Overview, in The Hippo Pathway: Methods and Protocols, A. Hergovich, Editor. 2019, Springer New York: New York, NY. p. 183-202.
481. Dupont, S., et al., Role of YAP/TAZ in mechanotransduction. Nature, 2011. 474(7350): p. 179-83.
482. Bassat, E., et al., The extracellular matrix protein agrin promotes heart regeneration in mice. Nature, 2017. 547(7662): p. 179-184.
483. Yin, X., et al., Post-myocardial infarction fibrosis: Pathophysiology, examination, and intervention. Front Pharmacol, 2023. 14: p. 1070973.
484. Yap, J., et al., Macrophages in cardiac remodelling after myocardial infarction. Nat Rev Cardiol, 2023. 20(6): p. 373-385.
485. Kwon, S.H. and A.S. Gopal, 3D and 4D ultrasound: Current progress and future perspectives. Current Cardiovascular Imaging Reports, 2017. 10: p. 1-13.